INSTITUTE OF GEOSCIENCES

Imaging and modeling of hydraulic fractures in crystalline rock via induced seismic activity

Peter Niemz

Cumulative dissertation

to obtain the academic degree "doctor rerum naturalium" (Dr. rer. nat.)
in the scientific discipline Seismology.

Submitted to the
Faculty of Mathematics and Natural Sciences
at the University of Potsdam, Germany.

Prepared at
Section 2.1 (Physics of Earthquakes and Volcanoes) &
Section 2.6 (Seismic Hazard and Risk Dynamics)
Department of Geophysics, Helmholtz Centre Potsdam -
GFZ German Research Centre for Geosciences.
&
Institute of Geosciences, University of Potsdam, Germany.

Date of disputation: 9 June 2022

Academic advisor: Prof. Dr. Arno Zang, University of Potsdam, Germany.
Second advisor: Prof. Dr. Torsten Dahm, University of Potsdam, Germany

Reviewers: 1. Prof. Dr. Torsten Dahm
2. Prof. Dr., Dipl.-Ing. Gerd Manthei
3. Dr. Volker Oye

Examining committee: 1. Prof. Dr. Torsten Dahm
2. Prof. Dr. Arno Zang
3. Prof. Dr., Dipl.-Ing. Gerd Manthei
4. Prof. Dr. Frank Krüger

Published online on the
Publication Server of the University of Potsdam:
https://doi.org/10.25932/publishup-55659
https://nbn-resolving.org/urn:nbn:de:kobv:517-opus4-556593

Statement of Originality

I hereby declare that this thesis is the product of my own work. All the assistance received in preparing this thesis and the sources used have been acknowledged. The work contained in this thesis has not been previously submitted for a PhD degree at any other higher education institution.

Potsdam, _____

_____

Peter Niemz

Table of Contents

Abstract

Enhanced geothermal systems (EGS) are considered a cornerstone of future sustainable energy production. In such systems, high-pressure fluid injections break the rock to provide pathways for water to circulate in and heat up. This approach inherently induces small seismic events that, in rare cases, are felt or can even cause damage. Controlling and reducing the seismic impact of EGS is crucial for a broader public acceptance. To evaluate the applicability of hydraulic fracturing (HF) in EGS and to improve the understanding of fracturing processes and the hydromechanical relation to induced seismicity, six in-situ, meter-scale HF experiments with different injection schemes were performed under controlled conditions in crystalline rock in a depth of 410 m at the Äspö Hard Rock Laboratory (Sweden) by Zang et al. (2017).

I developed a semi-automated, full-waveform-based detection, classification, and location workflow to extract and characterize the acoustic emission (AE) activity from the continuous recordings of 11 piezoelectric AE sensors. Based on the resulting catalog of 20,000 AEs, with rupture sizes of cm to dm, I mapped and characterized the fracture growth in great detail. The injection using a novel cyclic injection scheme (HF3) had a lower seismic impact than the conventional injections. HF3 induced fewer AEs with a reduced maximum magnitude and significantly larger b-values, implying a decreased number of large events relative to the number of small ones. Furthermore, HF3 showed an increased fracture complexity with multiple fractures or a fracture network. In contrast, the conventional injections developed single, planar fracture zones (Publication 1).

An independent, complementary approach based on a comparison of modeled and observed tilt exploits transient long-period signals recorded at the horizontal components of two broadband seismometers a few tens of meters apart from the injections. It validated the efficient creation of hydraulic fractures and verified the AE-based fracture geometries. The innovative joint analysis of AEs and tilt signals revealed different phases of the fracturing process, including the (re-)opening, growth, and aftergrowth of fractures, and provided evidence for the reactivation of a preexisting fault in one of the experiments (Publication 2). A newly developed network-based waveform-similarity analysis applied to the massive AE activity supports the latter finding.

To validate whether the reduction of the seismic impact as observed for the cyclic injection schemes during the Äspö mine-scale experiments is transferable to other scales, I additionally calculated energy budgets for injection experiments from previously conducted laboratory tests and from a field application. Across all three scales, the cyclic injections reduce the seismic impact, as depicted by smaller maximum magnitudes, larger b-values, and decreased injection efficiencies (Publication 3).

Zusammenfassung

Hydraulisch-stimulierte tiefengeothermale Systeme (Enhanced Geothermal systems, EGS) gelten als einer der Eckpfeiler für die nachhaltige Energieerzeugung der Zukunft. In diesen geothermalen Systemen wird heißes Tiefengestein durch Fluidinjektionen unter hohem Druck aufgebrochen, um Wegsamkeiten zur Erwärmung von Wasser oder anderen Fluiden zu schaffen. Beim Aufbrechen werden zwangsläufig kleine seismische Ereignisse ausgelöst (induzierte Seismizität), die in sehr seltenen Fällen an der Oberfläche spürbar sind, jedoch in extremen Fällen auch Schäden verursachen können. Die Kontrolle bzw. die Reduzierung der seismischen Aktivität in EGS ist daher ein entscheidender Punkt, damit diese Art der Energiegewinnung eine breite gesellschaftliche Akzeptanz findet.

Grundlage dieser Dissertation ist eine Serie von kontrollierten, hydraulischen Bruchexperimenten mit Bruchdimensionen von einigen Metern. Die Experimente wurden in einer Tiefe von 410 m in kristallinem Gestein eines Versuchsbergwerks (Äspö Hard Rock Laboratory, Schweden) mit unterschiedlichen Injektionsstrategien durchgeführt. Die detaillierte Auswertung der Bruch-Experimente in dieser Dissertation zielt darauf ab, die Nutzbarkeit von hydraulischen Stimulationen (hydraulic fracturing, HF) in EGS zu untersuchen und das Verständnis von Bruchprozessen sowie der hydromechanischen Beziehung zur induzierten Seismizität zu verbessern.

Um die Schallemissionsaktivität (acoustic emissions, AE), die durch 11 piezoelektrische AE-Sensoren kontinuierlich aufgezeichnet wurde, zu extrahieren und zu charakterisieren, wurde ein halbautomatischer, wellenformbasierter Detektions-, Klassifizierungs- und Lokalisierungsworkflow entwickelt. Mit Hilfe des resultierenden Katalogs von 20000 AEs wurde das Bruchwachstum detailliert kartiert und charakterisiert. Das Experiment mit der neuartigen, zyklischen Injektionsstrategie (HF3) weist einen geringeren seismischen Fußabdruck auf als die Standard-Injektionsstrategie. HF3 induzierte weniger AEs und eine kleinere Maximalmagnitude. Außerdem hatte das Experiment einen signifikant höheren b-Wert, was einer verringerten Anzahl von großen AEs relativ zur Anzahl der kleineren AEs entspricht. Darüber hinaus zeigte HF3 eine erhöhte Komplexität im Bruchmuster mit mehreren Brüchen bzw. einem Netzwerk von Brüchen. Im Gegensatz dazu entwickelten die Standard-Injektionen einzelne, ebene Bruchzonen (Publikation 1).

Zusätzlich zu den induzierten AEs wurden transiente, langperiodische Signale auf den horizontalen Komponenten von zwei Breitband-Seismometern, die wenige Meter von den Brüchen installiert waren, ausgewertet. Diese Signale wurden als Neigungssignale interpretiert und mit modellierten Neigungssignalen verglichen. Der Vergleich zeigt unabhängig, dass hydraulische Brüche geöffnet wurden und bestätigt, dass die AE-basierte Analyse die Bruchgeometrie verlässlich kartieren kann. Die gemeinsame Betrachtung von AEs und Neigungssignalen offenbart

verschiedene Phasen des Bruchprozesses: das (wiederholte) Öffnen des Bruches, das Bruchwachstum und das weitere Wachsen des Bruches nach dem Ende der Injektion. Außerdem liefert die Analyse Hinweise auf die Reaktivierung einer natürlichen Bruchzone in einem der Experimente (Publikation 2). Eine neuentwickelte und hier präsentierte Wellenform-Ähnlichkeitsanalyse, die Informationen des gesamten Sensornetzwerkes nutzt und zum ersten Mal auf einen umfangreichen AE-Katalog angewendet wurde, unterstützt diese Interpretation.

Um zu validieren, ob die verringerte Seismizität während der zyklischen Injektion auf der Meter-Skala (Bergwerk) auf andere Maßstäbe übertragbar ist, wurden Energie-Budgets für Injektionsexperimente aus zuvor durchgeführten Laborversuchen und aus einem Tiefengeothermie-Projekt berechnet. Über alle drei Skalen hinweg zeigen die zyklischen Injektionen einen verringerten seismischen Fußabdruck mit kleineren Maximalmagnituden, größeren b-Werte und einem kleineren Verhältnis von seismisch-abgestrahlter zu injizierter Energie (Publikation 3).

1 Introduction

This chapter provides a brief introduction to injection-induced seismicity and enhanced geothermal systems in general and to the in-situ mine-scale experiments at the Äspö Hard Rock Laboratory (HRL) in Sweden (Zang et al., 2017) in particular.

1.1 Injection-induced seismicity

Industrial activities in the subsurface have the potential to induce seismic events that, in rare cases, can be felt at the surface or may even cause damages to buildings or the population. Apart from the extraction of resources, e.g., in underground mines or gas reservoirs (e.g., Oye et al., 2005; van Thienen-Visser & Breunese, 2015), the injection of fluids into the ground can induce felt seismicity (Ellsworth, 2013; Foulger et al., 2018). This concerns a wide range of geotechnical applications, reaching from geothermal energy production (e.g., Diehl et al., 2017; Grigoli et al., 2018; Häring et al., 2008; Kim et al., 2018; Zang et al., 2014) and underground gas storage (e.g., Cesca et al., 2014; Cesca et al., 2021) to the exploitation of hydrocarbon resources (e.g., Clarke et al., 2014; Keranen et al., 2014; Schultz, Skoumal, et al., 2020), including both hydraulic fracturing and wastewater disposal. Due to the increase of industrial activity in these domains and the increased awareness for accompanying seismic activity, injection-induced seismicity became a topic of public concern and a major topic in geosciences in recent years (Grigoli et al., 2017). While the mitigation of large induced events is crucial to retain the public acceptance of subsurface operations, e.g., regarding geothermal energy production, the analysis of induced seismic activity is an important and highly valuable tool to monitor, understand, and control subsurface operations (e.g., Maxwell et al., 2009). In this thesis, I exploit the information contained within the induced seismic activity to study fracturing processes during in-situ, mine-scale experiments conducted at Äspö HRL.

1.2 Enhanced geothermal systems

1.2.1 Concept

Geothermal energy is considered a cornerstone of future, sustainable energy supply (Giardini, 2009; Stauffacher et al., 2015). However, in regions without volcanic activity, this requires a stimulation of the subsurface to produce an efficient heat exchange at depth, an enhanced

geothermal system (EGS, also referred to as hot dry rock system). Suitable temperatures are typically reached at depths of several kilometers, which often implies the stimulation of crystalline basement rocks (McClure & Horne, 2014). This thesis concerns hydromechanical fracture processes due to high-pressure fluid injections, noting that thermal or chemical processes can also drive fracturing. The stimulation can result in both, the opening of new tensile fractures within the intact rock (hydraulic fracturing) and the reactivation of preexisting shear faults (hydraulic shearing). It is still debated which stimulation process is dominant in a particular geological setting or in particular experiments (McClure & Horne, 2014). Independent of the dominant process, new or reactivated fractures and faults serve as pathways for fluids, consequently resulting in an increased permeability. In geothermal energy production, the creation of new fluid pathways increases the contact surface between the hot rock and the cold fluid pumped into the subsurface. Hydraulic shearing is often favored over hydraulic fracturing in the presence of known preexisting faults since the permeability increase is expected to be larger and remanent (Gischig & Preisig, 2015). However, wellhead pressures larger than the minimum principal stress provide evidence that hydraulic fracturing has occurred in most EGS projects (McClure & Horne, 2014). The controlled opening of new fractures in HF can help to overcome risks arising from the reactivation of preexisting faults, as done in injections that aim for hydraulic shearing in EGS. While hydraulic fracture growth is well-studied in shale and sedimentary rock, it is unclear whether the knowledge can be transferred directly to crystalline rock (Fu et al., 2021). The interpretation of the acting processes is further complicated by the presence of aseismic processes that are not detectable by typical seismic monitoring equipment (e.g., Cornet et al., 1997; Guglielmi et al., 2015). The observations and interpretations from the mine-scale experiments at Äspö contribute to a better understanding of the growth of hydraulic fractures in crystalline rock, including the characterization of the influence of the injection parameters and further external factors.

1.2.2 Induced seismicity

Aside from the mechanisms acting during fluid injections, the seismic impact of the injections remains another critical aspect in the study of enhanced geothermal systems. Enhancing a geothermal system by breaking the rock mass via high-pressure fluid injections inherently induces a seismic response. However, only in rare cases, these induced earthquakes are felt at the surface. The Basel Geothermal Project and the EGS experiments at Pohang are prominent cases of felt and damaging induced seismicity due to fluid injection in enhanced geothermal systems (Häring et al., 2008; Kim et al., 2018). The Basel project was eventually suspended after an earthquake of magnitude M_L3.4 (Häring et al., 2008). The same applies to the experiments at Pohang, which triggered an M_w5.5 event (Ellsworth et al., 2019; Grigoli et al., 2018). More recently, several >M3 earthquakes were reported from an EGS near Strasbourg, France (Schmittbuhl et al., 2021). There is evidence that the massive fluid injection triggered the slip of a nearby natural fault in each of these cases (Deichmann & Giardini, 2009; Ellsworth et al., 2019; Schmittbuhl et al., 2021). Contrary, in many other EGS, there was no felt seismicity, e.g., at Helsinki EGS (Kwiatek et al., 2019). A better understanding of fluid and fracture-related processes during injections is essential for the mitigation of felt seismicity and for a successful and efficient implementation of EGS. Many strategies for lowering the seismic impact of fluid injection have been proposed and

have been applied, e.g., limitations of injection volumes (McGarr, 2014), traffic light systems (Bommer et al., 2006; Schultz, Beroza, et al., 2020), and alternative injection schemes (Hofmann et al., 2019; Hofmann et al., 2021; Zang et al., 2017; Zang et al., 2013).

1.3 In-situ, mine-scale injection experiments

In recent years, mine-scale experiments in crystalline rock became the focus of different research groups since crystalline rock is usually found at a depth of a few kilometers, where thermodynamic conditions are expected to be favorable for an efficient energy production in large-scale geothermal projects. However, the great depth limits monitoring capabilities, so mine-scale experiments provide the best compromise between providing realistic stress and site conditions, that can only be simulated to a certain extent in laboratory experiments (e.g., Haimson, 1981), and a dense monitoring of the processes acting during fluid injections. Important recent mine-scale hydraulic fracturing experiments in crystalline rock are the experiments of Zang et al. (2017) conducted at the Äspö HRL, the EGS Collab project (Schoenball et al., 2020), and the Grimsel experiments (Amann et al., 2018). The experiments strive for a better understanding of processes acting in deep EGS, including hydraulic fracturing growth (Äspö), shear stimulation or a mixture of both (Grimsel, EGS Collab). My thesis contributes to the ongoing research in this domain via detailed analyses and the interpretation of different continuous seismological data sets recorded during the injections at Äspö HRL. Such controlled injection experiments at mine-scale provide excellent conditions to approach the research questions presented in Chapter 2. More generally, the findings contribute to the ongoing optimization process of innovative injection schemes that have the potential to lower the seismic impact of enhanced geothermal systems.

1.3.1 Experimental setup at Äspö HRL

The in-situ hydraulic fracturing experiments of Zang et al. (2017), which provide the basic data sets analyzed in this cumulative thesis, were conducted at a depth of 410 m within granitic basement rock in the Äspö HRL. The experimental setup intends to bridge the gap between laboratory and field-scale. The injection borehole with a length of 28 m was drilled sub-horizontally from an adjacent tunnel matching the direction of the least principal stress. Three monitoring boreholes containing uni-directional piezoelectric borehole sensors surrounded the injection borehole. Additional piezoelectric sensors were located inside the tunnel walls. The sensors are able to detect acoustic emissions (AE) in the frequency range between 1 kHz and 100 kHz (Zang et al., 2017). For relatively large events, the records of acoustic emissions look similar to seismograms with clear onsets of first arriving P phases and secondary S phases (Manthei, Eisenblätter, et al., 2001). In fact, AEs are tiny earthquakes with fracture sizes of a millimeters to decimeters (Bohnhoff et al., 2009; Dahm, 2001). An essential feature of the Äspö experiments was the coverage of a broad frequency range within the monitoring setup to record different aspects of the experiments: Besides the piezoelectric AE sensors (1 kHz - 100 kHz), accelerometers (50 Hz - 25 kHz) were installed at the tunnel walls, and broadband seismometers (mHz - 100 Hz) and geophones (4.5 Hz to 1 kHz) were set up in adjacent tunnels (Fig. 1.1). My thesis exploits this

unique monitoring setup, spanning the full seismic spectrum, by comparing AE and broadband signals registered during high-pressure fluid injections.

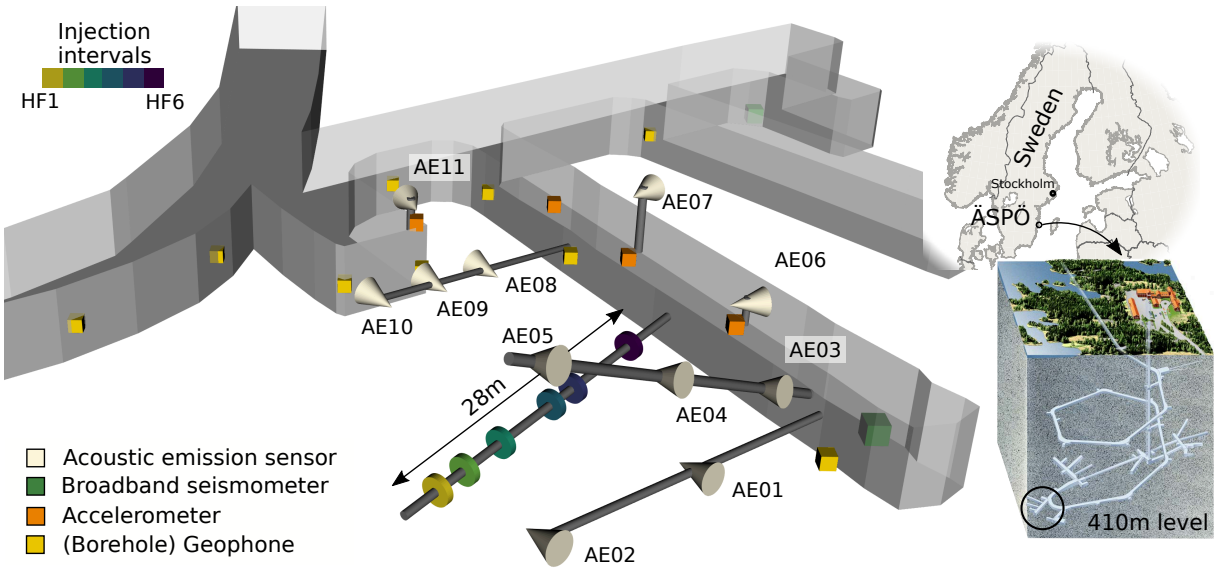

Figure 1.1: The hydraulic fracturing experiments were conducted at a tunnel of the Äspö HRL at a depth of 410 m. Colored discs indicate the six experiments in the central injection borehole. The experiments were monitored by a network of complementary sensors in the tunnels and the three monitoring boreholes. Lower right image modified after López-Comino et al. (2017).

1.3.2 Injection schemes

Six independent injections experiments (HF1 to HF6) were performed at different segments of the 28 m long injection borehole (Fig. 1.1). In each of the experiments, 20 l to 30 l of tap water were injected into the rock from sealed, fracture-free packer intervals. Three different injection schemes were tested:

(a) conventional continuous (HF1,HF2,HF4,HF6)

(b) cyclic progressive (HF3, short cyclic)

(c) cyclic pulse (HF5, short pulse)

The injection schemes differ in the initial fracturing stage. In the conventional scheme (Fig. 1.2a), the injection pressure is continuously increased until the rock fails at the fracture breakdown pressure (FBP). In contrast, the initial fracturing stage of the cyclic progressive approach (HF3, Fig. 1.2b) consists of several pressurization steps with depressurization phases in between. In each step, the injection pressure is increased by 10 to 20% until reaching the FBP. In the cyclic pulse pressurization (HF5, Fig. 1.2c), a secondary pump adds a pulsating pressurization to the cyclic injections (Zang et al., 2017). The latter two schemes shall weaken the rock by hydraulic fatigue (Zang et al., 2019) to produce more complex fracture networks in the following refracturing stages, which dissipates the emitted seismic energy and enhances the permeability.

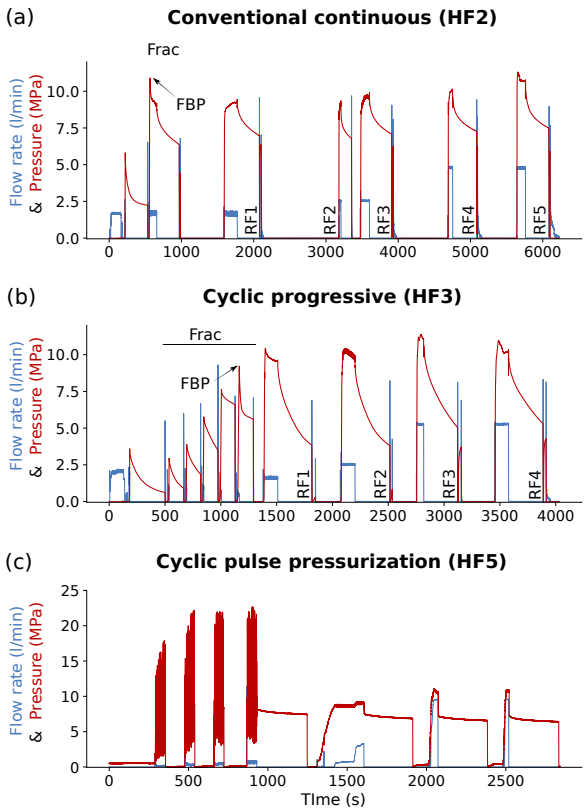

Figure 1.2: The three subplots show the injection pressure and the flow rate versus time for the tested injection schemes. (a) In the conventional continuous scheme (here HF2, but also HF1, HF4, and HF6), the fracturing stage (Frac) consists of only one pressurization phase. (b) The cyclic progressive injection scheme (HF3) is characterized by multiple phases of pressurization and depressurization in the fracturing stage. The target pressure is increased in each phase until reaching the fracture breakdown pressure (FBP). The following refracturing stages (RF) are similar in both schemes. (c) The cyclic pulse injection (HF5) is similar to the cyclic progressive scheme, but pressurization is pulsating. The fracturing stages are followed by 3 to 5 refracturing stages. The pressurizations seen before the fracturing stages in the a and b are attributed to integrity tests.

1.3.3 Continuous recordings of injection-induced seismic signals

During the experiments, the sensors recorded the AE activity in two modes: triggered and continuous. The triggered recording systems helped to track and control the fracture evolution during the stimulation (Zang et al., 2017), but it is limited to the largest events since the triggering threshold was set conservatively to exclude noise events (Kwiatek et al., 2018). The sparse triggered catalog of 196 relocalized AEs reveals a migration of the AE activity away from the borehole or towards the borehole, depending on the injection stage (Kwiatek et al., 2018; Zang et al., 2017). The orientations and the extents of the hypocentral cloud are consequently only rough estimates, which cannot resolve details of the spatiotemporal fracture growth. Zang et al. (2017) and Kwiatek et al. (2018) anticipated that the continuous recordings of the Äspö experiments contain many more events. These events can shed light on processes that cannot be studied relying on the largest events only, such as the early fracturing stages of HF3 or the experiments HF4 and HF5, for which there are no events in the triggered catalog (Zang et al., 2017). López-Comino et al. (2017) proved the potential of full-waveform techniques (detection

and location) by analyzing the continuous waveforms of one of six experiment (HF2).

1.4 Structure of the thesis

1.4.1 Overview of publications included as chapters of this thesis

This cumulative thesis is comprised of three main publications. Two of these focus on hydraulic fracturing growth in the context of enhanced geothermal systems, based on the seismological analysis and interpretation of in-situ, mine-scale injection experiments in crystalline rock (Niemz et al., 2020; Niemz et al., 2021). My thesis improves the approach of López-Comino et al. (2017), which included only a single experiment, by incorporating an additional event classification step into a full-waveform-based workflow for the continuous AE recordings to ensure a uniform treatment of the continuous waveforms across all six experiments. This workflow provides comparable catalogs based on a common detection threshold. The catalogs are a prerequisite for a detailed comparative analysis of the different experiments, going well-beyond the aforementioned studies of López-Comino et al. (2017) and Kwiatek et al. (2018). In particular, the decreased detection threshold provides a more detailed insight into the early processes of each injection stage. The catalog of triggered events cannot resolve this phase since the first events were recorded only after 30 to 120 sec. Furthermore, I studied novel observations of long-period transients recorded on two broadband seismometers. These transients are tilt-induced deformation signals, which can depict complementary aspects of the fracturing process since it is uncertain whether the AE activity alone can successfully track the full fracture extent and the creation of an efficient fracture.

The third paper, a co-authored publication (Zang et al., 2021), includes two additional scales: laboratory injection experiments inducing fractures of a few centimeters in length and the field-scale with deep injections and fracture networks extending several hundreds of meters or a few kilometers. This publication reviews processes acting during cyclic fluid injections across all three scales in a comparative way.

1. **P. Niemz**, S. Cesca, S. Heimann, F. Grigoli, S. von Specht, C. Hammer, A. Zang, and T. Dahm. Full waveform-based characterization of acoustic emission activity in a mine-scale experiment: a comparison of conventional and advanced hydraulic fracturing schemes. Geophysical Journal International, 222(1):189–206, 2020. https://doi.org/10.1093/gji/ggaa127

   P.N. conceptualized the workflow and performed all formal analyses, including the setup and tuning of the existing tools for the detection, classification, and location of AEs, the implementation of the magnitude and b-value calculation and the implementation of the spatial clustering for the fracture plane approximation, and interpreted the results. P.N. wrote the first draft of the manuscript and was responsible for the visualization of the results.

2. **P. Niemz**, T. Dahm, C. Milkereit, S. Cesca, G. Petersen, A. Zang. Insights into hydraulic

fracture growth gained from a joint analysis of seismometer-derived tilt and acoustic emissions. Submitted to Journal of Geophysical Research: Solid Earth. 2021.

> P.N. partly conceptualized the study (together with TD), performed the formal analyses (tilt extraction, forward modeling of tilt signals), and interpreted the results. P.N. wrote the first draft of the manuscript and was responsible for the visualization of the result.

3. A. Zang, G. Zimmermann, H. Hofmann, **P. Niemz**, K. W. Kim, M. Diaz, L. Zhuang, J. S. Yoon (2021). Relaxation damage control via fatigue-hydraulic fracturing in granitic rock as inferred from laboratory-, mine-, and field-scale experiments. Scientific Reports, 11(1), 81–96. https://doi.org/10.1038/s41598-021-86094-5

> P.N. partly conceptualized (together with AZ) and performed the energy calculation (seismic energies and the scaling relations) P.N. estimated the b-values at all three scales: laboratory, mine, and field. P.N. also contributed to the absolute calibration of the laboratory sensors, a prerequisite for the energy calculation. P.N. was responsible for the visualization of the results.

1.4.2 Additional relevant publications

Large data sets, such as massive seismic swarms or AE activity, do not allow a detailed analysis of every single event. Instead, cluster analyses can help to summarize and understand important aspects of the acting processes. Therefore, I refer to two further studies that I co-authored in the course of my doctoral studies. In Petersen and Niemz et al. (2021), we introduced a new full-waveform-based network-similarity approach to characterize and map faults and fractures. The approach was implemented in the python-based toolbox *Clusty*, which I applied to natural (Petersen and Niemz et al., 2021) and induced (Cesca et al., 2021) earthquake sequences. This new approach complements the seismological analyses presented in the three main publications and provides additional insight into rupture processes of injection-induced seismicity based on seismic waveform similarities. The two publications are not included as chapters of this thesis, but results and methods are discussed in Chapter 3.2.1, Chapter 7, and Appendix A.

1. G. Petersen, **P. Niemz**, S. Cesca, V. Mouslopoulou, GM. Bocchini (2021). Clusty, the waveform-based network similarity clustering toolbox: concept and application to image complex faulting offshore Zakynthos (Greece). Geophysical Journal International, 224(3),2044–2059. https://doi.org/10.1093/gji/ggaa568

> P.N. and G.P. jointly conceptualized the study, implemented the toolbox, performed the analysis, and wrote the first draft of the manuscript. More specifically, P.N. implemented the parallelized computation of the cross-correlation values of the single stations and event-pairs, parts of the methods to compute the network similarity from the cross-correlation values (e.g., the weighted sum following Shelly et al. (2016)) and the harmonization of results obtained from

different clustering settings and multiple frequency ranges. Furthermore, he implemented the clustering based on DBSCAN and optics from scikit-learn and several analysis/result plots (e.g., the network plot and the flow diagram). What is mentioned here as implementation also includes the study of the theoretical background. Additionally, he performed the principal component analysis of the clustering results and the surface projection analysis to identify causative and auxiliary planes of the representative moment tensors. Concerning the writing of the manuscript, P.N. wrote the first drafts of the paragraphs related to the implementation, analysis, and discussion of the aforementioned contributions to the code.

2. S. Cesca, D. Stich, F. Grigoli, A. Vuan, J. A. López Comino, **P. Niemz**, E. Blanch, T. Dahm, W. L. Ellsworth (2021). Seismicity at the Castor gas reservoir driven by pore pressure diffusion and asperities loading. Nature Communications 12, 4783. https://doi.org/10.1038/s41467-021-24949-1

   P.N. performed the full-waveform-based event clustering using the co-developed Clusty toolbox (Publication 4), and the analysis of P/S and Rayleigh/Love amplitude ratios.

2 | Objectives and research questions

This chapter outlines the overarching research questions (RQ) that structured my doctoral studies and refers to the publications of my cumulative thesis in which these questions are addressed. The questions are divided into the understanding of fundamental fracturing processes (RQ1 and RQ2), a technical domain (RQ3), and a methodological domain (RQ4). The technical domain focuses on discussing the seismological footprints of different injection schemes tested in the mine-scale experiments at Äspö. Additionally, the technical domain includes a comparative analysis across three scales including laboratory experiments, the Äspö mine experiments and a field application (RQ 3). The methodological domain concerns the relative study of small seismic events induced during the Äspö experiments and during another injection-induced seismic series (RQ4). The findings motivated by these research questions are discussed in Chapter 7.

Research question 1

How do hydraulic fractures grow?

> By taking advantage of the dense monitoring setup deployed in the experiments at the Äspö HRL, I was able to track in great detail the spatiotemporal evolution of meter-scale hydraulic fractures (Publication 1, Chapter 4, see also Chapter 3.1). Additionally, I depict different fundamental phases of fracture growth in Publication 1 (Chapter 4) and Publication 2 (Chapter 5). A detailed understanding of hydraulic fractures can help to limit fracture growth and eventually better control induced seismic activity in EGS.

Research question 2

Which processes accompany the hydraulic fracture growth, and how are these processes manifested in the data of the complementary monitoring setup?

> The fracturing process is accompanied by direct and indirect responses of the stimulated rock, recorded by the complementary monitoring setup. On larger scales, fracture evolution during injection experiments or commercial stimulations is commonly monitored by mapping microseismic activity using geophones or seismometers in boreholes and at the surface, respectively. In meter-scale experiments, seismic monitoring using a complementary network of multiple sensors, including piezoelectric AE sensors, was only conducted in

recent years (Amann et al., 2018; Schoenball et al., 2020; Zang et al., 2017). By analyzing these records, I was able to track stress changes, an indirect response of the rock, induced in the vicinity of the growing hydraulic fracture (Publication 1, Chapter 4). Independent observations of tilt-induced transients recorded on broadband seismometers deployed very close to the injection borehole provide a direct estimate of the fracture evolution (Publication 2, Chapter 5). The two complementary data sets helped to characterize the processes that accompany the hydraulic fracture growth.

Research question 3

How do different injection schemes influence the seismic impact and the fracture geometry?

A major aim of ongoing research regarding EGS is the mitigation of felt seismicity during high-pressure fluid injections while retaining permeability enhancements. Besides the limitation of injection rates and volumes, alternative injection schemes could lead to a reduction of larger induced seismic events. In the mine-scale experiment at Äspö HRL, tests with different injection schemes were conducted. The seismic impact of these experiments, as well as differences in the fracture geometry are studied in Publication 1 (Chapter 4) and Publication 2 (Chapter 5), respectively. However, it is still debated whether the observations and results obtained in the mine (or laboratory) scale can be transferred to the field-scale (e.g., Gischig et al., 2020). Publication 3 (Chapter 6) addresses this problem using an energy budget approach, which allows for a comparison of innovative injection schemes across three scales: laboratory, mine, and field-scale.

Research question 4

How can we resolve further details of fracture and fault evolution by exploiting full waveforms of small seismic events?

The study of source processes of small induced seismic events can provide vital information for the understanding of fracture evolution or for the fault characterization. However, source studies for microseismic events or AE are often not feasible due to limitations arising, e.g., from the instrumentation, low signal-to-noise ratios, or simplified velocity models. Relative approaches can help to overcome those limitations to get detailed insights regarding the fracture evolution or the activation of natural faults. In Chapter 3.2.1, I present a *python* toolbox that I co-developed during my doctoral studies (Publication 4, Petersen and Niemz et al., 2021). It exploits the relative similarity of seismic events via seismic waveform-similarity studies across a network of stations or sensors. Its application to the Äspö data set and new findings from the waveform clustering are described in Chapter 7.4.

3 | Developed and applied methods

3.1 Compiling a catalog of AEs from continuous recordings

To study hydraulic fracturing growth and the acting processes during the Äspö injection experiments, I analyzed the continuous records of the AE sensors (Chapter 4, Niemz et al., 2020). The enhanced AE catalog based on these continuous records was fundamental for the detailed mapping of the fracture growth in space and time, the robust analysis of frequency-magnitude distributions (Chapter 4, Niemz et al., 2020), and the comprehensive first-order estimation of seismic energies (Chapter 6, Zang et al., 2021).

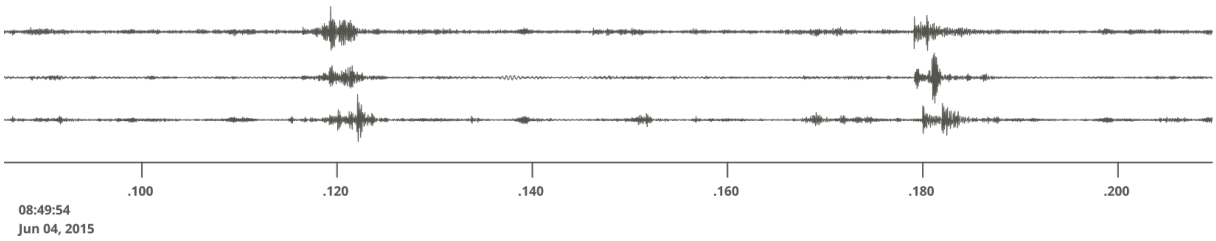

Figure 3.1: AE waveforms examples (120 ms) from three AE sensors recorded during HF2-RF5 (bandpass filter: 3-20 kHz). Two large AEs dominate the record, while many more small events are visible in between. Time scale in fractions of a second.

Fig. 3.1 shows waveform examples from the fifth refracturing stage of HF2 (HF2-RF5). Apart from two large AEs, many more events with a low signal-to-noise ratio (SNR) are visible in between. Low SNRs are characteristic of the AE activity induced during the experiment.

The vast amount of data resulting from the continuous, highly-sampled (1 MHz) AE monitoring and AEs with low SNR pose new challenges to the data analysis. Publication 1 (Chapter 4) describes a semi-automated workflow to overcome these challenges. The workflow combines the event detection of the massive AE activity with an event classification to reject false detections and with a location procedure. It incorporates existing seismological tools that were adjusted to highly sampled AE data and tuned consistently to compile a uniform catalog, which allows for the comparative study of different injection experiments (Niemz et al., 2020, Chapter 4). In the following, the single steps of the semi-automated workflow (detection, classification, location, and magnitude calculation) are introduced briefly. More details can be found in Niemz et al. (2020) (Section 2 in Chapter 4). The workflow presented here is not limited to the study of AEs in this particular experiment but is applicable in other seismological settings.

Full waveform detection

The pumping systems and working noise from the adjacent tunnel produce high noise levels, while the induced events have very small magnitudes. This results in predominately low signal-to-noise ratios and hinders the usage of detection and location methods based on phase picking. To overcome this limitation, I applied full-waveform approaches, which do not require a manual picking of phases. The limited AE source region of 30x30x30 m with sensors located directly adjacent to it provides a suitable setup for a (semi-)automated workflow of full-waveform methods. In the limited source volume, the workflow can process the vast amount of data (120 GB/h) uniformly with adequate precision.

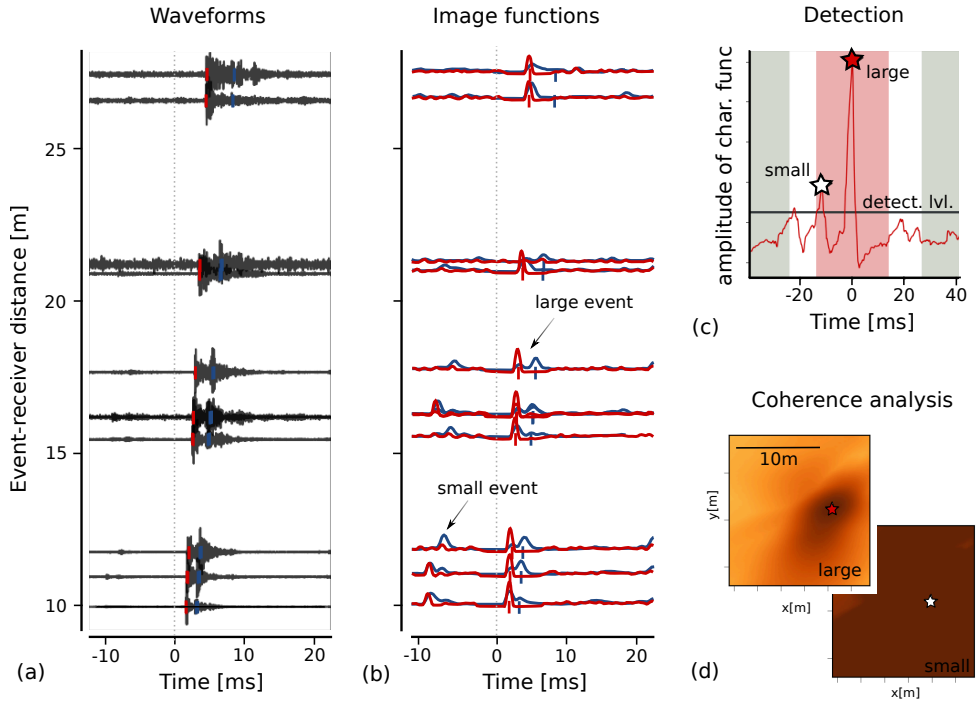

Figure 3.2: Full waveform detection. For every (moving) time window, input waveforms (a) are converted to two image functions (red and blue traces in b) that emphasize and simplify waveform characteristics. In this example, a small AE precedes a larger one. Despite the presence of the large event, the image functions represent the small event appropriately. A coherence analysis samples the entire precalculated spatiotemporal grid. If the amplitude of the stacked characteristic functions exceeds the detection level (c), *Lassie* provides the hypocenter (d) and the origin time of the newly detected event.

I employ the full-waveform detector *Lassie* to detect AEs in the continuous waveforms (Heimann et al., 2017; López-Comino et al., 2017). The detection relies on a migration approach and a coherence analysis of the back-propagated signal on a spatiotemporal grid. The detector can analyze the continuous recordings directly. Therein, the moving windows of the continuous waveforms are first converted to image functions (Fig. 3.2a-b). The two used image functions are tuned to include (1) energetic, sharp waveform onsets, e.g., from P phases, and (2) emergent onsets, e.g., the S phase within the P coda. Using image functions instead of full-waveforms helps to reduce the computation time, especially for highly sampled data, as recorded during the Äspö experiments. The detection level and the weightings of the image functions in

the combined characteristic function were tuned together for all experiments to ensure a uniform detection catalog. The detection threshold was set to a low level. While this ensures as many AE detections as possible, it also introduces many false detections that must be excluded in the following AE classification step. When the amplitude of the stacked characteristic functions of the sensors exceeds the detection level (Fig. 3.2c), Lassie provides a preliminary hypocenter location. Due to the tuning of the image function for a sensitive detection, the resulting location is only a rough estimate (Fig. 3.2d). The later relocation step of the full-waveform workflow provides the refined catalog location (see Section 3.1). The origin times provided by *Lassie* are used to cut the waveforms into 20 ms windows for the subsequent classification and localization.

Full waveform classification

In the subsequent step, the waveform classification tool excludes noise signals from the detections obtained with *Lassie*. These signals can originate from the ventilation system or working noise in the adjacent tunnel but also from electronic spikes in the recording system. The noise signals are often more energetic than the AEs induced around the opening fracture. The rejection of such signals is crucial for further automated analyses and for obtaining a reliable AE catalog without lowering the general detection threshold. Due to the close location of AEs and sensors, the waveforms can change significantly during the injections. To remain as flexible as possible regarding the type of signal to be recorded, I incorporated the Hidden Markov Model classification tool ASESS developed by Hammer et al. (2012) into the workflow. It is more flexible than template matching approaches because it is trained on waveform features (Fig. 3.3) of only a few example waveforms per event class and can recognize signals with a higher variability in the waveforms (Hammer et al., 2012; Hammer et al., 2013).

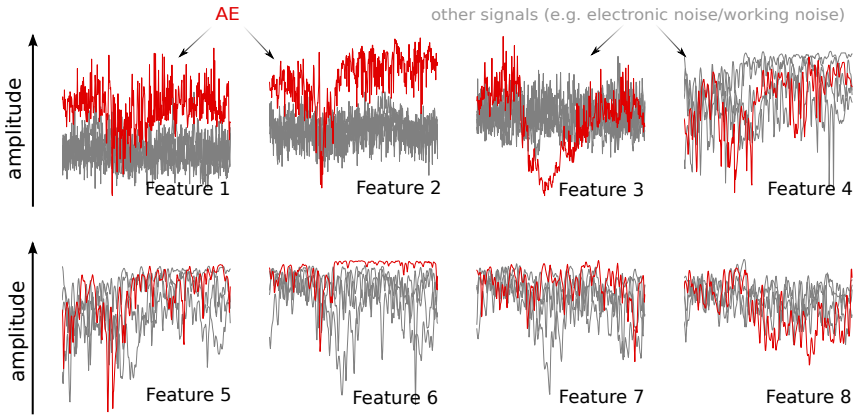

Figure 3.3: Full waveform classification. The hidden Markov model is trained on waveform features extracted from the full waveforms. These features were selected to emphasize the difference between AEs and noise signals. For details, see Section 2.3 in Chapter 4.

I evaluated the performance of the trained model by comparing the classification results with the manual classification of López-Comino et al. (2017). The comparison shows a good agreement, while I was able to integrate 50% more AEs into the enhanced catalog. Furthermore, the training on varying example waveforms showed that the choice of the example waveforms is not critical. Finally, the trained model is used as a classifier. To increase the computational

efficiency of the tool, I implemented a parallelization of the feature calculation. Detections classified as AEs at least at three sensors were included in the catalog. For more details see Section 2.3 in Chapter 4.

Full waveform location

Once classified and separated from false detections, the events are located using a full-waveform-stacking locator (Grigoli et al., 2013; Grigoli et al., 2014, WSL/LOKI). It relies on an approach similar to the detection algorithm. It is similarly noise-robust and does not require manual phase picking. To locate the AEs, normalized STA/LTA (short-time-average over long-time-average) traces computed from energy-based characteristic functions for each sensor are stacked along theoretical travel times of P and S corresponding to a hypocentral location and an origin time. After all possible locations and origin times within the precalculated spatiotemporal location grid are tested, the absolute maximum of the retrieved multidimensional coherence matrix provides a best fitting hypocenter (Fig. 3.4). Contrary to the detector, which is tuned for a sensitive detection, the locator is tuned for a precise location. Since there is only a single trace per sensor, the tuning of the locator is only based on the length of the short time window and the long time window, governing the steepness of the STA/LTA. The tuning and the smaller grid spacing of the precalculated spatiotemporal grid (0.1 m instead of 1 m) result in a better resolution of the hypocentral parameters (Fig. 3.4), which is crucial for a reliable magnitude calculation (Section 3.1), as well as for the following spatial analyses (Section 3.2.1). Location uncertainties were only estimated for a few exemplary events because the procedure is computationally expensive. Due to the monitoring setup with sensors mostly above the events, the locations have increased uncertainties in the vertical direction (see Section 2.4 in Chapter 4 for details).

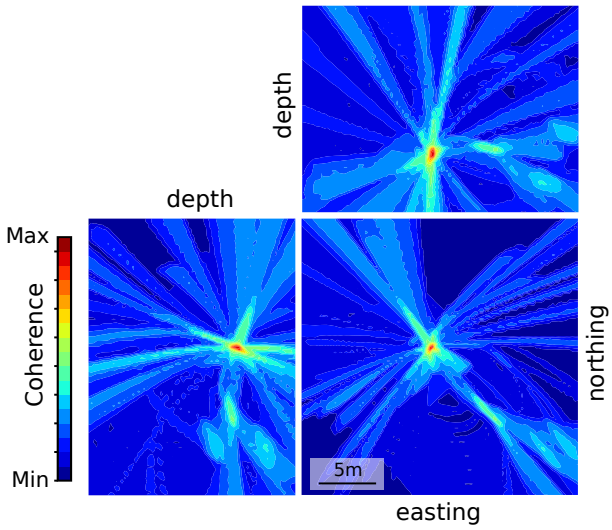

Figure 3.4: Full waveform location. The coherence matrix resulting from the waveform stacking along the spatiotemporal location grid provides a more constraint hypocenter for the large AE presented in Fig. 3.2d.

Magnitude estimation

A direct absolute magnitude estimation is not feasible due to the sensors' unknown response characteristics and variations in the coupling to the rock. Instead, I calculate relative magnitudes for AEs recorded by at least six sensors with a suitable SNR. The threshold assures a reliable magnitude estimation, which is important for the subsequent statistical analyses. A reliable catalog is a prerequisite for understanding how hydraulic fractures grow and whether larger seismic events can be mitigated using advanced injection schemes. The relative magnitude (M_{AE}) is commonly used for AEs in laboratory experiments (Manthei & Eisenblätter, 2008) and at mine scale (Köhler et al., 2009; Maghsoudi et al., 2013). M_{AE} is based on the maximum amplitudes across the sensor network, corrected for geometrical spreading and a uniform attenuation of the rock volume (for details, see Section 2.5 in Chapter 4). Amplitudes were measured from band-pass filtered waveforms (7-11 kHz). M_{AE} can be directly used to analyze frequency-magnitude distributions and estimate the b-value (Cox & Meredith, 1993; Gutenberg & Richter, 1944).

3.2 Study of fracture growth and processes

The continuous recording system installed during the hydraulic fracturing experiments at Äspö HRL proved to be highly effective as it substantially increased the number of detected and analyzed events. I compiled a catalog of approximately 20,000 AEs induced during the experiments (Publication 1, Chapter 4). The triggered recording system could only provide a catalog of 196 AEs (Kwiatek et al., 2018; Zang et al., 2017) since triggered systems are limited due to dead times and relatively high triggering thresholds to avoid false detections. Another prerequisite for the 100-fold increase of detected and localized AEs in the enhanced catalog was the robust workflow presented above. The occurrence of the first events close to the injection intervals and the clustering of AEs in distinct zones supports the reliability of the workflow leading to the enhanced catalog. The enhanced catalog with abundant AEs within each (re-)fracturing stage was crucial for the detailed study of fracture growth and induced seismicity since the statistics-based methods described below are only reliable for a large sample.

3.2.1 Cluster analyses

Hypocentral clustering

When analyzing big data sets, it is crucial to reduce the amount of data while retaining the information within. In the case of the injection experiments at Äspö, the aggregation of AEs around the opening hydraulic fracture suggests using spatial clustering to overcome the uncertainties in single event locations (see Niemz et al. (2020) and Section 7.2 for a discussion on the processes leading to the spatial clustering of AEs). When considering the spatial clustering results, uncertainties of single event locations are less relevant. To study the fracture growth during the Äspö experiments, I implemented a spatial cluster analysis based on the expectation-maximization algorithm (Dempster et al., 1977; Specht et al., 2017) to identify fracture planes (single or multiple) based on the AE locations of each (re-)fracturing stage. The EM algorithm

provides clusters of events, here interpreted as fracture planes and full covariance information to estimate the extent of the given cluster. The algorithm fits mixture models of multivariate (3D) Gaussian distributions to the AE clouds. The mixture models can consist of multiple components. Each component describes a distribution assigned to a single fracture zone represented by a mean vector μ (the center of an ellipsoid) and the covariance matrix Σ (related to its extent). The fitting procedure iterates the following two steps: (1) In the expectation step, the probabilities for the hypocenters to lie within a cluster are determined based on the mixture model. (2) In the maximization step, the algorithm determines new estimates of $\hat{\mu}$ and $\hat{\Sigma}$, maximizing the likelihood based on the probabilities from the expectation step. The optimal number of fracture zones (components) for each (re-)fracturing stage is determined by simultaneously maximizing the log-likelihood of the individual components of the mixture model. The implementation always integrates a noise class, which incorporates biased hypocenter locations, e.g., at the grid boundary (see Section 3.1) to ensure that the mapped fracture extent is reliable. Finally, the two largest eigenvalues of the covariance matrix of each component are used to calculate the 95% confidence region, which I define as spanning an elliptic fracture plane (Publication 1, Chapter 4).

Waveform clustering

While the clustering applied in Publication 1 (Chapter 4) and described above relies only on the hypocentral locations in the enhanced catalog, which was obtained via full-waveform approaches, the waveforms contain much more information on the fracturing process. Directly extracting information on focal mechanisms is limited to a few large events in the case of the Äspö experiments (Kwiatek et al., 2018) due to instrumental limitations, such as unknown coupling conditions of the AE sensors to the rock and an uncalibrated response of the sensors. Furthermore, the events have low SNRs and a particularly high frequency content even exceeding 20 kHz. Relative approaches can help to overcome the aforementioned limitations regarding source studies. The relative analysis of two events cancels out effects of the instrument and the event-receiver path, as long as the events are close to each other and far away from the receiver. The waveform-based clustering toolbox *Clusty* (Publication 4, Petersen and Niemz et al., 2021) exploits the opportunities of relative waveform analyses. It was developed to provide a flexible tool to analyze waveforms over a broad range of magnitudes, from acoustic emissions to earthquake sequences and swarms. It relies on the analysis of waveform similarity, a joint measure for the similarity of the hypocentral location and focal mechanism of two events (Geller & Mueller, 1980; Got & Fréchet, 1993).

The waveform clustering of events into groups is often based on waveform similarities at the single stations (e.g., Baisch et al., 2006). Depending on the focal mechanism involved, this might produce unreliable results when waveforms are coincidentally very similar at the particular azimuth of the station. To overcome this limitation, *Clusty* first calculates an event similarity based on waveform similarities from a network of stations (,e.g., Aster & Scott, 1993; Duboeuf et al., 2019; Maurer & Deichmann, 1995) and subsequently clusters events by the combined network similarity (Fig. 3.5, Publication 4, Petersen and Niemz et al., 2021). The network similarity is more robust and, at the same time, more sensitive than a single-station waveform similarity approach, as it samples a larger azimuthal range. When seismic events migrate along

a fault, waveforms at a sensor can change gradually due to the relative change in location. In contrast, the mechanism would be expected to remain stable. While events very close to each other should be highly similar, events in different parts of an extended fault zone might show considerable variations within their waveforms. However, the gradual change in between can be tracked with a chain-like clustering algorithm like DBSCAN (Ester et al., 1996). This approach enables the mapping of faulting and fracturing processes. The appropriate tuning of the clustering parameters is of utmost importance to obtain meaningful results. The analysis plots implemented in *Clusty* allow to gain full control in the tuning process (Appendix A.2, Petersen and Niemz et al., 2021). I will discuss preliminary results of the waveform similarity cluster analysis from the Äspö experiments in Chapter 7.4.

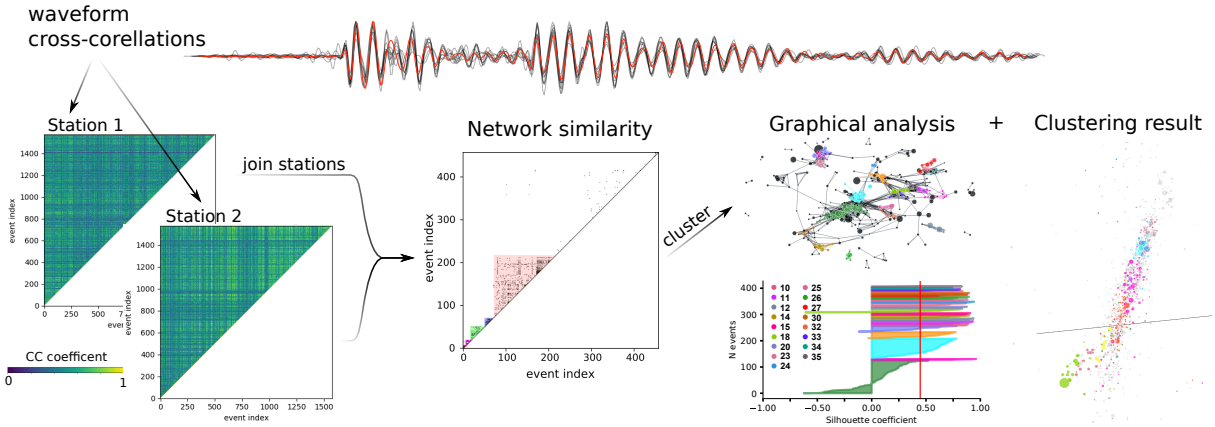

Figure 3.5: Full waveform clustering. Schematic steps in the analysis of waveform similarities in *Clusty* from single-station waveform cross-correlations to a joint network similarity, as a proxy for event similarity. The event clustering based on the network similarity relies on a thorough tuning of the clustering result based on different metrics and visualization plots. The results of the waveform similarity analysis help to map fractures and faults.

3.2.2 Analysis of tilt induced signals from broadband seismometers

The second data set, which complements the AE catalog, is obtained from injection-induced tilt signals from continuous recordings of two seismometers installed in the tunnels close to the injections. Tilt affects a seismometer by a small horizontal axis rotation of its reference frame, deflecting the horizontal components away from the gravitational potential plane (inset in Fig. 3.6). The seismometer responds to this small rotation with long-period pulses on the horizontal components, while the vertical component remains largely undisturbed (Rodgers, 1968; Wielandt & Forbriger, 1999).

Tilt signals on broadband seismometers are well known from volcanic settings, where these signals are attributed to large-scale fluid processes, such as the intrusion of magma via dykes in the vicinity of the seismometers (e.g., Battaglia et al., 2000; Gambino et al., 2007). The hydraulic fractures induced during the experiments at Äspö can be considered as engineered equivalents to volcanic dykes. In earthquake or volcano seismology, the tilt signal is generally only dominant when the frequency response to the true acceleration decays below the lower corner frequency f_c of the seismometer (Wielandt & Forbriger, 1999, see also Fig. 3.6). Contrary, in the case of the

Äspö experiments, the lack of seismic signals in the frequency range of the seismometers allows for a direct extraction of the tilt signal induced during the injection experiments also above f_c. The tilt time series $\Theta(t)$ are extracted from the seismograms following Battaglia et al. (2000):

$$\Theta(t) = -\frac{1}{g}\frac{dp(t)}{dt}, \tag{3.1}$$

with $p(t)$ being a horizontal or radial seismic trace corrected for the instrumental response and g being the gravitational acceleration. Consequently, I use the maximum tilt magnitude and the tilt direction of the single injection stages to validate the AE fracture plane estimates independently by comparing observed tilts and theoretical tilts calculated from dislocations models (Okada, 1992). The dislocation models — calculated using the Okada source implementation of the *pyrocko* toolbox (Heimann et al., 2017) — represent the tensile opening of a hydraulic fracture, defined by the AE fracture planes. The methods are described in detail in Publication 2 (Chapter 5). The joint analysis of tilt signals and AEs, presented here, draws a more complete picture of the fracturing processes acting during the different HF experiments.

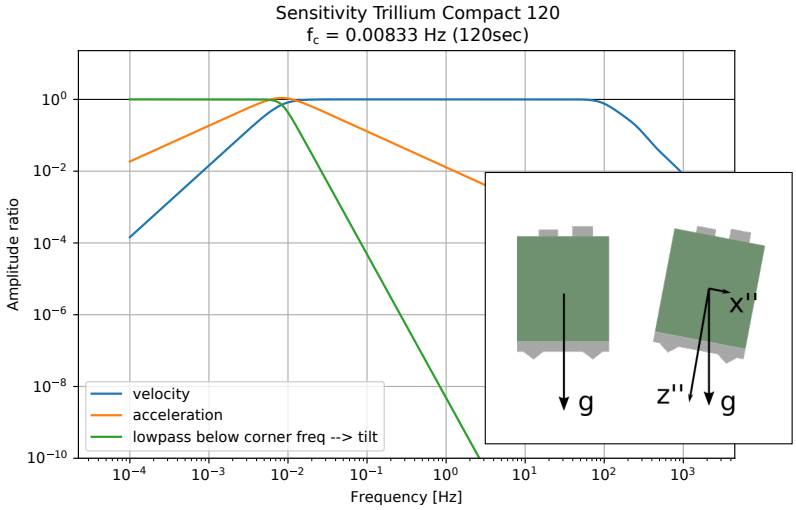

Figure 3.6: Frequency response of a Trillium Compact 120 seismometer, as used in the Äspö experiments, for velocity, acceleration, and tilt. Inset: Tilting the seismometer changes the reference frame. Consequently, there is an additional acceleration on the horizontal components. From Niemz et al. (2021).

3.3 The seismic impact of subsurface injections

3.3.1 Seismic catalog statistics

The seismic impact of injections was studied based on the event catalogs of the experiments, considering maximum magnitudes, the number of events, and the b-value from the frequency-magnitude relation of Gutenberg and Richter (1944) (Publication 1 and 3, Chapter 4 and 6). Graphically, the b-value is the negative slope of the cumulative number of events (logarithmic) within a given earthquake catalog plotted over magnitude. The b-value can be described as a

measure for the relative number of large events compared to the number of small events. A shift to larger b-values can be interpreted as a mitigation of large events. Before the b-value estimation, I independently estimated the magnitude of completeness (M_c) using the change-point detection method (MBASS, Amorèse, 2007), which detects changes in the slope of the frequency-magnitude distribution. The approach provides a conservative estimate of M_c (Mignan & Woessner, 2012), to assure that the b-value is unbiased by the choice of M_c. b-values are calculated by a common maximum likelihood estimator corrected for magnitude binning and measurement errors (Marzocchi & Sandri, 2009; Tinti & Mulargia, 1987):

$$b = \frac{1}{ln(10)\,\Delta M} ln(p) \tag{3.2}$$

$$p = 1 + \frac{\Delta M}{\hat{\mu} - M_c} \tag{3.3}$$

where ΔM is the bin size and $\hat{\mu}$ is the mean of the binned magnitudes above M_c.

3.3.2 A comparative study of energy partition during high-pressure injections

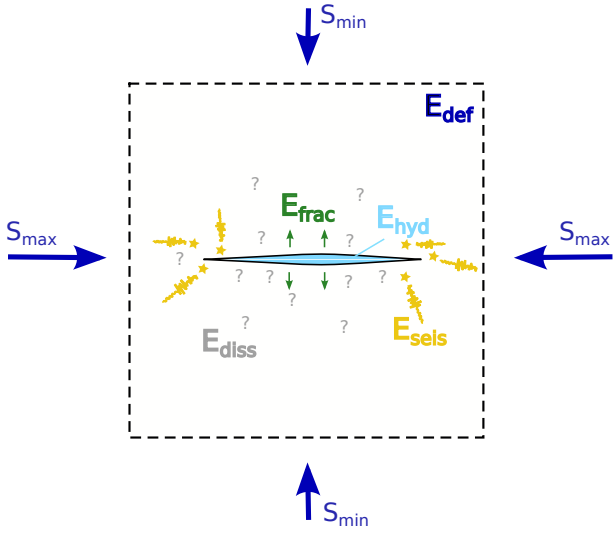

Figure 3.7: Schematic sketch of the energy budget approach with the following contributions: (1) potential deformation energy (E_{def}) from efficient stresses within the rock volume, (2) hydraulic energy (E_{hyd}), the energy required to open the fracture (E_{frac}), (3) the seismically radiated energy (E_{seis}), and the energy dissipated within the fracturing (E_{diss}), e.g., via temperature changes.

In order to study the differences in the processes acting during conventional and cyclic injection schemes, energy budgets were estimated over three different scales, including laboratory experiments (Zhuang et al., 2020; Zhuang et al., 2019), the mine-scale experiments at Äspö (Niemz et al., 2020; Niemz et al., 2021; Zang et al., 2017), and a field application (Hofmann et al., 2019). This approach combines findings obtained during the ongoing optimization of alternative injection schemes across the three scales.

The energy budgets (Eq. 3.4) include the hydraulic energy (E_{hyd}) supplied to the system during the injection and the potential deformation energy within the rock (E_{def}) on one side and the dissipated energy (E_{diss}), the fracture opening energy (E_{frac}), and the radiated seismic energy (E_{seis}) on the other side (Zang et al., 2021).

$$E_{def} + E_{hyd} = E_{seis} + E_{frac} + E_{diss} \tag{3.4}$$

The dissipated energy is unconstrained. The deformation energy and the hydraulic energy were inferred from the experimental setup. Estimating the two remaining components, fracture energy and seismic energy, requires the application of scaling relations for magnitudes and fracture extents. At mine-scale and laboratory-scale, the fracture extent is considered to be well-known. For the field application, the fracture/fault extent was estimated indirectly using the magnitude fault area relation of Wells and Coppersmith (1994). Vice-versa, absolute magnitudes were only available for the field-scale injection and the relative magnitudes from the two other scales had to be calibrated. The mine-scale magnitudes were calibrated via a scaling based on the largest events for which direct M_w estimates were available from Kwiatek et al. (2018). The laboratory catalogs were calibrated via ball-drop calibration experiments (for details see supplement of Publication 3, Chapter 6).

4 | First publication

Full-waveform-based characterization of acoustic emission activity in a mine-scale experiment: a comparison of conventional and advanced hydraulic fracturing schemes

P. Niemz, S. Cesca, S. Heimann, F. Grigoli, S. von Specht, C. Hammer, A. Zang, and T. Dahm (2020)

Published in Geophysical Journal International, 222(1):189–206
https://doi.org/10.1093/gji/ggaa127

The supplementary material of this publication is available online at
https://doi.org/10.1093/gji/ggaa127.

Geophysical Journal International

Geophys. J. Int. (2020) **222,** 189–206
GJI Seismology

doi: 10.1093/gji/ggaa127

Full-waveform-based characterization of acoustic emission activity in a mine-scale experiment: a comparison of conventional and advanced hydraulic fracturing schemes

Peter Niemz [1,2] Simone Cesca,[1] Sebastian Heimann,[1] Francesco Grigoli [3] Sebastian von Specht,[1,4] Conny Hammer,[3] Arno Zang[1,2] and Torsten Dahm[1,2]

[1] *GFZ German Research Centre for Geosciences, Potsdam, Germany. E-mail: pniemz@gfz-potsdam.de*
[2] *Institute of Geosciences, University of Potsdam, Potsdam, Germany*
[3] *Swiss Seismological Service, ETH-Zurich, Zurich, Switzerland*
[4] *Earthquake-Disaster & Risk Evaluation and Management (E-DREaM) Center, National Central University, Taiwan*

Accepted 2020 March 13. Received 2020 March 11; in original form 2019 September 2

SUMMARY

Understanding fracturing processes and the hydromechanical relation to induced seismicity is a key question for enhanced geothermal systems (EGS). Commonly massive fluid injection, predominately causing hydroshearing, are used in large-scale EGS but also hydraulic fracturing approaches were discussed. To evaluate the applicability of hydraulic fracturing techniques in EGS, six *in situ*, multistage hydraulic fracturing experiments with three different injection schemes were performed under controlled conditions in crystalline rock at the Äspö Hard Rock Laboratory (Sweden). During the experiments the near-field ground motion was continuously recorded by 11 piezoelectric borehole sensors with a sampling rate of 1 MHz. The sensor network covered a volume of 30×30×30 m around a horizontal, 28-m-long injection borehole at a depth of 410 m. To extract and characterize massive, induced, high-frequency acoustic emission (AE) activity from continuous recordings, a semi-automated workflow was developed relying on full waveform based detection, classification and location procedures. The approach extended the AE catalogue from 196 triggered events in previous studies to more than 19 600 located AEs. The enhanced catalogue, for the first time, allows a detailed analysis of induced seismicity during single hydraulic fracturing experiments, including the individual fracturing stages and the comparison between injection schemes. Beside the detailed study of the spatio-temporal patterns, event clusters and the growth of seismic clouds, we estimate relative magnitudes and *b*-values of AEs for conventional, cyclic progressive and dynamic pulse injection schemes, the latter two being fatigue hydraulic fracturing techniques. While the conventional fracturing leads to AE patterns clustered in planar regions, indicating the generation of a single main fracture plane, the cyclic progressive injection scheme results in a more diffuse, cloud-like AE distribution, indicating the activation of a more complex fracture network. For a given amount of hydraulic energy (pressure multiplied by injected volume) pumped into the system, the cyclic progressive scheme is characterized by a lower rate of seismicity, lower maximum magnitudes and significantly larger *b*-values, implying an increased number of small events relative to the large ones. To our knowledge, this is the first direct comparison of high resolution seismicity in a mine-scale experiment induced by different hydraulic fracturing schemes.

Key words: Fracture and flow; Spatial analysis; Statistical methods; Time-series analysis; Induced seismicity.

1 INTRODUCTION

Due to depletion of fossil fuel resources and the effect of climate change many countries are striving for alternative energy supplies while reducing carbon dioxide emissions. Geothermal energy is often considered as one of the corner stones of this transition (Kolditz *et al.* 2013; Stauffacher *et al.* 2015). However, in many settings except for volcanic active regions, geothermal power can only be

used efficiently in enhanced geothermal systems (EGS) by applying different stimulation techniques based on mechanical, chemical or thermal processes. Commonly, massive fluid injections [e.g. Basel, Switzerland (Häring *et al.* 2008) or Espoo, Finnland (Kwiatek *et al.* 2019)] are used in EGS (Majer *et al.* 2007), but also other experimental approaches such as controlled multistage (Petty *et al.* 2013) or multifrac (Meier *et al.* 2015) stimulations were conducted or discussed for geothermal purposes. The predominant aim of massive fluid injections is the shear reactivation of pre-existing fractures (mode II fractures, hydroshear) in order to increase the permeability of the surrounding rock mass (Gischig & Preisig 2015). The study of Norbeck *et al.* (2018) found evidence that in this type of stimulation, hydraulic fracturing (HF) also contributes to the observed increase in permeability in mixed-mode fracture mechanisms. In HF the permeability increase is caused by the formation of new fractures within the rock mass (mode I fractures, tensile). The advantages and drawbacks of hydraulic fracturing in EGS are also discussed by Gischig & Preisig (2015). As in other industrial activities involving fluid injections, for example wastewater disposal or shale gas extraction, induced seismicity is one hazard arising from EGS operations and also a subject of public concern (e.g. Häring *et al.* 2008; Zang *et al.* 2014; Grigoli *et al.* 2017). Therefore, the mitigation of induced seismicity in EGS, while retaining or even increasing permeability enhancement is of major interest in research and engineering (Gaucher *et al.* 2015; Lee *et al.* 2019). Apart from the monitoring of microseismicity during large-scale EGS projects (see Zang *et al.* 2014, and references therein) the fundamental knowledge about microscale processes active during fluid injections into crystalline rock and the influence of the type of fluid injected into the rock was mostly gained through laboratory experiments using acoustic emission (AE) monitoring (e.g. Zoback *et al.* 1977; Majer & Doe 1986; Kranz *et al.* 1990; Stanchits *et al.* 2014). Laboratory experiments and discrete element modelling indicate that within crystalline rock, cyclic progressive injection schemes (fatigue hydraulic fracturing) can achieve a mitigation of large events and permeability enhancements (Zang *et al.* 2013; Zhuang *et al.* 2016, 2019). Moreover, these experiments showed that advanced injection schemes with multiple pumps and variable flow rates allow to design fractures and fracture damage zones with different geometries, for example short and compact versus long and persistent.

To verify this hypothesis at larger scale Zang *et al.* (2017) conducted six *in situ*, multistage HF experiments (HF1–HF6) with AE monitoring at the Äspö Hard Rock Laboratory (HRL) in Sweden. Such mine-scale, *in situ* HF experiments intend to bridge the gap between micro and macroscale but are rarely realized, because of the difficult logistics and the high installation costs. Eisenblätter (1988) and Dahm *et al.* (1999) conducted *in situ* HF tests in rock salt, mapping planar, unilateral fracture growth based on AE activity around the injection interval. *In situ* HF experiments in crystalline rock were conducted by Sasaki (1998) and Niitsuma *et al.* (1993). Besides the pioneering HF experiments for geothermal purposes at Äspö Hard Rock Laboratory, Sweden (Zang *et al.* 2017), there are other recent mine-scale hydraulic fracturing experiments aiming for a better understanding of underlying seismo-hydromechanical processes and scaling relations between laboratory experiments and a potential application in large-scale EGS: One experiment at the Grimsel test site, Switzerland (Amann *et al.* 2018), at the same depth level as at Äspö HRL (450 m), and another experiment at very shallow depth (120 m) at Reiche Zeche, Germany (Dresen *et al.* 2019). The EGS Collab project also started geothermal *in situ* experiments at the Sanford Underground Research Facility, South Dakota, USA, including hydraulic fracturing experiments (Kneafsey *et al.* 2018; Morris *et al.* 2018).

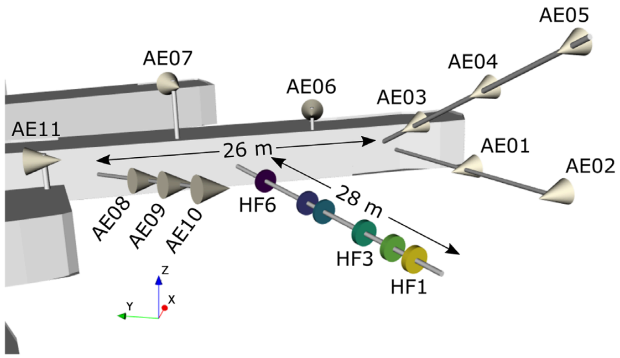

Figure 1. Experimental setup: 11 piezoelectric, single-component borehole sensors (beige cones) covering a volume of 30×30×30 m of crystalline rock around a 28-m-long injection borehole recorded AEs. The sensors are oriented towards the stimulated volume. Injection intervals are colour-coded: HF1 (yellow), HF2 (light green), HF3 (teal), HF4 (light blue), HF5 (dark blue) and HF6 (purple).

In this study, we present a detailed insight into fracture growth and AE activity induced by three different injection schemes based on the analysis of continuous AE recordings from the Äspö experiments conducted by Zang *et al.* (2017) at a depth of 410 m. The Äspö HRL has been a facility for research in nuclear waste disposal for many years (since 1995). The detailed knowledge about geology, hydraulics and rock stress was used by Zang *et al.* (2017) for stimulation tests to optimize geothermal heat exchangers, which is another research focus. *In situ* stress state studies close to the site of the HF experiments indicate that the largest principle stress is the maximum horizontal stress $\sigma_1 = S_H$ (strike: ∼N120°E, 22–27 MPa, Klee & Rummel 2002; Ask 2003, 2006). The orientation of intermediate and least principle stresses is ambiguous as they are similar in magnitude with 8.1 MPa $< \sigma_2 <$ 11 MPa and 9.5 MPa $< \sigma_3 <$ 12 MPa. Ask (2006) found that σ_3 is inclined vertically with a dip of about 80° at depth of 380 and 450m, while σ_3 is assumed to be the minimum horizontal stress at a depth of 456 m in Klee & Rummel (2002). The experiments presented here were conducted in three different rock types cut by the injection borehole: Ävrö granodiorite (HF1–HF3), fine-grained diorite-gabbro (HF4 and HF5) and fine-grained granite (HF6). The rock mass at Äspö HRL is naturally fractured due to brittle deformation under varying regional stress regimes (Zang *et al.* 2017).

A network of 11 piezoelectric borehole sensors spanning a volume of approximately 30×30×30 m around the 28-m-long injection borehole recorded induced acoustic emissions (AEs) during the stimulations (Fig. 1). These piezoelectric sensors are most sensitive in the frequency range of 1–100 kHz, but sampling rates were extended to 1 MHz. The single component instruments were installed in three monitoring boreholes and at the tunnel walls. Each instrument was oriented towards the stimulated rock mass. The injection borehole dips slightly downwards and is oriented subparallel to the direction of minimum horizontal stress. The monitoring boreholes are oriented upwards to allow outflow of water from a hydrological conductor within the stimulated rock mass. The packer-controlled test intervals in the injection borehole were chosen after a visual inspection of borehole images and the core to ensure that there were no preexisting fractures at the stimulation intervals. The injection intervals have a reduced length of 0.5 and 0.25 m for HF1–HF3

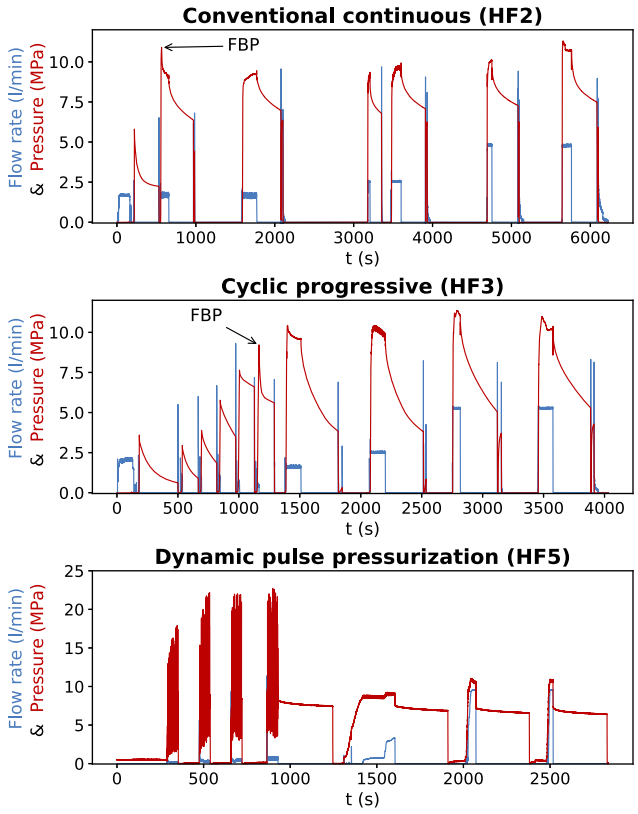

Figure 2. The three subplots show the injection pressure and the flow rate versus time for the tested injection schemes. In the conventional continuous scheme (upper panel, here HF2, but also HF1, HF4 and HF6) the fracturing stage consists of only one pressurization phase until the fracture breakdown pressure (FBP) is reached. The cyclic progressive injection scheme (middle, HF3) has multiple pressurization and depressurization phases during the fracturing stage. The target pressure is increasing in each phase until FBP. The following refracturing stages are similar in both schemes. The dynamic pulse injection (lower panel, HF5) is similar to the cyclic progressive scheme, but pressurization is pulsating. The fracturing stage is followed by 3–5 refracturing stages.

and HF4–HF6, respectively. During the experiments three fluid-injection schemes were tested: conventional continuous, cyclic progressive and dynamic pulse pressurization, the latter two being fatigue hydraulic fracturing (FHF) schemes. In conventional hydraulic fracturing schemes (HF1, HF2, HF4 and HF6) the flow rate is kept constant until the occurrence of the fracture breakdown pressure, while in the cyclic progressive injection scheme (HF3) there is a frequent change of pressurization and depressurization phases while the target pressure is increasing stepwise (Fig. 2). The third tested injection scheme (dynamic pulse injection HF5) is based on the cyclic progressive scheme but interval pressure is applied in a pulsating way. More detailed descriptions of the experimental setup and the FHF injection schemes are given in Zang *et al.* (2017).

The *in situ* monitoring of induced seismicity is crucial to control the hydraulic fracturing process. In the case of the Äspö HF experiments, this was assured by using a trigger system and a rapid analysis of event locations. However, short interevent times and the chosen trigger level limit the detection capability. Therefore, a complementary continuous recording system was active simultaneously during each HF experiment (Zang *et al.* 2017). Based on the *in situ* triggered recordings Zang *et al.* (2017) presented a catalogue of 196 manually reviewed AEs but stressed, based on visual inspections, that many more events are expected to be recorded by the continuous system. Due to the large amount of continuous data, we developed a semi-automated workflow which relies on waveform based detection, classification and location procedures, to extract and characterize high-frequency AEs expected to be induced ahead of or close to the fracture tip (Dahm *et al.* 1999; Dahm 2001; Warpinski *et al.* 2012). Thus, AEs recorded during the injection should map the hydraulic fracturing growth which can be described in terms of orientation, extent and velocity. The processing workflow is set up and refined for all six HF experiments based on the work of López-Comino *et al.* (2017) who analysed the conventional continuous injection experiment HF2. The stack-and-delay detection approach described in López-Comino *et al.* (2017) was modified to account for short inter-event times. Additionally, we setup a classifier based on Hidden Markov Models (Beyreuther *et al.* 2012; Hammer *et al.* 2013) to exclude false detections originating among others from electronic noise, working noise in the adjacent tunnels or long-period noise. The detected AEs are located using an automated full waveform location algorithm based on stacking characteristic functions along pre-computed traveltime surfaces (Grigoli *et al.* 2013, 2014). Relative magnitudes are calculated using maximum amplitudes across the network. The extracted AE catalogues for each HF experiment are analysed separately to point out differences between the applied injection schemes in regard to fracture growth and the activity of very weak AE signals emitted at the propagating fracture tip.

2 DATA AND METHODS

2.1 Data and signal quality

AE signals induced by hydraulic fracturing resemble seismic waveforms. Larger events show distinct onsets of *P* and *S* phases (Zang *et al.* 2017; Kwiatek *et al.* 2018). Weaker AEs present more noisy waveforms and phase identification as well as manual or automated phase picking become more challenging and inaccurate. By analysing the continuous recordings we aim to include the large number of small, low signal-to-noise ratio (SNR) events (Fig. 3). The stacked frequency spectra for each sensor based on approximately 6000 events from experiment HF2 (Fig. 4) show two dominant frequency peaks (5–7 kHz and 7–10 kHz). Low frequency noise is dominant below 3 kHz. We observe that the frequencies of spectral peaks do not change systematically with the hypocentral distance and magnitude. The sensitivity of the sensors depends on the coupling of the instrument to the rock and the incidence angle of the incoming wave (Manthei 2005). Given a sufficient coupling, the closest sensors also record energy in the band of 12–20 kHz, though this peak is less pronounced. For frequencies above 20 kHz we observe additional spectral peaks, which we attribute to noise emitted by ventilation and electronics. The stacked frequency spectra of sensors AE03 and AE08 indicate bad coupling as they deviate significantly from all other spectra and do not show any high frequency spectral peak. Based on the spectral analysis of the AE signals the waveforms were bandpass filtered between 3 and 20 kHz for all further processing.

2.2 Automated seismic event detection within continuous records

AEs within the continuous waveforms were detected using the Lassie detector (López-Comino *et al.* 2017), based on the Pyrocko toolbox (Heimann *et al.* 2017). The detection relies on a migration

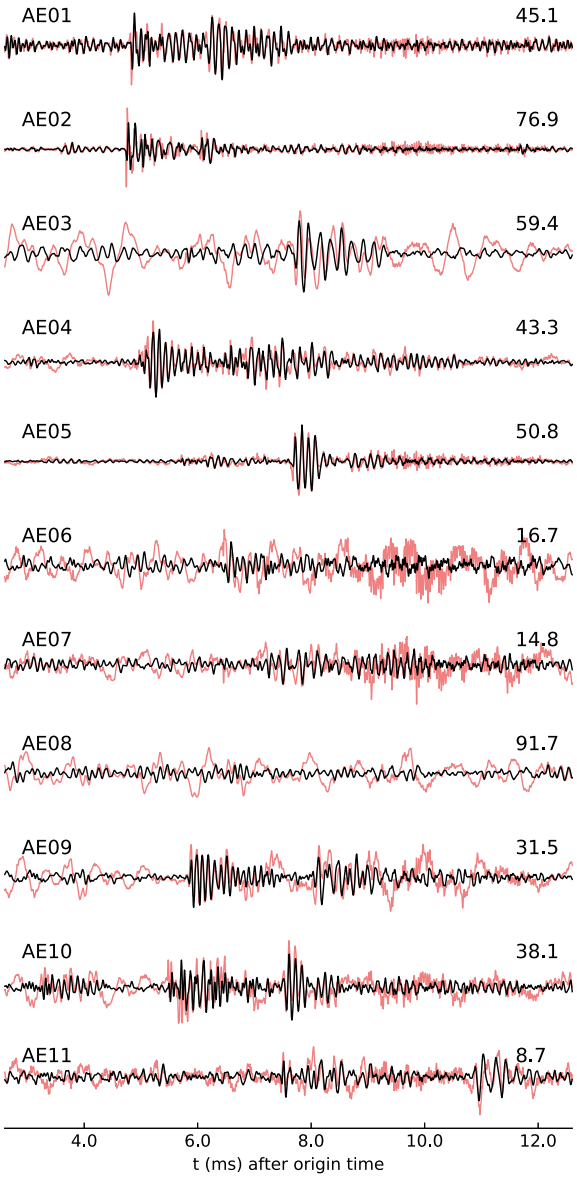

Figure 3. AE waveforms of an M_{AE} 2.5 event with reduced SNRs recorded at the piezoelectric sensors. This example is representative for the targeted small magnitude events of this study with emergent or missing phase onsets and high noise. The maximum amplitude is given above each trace. The red traces, bandpass filtered between 0.5 and 50 kHz, show low frequency noise disturbances (e.g. AE03, AE09 and AE10) and the high-frequency signal of the pumping system (e.g. end of trace at AE06 and AE07). The black traces show the signal with the narrower bandpass filter (3–20 kHz) chosen for the further processing.

approach using characteristic functions calculated from full waveforms and a coherence analysis of the back-propagated signal on a spatio-temporal grid. Theoretical traveltimes at all receivers were calculated for grids of 15×15×15 m (grid spacing of 1 m) centred around the mid-interval of each injection experiment using a homogeneous, full-space velocity model. *P*- and *S*-wave velocities were set to 5800 and 3200 m s^{-1}, respectively, based on estimates from

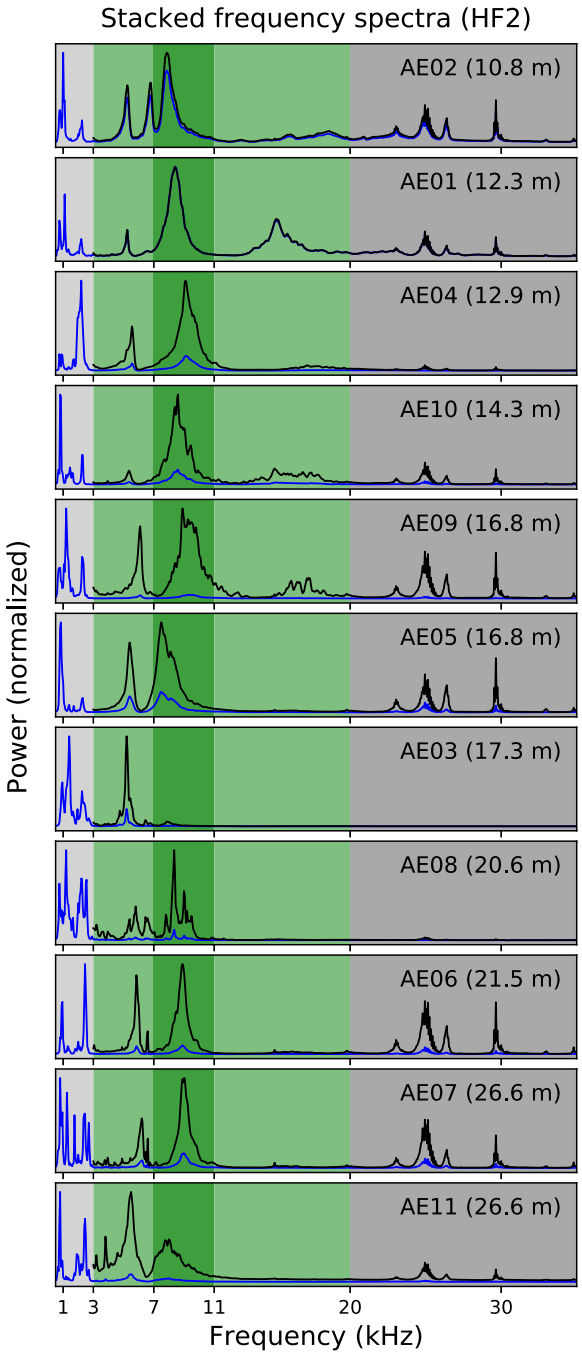

Figure 4. Sensor-wise stacked frequency spectra of approximately 6000 events in the catalogue of HF2 show two dominant frequency peaks (5–7 kHz and 7–10 kHz) and low frequency noise below 3 kHz (light grey area). High-frequency spectral spikes are attributed to noise emitted by ventilation and electronics (dark grey area). The blue line shows the normalized spectral power between 0.5 and 35 kHz, while the black line is normalized for frequencies between 3 and 35 kHz. Variations among the sensors arise from differing event-station travel paths and the coupling of the instrument to the rock. The chosen bandpass filters for the processing workflow and the magnitude estimation are indicated by light green and dark green background colours, respectively.

active, ultrasonic transmission tests (Zang *et al.* 2017). Kwiatek *et al.* (2018) validated the velocity model through a Wadati diagram using manually picked *P* and *S* arrivals as well as through known locations of hammer hits. The extent of the traveltime grids was chosen according to the spatial distribution of hypocentral locations in the triggered catalogue (Zang *et al.* 2017; Kwiatek *et al.* 2018). The characteristic functions are built as a composition of two weighted image functions. (1) The short-time-average/long-time-average (STA/LTA) image function is sensitive to sharp onsets, such as from a *P* phase. This image function has an increased weighting in the characteristic functions. (2) The wave packet image function based on a moving average of the energy trace is sensible to transient wave packets, like, for example a phase and its coda. We tune it to be sensible to the *S* wave emerging out of the *P* coda. When exceeding a given threshold for the amplitude of the stacked characteristic functions of all stations, Lassie provides a detection with a preliminary hypocentre and an origin time. Since the imaging functions are tuned for a robust detection in our case and therefore smoothed, the obtained location is rejected and only the origin time is used to cut the waveforms for subsequent classification and localization. The computation time of the joint detection/location process and the precision of the hypocentres depend on the resolution of the traveltime grids. The number of detections and the rate of false detections is influenced by both the pre-calculated traveltime grids and the chosen detection threshold. The weighting of the image functions and the detection threshold were tuned for the ensemble of experiments and used for each experiment to ensure a comparable detection level.

2.3 Event classification

In order to exclude non-seismic signals (e.g. spikes related to electromagnetic waves) from the massive number of detections, we set up a Hidden Markov model (HMM) classifier using the Advanced Seismic Event Spotting System (ASESS) (Hammer *et al.* 2012, 2013). It is able to provide event classifications based on a single reference trace for each seismic signal class. The classification is not based directly on the raw trace but short term wave field attributes are extracted from each reference signal (i.e. AEs and noise) and build the input for the classifier. During the classification stage the feature sets are compared to the features extracted from the windowed continuous waveforms. Compared to event template matching techniques in time or frequency domain, an HMM is able to describe a wider range of variations in the signals of the same class while the choice of the reference event(s) only has a limited influence on the classification result (Hammer *et al.* 2012). In this study, the algorithm is trained on the first three cepstral coefficients, the instantaneous frequency and five half-octave bands (covering a frequency range from 3 to 25 kHz) to recognize the event class and a single, unified noise class [see Hammer *et al.* (2012) for details on the calculation of these features]. The features were chosen based on a trial and error approach to best describe differences between noise and event class using a small subset of detections and the manually checked triggered catalogue of Kwiatek *et al.* (2018). As a reference signal for the AE class, we manually chose one event from each experiment having an intermediate amplitude of the characteristic function obtained from the detection algorithm. The influence of the reference event was tested by training the algorithm using different reference events. The number of events classified as AEs does not differ significantly. Noise templates were likewise selected manually to include different kinds of noise, for example long-period signals, electromagnetic spikes or work-related signals [see Fig. 3 and López-Comino *et al.* (2017) for examples of noise]. For the classification, time windows around the Lassie detections are extracted from the continuous waveform and fed into the classifier. The time window was set to 20 ms including 5 ms before the preliminary origin time of the corresponding detection and 15 ms after. The rather long window length accounts for the rough first estimate of the hypocentre and the origin time and assures that the event is within the window at all sensors. However, the dead time associated with this approach limits the maximum number of events detectable per second to 50. We do not rely on a single station classification based on the closest sensor, but use the six sensors closest to the injection interval of each HF experiment. When an event, which was detected before by Lassie, is assigned to the AE event class at three or more station, it is integrated into the AE catalogue. Using this approach, we are not only able to exclude false detections, such as noise events, but also AEs that are only recorded at one or two sensors before starting the computationally expensive, refined localization. These AEs are referred to as non-locatable events because we reject the preliminary location from the joint detection/location of Lassie.

2.4 Automated seismic event location

For the localization of AEs, we use the automated location tool *LOKI*. It is a noise robust and picking free location method that exploits the full waveform information content of seismic recordings (Grigoli *et al.* 2013, 2014). The location process is based on the stacking of normalized STA/LTA traces computed from energy based characteristic functions (Grigoli *et al.* 2013). Trace normalization is performed to remove the effect of geometrical spreading and to avoid that the stacking is dominated by stations close to the source. To locate a seismic event, the normalized STA/LTA traces are stacked along theoretical traveltimes of *P* and *S* corresponding to a potential hypocentre location. The process continues by iterating this procedure for all temporal samples of the recorded traces and for all possible source locations within a predetermined seismogenic volume. We finally retrieve a multidimensional coherence matrix whose absolute maximum corresponds to the spatio-temporal coordinates of the seismic event. Event waveforms are windowed as described in the classification section. By using time windows the procedure inherently favors larger events in the presence of a smaller event within the same time window. The same applies to the automatic amplitude picking for the magnitude estimation. This results in a dead time of 15 ms after a large event, except when the subsequent event is even larger. For the refined localization the spacing of the traveltime grids is reduced to 0.1 m. Owing to the network architecture with single component sensors oriented towards the fracturing borehole only a single STA/LTA for both, *P* and *S*, is calculated per sensor. The short-time window and long-time window are set to 0.2 and 0.52 ms, respectively. For an uncertainty estimation Grigoli *et al.* (2013) suggest repeated localization while varying both, the short and long time window, as well as jackknifing by removing one station at a time. We propose another approach, assuming a Gaussian error distribution similar to a picking uncertainty to shift the input traces in a given range randomly in time. The range is set based on the residuals between the maximum of the STA/LTA traces of the input waveforms and the theoretical timing of the STA/LTA maximum determined in the coherence analysis. After repeating this approach several times, we calculate the weighted

mean and the standard deviation of the given hypocentre locations. As suggested by Grigoli *et al.* (2013) the weights are set equal to the maximum coherence of a solution, so that high coherence solutions have larger weights. Since this approach requires many expensive relocations, we only calculate uncertainties for selected events to obtain a qualitative estimate of the location uncertainties.

2.5 Magnitude estimation

Event magnitudes are estimated using a relative magnitude scale (M_{AE}) based on a linear regression of amplitudes over distance. The decay of amplitudes with event-receiver distance can be described by the product of geometrical spreading and wave attenuation by damping as

$$A(r) \sim \frac{1}{r} \exp(-\alpha\, r), \tag{1}$$

with the measured amplitude A, event-receiver distance r and the damping coefficient α (Manthei & Eisenblätter 2008). We extract maximum amplitude values from the bandpass filtered (7–11 kHz) 20 ms event windows. The filter includes the most prominent high-energy peak in the stacked spectra of Fig. 4. The event-receiver distance is normalized to a reference distance r_0 reflecting the network geometry, here 20 m, in accordance with Zang *et al.* (2017). The measured maximum amplitudes A are first converted to μV and subsequently to a logarithmic decibel scale following a convention in acoustic emission studies (Köhler *et al.* 2009; Zang *et al.* 2017):

$$A[\mathrm{d}B_{AE}] = 20\ \log_{10}(A[\mu V]). \tag{2}$$

Based on eqs. (1) and (2) we obtain eq. (3) describing a linear relation between the corrected amplitudes $A_{cor}(r)$ and the event-station distance. $A_{cor}(r)$ is corrected for geometrical spreading and the amplifier gain of the recording system (here 20 dB).

$$A_{cor}(r) = 20\ \log_{10}\left(\frac{A[\mu V]\, r}{r_0}\right) - gain[dB] = -\alpha\, r + C, \tag{3}$$

First, eq. (3) is used to estimate the uniform damping coefficient α across the studied rock volume based on large events, recorded with SNR > 2 at more than 7 sensors. To get α, the corrected amplitudes $A_{cor}(r)$ are plotted over distance r for each event. We optimize the summed misfit (L2 norm) of the linear regression fits of all chosen events and obtain a best uniform damping coefficient $\alpha = 0.80$ db m^{-1}.

In a second step, the magnitudes of the single events are estimated using an L2 norm regression with a fixed slope α, searching for the best fitting intercept C. The magnitude M_{AE} is then defined as the ordinate of the reference distance r_0:

$$M_{AE} = A_{cor}(r_0) = -\alpha\, r_0 + C. \tag{4}$$

Since this approach was developed for triggered recordings, we include only sensors with a SNR above 2, otherwise noise amplitudes would bias the magnitude estimation. Only events passing the SNR threshold at more than five sensors are considered for the magnitude estimation. By dividing the relative magnitude by 20, we are able to directly use it in the calculation of the Gutenberg–Richter b-value (Gutenberg & Richter 1944; Cox & Meredith 1993). The magnitude of completeness M_c for each experiment is the median magnitude of completeness calculated using the bootstrap based change-point detection method with a bin size ΔM of 0.05 magnitude units (Amorèse 2007). This provides a conservative estimate of M_c (Mignan & Woessner 2012). Under the assumption that the Gutenberg–Richter relation is valid for this particular case (Kwiatek *et al.* 2018), b-values and corresponding errors are estimated using a formulation corrected for measurement errors and magnitude binning (Tinti & Mulargia 1987), which is also suitable for small data sets (Marzocchi & Sandri 2009). Therein b is defined as:

$$b = \frac{1}{\ln(10)\ \Delta M} \ln(p) \tag{5}$$

with

$$p = 1 + \frac{\Delta M}{\hat{\mu} - M_c}, \tag{6}$$

where $\hat{\mu}$ is the mean of the binned magnitudes above M_c. The asymptotic error is given by

$$\hat{\sigma}_b = \frac{1 - p}{\ln(10)\Delta M\sqrt{Np}} \tag{7}$$

with N being the number of events above M_c. The advantages of these formulations are discussed in detail in Marzocchi & Sandri (2009). Only subcatalogues with more than 50 events exceeding the magnitude of completeness were analysed. The significance of the changes in b was tested using a bootstrap approach provided in the *R* package *GRTo* (Amorèse *et al.* 2010).

2.6 Spatial clustering and fracture plane estimation

Based on the assumption that micro shear events are induced around the fracture tip and to a smaller extent also in the walls around the fracture, we infer the orientation and growth of the fracture zones from the AEs scattered around the opening fractures (Fig. 5). We use the expectation maximization algorithm (EM) (Dempster *et al.* 1977) to identify single or multiple fracture planes based on the hypocentre locations of the AEs of each (re-)fracturing stage. The inferred fracture planes are a 2-D approximation of the ellipsoidal AE clusters. EM is an iterative algorithm to find maximum likelihood estimators of parameters in a statistical model. The statistical model is a mixture of multivariate (3-D) truncated Gaussian distributions. The parameters are estimated by simultaneously maximizing the log-likelihoods of the individual components of the mixture model. Each component of the mixture model describes a distribution assigned to a single fracture zone. The parameters of a component describe the fracture plane location, represented by the mean vector μ, and its extent, related to the covariance matrix Σ. In addition to the observed hypocentre locations, the model also depends on unobserved, latent variables, in our case on the hypocentre classification as rather lying in one of the fracture planes or apart from it, which we define as a noise class with large variances of 1000 m in each direction (Specht *et al.* 2017). The noise model iteratively shrinks towards the grid and incorporates random locations caused by noise contamination in the seismic data or overlapping events. The optimal number of components M, thus the number of fracture planes chosen for each (re-)fracturing stage, is determined by maximizing the likelihood of the mixture model (eq. 8). Due to the number of hypocentres, we limit the maximum number of fracture planes tested for each stage to three.

The complete mixture model of all M components with N observed hypocentres and the component weights w_i is defined as

$$ln\ \mathcal{L} = \sum_{k=1}^{N}\sum_{i=1}^{M} w_i\ \ln p(\mathbf{x}_k|\boldsymbol{\mu}_i, \Sigma_i) \quad \text{with} \quad \sum_{i=1}^{M} w_i = 1. \tag{8}$$

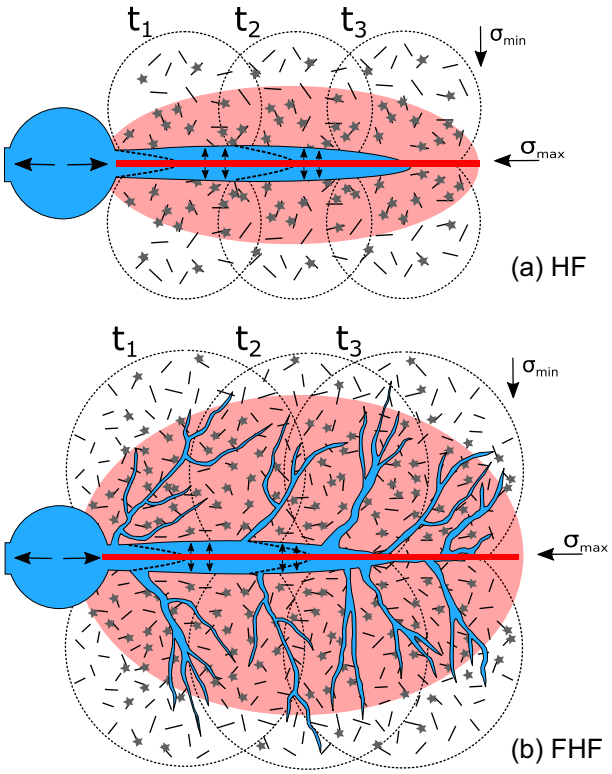

Figure 5. Simplified 2-D schematic of the fracture growth model for conventional continuous HF (a) and fatigue hydraulic fracturing (b) for a single fracture plane. For simplicity, the fracture growth is only shown in one direction. With EM clustering we map the migration of the AEs (grey stars) induced at the fracture tip, here indicated for three time steps (t_1 to t_3). AE are predominately observed close to the fracture. The light red zone represents the ellipsoidal fracture zone obtained from the EM clustering of the AEs. Subsequently, the fracture zone is approximated by the two largest axes of the ellipsoid spanning the assumed fracture plane, and its planarity. The fracture plane is indicated by a red line.

The statistical model of a single component is given by the probability density function

$$p\,(\mathbf{x}|\boldsymbol{\mu},\,\Sigma) = \frac{1}{\mathbf{F}}\,\frac{1}{\sqrt{2\pi^3\mid\Sigma\mid}}\,e^{-0.5\,(\mathbf{x}-\boldsymbol{\mu})^T\,\Sigma^{-1}(\mathbf{x}-\boldsymbol{\mu})}, \tag{9}$$

where $\mathbf{F}$ is the truncation factor as the product of the j directional truncation factors F_j:

$$F_j = 0.5\,\left(\mathrm{erf}\left(\frac{x_{j,\max}-\mu_j}{\sqrt{2\,\Sigma_{jj}}}\right) - \mathrm{erf}\left(\frac{x_{j,\min}-\mu_j}{\sqrt{2\,\Sigma_{jj}}}\right)\right). \tag{10}$$

It facilitates that the integral of p is unity (Specht *et al.* 2017). In the model space it is equivalent to an abrupt cut-off of the distribution function at the grid boundaries. Additionally, we omit hypocentres located at the grid boundaries before the analysis as these locations are expected to be biased. Each iteration in the EM is based on two steps. In the expectation step, the probabilities for the data are determined based on the mixture model. In the maximization step, the algorithm determines new estimates of $\hat{\mu}$ and $\hat{\Sigma}$ maximizing the likelihood based on the probabilities from the expectation step. The iteration stops when the change of the weights is below a given value. The mean vector and the covariance calculated from the hypocentres of each experiment or substage, respectively, are used as *a priori* information. This assures that the iterative search for clusters starts close to the location of the fracture initiation. To obtain statistically meaningful results the algorithm was only applied to substages with more than 300 located events. The EM algorithm does not only provide clusters of events, here interpreted as fracture planes, but also full covariance information to estimate the extent of the given cluster. The two largest eigenvalues of the covariance matrix are used to calculate the 95 per cent confidence region which we define as the elliptic fracture plane to compare the fracture development of the experiments and the substages. The planarity ζ of the clusters (fracture zones) is tested *a posteriori* by

$$\zeta = 1 - \frac{c}{\sqrt{ab}} \tag{11}$$

with a and b being the two largest eigenvalues of the covariance matrix and c being the third eigenvalue. One corresponds to a plane while zero indicates a sphere. We estimate the uncertainty of both the fracture area and its orientation by jackknifing, resampling 90 per cent of the data 10 000 times. Since the convergence in EM depends on the chosen starting values, we conducted a test with a randomization of μ and Σ drawing from normal distributions: For μ around the centre of the injection interval and for Σ around 1 m. The standard deviation of these distributions is 0.5 m in each direction. It was found that the deviation originating from the starting conditions is within the error estimated based on the jackknife approach (Table 1).

3 RESULTS

3.1 Acoustic emission activity

More than 19 600 fracture-induced events were identified and located based on the continuous recordings. In comparison, the original catalogue of AEs based on triggered recordings contained only 196 stronger events (M_w –3.5 to –4.2, Zang *et al.* 2017; Kwiatek *et al.* 2018). HF1 and HF2 each contributed almost a third of the total events, while HF3, HF4 and HF6 contributed only 14, 3 and 20 per cent, respectively. The cyclic pulse injection experiment HF5 induced no locatable event. In the following section, the AE activity is described based on approximately 4300 events, for which we were able to estimate magnitudes. The lower bound for magnitude estimates is roughly $M_{AE}2$. We will refer to all AEs above this magnitude as larger events. Absolute event numbers for each experiment are given in Table 1. Most of the AEs are induced during the pressurization phases. In later stages of the experiments, AEs are also induced during the shut-in phases and single AEs may occur up to several minutes after the end of the pressurization (Fig. 6). The AE catalogue of this study is available in the online supplement (S1).

3.2 Spatio-temporal migration of AE activity

The hypocentres of conventional experiments (HF1, HF2, HF4 and HF6) are spatially clustered in elongated, planar regions (Fig. 7). Contrary, the AE cloud of HF3 is rather diffuse and of smaller vertical extent. The hypocentres are symmetrically distributed to the left and to the right of the borehole but mainly above it (Fig. 8). For the conventional fracturing experiments the extent of the AE clouds is asymmetric in regard to the test intervals, both horizontally and vertically (see e.g. Fig. 6). The AEs are mostly located at only one side of the injection borehole. In the vertical direction the events are predominately located above the borehole, up to 4.5 m above the injection interval, while below the borehole, the extent is limited to approximately 2 m. Taking advantage of the increased AE catalogue, we are able to track the migration of the AEs. For each stage, AEs migrate away from the injection interval. For HF2,

Table 1. Summary of the six HF experiments based on different injection schemes: conventional continuous (HF1, HF2, HF4 and HF6), cyclic progressive (HF3) and dynamic pulse (HF5). Rock types are given below the experiment name: AG (Ävrö granodiorite), fgDG (fine-grained diorite-gabbro) and fgG (fine-grained granite). For each experiment or substage, the total number of events (N) is accompanied by the maximum magnitude, the magnitude of completeness (M_c), the b-value and its asymptotic error as well as the number of events above M_c. The fracture planes estimated from the AE clouds of each substage with $N \geq 300$ using the EM algorithm are described by area and orientation (strike/dip) including the standard deviations (SD) based on 1000 jackknife runs. The strike is corrected for true north in regard to ÄSPÖ coordinate system (Rhen *et al.* 1997). The union area describes the surface formed by all substage planes when projected onto a common plane (see Fig. 12). For HF3 only the single stage area but no union area is given since the resulting ellipses are not within a common plane. The area given for HF4 includes all events without single stage estimates. * terminated prematurely due to problems with the recording system, ** discontinued due to a leakage connecting the injection interval and the open borehole.

Exp. Scheme	Stage	V_{inj} (l)	q_{mean} ($\frac{l}{min}$)	N (with M_{AE})	$M_{\max}$	M_c	b	$N \geq M_c$	Area (m^2)	Union area (m^2)	Strike/dip
HF1		26.86		6403 (841)	3.51	2.50	1.89 ± 0.08	529	–	–	–
(AG)	F	0.77	0.98	177 (7)	2.69	–	–	–	–	–	–
conv	RF1	2.67	1.29	1164 (87)	3.36	2.40	1.91 ± 0.23	67	21.3 ± 0.9	21.3 ± 0.9	154.6/55.7 ± 1.6/0.6
	RF2	4.41	1.59	1352 (141)	3.15	2.45	2.24 ± 0.24	89	22.8 ± 0.5	29.7 ± 1.1	130.3/55.9 ± 1.0/1.3
	RF3	5.15	2.43	1044 (163)	3.17	2.45	1.71 ± 0.16	12	22.1 ± 0.5	31.3 ± 1.2	129.5/50.7 ± 1.1/1.3
	RF4	4.62	4.55	702 (108)	3.17	2.55	1.97 ± 0.26	59	25.9 ± 0.9	33.9 ± 1.5	120.7/54.4 ± 1.5/1.2
	RF5	9.24	4.68	1886 (327)	3.51	2.60	2.03 ± 0.16	170	33.3 ± 0.9	38.7 ± 1.7	120.5/54.5 ± 1.2/0.6
HF2		29.7		6085 (1577)	3.92	2.50	1.72 ± 0.06	936	–	–	–
(AG)	F	3.8	1.7	817 (192)	3.14	2.50	2.66 ± 0.29	83	8.2 ± 0.3	8.0 ± 0.3	130.9/73.7 ± 0.9/0.5
conv	RF1	5.0	1.7	1091 (230)	3.29	2.30	1.59 ± 0.12	169	17.9 ± 0.3	17.9 ± 0.4	127.6/64.6 ± 0.7/0.3
	RF2*	1.2	2.5	6 (3)	2.44	–	–	–	–	–	–
	RF3	5.5	2.5	1145 (287)	3.31	2.50	2.00 ± 0.16	154	25.6 ± 0.4	26.4 ± 0.6	124.1/64.8 ± 0.6/0.2
	RF4	4.8	4.8	944 (233)	3.67	2.50	1.54 ± 0.13	141	16.0 ± 0.7	26.5 ± 0.9	120.8/65.9 ± 1.3/0.3
sec.	RF4								11.1 ± 3.3	–	88.7/31.4 ± 5.9/6.0
	RF5	9.4	4.8	2064 (628)	3.92	2.55	1.67 ± 0.08	418	24.6 ± 0.4	34.2 ± 1.0	120.7/62.7 ± 0.4/0.2
sec.	RF5								10.0 ± 0.7	–	109.7/40.3 ± 10.5/12.5
HF3		25.24		2866 (606)	3.18	2.50	2.34 ± 0.14	279	–	–	–
(AG)	F	0.64	0.72	1 (0)	–	–	–	–	–	–	–
prog	RF1	3.3	1.6	308 (70)	2.91	2.25	–	45	12.0 ± 0.6	–	44.8/81.4 ± 7.1/2.4
	RF2	5.2	2.5	406 (96)	2.97	2.35	–	48	12.8 ± 0.5	–	189.2/75.2 ± 10.9/2.7
	RF3	5.6	5.3	544 (115)	3.10	2.55	2.43 ± 0.32	59	14.1 ± 0.4	–	141.9/45.2 ± 4.4/1.3
	RF4	10.5	5.3	1607 (325)	3.18	2.50	2.33 ± 0.17	185	16.4 ± 0.3	–	120.3/34.3 ± 4.8/0.7
HF4		4.16		532 (121)	2.76	2.15	2.54 ± 0.28	78	37.7 ± 1.3	–	35.1/81.2 ± 1.1/0.6
(fgDG)	F	0.27	0.48	264 (57)	2.76	2.20	–	20	–	–	–
conv	RF1	1.8	0.53	212 (52)	2.58	2.15	–	36	–	–	–
	RF2**	2.09	0.61	56 (12)	2.59	–	–	–	–	–	–
HF5		16.37		0 (0)	–	–	–	–	–	–	–
(fgDG)	F	1.7	0.4	–	0 (0)	–	–	–	–	–	–
pulse	RF1	4.3	1.4	–	0 (0)	–	–	–	–	–	–
	RF2	6.5	7.0	–	0 (0)	–	–	–	–	–	–
	RF3	3.8	6.0	–	0 (0)	–	–	–	–	–	–
HF6		24.1		3870 (1157)	3.71	2.50	1.94 ± 0.08	564	–	–	–
(fgG)	F	8.72	4.89	1889 (569)	3.71	2.55	1.98 ± 0.13	240	25.8 ± 0.6	23.7 ± 0.6	117.2/88.9 ± 1.7/0.3
conv	RF1	5.11	6.64	690 (221)	3.51	2.45	1.86 ± 0.17	126	32.8 ± 1.0	35.7 ± 1.2	140.5/89.6 ± 0.8/0.4
	RF2	5.09	6.45	716 (198)	3.49	2.40	1.71 ± 0.15	132	15.6 ± 8.6	36.4 ± 8.7	347.1/81.6 ± 13.1/1.4
	RF3	5.18	6.97	575 (169)	3.30	2.35	1.68 ± 0.16	105	37.7 ± 5.9	46.8 ± 10.5	143.2/86.1 ± 3.8/0.8

HF4 and HF6 this migration is predominately upwards, while for HF1 AEs are migrating mainly laterally. During the end of the stages HF2–RF4 and HF2–RF5, there is an additional migration of AEs in the direction of HF1 below the borehole (Fig. 6, third row). The compact, symmetric growth of the AE cloud of HF3 has no dominant direction of migration. 2-D plots of the AE cloud of HF1, HF4 and HF6 are given in Figs S4, S5 and S6.

By stage wise analyses of planar structures within the AE clouds using Gaussian mixture model fitting, we found that for each stage the AE clouds are best described by one fracture plane class and the noise class. The fracture planes are similarly oriented in the (re-)fracturing stages of HF1, HF2 and HF6, with strike directions between 120° and 150° (Fig. 9). The dip of these planes is increasing towards the well head, but is stable within the experiments. Planes fit to the cloud of HF1 dip by 55° while the planes estimated for HF6 are dipping almost vertically. Generally, the fitted planes dip towards the deeper part of the borehole. To describe the secondary AE migration during HF2, we additionally allowed two fracture planes in the EM clustering based on the maximum likelihood model for two fracture plane classes. In this case, the algorithm only converges stably for HF2–RF4 and HF2–RF5 with a secondary plane dipping less steep in the direction of the pre-fractured zone of HF1 (Table 1). The secondary fracture plane class does not significantly alter the extent and the orientation of the main fracturing plane. Since the stages of HF4 are below the threshold of 300 events, we only calculate an overall estimate. The resulting plane strikes parallel to the borehole. Once again, there are prominent differences for the cyclic progressive injection scheme of HF3. We found varying strike directions of steep dipping planes for the first two stages, but moderately dipping planes situated mainly above the

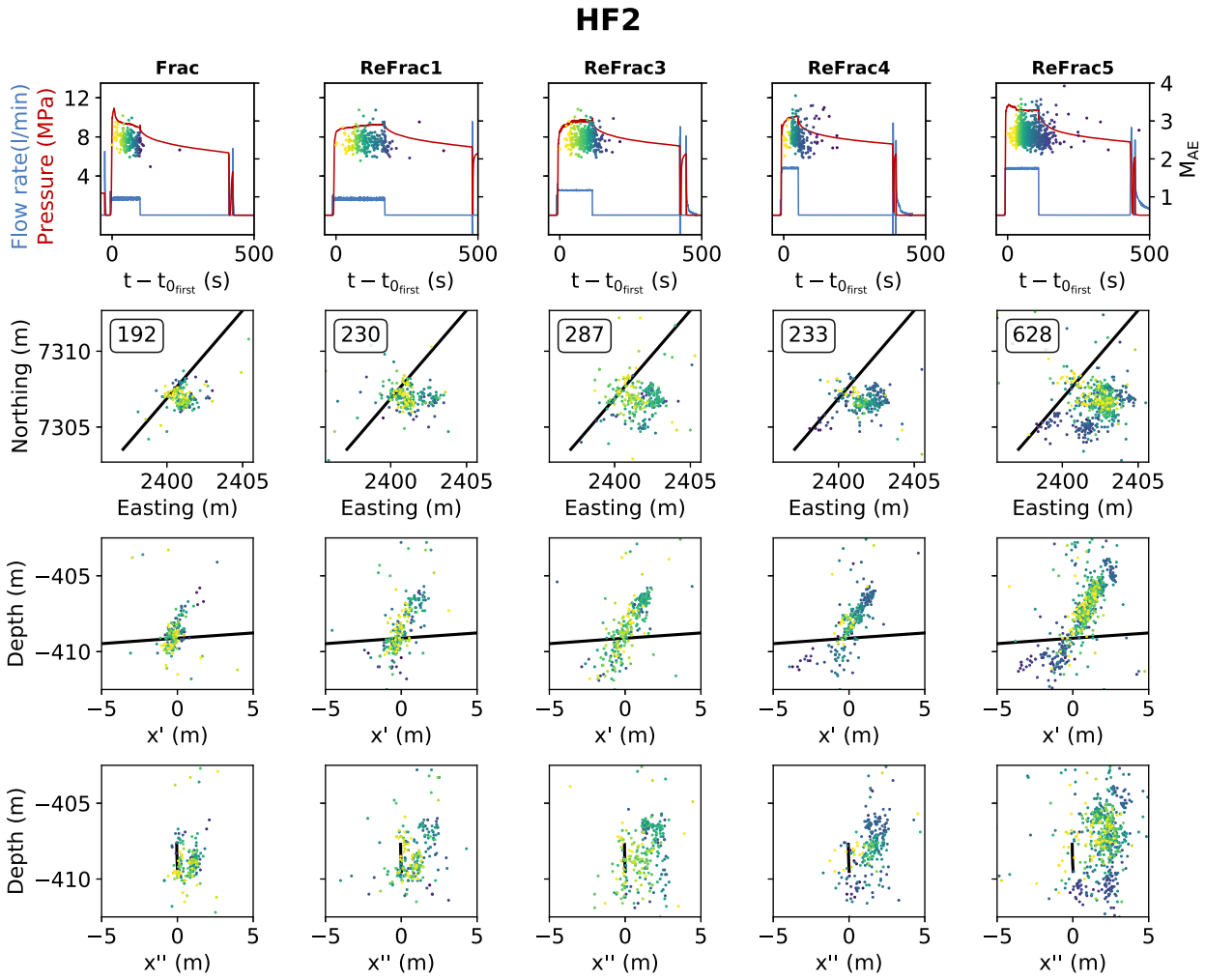

Figure 6. AE activity during the (re-)fracturing stages (columns) of the conventional continuous experiment HF2: The uppermost row shows the injection parameters and the occurrence of AEs including their magnitudes over time. The time is normalized to the first AE occurrence in each stage. Only events with magnitude estimates are plotted. The number of events is given in the second row. The following rows depict the spatio-temporal migration including a map view and two depth sections along fracturing borehole (x') and perpendicular to it (x"), respectively. The events are colour-scaled by origin time (see first row). AEs predominately migrate upwards at the southeast side of the borehole. During late phases in HF2–RF4 and HF2–RF5 there is a secondary downward migration. Post-injection activity increases during late stages (first row).

borehole for the last two stages. The second set of planes strikes similarly to the planes of the continuous experiments HF1, HF2 and HF6. In general, the area of the substage planes is growing continuously in the conventional experiments reaching more than 30 m^2. Conversely, the fracture zones of the more complex multiple plane setup of HF3 show only a slight increase in size after the first activation, reaching at most 16 m^2. When calculating the planarity of the ellipsoids of the inferred fracture zones, we see a clear difference between the continuous experiments (0.78–0.94) and HF3 (0.51–0.71).

3.3 Frequency magnitude distribution

The magnitude of completeness is 2.50 for all experiments except HF4, where the catalogue is complete down to a magnitude of 2.15. The highest magnitude event (M_{AE} 3.92) was induced during the last refrac of HF2, when the AEs migrated towards the previously fractured volume of HF1 (Fig. 7). Except for the discontinued experiment HF4 (M_{max} 2.76), the conventional continuous injection experiments induced higher maximum magnitudes (3.51, 3.92 and 3.71) than HF3 (3.18). By analysing the single (re-)fracturing stage, we gain insight into the characteristics of the AE activity induced during the experiments. For the continuous experiments, we observe a distinct step in induced magnitudes and the number of larger events, when the fracture breakdown pressure or the fracture reopening pressure is reached. Such a step is absent or less pronounced in experiment HF3 (see Fig. 6, first row, especially during HF2–RF4 and HF2–RF5 and Fig. 8). For HF1, HF2 and HF3 the induced maximum magnitudes increase gradually during the refracturing stages. In contrast, the largest events of the experiments HF4 and HF6 are induced during the fracturing stage and the maximum magnitudes decrease gradually in the subsequent refracturing stages. A comparison of the frequency–magnitude distributions (FMD) indicates that there are two ranges of *b*-values. The seismicity induced by the progressive injection scheme (HF3) and by experiment HF4 has an increased number of small events relative to the large ones. The *b*-values for these experiments are 2.34 and 2.51. HF1, HF2 and HF6 have significantly lower *b*-values of 1.89, 1.72 and 1.94, respectively (Fig. 10). The stage-wise changes are not always significant since the number of events is smaller, however the *b*-values show a

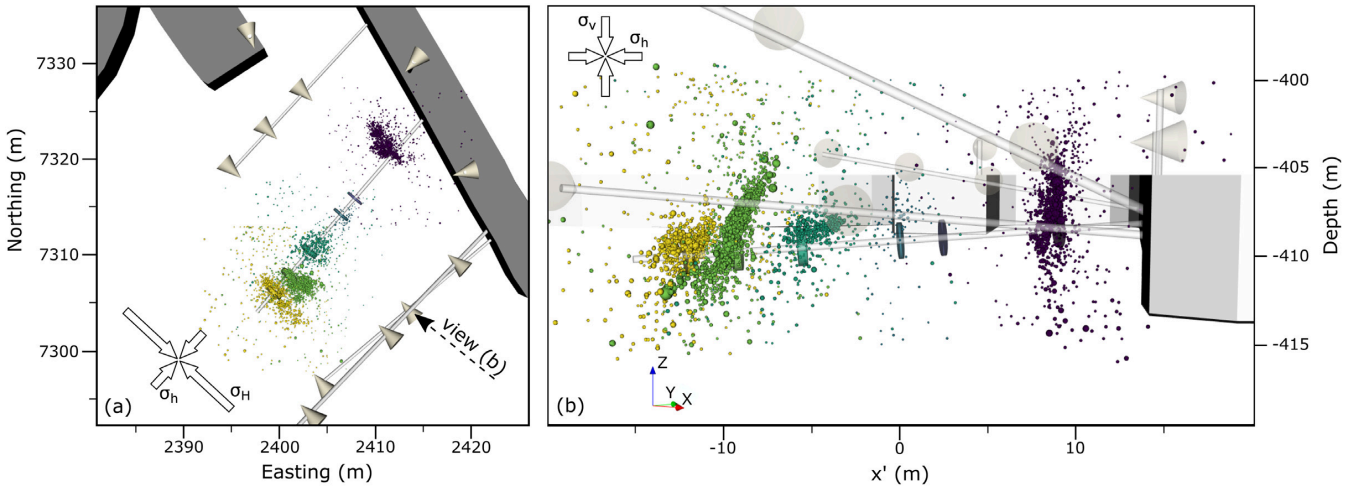

Figure 7. AE hypocentres for all experiments except HF5, for which no locatable event could be extracted. Injection intervals and AE hypocentres are colour-coded as in Fig. 1. The symbol size represents the magnitude. The direction of view in (b) is indicated in (a). AE hypocentres are predominately located above the borehole. The AE clouds of HF2, HF4 and HF6 are elongated in *z*-direction and mainly on one side of the borehole, while the cloud of HF1 is extended in south-east direction. These zones describe the fracture zones of the associated experiment. In experiment HF2 a secondary branch of AE activity reaches the pre-fractured zone of HF1. The more diffuse AE cloud of HF3 is located above the borehole while being oriented subparallel to it. Due to the small number of events with small magnitudes the location of the cloud of HF4 is less obvious (see Fig. S5 for more details). *In situ* stresses from Klee & Rummel (2002) are indicated by white arrows. An animated version of this figure is provided in the online supplement (S2).

decreasing trend from one stage to another within the experiments HF2, HF3 and HF6 (Table 1).

4 DISCUSSION

The study of massive AE activity induced by HF experiments with different injection schemes and a subsequent comparison requires, at least, an unbiased and consistent workflow able to automatically process large amounts of continuous, highly sampled (1 MHz) waveform data with tens of thousand of events. With our approach we are for the first time able to (semi-)automatically map such massive AE activity occurring in distinct clusters for multiple *in situ* fracturing experiments. Due to the uniform magnitude of completeness of the different experiments, we consider that the entire workflow is able to provide comparable catalogues for the single experiments. By estimating the magnitude of completeness within depth intervals of 1 m we observe a strong depth dependence of M_c. At the depth of the stimulation borehole (–407 to –410 m) M_c is 2.50, which is in accordance with the overall estimate of M_c. Due to the experimental setup with a downward dipping stimulation borehole and upward dipping monitoring boreholes, the detection capabilities are reduced below the stimulation borehole, while being better above it. In the uppermost depth interval (–401 to –402 m) M_c reaches 2.20, while M_c is 2.65 in the lowermost tested interval (–412 to –413 m). M_c also depends on the AE rate, as it controls the physical dead-time for the detection of small events in the coda of the larger ones. The smaller M_c for HF4 is attributed to the reduced AE rate due to the small injected volume (Table 1). Given the lack of frequent larger events in HF4, we are able to process smaller events otherwise not resolved.

The usage of single-component AE borehole sensors hinders the detection and location of AEs since the discrimination of *P* and *S* phases is difficult, especially for multiple events close in time. Reflected phases at the tunnel wall, mostly observed for HF6, introduce further uncertainties. Moving towards the network's centre and the tunnel wall (i.e. from HF1 to HF6), the proportion of located events also having magnitude estimates increases gradually due to an improved azimuthal sensor coverage and two sensors at the tunnel wall. The three experiments HF2, HF3 and HF4 in the centre of the sensor network have similar ratios. Since all completed experiments have a common magnitude of completeness, the changes in detection capability have no influence on the calculation of the *b*-value which only considers events above M_c. By re-estimating the fracture plane geometry using only events above M_c, we found that the mapped fracture plane area is reduced by 10–20 per cent but the centres and the orientations of the fracture planes are stable. This implies that detection capabilities do not bias the fracture plane estimation but including smaller AEs enables us to follow the fracture farther away from the injection interval.

The magnitude calibration suggested in Kwiatek *et al.* (2018) cannot be used here because it was obtained from the largest events only and low-frequency noise gets dominant for small events. However, our robust relative magnitude estimates allow comparing the different injection schemes. Deviations in relative magnitude estimates compared to López-Comino *et al.* (2017) and Zang *et al.* (2017) (2.45 and 2.79 compared to 3.92) arise from the choice of a different frequency bandpass filter for the measurement of maximum amplitudes as well as from a different attenuation coefficient here determined uniformly for all experiments.

The spatial clustering of the AEs in distinct fracture zones as well as the location of early events of each substage close to the injection interval support the reliability of the absolute locations. Uncertainty estimates for the grid search based location technique are computationally expensive, so we may only provide a qualitative estimate by assessing it for single events. The location uncertainty is larger in vertical direction due to the network geometry and the fact that most of the detected events (∼75 per cent) are located below the sensor network. For small events the weighted standard deviation of the repeated locations is not exceeding 0.5 m in both horizontal directions and 2.0 m in the vertical direction. In general, the hypocentre uncertainty strongly depends on the location within the network as well as on the signal-to-noise ratio and the number of sensors recording the event, thus on the event size. By fitting normal distributions within the EM clustering and with the covariance

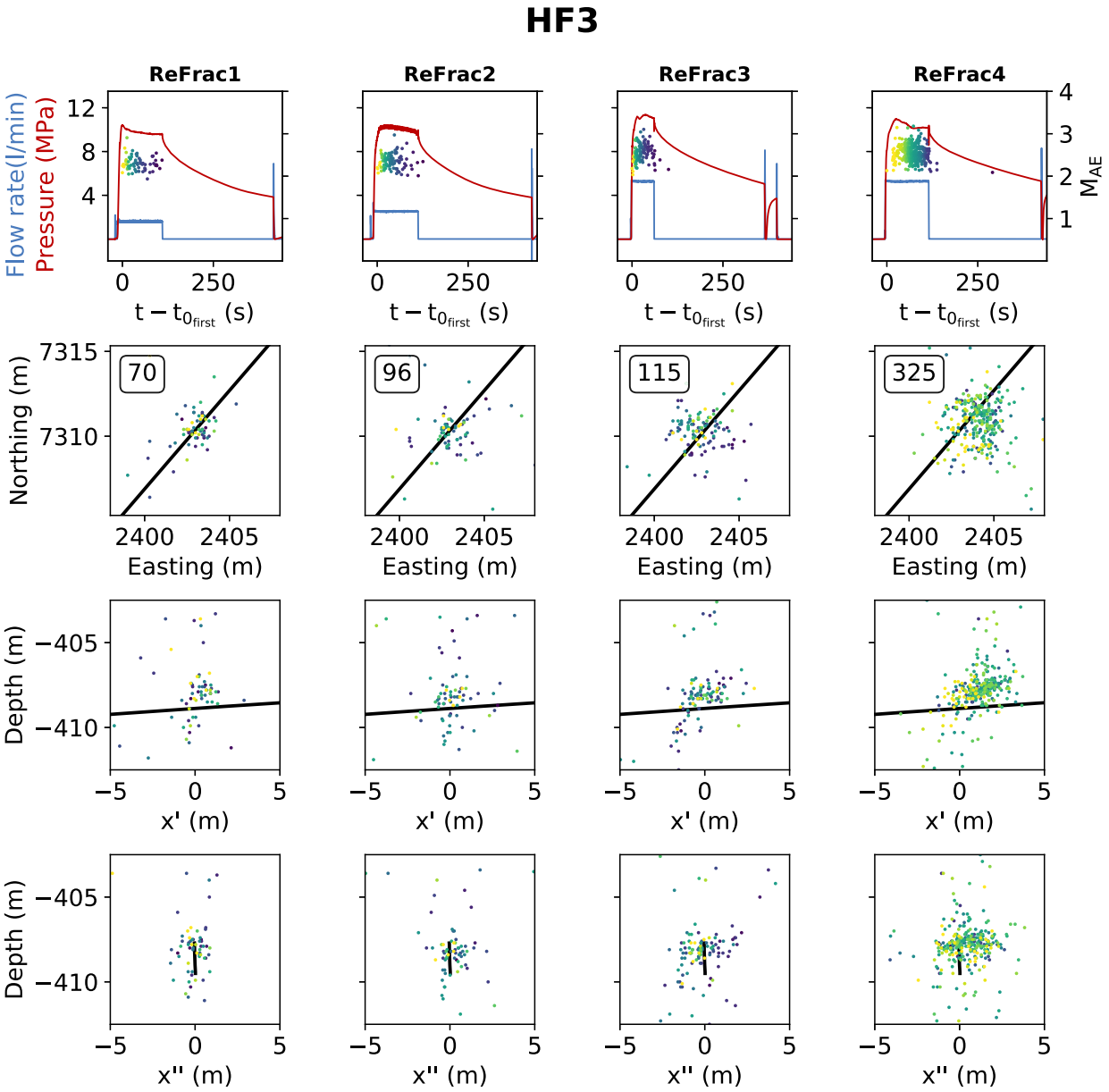

Figure 8. AE activity during the (re-)fracturing stages of the cyclic progressive HF3: Post-injection activity is very low (first row). AEs migrate symmetrically around the injection interval. During HF3–RF3 and HF3–RF4 the AE activity migrates predominately above the borehole in the direction of the well head. Only events with magnitude estimates are plotted. See caption of Fig. 6 for a detailed description of the plot features.

analysis, we account for the increased uncertainties of the single event locations, as long as the location errors are unbiased. The latter was verified based on the jackknife (Quenouille 1956; Sharot 1976). Therefore, we can describe the clusters, thus the fracture geometry, without knowing the single event location uncertainties.

Since the experiment HF4 was not completed due to a leakage behind the packer during the second refracturing stage (Zang *et al.* 2017), the group of the continuous, conventional injection schemes hereafter only refers to HF1, HF2 and HF6. In general, the number of induced AEs and the maximum magnitude are positively correlated with the injected fluid volume while the injection rate has only a second order effect. Figg.11(a)–(d) shows that the continuous experiments induced more events and higher maximum magnitudes in each stage compared to the cyclic progressive scheme while the injected volume, the flow rates and the hydraulic energy (product of injected volume and injection pressure) pumped into the system are similar. The injected volume and the supplied hydraulic energy in the dynamic pulse injection experiment HF5 do not reach the values of the last stage (RF4 or RF5) of the other experiments but are assumed to be large enough to induce AEs in case the same processes were active during the injection. The same applies to the cyclic fracturing stage of HF3 having less AEs than HF4-F and HF1-F despite a similar amount of supplied hydraulic energy (Fig. 11a). The cumulative seismic energy of the induced events is larger for the continuous experiments, implying an increased seismic injection efficiency (seismic energy divided by hydraulic energy, Maxwell *et al.* 2008), thus more pumped-in energy is released by AE activity [Fig. 11(e) and (f)]. The small number of AEs induced during HF4 and the lack of AEs during HF5, on the one hand, may be attributed to a higher attenuation of the fine-grained diorite-gabbro only stimulated during these two experiments. On the other hand, the AE reduction could also be explained by the injection protocol.

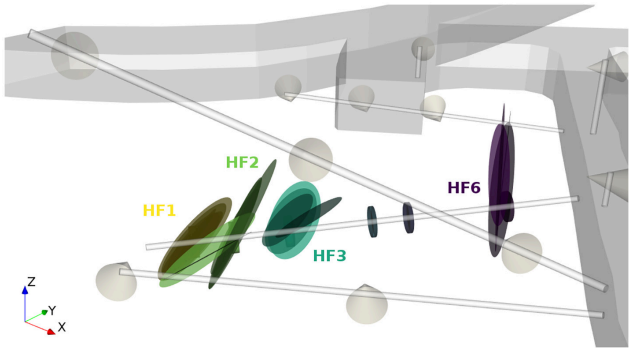

Figure 9. The fracture planes for the single (re-)fracturing) stages estimated from the corresponding AE cloud using the EM algorithm are colour-coded as in Fig. 1. Overlapping fracture zones appear darker. The stage-wise fracture plane estimates of the continuous experiments (HF1, HF2 and HF6) have similar strikes and dips while the fracture zones estimated for HF3 have switching strikes and dips, describing a more complex fracture volume. The secondary fracture zone mapped for HF2 dips towards the pre-fractured volume of HF1. It is not reaching HF1, as seen in this projection. The fracture plane estimated for HF4 is not shown here, to focus on the difference between the completed continuous experiments and HF3. An animated version of this figure is provided in the online supplement (S3).

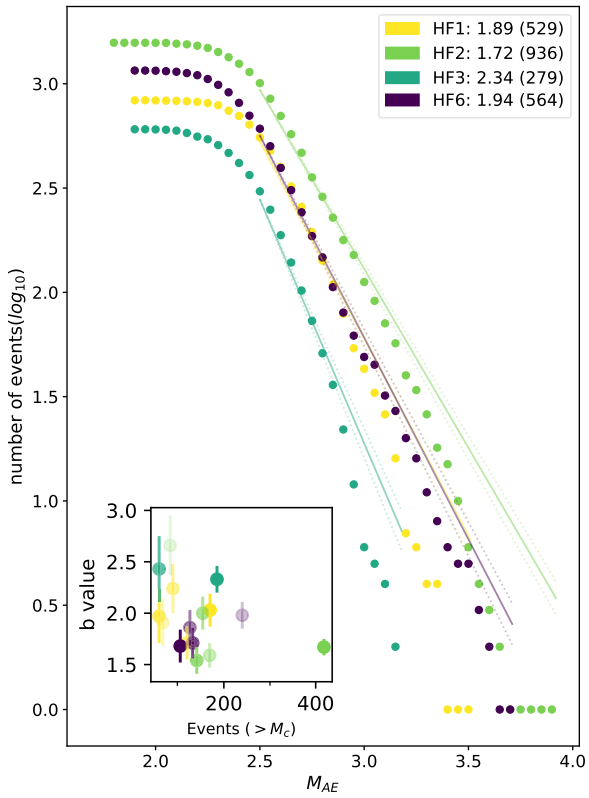

Figure 10. The frequency magnitude distributions of the HF experiments reveal a high *b*-value for the cyclic progressive injection experiment HF3 and lower *b*-values for the conventional continuous experiments (HF1, HF2 and HF6). The asymptotic error is shown by dotted lines. HF4 is not included, because the experiment was stopped prematurely. The inset shows stage-wise *b*-values, with shades getting darker from the fracture stage to the last refracturing stage. The error bars show the asymptotic error for each stage based on eq. (7). The number of events above M_c used in the calculation of stage-wise *b* is not biasing the *b*-value estimates when exceeding 100 events. For less events such an influence can not be ruled out.

In case of the continuous experiment HF4, the protocol was stopped prematurely resulting in a reduced injected volume. HF5 is the only dynamic pulse injection protocol in which other fracturing processes might act. However, the available data and the experimental setup prevent gaining insights into these processes. We suppose that HF5 induced AEs below the detection threshold, as the seismic energy is quickly attenuated within the fine-grained diorite-gabbro. Increased detection capabilities of the sensor network may have been able to reveal the AE activity induced by this advanced scheme at the given scale.

The spatial AE patterns of the HF experiments are influenced by complex interactions of the injection protocol (with variations in injection rate and injected volume) and local stress heterogeneities from varying sources. Asymmetric growth, as mapped for all experiments, is commonly reported for microseismicity induced by hydraulic fracturing (see e.g. Eisner *et al.* 2006; Fischer *et al.* 2009; Downie *et al.* 2010; Rutledge *et al.* 2013). A visual inspection of all located events (note that in Figs 6 and 8 only events above M_c are plotted) shows that in the first stages of HF2 and HF3 the events are located almost equally above and below the borehole (see Fig. S7). The vertical asymmetry can at least partly be attributed to the reduced detection capabilities below the borehole. In later stages the influence of local stress gradients from buoyancy effects suggested by López-Comino *et al.* (2017) might be dominant. Our unique explanation for the unidirectional lateral growth is the presence of lateral stress gradients, as suggested by Dahm *et al.* (2010). The lateral growth is well observed also for HF6, which has an excellent azimuthal sensor coverage. In contrast to the conventional experiments, we observe only a vertical, but no lateral asymmetry within the AE cloud induced during the cyclic progressive injection experiment HF3. A local anomaly in the stress gradient at the location of HF3 is unlikely, as the neighbouring injections (HF2 and HF4) show a similar lateral asymmetry to the southeast. Instead, the symmetry of the AE cloud of HF3 may be the result of the cyclic loading of the rock during the fracturing stage: by fatigue weakening of the rock, local stress gradients could be canceled out. The switching strike directions of the fracture planes and the steep dipping angles within experiment HF6 are most likely caused by the influence of the tunnel wall. AE clouds matching the contour of tunnel walls and cavities were observed in rock salt and attributed to the influence of the free surface of the wall on the local stress state affecting a zone of approximately 10 m around the tunnel (Manthei *et al.* 2001; Maghsoudi *et al.* 2014). Krietsch *et al.* (2019) found stress variations in magnitude but also in orientation when approaching a shear zone in crystalline rock within the Grimsel URL influencing up to 30 m. We conclude that the tunnel wall is also responsible for the distinct, gradual steepening of the mapped fracture planes of the continuous experiments. Since the tunnel is parallel to the largest principal stress, there is no stress perturbation influencing the strike of the approximated fracture zones in the deeper part of the borehole. The strike of the fracture planes is in very good agreement with the stress estimates of Klee & Rummel (2002) and Ask (2006) and also in good agreement with the orientations reported in Zimmermann *et al.* (2019) based on impression packer tests, a method where induced fractures inside the borehole are imprinted into the rubber sleeve of an inflatable packer. The best compatibility in regard to the strike is observed in the latest refracturing stages of the experiments HF1–HF3. The impression packer tests also depict several fractures with varying strikes for HF4 and a single fracture for HF5, but none of those can be resolved due to the low number or the lack of AEs, respectively. The single fracture plane mapped parallel to the borehole for HF4 is most probably the result of the

joined fitting of the multiple fractures which are only growing to one side of the borehole. It is important to state, that the fracture plane dips determined by the EM algorithm may deviate from the impression packer test results because they are not necessarily centred or even intersecting the injection interval but constrained by the AE cloud, that maps the stress conditions at some distance from the borehole. Further, the EM algorithm is not able to differentiate between a single large fracture plane and many smaller planes closely distributed along the assumed large fracture plane owing to the scatter of the AE locations, for example due to the homogeneous velocity model and resolution limitations caused by the discretization on the traveltime grid. Local changes in the stress distribution around the borehole may introduce small variations in strike and dip of the substage fracture planes developing during the conventional continuous experiments. By inverting first motion polarities Kwiatek *et al.* (2018) found heterogeneous focal mechanisms, partly alternating between reverse faulting and strike slip. This implies switching of the directions of σ_2 and σ_3, thus variable stress conditions, probably due to seismic and aseismic processes induced by the fluid injection (Schoenball *et al.* 2014; Ziegler *et al.* 2017; Kwiatek *et al.* 2018). Based on few events, Kwiatek *et al.* (2018) suggested that AEs induced during the experiments are the result of failure inside very complex fracture networks developing without the presence of a large scale fracture. In the light of the much larger number of located AEs in our catalogue and their clustering in fracture planes, we propose an alternative interpretation of the AE cloud of the conventional injection experiments as the footprint of an opening and closing of subplanar hydraulic fractures strictly matching the local stress conditions. The presence of a main fracture plane which is reactivated and enlarged in subsequent stages is well mapped for the continuous experiments. The increased planarity of the ellipsoidal clusters of these experiments supports the approximation as fracture planes. In contrast, the plane fits for the substages of HF3 show a clear trend of decreasing dip and switching strike as well as a reduced planarity. This might be attributed to the fracturing of a weakened zone, produced by the cyclic progressive injection, inducing multiple fractures instead of a single fracture, thus a more complex fracturing network as suggested by Kwiatek *et al.* (2018). The numerical test of the respective injection schemes in Zang *et al.* (2013) predicted a smaller fracture area for the cyclic progressive scheme and multiple, conjugated fractures. Such complex patterns were also found in the laboratory experiments of Zhuang *et al.* (2019). These experiments also show that the fracture breakdown pressure and the maximum induced event magnitude are significantly lower when applying cyclic injections. The rock mass weakened by the cyclic treatment in these experiments is prone to fail by low energy grain boundary cracks while building complex fracture surfaces. In contrast the monotonic schemes might rather produce transgranular cracks and narrow fracturing zones (Zang *et al.* 2019).

In some substages we observe a spatial gap between the AE cloud and the injection interval, which is also reflected in the estimated fracture zone (Fig. 12 and lower right-hand corner subplot of Fig. 6). This pattern was also observed in larger scale hydraulic fracturing experiments where the seismicity in refracturing phases only started when previously induced fractures were re-inflated (Sasaki 1998). However, by adding the smallest located events to our analysis the apparent gap vanishes (see Fig. S7). The dominance of larger events and the increased seismicity rate farther away from the injection point during the refracturing stages indicate that we predominately map the further growth of the fracture not its reopening close to the borehole. As a consequence, the fractured area is not simply

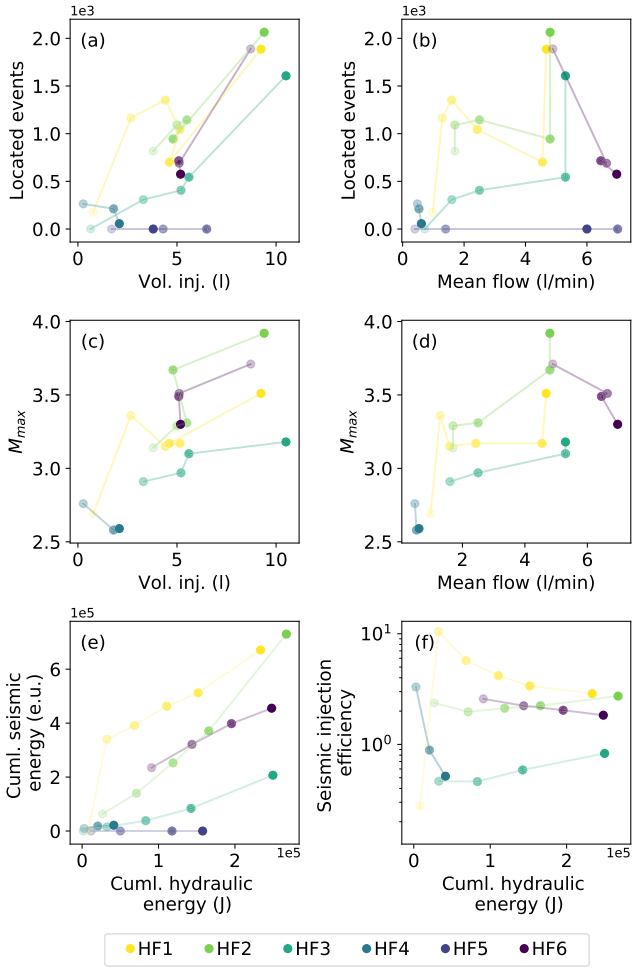

Figure 11. (a–d) The number of AEs and M_{max} increase with the injected volume and in a smaller degree also with the mean flow. The shades from light to dark depict the development from the fracture stage to the last refracturing stage. The fatigue hydraulic fracturing (FHF) schemes HF3 and HF5 induce less or no AEs, respectively, compared to the conventional continuous injections, while the injection parameters are similar. (e–f) Also the cumulative seismic energy, and consequently the seismic injection efficiency, are lower for the FHF schemes. Note that the prematurely stopped experiment HF4 was conducted with reduced volumes and mean flows.

represented by the extent of the seismic cloud of the last refracturing stage. Instead, the fractured area is the cumulative area of the fracture planes of all substages (union area, Fig. 12), as we could miss small AEs induced during the reopening of fractures of previous stages. The increased seismicity at the tip can be explained by larger stress changes due to an increased opening rate. This observation is also in agreement with the hypothesis of buoyancy effects influencing the fracture growth. Nevertheless, we like to point out that aseismic processes might play an important role in hydraulic fracturing (Goodfellow *et al.* 2016), so the fracture zones mapped by AEs are not necessarily showing the total fracture extent. Evidence for large amounts of aseismic slip in massive fluid injections was reported for experiments in granitic basement rock at Le Mayet de Montagne and Soultz, respectively (Scotti & Cornet 1994; Cornet *et al.* 1997; Cornet 2016). In a small-scale, *in situ* fluid injection experiment in pre-fractured carbonate rock Duboeuf *et al.* (2017) found that more than 96 per cent of the deformation was aseismic. Due to the relative magnitude scale used in our study we are not

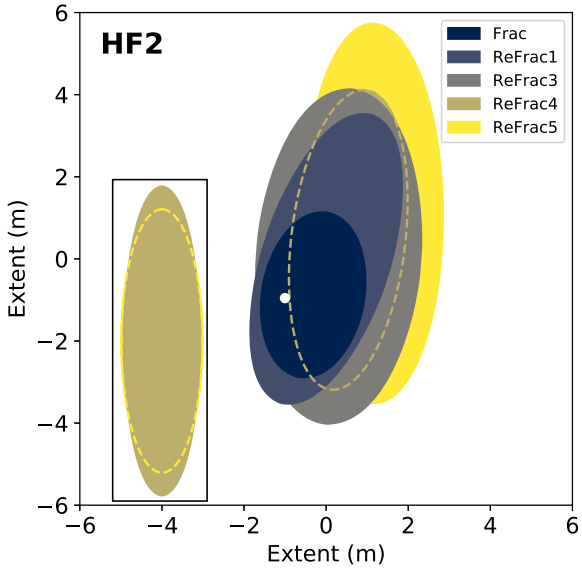

Figure 12. In plane projection of the substage fracture zones of HF2 determined from the AE cloud using the EM algorithm. The fracture is growing continuously upwards at the right side of the borehole (white dot). The dashed line shows the extent of the mapped fracture zone of ReFrac4, that did not grow beyond the extent of ReFrac3. Meanwhile, the secondary fracture zone was activated (inset).

able to quantify the seismic energy release. Thus, the amount of hydraulic energy released in aseismic motions can not be estimated.

In regard to the secondary fracture zone mapped in HF2–RF4 and HF2–RF5 we assume that not enough hydraulic energy was provided to the system as only the flow rate was increased but the injected volume slightly decreased. Instead of growing further upwards, AEs migrate downwards in the direction of HF1. Only when increasing the injected volume in HF2–RF5 there was again enough energy available in the system to let the main fracture propagate further. The secondary fracture predominantly grew during the shut-in phase. When analysing only those events occurring after the stop of the injection, we find even lower *b*-values of 1.3 and 1.4, exclusively in HF2–RF4 and HF2–RF5. A reduced *b*-value, closer to 1, could imply that the secondary fault was in fact no newly opened fracture but a reactivation of a preexisting fault (Maxwell *et al.* 2009). The presumed fault could be of natural origin or represents an interaction with the previously fractured zone of HF1. However, the orientation of this reactivated fault is not well constraint due to the reduced number of events.

The statistical distribution of event magnitudes, described by the *b*-value, can shed light onto local stress conditions (Schorlemmer *et al.* 2005) and provides further insight into the fracturing processes acting during the stimulation. The *b*-values calculated here are within the common range of 1.5–2.7 estimated in large scale hydraulic fracturing data sets (see e.g. Eaton *et al.* 2014). Repeated calculations of *b* for each experiment based on a subset of 200 randomly sampled events proved the independence of the *b*-value from the total number of events. On the substage level, the subsets were reduced to 50 and 100 events. For *b*-values calculated with at least 100 events above M_c, we observe no general correlation between the number of events and *b*. For smaller event numbers a bias of *b* cannot be ruled out. This is also reflected by the asymptotic errors calculated for the *b*-values (see inset of Fig. 10). The deviation from the Gutenberg–Richter distribution for large magnitudes is a common observation for mine scale AE experiments (see e.g. Maghsoudi

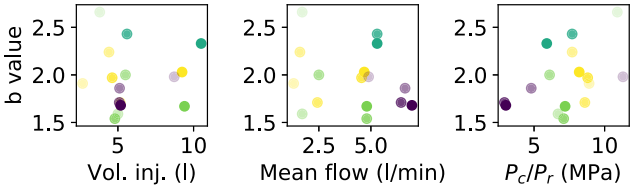

Figure 13. The *b*-value estimates are largely independent of the injection parameters (injected volume, flow rate, injection pressure). Colour scale according to Fig. 10.

et al. 2014). The lack of large events can be explained by physical limitations of the fracture size due to the injected volume of water. It is often also attributed to a bias from uncorrected attenuation effects (Weiss 1997) or the highpass filtering of the raw waveforms (Kwiatek *et al.* 2010). Attenuation is accounted for in our case but it is not known in detail and set to a uniform value. However, since the chosen *b* estimator basically weights the binned data by the number of event in each bin, less numerous large magnitude events inherently have a smaller influence on the *b*-value. In general, it is expected that the *b*-value decreases with increasing applied stress (Scholz 1968). However, it might further depend on heterogeneities of the rock (Mogi 1967) as well as on the stress intensity factor known from fracture mechanics (Meredith & Atkinson 1983). Wessels *et al.* (2011) suggest that elongated, linear seismicity clouds have lower *b*-values, as found for the continuous injection experiments. Higher *b*-values—as observed for the cyclic progressive experiment HF3—imply a more complex fracture system with an increased number of small events, and thus a more effective stimulation. Igonin *et al.* (2018) propose that low *b*-values are associated with fracture zones in accordance with the local stress conditions, while higher *b*-values might define fracture zones that show deviations from the local stress regime. Therefore, the decrease in the *b*-value in the course of the experiments HF6 and HF2 (Table 1) may indicate that the AE activity more and more aligns with the local stress conditions. This independent observation supports the findings from the fracture plane analysis with later stage planes being best aligned with the regional stress field estimate. There is no clear correlation between *b*-values and the injection parameters (Fig. 13). Small differences in the *b*-value among the continuous experiments can be attributed to either geological features and local stress heterogeneities or deviations in the chosen injection scheme, especially for experiment HF6 in regard to the injected volume and mean flow rate (Table 1).

Despite the absence of locatable AEs, the dynamic pulse injection experiment HF5 had the highest permeability increase (2.3 mD after F/26.4 mD after last RF) among all experiments, while HF4 in the same rock type only reached permeabilities of 0.2–3 mD. The permeability was estimated by Zimmermann *et al.* (2019) after each (re-)fracturing stage based on a pressure decline curve analysis. In contrast to HF5, the other FHF experiment HF3 had lower permeabilities (0.4/2.0 mD) compared to the conventional experiments (HF1: 0.6/7.1 mD, HF2: 1.3/4.8 mD) which were conducted in the same rock type as HF3. This observation is in agreement with the results of laboratory experiments on about 60 intact granite samples of Zhuang *et al.* (2019) comparing cyclic and monotonic (conventional) injections schemes.

During the continuous experiments the maximum induced magnitudes occur at the end or even after the injection was stopped, a pattern also observed for massive fluid injections such as at Basel (Häring *et al.* 2008) or Pohang (Grigoli *et al.* 2018; Ellsworth *et al.*

2019). In the cyclic progressive experiment HF3 the maximum magnitude event is induced during the injection and the post-injection AE activity is reduced compared to the continuous experiments. The observed patterns regarding the maximum magnitude, the event number and the event timing are in agreement with the numerical modeling results in Zang *et al.* (2013). This finding supports the concept of fatigue hydraulic fracturing, namely the repeated relaxation of crack tip stresses when using advanced fluid injection schemes. While our interpretation of the influence of the injection style on seismic and hydraulic properties relies on six *in situ* tests only, we consider the strategy of optimizing the injection style at laboratory scale and in subsequent field tests as beneficial (low cost – high impact). We plan to pursue this strategy: After further laboratory studies aiming on detailed insights into the processes acting during FHF as well as on the optimization of the injection scheme for higher permeability enhancement, we intend to go back to the Äspö HRL and apply the optimized injection scheme at the same experimental site. Our findings have the potential to create confidence in new, innovative fracturing concepts for energy extraction technologies.

5 CONCLUSIONS

The study of six *in situ* hydraulic fracturing experiments with different injection schemes at mine-scale revealed striking differences regarding the seismic impact of conventional continuous injections and fatigue hydraulic fracturing schemes developed for the mitigation of large events with potential application in enhanced geothermal systems. The semi-automated analysis of massive, highly sampled, continuously recorded AE activity provides detailed insight into the fracture developments during conventional continuous and cyclic progressive injections. Without manual phase picking for thousands of events, we are able to extract reliable AE catalogues based on automated migration approaches for detection and location as well as a semi-automated classification of AEs and noise events based on a Hidden Markov model classifier. Despite providing a similar amount of hydraulic energy to the systems, the cyclic progressive injection scheme has a lower seismic impact than the conventional continuous scheme. However, the permeability enhancement of the cyclic progressive test is smaller, which is in accordance with laboratory test. Further optimizations of this injection scheme in laboratory experiments are intended. The dynamic pulse pressurization scheme induced no locatable events, although the largest increase in permeability of all experiments was observed. Compared to the continuous injection scheme, the cyclic injection experiment has a lower seismicity, lower maximum magnitudes and significantly larger *b*-values, implying an increased number of small events relative to the large ones. It further has a lower seismic injection efficiency. Hence, the seismic energy release is dissipated in a relatively large number of small events while the maximum induced magnitude is reduced. The EM based clustering of the induced AEs and the *b*-value analyses reveal significant differences in the fracturing process between the cyclic progressive injection scheme and the conventional continuous scheme. While the conventional continuous experiments induce planar, elongated fracture planes with stable orientations throughout the (re-)fracturing stages, the progressive scheme induces a more complex fracture pattern with variably oriented fracture planes. This difference is also reflected in the *b*-value estimates being lower for the continuous experiments. Changes in *b*-value are largely independent of the hydraulic parameters (injection rate, pumping pressures and injected volume) and therefore attributed to the different fracturing processes induced by the different injection schemes. For this particular experiment, it was shown that fatigue hydraulic fracturing schemes can successfully mitigate larger induced events. The injection scheme has the potential to reduce the seismic impact of enhanced geothermal systems, eventually also leading to a broader public acceptance of this alternative energy supply. In future works, existing numerical modeling approaches, enriched with the AE locations mapped during the *in situ* experiments, will be used to shed light onto the microfracturing processes ahead of the hydraulic fracturing tip during the different fluid-injection schemes.

ACKNOWLEDGEMENTS

The *in situ* experiment at Äspö Hard Rock Laboratory (HRL) was supported by the GFZ German Research Center for Geosciences (75 per cent), the KIT Karlsruhe Institute of Technology (15 per cent) and the Nova Center for University Studies, Research and Development Oskarshamn (10 per cent). An additional in-kind contribution of the Swedish Nuclear Fuel and Waste Management Co (SKB) for using Äspö HRL as test site for geothermal research is greatly acknowledged. P. N. is currently funded by the BMBF (German Federal Ministry of Education and Research) project SECURE (grant agreement No. 03G0872A). F. G. is funded by the European Union's Horizon 2020 research and innovation program under the Marie Skodowska-Curie grant agreement No. 790900. Data were preprocessed using the `python` based seismology environment `pyrocko`, available at https://pyrocko.org (Heimann *et al.* 2017). The detection algorithm *Lassie* used in this study is available at https://gitext.gfz-potsdam.de/heimann/lassie. The Gutenberg-Richter toolbox *GRTo* is available at https://cran.r-project.org/web/packages/GRTo/index.html. We like to thank G. M. Petersen as well as T. Davis for scientific discussions and extensive proof reading. We further thank the editor, John Townend and an anonymous reviewer for their helpful comments and constructive suggestions that improved the manuscript.

REFERENCES

Amann, F. *et al.*, 2018. The seismo-hydromechanical behavior during deep geothermal reservoir stimulations: open questions tackled in a decameter-scale in situ stimulation experiment, *Solid Earth,* **9**(1), 115–137.

Amorèse, D., 2007. Applying a change-point detection method on frequency-magnitude distributions, *Bull. seism. Soc. Am.,* **97**(5), 1742–1749.

Amorèse, D., Grasso, J.-R. & Rydelek, P.A., 2010. On varying b-values with depth: results from computer-intensive tests for Southern California, *Geophys. J. Int.,* **180**(1), 347–360.

Ask, D., 2003. Evaluation of measurement-related uncertainties in the analysis of overcoring rock stress data from Äspö HRL, Sweden: a case study, *Int. J. Rock Mech. Min. Sci.,* **40**(7), 1173–1187.

Ask, D., 2006. New developments in the integrated stress determination method and their application to rock stress data at the Äspö HRL, Sweden, *Int. J. Rock Mech. Min. Sci.,* **43**(1), 107–126.

Beyreuther, M., Hammer, C., Wassermann, J., Ohrnberger, M. & Megies, T., 2012. Constructing a Hidden Markov Model based earthquake detector: application to induced seismicity: Constructing a HMM based earthquake detector, *Geophys. J. Int.,* **189**(1), 602–610.

Cornet, F.H., 2016. Seismic and aseismic motions generated by fluid injections, *Geomech. Ener Environ,* **5,** 42–54.

Cornet, F.H., Helm, J., Poitrenaud, H. & Etchecopar, A., 1997. Seismic and aseismic slips induced by large-scale fluid injections, in *Seismicity Associated with Mines, Reservoirs and Fluid Injections,* Pageoph Topical Volumes, pp. 563–583, Birkhäuser Basel.

Cox, S. & Meredith, P., 1993. Microcrack formation and material softening in rock measured by monitoring acoustic emissions, *IInt. J. Rock Mech. Min. Sci. Geomech. Abstr.,* **30**(1), 11–24.

Dahm, T., 2001. Rupture dimensions and rupture processes of fluid-induced microcracks in salt rock, *J. Volc. Geotherm. Res.,* **109**(1), 149–162.

Dahm, T., Manthei, G. & Eisenblätter, J., 1999. Automated moment tensor inversion to estimate source mechanisms of hydraulically induced microseismicity in salt rock, *Tectonophysics,* **306**(1), 1–17.

Dahm, T., Hainzl, S. & Fischer, T., 2010. Bidirectional and unidirectional fracture growth during hydrofracturing: role of driving stress gradients, *J. geophys. Res.,* **115**(B12322), 1–18.

Dempster, A.P., Laird, N.M. & Rubin, D.B., 1977. Maximum likelihood from incomplete data via the EM algorithm, *J. R. Stat. Soc., B,* **39**(1), 1–22.

Downie, R., Kronenberger, E. & Maxwell, S.C., 2010. Using microseismic source parameters to evaluate the influence of faults on fracture treatments: a geophysical approach to interpretation, in *Proceedings of the SPE Annual Technical Conference and Exhibition,* Vol. SPE 134772, Society of Petroleum Engineers, Florence, Italy.

Dresen, G., Renner, J., Bohnhoff, M., Konietzki, H., Kwiatek, G., Klee, G. & Backers, T., 2019. STIMTEC—a mine-back experiment in the Reiche Zeche underground laboratory, *Geophys. Res. Abstr.,* **21,** EGU2019–9357.

Duboeuf, L., Barros, L.D., Cappa, F., Guglielmi, Y., Deschamps, A. & Seguy, S., 2017. Aseismic motions drive a sparse seismicity during fluid injections into a fractured zone in a carbonate reservoir, *J. geophys. Res.,* **122**(10), 8285–8304.

Eaton, D.W., Davidsen, J., Pedersen, P.K. & Boroumand, N., 2014. Breakdown of the Gutenberg-Richter relation for microearthquakes induced by hydraulic fracturing: influence of stratabound fractures, *Geophys. Prospect.,* **62**(4), 806–818.

Eisenblätter, J., 1988. Localisation of fracture planes during hydraulic fracturing experiments in a salt mine, in *Acoustic Emission,* pp. 291–303, ed. Eisenblätter, J., DGM Informationsgesellschaft Verlag.

Eisner, L., Fischer, T. & Le Calvez, J.H., 2006. Detection of repeated hydraulic fracturing (out-of-zone growth) by microseismic monitoring, *Leading Edge,* **25**(5), 548–554.

Ellsworth, W.L., Giardini, D., Townend, J., Ge, S. & Shimamoto, T., 2019. Triggering of the Pohang, Korea, earthquake (Mw 5.5) by enhanced geothermal system stimulation, *Seismol. Res. Lett.,* **90**(5), 1844–1858.

Fischer, T., Hainzl, S. & Dahm, T., 2009. The creation of an asymmetric hydraulic fracture as a result of driving stress gradients, *Geophys. J. Int.,* **179**(1), 634–639.

Gaucher, E., Schoenball, M., Heidbach, O., Zang, A., Fokker, P.A., van Wees, J.-D. & Kohl, T., 2015. Induced seismicity in geothermal reservoirs: a review of forecasting approaches, *Renew. Sustain. Ener. Rev.,* **52,** 1473–1490.

Gischig, V.S. & Preisig, G., 2015. Hydro-fracturing versus hydro-shearing: a critical assessment of two distinct reservoir stimulation mechanisms, in *Proceedings of the 13th ISRM International Congress of Rock Mechanics,* International Society for Rock Mechanics and Rock Engineering, Montreal, Canada.

Goodfellow, S.D., Nasseri, M.H.B., Maxwell, S.C. & Young, R.P., 2016. Hydraulic fracture energy budget: Insights from the laboratory, *Geophys. Res. Lett.,* **42**(9), 3179–3187.

Grigoli, F., Cesca, S., Vassallo, M. & Dahm, T., 2013. Automated seismic event location by travel-time stacking: an application to mining induced seismicity, *Seismol. Res. Lett.,* **84**(4), 666–677.

Grigoli, F., Cesca, S., Amoroso, O., Emolo, A., Zollo, A. & Dahm, T., 2014. Automated seismic event location by waveform coherence analysis, *Geophys. J. Int.,* **196**(3), 1742–1753.

Grigoli, F. *et al.*, 2017. Current challenges in monitoring, discrimination, and management of induced seismicity related to underground industrial activities: a European perspective, *Rev. Geophys.,* **55**(2), 310–340.

Grigoli, F. *et al.*, 2018. The November 2017 Mw 5.5 Pohang earthquake: a possible case of induced seismicity in South Korea, *Science,* **360**(6392), 1003–1006.

Gutenberg, B. & Richter, C.F., 1944. Frequency of earthquakes in California, *Bull. seism. Soc. Am.,* **34,** 185–188.

Hammer, C., Beyreuther, M. & Ohrnberger, M., 2012. A seismic-event spotting system for volcano fast-response systems, *Bull. seism. Soc. Am.,* **102**(3), 948–960.

Hammer, C., Ohrnberger, M. & Fäh, D., 2013. Classifying seismic waveforms from scratch: a case study in the alpine environment, *Geophys. J. Int.,* **192**(1), 425–439.

Häring, M.O., Schanz, U., Ladner, F. & Dyer, B.C., 2008. Characterisation of the Basel 1 enhanced geothermal system, *Geothermics,* **37**(5), 469–495.

Heimann, S., *et al.*, 2017. Pyrocko—an open-source seismology toolbox and library, V. 0.3. GFZ Data Services. http://doi.org/10.5880/GFZ.2.1.2017.001.

Igonin, N., Zecevic, M. & Eaton, D.W., 2018. Bilinear magnitude-frequency distributions and characteristic earthquakes during hydraulic fracturing, *Geophys. Res. Lett.,* **45**(23), 12 866–12 874.

Klee, G. & Rummel, F., 2002. Rock stress measurements at the Äspö HRL. Hydraulic fracturing in boreholes KA2599G01 and KF0093A01, Tech. Rep. IPR-02-02, Swedish Nuclear Fuel and Waste Management Co., Stockholm.

Kneafsey, T.J. *et al.*, 2018. An overview of the EGS collab project: Field validation of coupled process modeling of fracturing and fluid flow at the sanford underground research facility, lead, SD, in *Proceedings of the 43rd Workshop on Geothermal Reservoir Engineering,* Vol. SGP-TR-213, Stanford University, Stanford, CA.

Köhler, N., Spies, T. & Dahm, T., 2009. Seismicity patterns and variation of the frequency-magnitude distribution of microcracks in salt, *Geophys. J. Int.,* **179**(1), 489–499.

Kolditz, O., Jakobs, L.A., Huenges, E. & Kohl, T., 2013. Geothermal energy: a glimpse at the state of the field and an introduction to the journal, *Geotherm. Ener.,* **1**(1), 1.

Kranz, R.L., Satoh, T., Nishizawa, O., Kusunose, K., Takahashi, M., Masuda, K. & Hirata, A., 1990. Laboratory study of fluid pressure diffusion in rock using acoustic emissions, *J. geophys. Res.,* **95**(B13), 21 593–21 607.

Krietsch, H., Gischig, V., Evans, K., Doetsch, J., Dutler, N.O., Valley, B. & Amann, F., 2019. Stress measurements for an in situ stimulation experiment in crystalline rock: integration of induced seismicity, stress relief and hydraulic methods, *Rock Mech. Rock Eng.,* **52,** 517–542.

Kwiatek, G., Plenkers, K., Nakatani, M., Yabe, Y. & Dresen, G., JAGUARS-Group, 2010. Frequency-magnitude characteristics down to magnitude -4.4 for induced seismicity recorded at Mponeng Gold Mine, South Africa, *Bull. seism. Soc. Am.,* **100**(3), 1165–1173.

Kwiatek, G., Martínez-Garzón, P., Plenkers, K., Leonhardt, M., Zang, A., von Specht, S., Dresen, G. & Bohnhoff, M., 2018. Insights into complex subdecimeter fracturing processes occurring during a water injection experiment at depth in Äspö Hard Rock Laboratory, Sweden, *J. geophys. Res.,* **123**(8), 6616–6635.

Kwiatek, G. *et al.*, 2019. Controlling fluid-induced seismicity during a 6.1-km-deep geothermal stimulation in Finland, *Sci. Adv.,* **5**(5), eaav7224.

Lee, K.-K. *et al.*, 2019. Managing injection-induced seismic risks, *Science,* **364**(6442), 730–732.

López-Comino, J.A., Cesca, S., Heimann, S., Grigoli, F., Milkereit, C., Dahm, T. & Zang, A., 2017. Characterization of hydraulic fractures growth during the Äspö Hard Rock Laboratory Experiment (Sweden), *Rock Mech. Rock Eng.,* **50**(11), 2985–3001.

Maghsoudi, S., Hainzl, S., Cesca, S., Dahm, T. & Kaiser, D., 2014. Identification and characterization of growing large-scale en-echelon fractures in a salt mine, *Geophys. J. Int.,* **196**(2), 1092–1105.

Majer, E.L. & Doe, T.W., 1986. Studying hydrofractures by high frequency seismic monitoring, *Int. J. Rock Mech. Mining Sci. Geomech. Abstr.,* **23**(3), 185–199.

Majer, E.L., Baria, R., Stark, M., Oates, S., Bommer, J., Smith, B. & Asanuma, H., 2007. Induced seismicity associated with enhanced geothermal systems, *Geothermics,* **36**(3), 185–222.

Manthei, G., 2005. Characterization of acoustic emission sources in a rock salt specimen under triaxial compression, *Bull. seism. Soc. Am.,* **95**(5), 1674–1700.

Manthei, G. & Eisenblätter, J., 2008. Acoustic emission in study of rock stability, in *Acoustic Emission Testing,* pp. 239–310, eds Grosse, C. & Ohtsu, M., Springer.

Manthei, G., Eisenblätter, J. & Dahm, T., 2001. Moment tensor evaluation of acoustic emission sources in salt rock, *Construct. Building Mater.,* **15**(5), 297–309.

Marzocchi, W. & Sandri, L., 2009. A review and new insights on the estimation of the b-value and its uncertainty, *Ann. Geophys.,* **46**(6), 1271–1282.

Maxwell, S.C., Shemeta, J., Campbell, E. & Quirk, D., 2008. Microseismic deformation rate monitoring, in *Proceedings of the SPE Annual Technical Conference and Exhibition,* Vol. SPE 116596, Society of Petroleum Engineers, Denver, CO, USA.

Maxwell, S.C. *et al.*, 2009. Fault activation during hydraulic fracturing, in *Proceedings of the SEG Technical Program Expanded Abstracts,* pp. 1552–1556, Society of Exploration Geophysicists, Houston, TX, USA.

Meier, P.M., Rodríguez, A. & Bethmann, F., 2015. Lessons learned from Basel: New EGS projects in Switzerland using multistage stimulation and a probabilistic traffic light system for the reduction of seismic risk, in *Proceedings of the World Geothermal Congress,* International Geothermal Association, Melbourne, Australia.

Meredith, P.G. & Atkinson, B.K., 1983. Stress corrosion and acoustic emission during tensile crack propagation in Whin Sill dolerite and other basic rocks, *Geophys. J. Int.,* **75**(1), 1–21.

Mignan, A. & Woessner, J., 2012. Estimating the magnitude of completeness for earthquake catalogs, *Community Online Resource for Statistical Seismicity Analysis,* doi:10.5078/corssa-00180805.

Mogi, K., 1967. Earthquakes and fractures, *Tectonophysics,* **5**(1), 35–55.

Morris, J.P. *et al.*, 2018. Experimental design for hydrofracturing and fluid flow at the DOE EGS collab testbed, in *Proceedings of the 52nd U.S. Rock Mechanics/Geomechanics Symposium,* Vol. ARMA 18-007, American Rock Mechanics Association, Seattle, WA, USA.

Niitsuma, H., Nagano, K. & Hisamatsu, K., 1993. Analysis of acoustic emission from hydraulically induced tensile fracture of rock, *J. Acoust. Emission,* **11,** S1–S18.

Norbeck, J.H., McClure, M.W. & Horne, R.N., 2018. Field observations at the Fenton Hill enhanced geothermal system test site support mixed-mechanism stimulation, *Geothermics,* **74,** 135–149.

Petty, S., Nordin, Y., Glassley, W., Cladouhos, T.T. & Swyer, M., 2013. Improving geothermal project economics with multi-zone stimulation: results from the Newberry Volcano EGS demonstration, in *Proceedings of the 38th Workshop on Geothermal Reservoir Engineering,* Vol. SGP-TR-198, Stanford University, Stanford, CA.

Quenouille, M.H., 1956. Notes on bias in estimation, *Biometrika,* **43**(3/4), 353–360.

Rhen, I., Gustafson, G., Stanfors, R. & Wikberg, P., 1997. Models based on site characterization 1986-1995, Tech. Rep. SKB TR 97-06, Swedish Nuclear Fuel and Waste Management Co., Stockholm.

Rutledge, J., Downie, R., Maxwell, S. & Drew, J., 2013. Geomechanics of hydraulic fracturing inferred from composite radiation patterns of microseismicity, in *SPE Annual Technical Conference and Exhibition,* Vol. SPE 166370, Society of Petroleum Engineers, New Orleans, LA, USA.

Sasaki, S., 1998. Characteristics of microseismic events induced during hydraulic fracturing experiments at the Hijiori hot dry rock geothermal energy site, Yamagata, Japan, *Tectonophysics,* **289**(1–3), 171–188.

Schoenball, M., Dorbath, L., Gaucher, E., Wellmann, J.F. & Kohl, T., 2014. Change of stress regime during geothermal reservoir stimulation, *Geophys. Res. Lett.,* **41**(4), 1163–1170.

Scholz, C.H., 1968. The frequency-magnitude relation of microfracturing in rock and its relation to earthquakes, *Bull. seism. Soc. Am.,* **58**(1), 399–415.

Schorlemmer, D., Wiemer, S. & Wyss, M., 2005. Variations in earthquake-size distribution across different stress regimes, *Nature,* **437**(7058), 539–542.

Scotti, O. & Cornet, F.H., 1994. In situ evidence for fluid-induced aseismic slip events along fault zones, *Int. J. Rock Mech. Min. Sci. Geomech. Abstr.,* **31**(4), 347–358.

Sharot, T., 1976. The generalized jackknife: finite samples and subsample sizes, *J. Am. Stat. Assoc.,* **71**(354), 451–454.

Specht, S., Heidbach, O., Cotton, F. & Zang, A., 2017. Data-driven earthquake focal mechanism cluster analysis, Tech. Rep. 17/01, GFZ German Research Centre for Geosciences, Potsdam.

Stanchits, S., Surdi, A., Gathogo, P., Edelman, E. & Suarez-Rivera, R., 2014. Onset of hydraulic fracture initiation monitored by acoustic emission and volumetric deformation measurements, *Rock Mech. Rock Eng.,* **47**(5), 1521–1532.

Stauffacher, M., Muggli, N., Scolobig, A. & Moser, C., 2015. Framing deep geothermal energy in mass media: the case of Switzerland, *Technol. Forecast. Social Change,* **98,** 60–70.

Tinti, S. & Mulargia, F., 1987. Confidence intervals of b values for grouped magnitudes, *Bull. seism. Soc. Am.,* **77**(6), 2125–2134.

Warpinski, N.R., Du, J. & Zimmer, U., 2012. Measurements of hydraulic-fracture-induced seismicity in gas shales, *SPE Product. Oper.,* **27**(03), 240–252.

Weiss, J., 1997. The role of attenuation on acoustic emission amplitude distributions and b-values, *Bull. seism. Soc. Am.,* **87**(5), 1362–1367.

Wessels, S., Kratz, M. & De La Pena, A., 2011. Identifying fault activation during hydraulic stimulation in the Barnett shale: source mechanisms, b values, and energy release analyses of microseismicity, in *SEG Technical Program Expanded Abstracts,* pp. 1463–1467, Society of Exploration Geophysicists, San Antonio, TX, USA.

Zang, A., Yoon, J.S., Stephansson, O. & Heidbach, O., 2013. Fatigue hydraulic fracturing by cyclic reservoir treatment enhances permeability and reduces induced seismicity, *Geophys. J. Int.,* **195**(2), 1282–1287.

Zang, A., Oye, V., Jousset, P., Deichmann, N., Gritto, R., McGarr, A., Majer, E. & Bruhn, D., 2014. Analysis of induced seismicity in geothermal reservoirs—an overview, *Geothermics,* **52,** 6–21.

Zang, A. *et al.*, 2017. Hydraulic fracture monitoring in hard rock at 410 m depth with an advanced fluid-injection protocol and extensive sensor array, *Geophys. J. Int.,* **208**(2), 790–813.

Zang, A., Zimmermann, G., Hofmann, H., Stephansson, O., Min, K.-B. & Kim, K.Y., 2019. How to reduce fluid-injection-induced seismicity, *Rock Mech. Rock Eng.,* **52,** 475–493.

Zhuang, L. *et al.*, 2016. Laboratory study on cyclic hydraulic fracturing of Pocheon granite in Korea, in *Proceedings of the 50th U.S. Rock Mechanics/Geomechanics Symposium,* Vol. ARMA-2016-163, American Rock Mechanics Association, Houston, TX, USA.

Zhuang, L. *et al.*, 2019. Cyclic hydraulic fracturing of Pocheon granite cores and its impact on breakdown pressure, acoustic emission amplitudes and injectivity, *Int. J. Rock Mech. Min. Sci. ,* **122,** 104065.

Ziegler, M.O., Heidbach, O., Zang, A., Martínez-Garzón, P. & Bohnhoff, M., 2017. Estimation of the differential stress from the stress rotation angle in low permeable rock, *Geophys. Res. Lett.,* **44**(13), 6761–6770.

Zimmermann, G., Zang, A., Stephansson, O., Klee, G. & Semiková, H., 2019. Permeability enhancement and fracture development of hydraulic in situ experiments in the Äspö Hard Rock Laboratory, Sweden, *Rock Mech. Rock Eng.,* **52,** 495–515.

Zoback, M.D., Rummel, F., Jung, R. & Raleigh, C.B., 1977. Laboratory hydraulic fracturing experiments in intact and pre-fractured rock, *Int. J. Rock Mech. Min. Sci. Geomech. Abstr.,* **14**(2), 49–58.

SUPPORTING INFORMATION

Supplementary data are available at *GJI* online.

Figure S1. Catalogue of induced AEs
Figure S2. animated version of Fig. 7
Figure S3. animated version of Fig. 9
Figure S4. AE activity during (re-)fracturing stages of HF1: post-injection activity increases during late stages but it is less pronounced compared to HF2 (from right to left, first row). AEs predominately migrate in southeast direction. The upward migration is limited to approximately 2 m. Only events with magnitude estimates are plotted. See caption of Fig. 6 for a detailed description of the plot features.
Figure S5. AE activity during (re-)fracturing stages of HF4: AE activity and injection parameters are aligned manually as correct

timings are missing (first row). AEs predominately migrate upwards, subparallel to the injection borehole. The experiment was discontinued due to a leakage during HF4-RF2. Only events with magnitude estimates are plotted. See caption of Fig. 6 for a detailed description of the plot features.

Figure S6. AE activity during (re-)fracturing stages of HF6: AE activity and injection parameters are aligned manually as correct timings are missing (first row). In contrast to HF1 and HF2 the fracturing stage is the most important stage in regard to AE activity. AEs predominately migrate upwards at the northwest side of the borehole. Only events with magnitude estimates are plotted. See caption of Fig. 6 for a detailed description of the plot features.

Figure S7. AE activity during the (re-)fracturing stages (columns) of the conventional continuous experiment HF2: All located events are plotted. While the main features described for Fig. 6 remain stable, the extent of the cloud of located events below the borehole is much deeper and the horizontal growth is rather symmetric in the first stages (F-RF3). The larger scatter of events reflects the presence of noise signals biasing the full waveform location of small events. See caption of Fig. 6 for a detailed description of the plot features.

5 | Second publication

Insights into hydraulic fracture growth gained from a joint analysis of seismometer-derived tilt and acoustic emissions

P. Niemz, T. Dahm, C. Milkereit, S. Cesca, G. Petersen, A. Zang (2021)

Published in Journal of Geophysical Research: Solid Earth, 126, e2021JB023057
https://doi.org/10.1029/2021JB023057

The supplementary material of this publication is available online at
https://doi.org/10.1029/2021JB023057.

JGR Solid Earth

RESEARCH ARTICLE
10.1029/2021JB023057

Insights Into Hydraulic Fracture Growth Gained From a Joint Analysis of Seismometer-Derived Tilt Signals and Acoustic Emissions

P. Niemz[1,2], T. Dahm[1,2], C. Milkereit[1], S. Cesca[1], G. Petersen[1,2], and A. Zang[1,2]

[1]GFZ German Research Centre for Geosciences, Potsdam, Germany, [2]Institute of Geosciences, University of Potsdam, Potsdam, Germany

Key Points:

- We present and model unique observations of tilt signals induced by hydraulic fractures on broadband seismometers
- The tilt magnitude is correlated with the injected volume and provides independent insight into fracture volume and fracturing efficiency
- A joint analysis of tilt and acoustic emissions helps characterizing the fracture growth and provides evidence for aftergrowth

Supporting Information:

Supporting Information may be found in the online version of this article.

Correspondence to:

P. Niemz,
pniemz@gfz-potsdam.de

Citation:

Niemz, P., Dahm, T., Milkereit, C., Cesca, S., Petersen, G., & Zang, A. (2021). Insights into hydraulic fracture growth gained from a joint analysis of seismometer-derived tilt signals and acoustic emissions. *Journal of Geophysical Research: Solid Earth*, *126*, e2021JB023057. https://doi.org/10.1029/2021JB023057

Received 19 AUG 2021
Accepted 14 DEC 2021

Author Contributions:

Conceptualization: P. Niemz, T. Dahm, C. Milkereit
Data curation: C. Milkereit, A. Zang
Formal analysis: P. Niemz, G. Petersen
Funding acquisition: T. Dahm, S. Cesca, A. Zang
Investigation: P. Niemz, C. Milkereit, A. Zang
Methodology: P. Niemz, T. Dahm
Project Administration: T. Dahm, A. Zang
Resources: C. Milkereit, A. Zang
Supervision: T. Dahm, S. Cesca, A. Zang

Abstract Hydraulic fracturing is performed to enhance rock permeability, for example, in the frame of geothermal energy production or shale gas exploitation, and can potentially trigger induced seismicity. The tracking of increased permeabilities and the fracturing extent is often based on the microseismic event distribution within the stimulated rock volume, but it is debated whether the microseismic activity adequately depicts the fracture formation. We are able to record tilt signals that appear as long-period transients (<180 s) on two broadband seismometers installed close (17–72 m) to newly formed, meter-scale hydraulic fractures. With this observation, we can overcome the limitations of the microseismic monitoring alone and verify the fracture mapping. Our analysis for the first time combines a catalog of previously analyzed acoustic emissions ([AEs] durations of 20 ms), indirectly mapping the fractures, with unique tilt signals, that provide independent, direct insights into the deformation of the rock. The analysis allows to identify different phases of the fracturing process including the (re)opening, growth, and aftergrowth of fractures. Further, it helps to differentiate between the formation of complex fracture networks and single macrofractures, and it validates the AE fracture mapping. Our findings contribute to a better understanding of the fracturing processes, which may help to reduce fluid-injection-induced seismicity and validate efficient fracture formation.

Plain Language Summary Hydraulic fracturing (HF) describes the opening of fractures in rocks by injecting fluids under high pressure. The new fractures not only can facilitate the extraction of shale gas but can also be used to heat up water in the subsurface in enhanced geothermal systems, a corner stone of renewable energy production. The fracture formation is inherently accompanied by small, nonfelt earthquakes (microseismic events). Occasionally, larger events felt by the population can be induced by the subsurface operations. Avoiding such events is important for the acceptance of HF operations and requires a detailed knowledge about the fracture formation. We jointly analyze two very different data sets recorded during mine-scale HF experiments: (a) the tilting of the ground caused by the opening of the fractures, as recorded by broadband seismometers—usually deployed for earthquake monitoring—installed close to the experiments and (b) a catalog of acoustic emissions, seismic signals of few milliseconds emitted by tiny cracks around the forming hydraulic fracture. The novel joint analysis allows to characterize the fracturing processes in greater detail, contributing to the understanding of the physical processes, which may help to understand fluid-injection-induced seismicity and validate the formation of hydraulic fractures.

1. Introduction

Monitoring the movement of fluids in rocks remains one of the major challenges in geosciences. Fluids can migrate in diffusion processes, or focused in channels as in hydraulic fracturing, or in a mixture of both processes. A broad variety of research topics relies on the detailed knowledge about the increase of permeabilities and the fracture evolution. This includes the triggering of natural or induced earthquakes, the study of magmatic systems beneath volcanoes, and the exploitation of the subsurface for example, for oil/gas extraction or geothermal energy production in enhanced geothermal systems.

In this study, we focus on the analysis of hydraulic fracturing, which can be used to develop enhanced geothermal systems by increasing the contact surface between the injected cold fluid and the hot rock via the creation of new fluid pathways. Hydraulic fractures, generated by the injection of fluids into the rock, are often characterized by studying high-frequency microearthquakes, which accumulate at the fracture tip and around the opening fractures (see e.g., Rutledge et al., 2013). In the case of hydraulic fractures of a few meters in length and some tens

Journal of Geophysical Research: Solid Earth 10.1029/2021JB023057

Validation: P. Niemz
Visualization: P. Niemz, G. Petersen
Writing – original draft: P. Niemz
Writing – review & editing: P. Niemz, T. Dahm, C. Milkereit, S. Cesca, G. Petersen, A. Zang

of liters of injected volume, acoustic emissions (AEs) with radiated energy in the kHz range are successfully monitored by piezoelectric sensors near the injection well (Amann et al., 2018; Zang et al., 2017). Although this approach provides indications of induced stress changes, the general layout of either simple planar fracture zones or complex networks of fractures (see e.g., McClure & Horne, 2014) and the geometry (orientation and extent) of the hydraulic fractures are only inferred indirectly. AEs are the result of the tensile opening (and closing) of the macrofractures. The response is considered indirect because failure is expected to occur at discontinuities in the process zone surrounding the fracture, due to stress changes produced by the macrofracture (Dahm, 2001; Dahm et al., 1999; 2010).

The microseismic approach is limited to cases with abundant seismic signals. In some cases, hydraulic fracturing is only accompanied by a low seismicity rate or no seismicity at all. Processes may be aseismic (e.g., Cornet et al., 1997; Guglielmi et al., 2015) or the seismic signals could be below the detection threshold due to a limited monitoring setup as well as local rock properties (e.g., high damping) and stress conditions. However, a lack of microseismic activity can also be caused by an inefficient fracture formation. This ambiguity cannot be resolved by microseismic analyses alone but requires additional information.

Long-period deformation signals are expected in the near-field of a growing hydraulic fracture and can provide independent, direct information about the geometry and the dynamic parameters of new fractures. However, they are rarely monitored in injection experiments. Such signals are considered to provide direct information on fracture growth, because they measure the deformation of the entire rock volume produced by the opening and growing macrofracture itself. In this sense, the monitoring of broader frequency ranges and the installation of different types of sensors (see e.g., Eaton et al., 2013) can provide independent observations regarding the fracture evolution that are crucial to study for example, stress memory effects within the rock (Kaiser, 1950). The Kaiser effect, reported for many geothermal production/test sites (Zang et al., 2014), implies that seismic activity is only induced in subsequent stimulations once the stress level of the previous stage is reached.

During a series of meter-scale hydraulic fracturing experiments (fracture areas of 10–50 m^2) in the Äspö Hard Rock Laboratory (HRL) in Sweden, Zang et al. (2017) set up a complementary monitoring system covering frequency ranges from mHz (long-period transients) to kHz (AEs) in distances of 5 m to several hundred meters. In this study, we analyze long-period pulses (Figure 1) recorded on the horizontal components of two broadband seismometers (Trillium Compact 120) installed in the tunnels adjacent to the injection borehole of the Äspö experiments. The analysis is complemented by a joint interpretation with the AE activity of the same experiment (Niemz et al., 2020).

Broadband seismometers are known to be sensitive to ground tilting, that causes long-period pulses on the horizontal components, while the vertical component is undisturbed (Rodgers, 1968; Wielandt, 2002; Wielandt & Forbriger, 1999). Such pulses are regularly observed in broadband seismic records (Wilson et al., 2017) but often treated as noise. In fact, electronic noise can produce very similar signals (Kinoshita, 2008). Usually, tilt-induced signals are attributed to very local effects during the passage of seismic waves (e.g., grains of sand breaking or moving below a seismometer foot or fatigue cracks inside the concrete instrument pier) and need to be corrected before earthquake source studies (Zahradník & Plešinger, 2005, 2010). In volcanic settings, however, near-field rotational motion has been associated with large-scale fluid processes like dyke intrusions (e.g., Battaglia et al., 2000; Gambino et al., 2007) or the inflation of magma chambers (e.g., Aoyama & Oshima, 2008; Genco & Ripepe, 2010; Wielandt & Forbriger, 1999; Wiens et al., 2005). Hydraulic fractures induced by fluid injections from boreholes generate similar, although much smaller, tilt signals. A few previous studies, with injected volumes of 10–85,000 m^3, showed that these small signals can be measured using surface or borehole tiltmeters (e.g., Holzhausen et al., 1985; Jahr et al., 2008; Lecampion et al., 2005).

Due to the small scale of the experiments with injected volumes below 0.04 m^3 and the complementary monitoring setup of the in situ mine experiments at Äspö HRL, we have the unique opportunity to study independent tilt signals recorded on broadband seismometers in addition to the distribution of high-frequency AEs (presented in Niemz et al., 2020). This analysis allows to obtain more detailed insights into the growth and the orientation of fractures, the fracturing process in general, and the causal connections of tilt signals and AE activity during the opening and the growth of hydraulic fractures.

Journal of Geophysical Research: Solid Earth 10.1029/2021JB023057

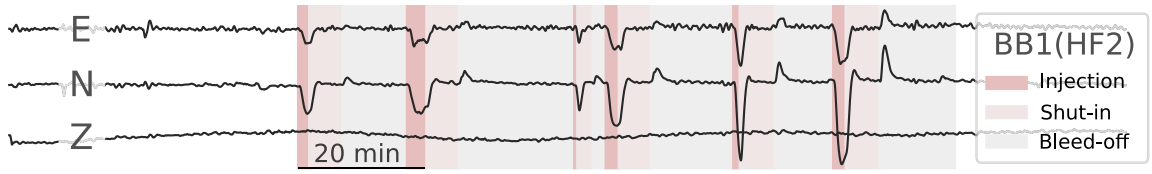

Figure 1. The lowpass-filtered (0.05 Hz) raw waveforms recorded by the broadband seismometer BB1 during the injection experiment HF2 show multiple long-period pulses on the horizontal components (common scaling for all traces). For an explanation of the color-coded injection phases, see Section 2.1.

2. Data and Methods

2.1. Experimental Setup

During the in situ mine experiments at the Äspö HRL, six multistage hydraulic stimulations (HF1–HF6) were conducted at a depth of 410 m in crystalline rock. The central, 28 m long injection borehole was drilled subparallel to the orientation of the minimum horizontal compressive stress (Zang et al., 2017). The injection experiments were monitored by an extensive network of complementary sensors (for details see Zang et al., 2017) covering frequency ranges between mHz and kHz (broadband seismometers from mHz to Hz, accelerometers from 50 Hz to 25 kHz, piezoelectric AE sensors from 1 to 100 kHz, see Figure 2). The distance of the two seismometers to the injection intervals in the fracturing borehole is between 17 and 29 m for sensor BB1 and 52–72 m for sensor BB2. We corrected the arbitrary horizontal orientation of the two broadband seismometers to agree with the local Äspö coordinate system using a Rayleigh wave polarization analysis (AutoStatsQ, Petersen et al., 2019). The single-component, side-view AE sensors were installed in three monitoring boreholes around the injection borehole and near the roof of the adjacent tunnels. These sensors are suitable to monitor seismic signals emitted by fractures in the scale of centimeters to decimeters, which accompany small-volume fluid injections. The accelerometers (Wilcoxon 736T) did record neither AEs nor long-period pulses or other related signals, despite the facts that the dominant frequency content of the AEs (3–20 kHz) is covered by the accelerometers and that both sensor types were collocated.

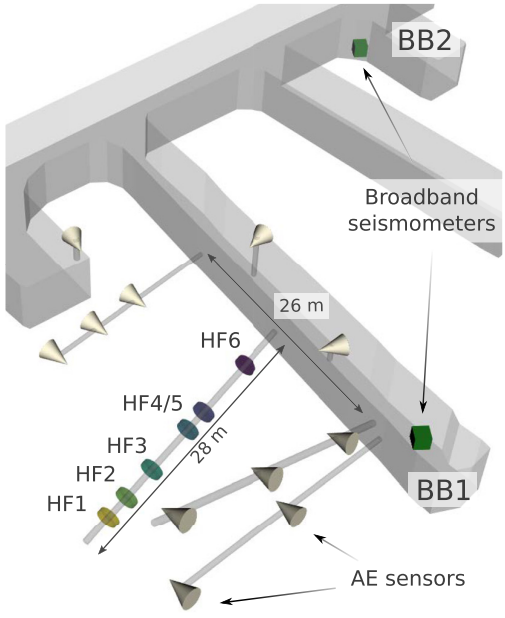

Figure 2. Experimental setup: the injection borehole with the color-coded injection intervals of six hydraulic fracturing (HF) experiments is surrounded by uniaxial acoustic emission (AE) borehole sensors for high-frequency monitoring (beige cones pointing into the direction of the sensor orientation). Two seismometers (green cubes, BB1/BB2) for long-period observations were installed on the floor of adjacent horizontally excavated tunnels (gray).

The hydraulic fracturing experiments were conducted in granitic basement rocks and with multiple injection schemes, mainly differing in the pressurization strategy. A conventional, continuous injection strategy was applied in the experiments HF1, HF2, HF4, and HF6 (see injection parameters in Figure 3). During HF3 a cyclic, progressive pressurization was used in the initial fracturing stages (Figure S5). A detailed description of the injection strategies can be found in Zang et al. (2017). During each experiment 25–30 L of water were injected into the sealed packer intervals in multiple stages in order to break the intact rock and grow hydraulic fractures. The experiments comprise an initial fracturing stage and up to five refracturing stages. Each stage consists of three phases: (a) in the injection phase, water is injected with a constant flow rate. (b) In the shut-in phase, the injection is stopped (flow rate is zero), but the borehole interval is still closed, so the pressure is maintained or slowly decreasing. (c) In the bleed-off phase, the interval is opened and previously injected water is allowed to flow back, while the remaining pressure is quickly decreasing (see flow and pressure in Figure 3).

2.2. Seismometer Response to Tilt

Long-period pulses are present in the horizontal traces of all injection experiments, except HF5, but most clearly seen for the experiments HF1–HF3 and for HF6. The lack of such signals on the vertical component is a strong argument for the observation of a tilt signal, as is the correlation with the injection phases (Figure 1).

Tilt is affecting a seismometer by a small horizontal axis rotation of its reference frame deflecting the horizontal components away from the gravitational

Journal of Geophysical Research: Solid Earth 10.1029/2021JB023057

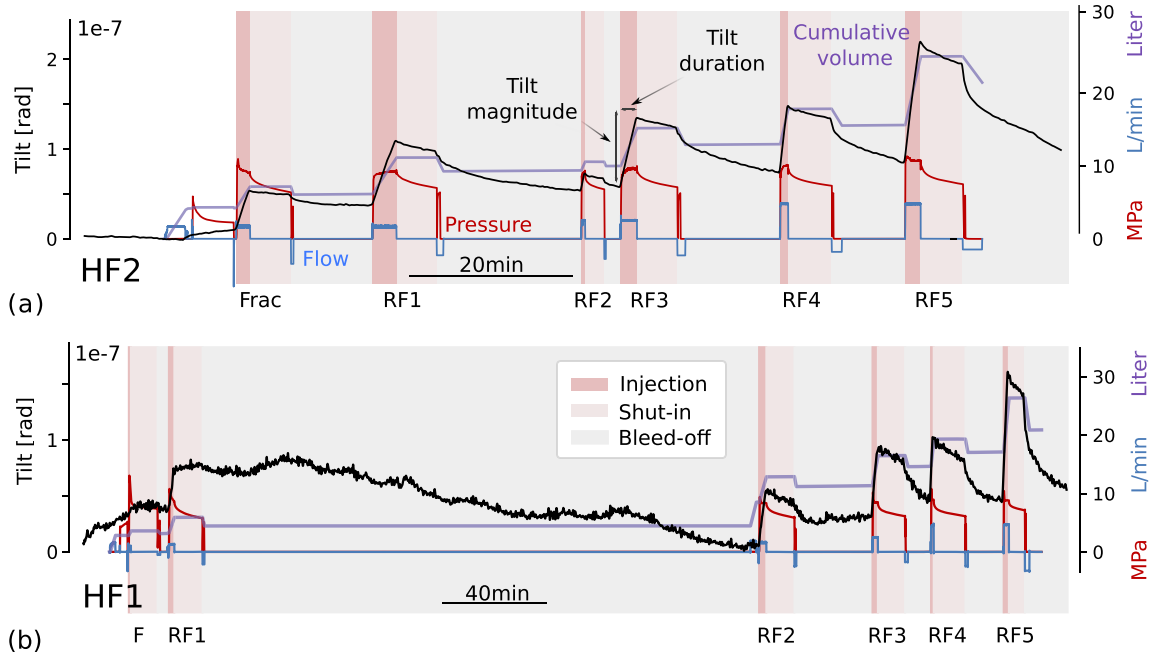

Figure 3. (a) Tilt time series from BB1 during experiment HF2 (black line), along with the cumulative injected volume (purple line), the flow rate (blue line), and the injection pressure (red line). Background colors indicate the timing of the three phases of the (re)fracturing stages. (b) Tilt time series from BB1 for experiment HF1. The long break is caused by experimental delays, but it shows how the seismometer slowly tilts back. The backflow was only tracked during the beginning of the bleed-off. Noise is stronger during HF1 compared to HF2 due to the smaller amplitudes of the transients.

potential plane (inset of Figure S1, Wielandt, 2012). This leads to a horizontal component of the gravitational acceleration, proportional to the sine of the tilt angle, which is measured in addition to a horizontal inertia motion (Rodgers, 1968; Wielandt, 2002). Consequently, the seismometer output is the superposition of two response functions: one denoted as "tilt-induced," leading to a transient signal in velocity, and another one for the "normal" translational motion (Kinoshita, 2008).

The seismometer response to tilt is the response to a step in acceleration that can be instantaneous (i.e., shorter than the corner period of the seismometer, Zahradník & Plešinger, 2005) or a time-dependent, ramp-like step (Kinoshita, 2008), depending on the tilt being transient or permanent. In the presence of translational motion from seismic waves, the tilt signal generally only becomes dominant below the lower corner frequency f_c of the seismometer (Wielandt & Forbriger, 1999), when the frequency response to the true acceleration decays (Figure S1). The tilt magnitude can either be estimated by forward modeling the response of the seismometer to a given input signal (e.g., Zahradník & Plešinger, 2005, 2010) or be directly read from the tilt signal extracted from the raw waveforms (e.g., Aoyama & Oshima, 2008; Battaglia et al., 2000; Genco & Ripepe, 2010). Both methods are based on the assumptions described above.

We apply the second approach to obtain a tilt time series $\Theta(t)$ following Battaglia et al. (2000):

$$\Theta(t) = -\frac{1}{g}\frac{dp(t)}{dt}, \tag{1}$$

with $p(t)$ being the seismometer output corrected for the velocity response of the instrument and g being the acceleration constant. The correction for the instrument response includes a band-pass filter with corner frequencies depending on the experiment and the instrument location. The lower corner frequency of the passband is set to 0.00005 Hz for BB1 and to 0.00075 Hz for BB2, the upper corner frequency is set to 0.05 Hz for both seismometers.

The small amplitude of the tilt-related signals and the presence of spontaneous high-amplitude pulses disturbing the records of BB2 require an increased lower corner frequency. The pulses may be attributed to non-tilt-related

Journal of Geophysical Research: Solid Earth 10.1029/2021JB023057

phenomena, for example, instrumental artifacts (Zahradník & Plešinger, 2010) or spontaneous tilt signals with uncertain cause (Zahradník & Plešinger, 2005) at any given time. Such signals are present in both seismometer records. Examples of spontaneous tilt signals disturbing the records are shown in Figure S2. We refer to those non-injection-related signals as noise signals. They contain high-frequency signals on all three components, which is not observed for the injection-induced tilt signals. As mentioned above, these noise signals could be attributed to electronic spikes or local events induced by the activity within the tunnel (see Figure S3). Apart from spontaneous events, for example, from thermally induced cracking in the floor (Wilson et al., 2017), hammer hits or dropping gear during the operations might induce small local events (high-frequency content) that trigger movements of grains below the seismometer feet, which in turn induces a tilt signal. Due to the low corner frequency of the used band-pass filters, the noise signals need to be removed by a linear interpolation (see, e.g., Figure S4 after stage HF2-RF1), limiting the contamination of the small-amplitude tilt signals recorded during the injection.

With very small tilt angles (here, in the range of 1e−7 rad) there is no need to distinguish between the tilt angle and its sine. For the Äspö experiments, studied here, there is no superposition of seismic (translational) signals and tilt signals, as reported for earthquakes or in volcanic settings (Kinoshita, 2008; Wielandt & Forbriger, 1999; Zahradník & Plešinger, 2005). The AEs accompanying the fracture growth have dominant frequencies of above 3 kHz, which is well beyond the upper corner frequency of the seismometer (Figure S1).

Generally, the tilt increases during the injection phase, reduces during the shut-in phase, and falls off more steeply during the bleed-off phase of each stage (Figures 3 and S4–S7). In the latter stage, the negative tilt gradient indicates that the instrument is partly tilting back to its previous level, while the open hydraulic fracture is partly closing. In the lowpass-filtered (0.05 Hz) raw seismogram, the end of the shut-in phase and the partial closing of the fracture is manifested as a signal with flipped polarity (Figure 1). The tilt time series shows a good correlation with the cumulative injected volume. The cumulative volume takes into account the backflow measured after the interval is opened (Zimmermann et al., 2019).

We observe a strong stage-wise correlation between the injection duration and the tilt duration, which we define as the time between the start of the injection and the maximum tilt within the stage (Figure 4a, see label in Figure 3a). The general observation of tilt durations being slightly longer than the injection durations is attributed to filter-effects introduced by the lowpass filter in the tilt conversion.

The tilt magnitude, which is defined as the difference between the tilt at the beginning of the injection and the maximum tilt within each stage (see label in Figure 3a), is correlated with the injected volume (Figure 4b). A similar correlation is found with the cumulative injected volume. The increasing tilt magnitude can be explained if the intact rock is fractured in the initial fracturing stage, and subsequently the fracture grows gradually and the opening increases due to the increasing amount of injected fluid. While the opening of a fracture requires high pressure, we observe no clear correlation between the tilt magnitude and injection pressure (see maximum and shut-in pressure in Figure S9). However, we observe an increase in tilt during the pressurization of the packer and the integrity test before HF2-F (Figure 3a) and during the fracturing stage of HF3 (Figure S5) before the rock fails and a fracture opens. This deformation is attributed to purely elastic deformation due to pressure inside the interval, which does not require the opening of a fracture. Apart from mapping fractures using AEs, we can differentiate pure elastic deformation and fracture growth by considering the formation breakdown pressure and the fracture reopening pressure, respectively, that is, a pressure drop when the fracture opens and grows, which is not expected in pure elastic deformation.

The mean tilt rate, computed by dividing the tilt magnitude by the tilt duration, correlates with the mean flow rate (Figure 4c). We assume that higher flow rates accelerate the fracture growth resulting in a faster tilting of the seismometer, thus a steeper tilt signal and an increased tilt rate. The fluid also fills preopened fractures quicker when the flow rate is increased. This implies an increase in channel width or diffusivity, respectively, as predicted by Dahm et al. (2010) and Weise et al. (1998).

There is no clear tilt signal for the initial fracture stages of the experiments HF1 and HF3, as will be discussed in Section 3. Additionally, long-period noise and gaps in the continuous recordings hinder an unambiguous tilt extraction for the initial fracturing stage of HF6.

Journal of Geophysical Research: Solid Earth 10.1029/2021JB023057

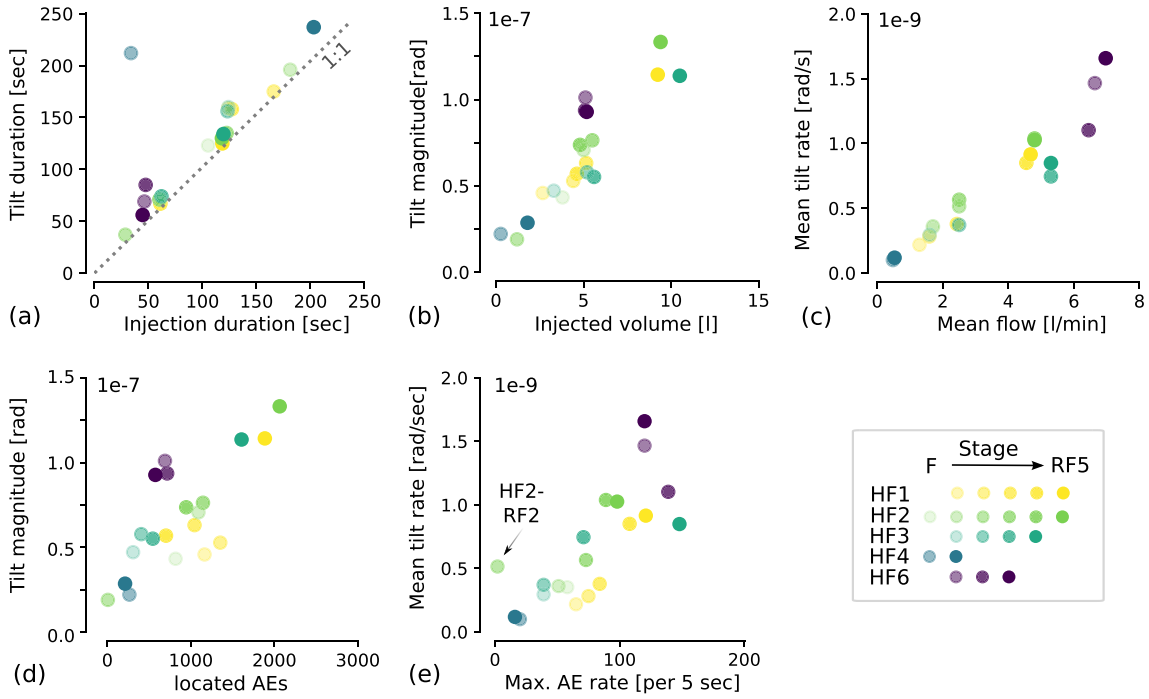

Figure 4. The tilt duration measured from the radial tilt trace (Figure 3) is correlated with the injection duration (a) and the tilt magnitude is correlated with the volume injected in each stage (b). The mean tilt rate is correlated with the mean flow rate (c). The tilt magnitude and the number of located AEs from Niemz et al. (2020) are linearly correlated (d). A clear correlation between mean tilt rate and maximum AE rate is seen except for low-AE activity stages and HF6 (e). The tilt magnitudes shown here are not corrected for the distance of the injection intervals to the seismometer, so deviating values for HF6 are attributed to the location close to the tunnel (see Figure 2). The correlation plot only includes stages for which clear tilt signals were recorded on BB1. Several initial fracturing stages are excluded since the signals do not emerge above the noise level.

2.3. Dislocation Modeling of Tilt

During the six injection experiments at Äspö HRL, approximately 20.000 AEs were detected and localized based on the continuous waveform data (Niemz et al., 2020). Based on the analysis of AEs only, Niemz et al. (2020) showed that planar single fractures of several meters length (Figure 5a) are a good first-order approximation for the tensile fractures induced during most of the HF experiments. Kwiatek et al. (2018) estimated moment magnitudes of −4.2 to −3.5 for the largest 196 events from triggered recordings. This magnitude range comprises picoseismic events with source dimensions in the order of centimeters to decimeters. Kwiatek et al. (2018) also inverted for moment tensors for a subset of the aforementioned AEs and found heterogeneous mechanisms, well described by double couple mechanisms, which indicates that these events have only small tensile components that could be attributed to the opening of the fracture. Additionally, the identified fault plane orientations do not coincide with the orientation of the macrofracture as mapped by the AEs. The different dimensions of the single AEs and the macrofractures, and the deviation in the orientation of fault/fracture planes show that AEs and tilt represent different aspects of the fracturing process. We interpret the AE activity as slip along preexisting joints/weaknesses within the fracture damage zone. These joints may slip when the opening macrofracture introduces local stress changes at its tip. In this model, AEs map the stress changes in the direct vicinity (damage or process zone) of the opening fracture, not the opening itself.

The linear correlation between the tilt magnitude and the number of AEs in the stage-wise catalog of Niemz et al. (2020) (Figure 4d) provides evidence for the causal connection between the two parameters and the injected volume, respectively. We study this causal connection by modeling the induced tilt based on dislocation sources, representing a tensile fault/fracture as mapped by the AE activity. The forward models were calculated using the approach of Okada (1992) as implemented in the *Pyrocko* toolbox (Heimann et al., 2017). The length and the width of each rectangular dislocation source were defined based on the cumulative fracture area and the ratio of the two half-axes of the elliptical fracture zones from Niemz et al. (2020). The opening of the tensile dislocation

Journal of Geophysical Research: Solid Earth 10.1029/2021JB023057

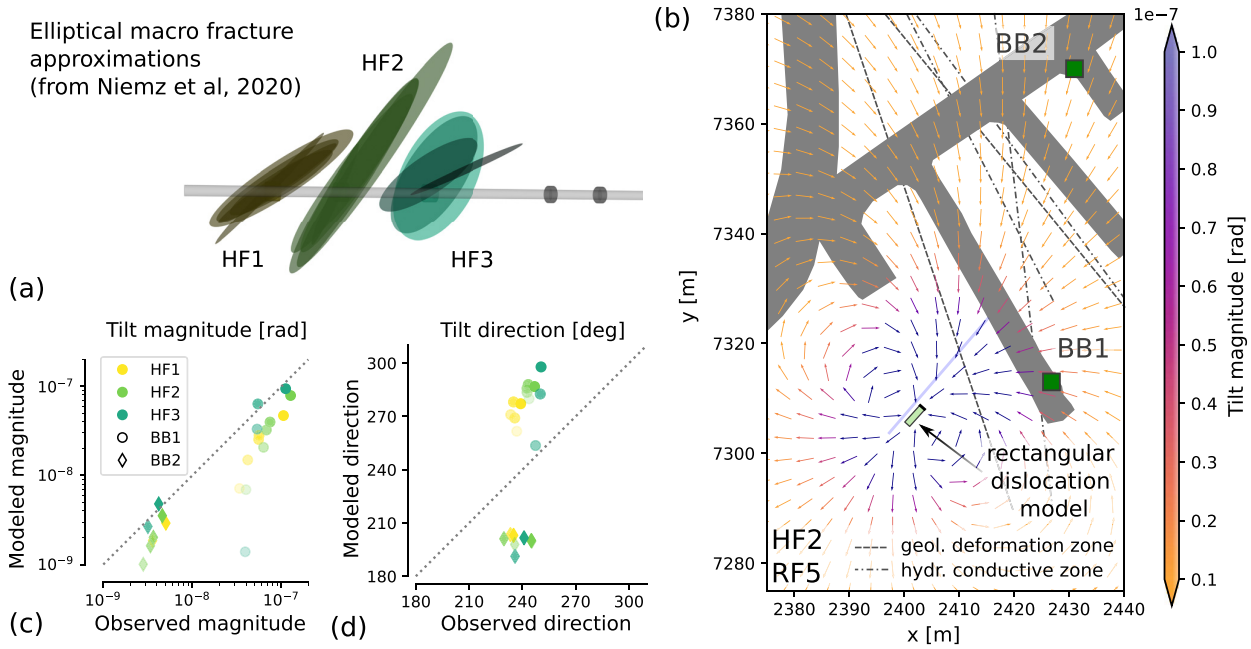

Figure 5. (a) Color-coded, stage-wise fracture plane estimates of the Äspö HF experiments, based on the AE hypocenters (Niemz et al., 2020). The fracture area and the orientation of the planes are used to forward model the tilt signals with rectangular dislocation sources (example for HF2-RF5 in (b)). The full-space models provide a good fit to the observed tilt magnitudes for most refracturing stages (c), but the tilt direction shows deflections of 30°–40° in opposite directions for the two seismometers (d). The color tones in (c) and (d) correspond to the (re)fracturing stages as indicated in the legend of Figure 4. Only stages with a clear tilt signal are plotted. The tunnel system, geological deformation zones, and hydraulically conductive zones are shown in gray but not accounted for in the simplified models (b, geology, and tunnels from SKB, 2013).

models (0.2–1.5 mm) is calculated from the cumulative fracture area and the cumulative injected volume for each stage (Table 1). During experiment HF3, no continuously growing macrofracture was formed, but multiple fractures (Niemz et al., 2020). In this case, we used the stage-wise, noncumulative fracture area.

However, the small number of observations using only two seismometers is not sufficient to resolve all parameters of the extended dislocation source (Lecampion et al., 2005). The small fracture extent of only a few meters poses additional limitations to the analysis. At distances larger than approximately twice the fracture's half-length—even less if the fracture is oriented parallel to the alignment of the instruments—tilt measurements cannot resolve the fracture extent and the opening independently (Lecampion et al., 2005). The seismometers are installed more than 17 m away from the mapped fractures, which have half-lengths of less than 6 m. Under this condition, the tilt signal is only sensitive to changes in fracture volume and fracture orientation. Consequently, we limit our analysis to a comparison of the observed tilt, described by magnitude and direction, with the theoretical tilt from forward models based on the fracture properties (Table 1) estimated from the AE activity (Niemz et al., 2020). We describe the tilt by its magnitude and direction. The direction corresponds to the maximum spatial gradient of the vertical displacement obtained as the azimuth from the north and the east component.

To include both seismometers, the lower corner frequency of the band-pass filter in the tilt extraction was set to 0.00075 Hz. The models show a good fit to the observed tilt magnitudes for most refracturing stages (Figure 5c). For the tilt directions indicated by the two seismometers, we find deflections of 30°–40° in opposite directions (Figure 5d).

3. Discussion

Considering the variety of factors influencing both measurements and modeling, we find a good agreement between the fracture plane approximations based on the AE analysis of Niemz et al. (2020) and the tilt signals reported in this study (discrepancies are discussed in a later paragraph). For experiments HF1 and HF2, the assumption of single planar macrofractures, as inferred by the AE hypocenter analysis, is independently confirmed by

Journal of Geophysical Research: Solid Earth 10.1029/2021JB023057

Table 1
The Input Parameters for the Forward Models of the Rectangular Dislocation Sources

Exp.	Stage	Strike	Dip	Length/width (m)	Cumul. vol. (L)	Opening (mm)	Center (x, y, z)	BB1	BB2
HF1	F	–	–	–/–	0.7	–	–		
HF1	RF1	154	56	7.5/2.8	3.1	0.15	7305.9, 2398.8, 409.3	m	
HF1	RF2	130	56	10.2/2.2	6.0	0.26	7305.0, 2399.9, 408.7	m	
HF1	RF3	130	51	13.0/1.7	9.6	0.43	7305.0, 2400.0, 408.6	m	
HF1	RF4	121	54	11.7/2.2	12.5	0.49	7305.4, 2399.5, 408.7	m	m
HF1	RF5	121	55	12.6/2.6	19.5	0.59	7305.3, 2399.8, 408.5	m	m
HF2	F	131	74	1.8/4.6	3.8	0.46	7306.9, 2401.0, 409.1	m	
HF2	RF1	128	65	1.8/10.0	6.9	0.39	7307.0, 2401.4, 408.3	m	m
HF2	RF2	–	–	–/–	6.2	–	–		
HF2	RF3	124	65	2.5/10.3	11.0	0.43	7306.8, 2401.7, 408.3	m	m
HF2	RF4	121	66	2.0/8.2	13.5	0.84	7306.7, 2401.9, 407.9	m	m
HF2	RF5	121	63	2.4/10.2	20.8	0.85	7306.5, 2402.6, 407.3	m	m
HF3	F	–	–	–/–	0.4	–	–		
HF3	RF1	45	81	1.8/6.5	3.6	0.30	7310.6, 2403.1, 408.3	m	
HF3	RF2	189	75	2.1/6.0	8.5	0.66	7310.4, 2403.1, 408.3	m	
HF3	RF3	141	45	3.2/4.4	13.9	0.99	7310.4, 2402.8, 408.2	m	m
HF3	RF4	120	34	3.7/4.4	23.6	1.44	7310.9, 2404.1, 407.8	m	m

Note. Only stages with clear tilt signals and fracture plane estimates in Niemz et al. (2020) are considered for the tilt modeling at stations BB1 and BB2 (modeling marked by "m" in the last columns). The experiment-wise cumulative volume was corrected for the back flow which was measured manually (Zimmermann et al., 2019).

the modeling of the tilt signals. In the fracture analysis for HF3, Niemz et al. (2020) found that the orientation of fitted planes changes substantially during the refracturing stages, as expected from the more compact, cloud-like AE distribution. Hence, the fracture geometry was assumed to be more complicated than a single macrofracture. The tilt observations provide additional evidence for this finding. The tilt direction rotates during the injections of HF3, even when considering the single stages separately (see Figure S10). This indicates that the fracture geometry is complex. It possibly formed a network of fractures with varying orientations developing farther away from the borehole wall. At the borehole wall, only two fractures were mapped after experiment HF3 in the previously intact interval using an impression packer test, in which a rubber sleeve is pressed against the borehole wall and cracks are imprinted (Zang et al., 2017).

The tilt signals provide an independent confirmation of the fracture orientation and the first-order geometry of the fracture as inferred from the AE activity (Niemz et al., 2020). It also shows that for this particular experimental setup, AEs are able to map the full extent of the opening macrofractures. As an additional test, we modeled the tilt signals using the stage-wise, not the cumulative injected volumes. In this case, the offset between modeled and observed tilt magnitudes (as shown in Figure 5c) becomes even larger. This shows that the fluid remaining inside the fractured rock volume plays an important role in the following stages. Furthermore, the theoretical modeling for the initial fracturing stages of HF1 and HF3 with less than 1 L of injected fluid explains the lack of a tilt signal in these stages. The theoretical tilt signal is too small to emerge out of the noise of the recorded traces.

The difference in the fracturing processes of HF2 and HF3 is documented in Figure 6. For the conventional, continuous experiment HF2, we observe that the increase of the tilt signal is largest at the beginning and then reduces during the injection (Figures 6a and 6c). This is even more evident by directly plotting the tilt rate, here the time derivative of the tilt signal (Figure 6c). The increased tilt rate at the beginning of the refracturing stages (Figure 6c, RF4 and RF5) can be explained by a quicker flow of the fluid into the previously opened fracture. After the reopening, the further growth is represented by a reduced rate of tilting. During the initial fracturing stage HF2-F, when a new hydraulic fracture is opening, the tilt rate is stable during the injection (Figure 6c).

The quick rise of the tilt rate at the beginning of refracturing stages is followed by a delayed increase of the AE rate. The temporal offset between the maximum tilt rate and the maximum AE rate is largest for the refracturing

Journal of Geophysical Research: Solid Earth 10.1029/2021JB023057

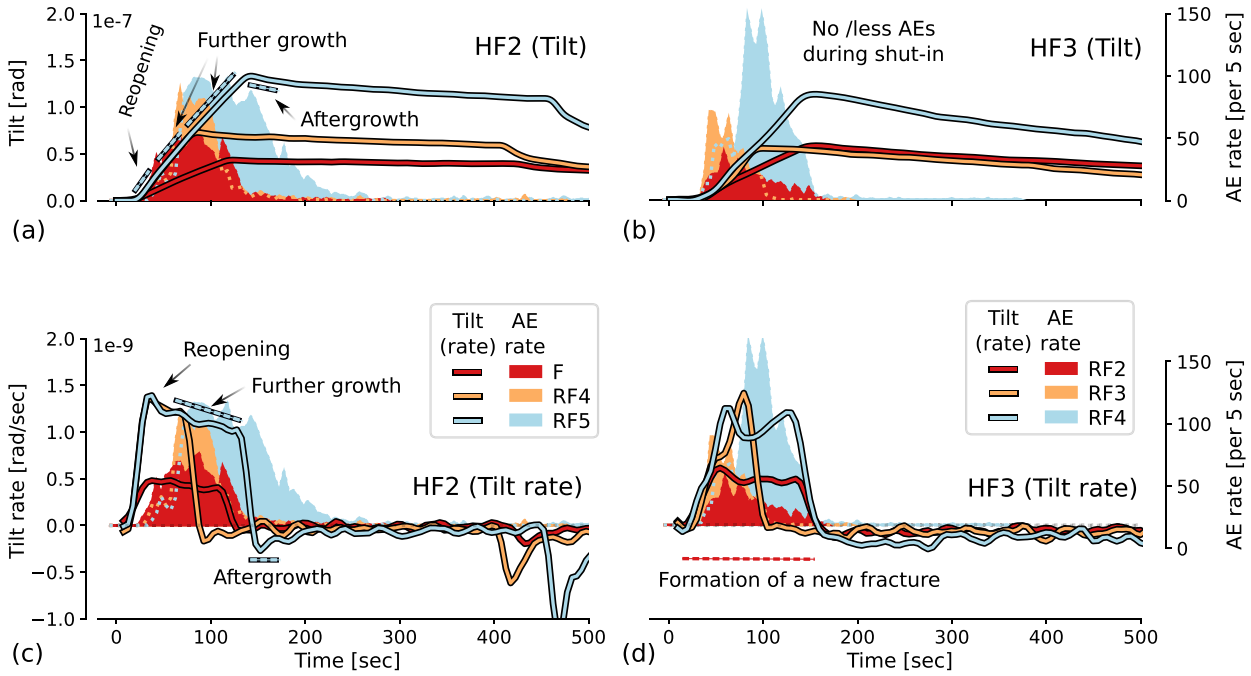

Figure 6. For the experiment HF2, the tilt (a) and more specifically the tilt rate (c) show distinct differences between the initial fracturing stage (F) and later refracturing stages (RF4, RF5). During HF2-F, the tilt rate is stable during the injection, while for RF4 and RF5, it is largest at the beginning of the injection and decreases afterward indicating that the fracture is reopened first and then continues to grow. The further growth is accompanied by an increase in AE activity (filled curves in the background, common scale at the right) as observed after the maximum tilt rate. Aftergrowth, a further growth of the fracture after the stop of the injection is observed for the refracturing stages showing considerable AE activity and a kink in the tilt signal. (b) For experiment HF3, we observe no/less activity after the shut-in, thus no aftergrowth. During the experiment HF3, the AE rates temporally coincide with the tilt rates (d), which points to the formation of new fractures. The initial fracturing stage of HF3 is not shown because we do not observe a tilt signal due to the small amount of injected water (see Table 1).

stages RF4 and RF5 (Figure 6c). This observation can be attributed to the Kaiser effect. In this context, it implies that significant AE activity is only induced after the previously opened hydraulic fracture is reinflated and the fracture continues to grow at the fracture tip.

For experiment HF3, the tilt rate and the AE rate increase simultaneously (Figure 6d), which indicates that the fracture/fractured volume did not experience excessive loading before, thus in each stage a new fracture or a new part of the fracture network is opened or activated. This is contrary to the reopening of the single macrofractures in experiments HF1 and HF2.

By studying the relation between the maximum AE rate and the mean tilt rate (Figure 4e), we identify several stages that deviate from an assumed linear relation: HF2-RF2 and the refracturing stages of HF6. We exclude HF6 at this point, because the tilt magnitudes are not corrected for the varying distances between injection interval and seismometer. The increased tilt magnitudes and mean tilt rates in this experiment (Figures 4b–4d) are attributed to its location close to the tunnel system (see Figure 2). For HF2-RF2, the mean tilt rate is considerably large, but due to technical reasons the continuous AE recording was only active during the last quarter of the interrupted injection, with only three AEs induced in this period. Despite the lack of data for the first part of the injection, we can assume that the maximum AE rate was not reached before. This assumption is based on the observation that in the other refracturing stages of HF2, the AE rate reaches its maximum during the last quarter of the injection. The absence of increased AE activity in the case of HF2-RF2 can be explained as follows: the previously opened fracture was only (partially) reinflated, without substantial AE activity (Kaiser effect), but could not grow farther, due to the small injected volume and the interruption of the injection, respectively.

Several limitations arising from the experimental setup hinder the forward modeling of the tilt signals of HF4–HF6. The timing between the injection time series of HF4–HF6 and the seismograms is not precisely known. Furthermore, the test interval of HF6 is located at a distance of only 4.8 m to the tunnel wall, which may bias the

Journal of Geophysical Research: Solid Earth 10.1029/2021JB023057

tilt signal. The conventional experiment HF4 did only induce few AEs above the detection threshold. Therefore, the planar fracture approximation has a large uncertainty (Niemz et al., 2020). The forward modeling failed to reproduce the observed signal, indicating that the number of AEs is insufficient to reliably map the fracture. The tilt signal of the initial fracturing stage of HF4 strongly deviates from the close correlation between tilt and injection duration (Figures 4a and S6), while the tilt magnitude and the mean tilt rate are in correspondence with the general correlations (Figures 4b and 4c). The tilt signal is much longer than anticipated from the linear relation to the injection duration (Figure 4a), suggesting that the fracture initiation in this experiment is different compared to HF1–HF3 and HF6. While the detected AE activity is too sparse to map stage-wise hydraulic fracture planes (Niemz et al., 2020) or a possibly reactivated fault, the period of increased AE rate coincides well with the tilt duration for HF4-F and HF4-RF1 (Figure S6b). In contrast to the other experiments where the increase in tilt, and therefore the fracture growth, is driven by the increasing amount of water injected into the rock, the tilt signal during HF4-F appears to be decoupled from the supply of fluid. The cause for this peculiar observation remains unclear since we have no detailed knowledge about the fault and fracture geometry farther away from the borehole.

During HF5 (pulse hydraulic fracturing with a secondary pumping system, see Zang et al., 2017), no AEs were detected. This could be attributed to the detection threshold (Niemz et al., 2020), to less favorable transmission properties of the rock type stimulated during HF4 and HF5 compared to the rock type stimulated in HF1 to HF3 (Zang et al., 2017), or to aseismic processes. In contrast to HF4, which is still showing small tilt signals (Figure S6), there was no injection-induced tilt signal recorded on BB1 during experiment HF5 (Figure S8). While aseismic fracture growth could be hypothesized when considering the lack of AEs, the missing of an injection-induced tilt signal shows that no hydraulic macrofracture was generated. This is important for the interpretation of induced seismicity and could only be found from the joint interpretation of the tilt signal and the AE activity. The high-frequency injection pulses of the secondary pump used during HF5 may have hindered the growth of a hydraulic fracture.

The models (see example for HF2-RF5 in Figure 5b) provide a good fit for the refracturing stages (darker tones in Figure 5c), only slightly underestimating the tilt magnitude for both broadband sensors. Increased model deviations are observed for the initial fracturing stages (light tones in Figure 5c), in which smaller injected volumes result in less induced AEs. The plane fitting approach applied by Niemz et al. (2020) may in these cases result in larger uncertainties and overestimated fracture extents. With a fixed injected volume, the estimated opening and, consequently, the tilt magnitude would be underestimated in the models. The modeled tilt direction of each stage shows a constant deflection of approximately 40° compared to the observed tilt direction for BB1 (Figure 5d). The model results for sensor BB2 show a varying deflection of opposite sign. As predicted by the model, the far-field sensor BB2 cannot resolve the rotation of the fracture planes within each experiment (see also Table 1). Scatter in the observed tilt directions is caused by a reduced signal-to-noise ratio (SNR) on instrument BB2, introducing larger uncertainties in tilt direction and magnitude (see an example of a tilt trace from BB2 in Figure S4). In this case, the seismometers even come close to the resolution limit of a fraction of nrad of common tiltmeters (e.g., Gebauer et al., 2009).

Deviations between observed and modeled tilt magnitudes and tilt directions may result from the simplified homogeneous model without taking into account the tunnel geometry, local heterogeneities in the elastic properties of the surrounding rock, and nearby fault zones.

Wielandt and Forbriger (1999) and Rohde et al. (2017) report considerable differences in tilt magnitude and tilt direction (up to 25°) even between collocated instruments in the same vault/location. Wielandt and Forbriger (1999) attributed this deflection to strain–tilt coupling influenced by an interaction of vault walls, filling, and the seismometer. Such cavity effects (Forbriger, 2012; Gebauer et al., 2009; Harrison, 1976a) are expected to be more important close to the tunnel wall, where the two seismometers were located (see Figure S3). Additionally, local inhomogeneities in rock types reflected by different elastic constants (e.g., Young's modulus [E] or Poisson ratio [ν]) can introduce very local strain-induced tilt signals (Gebauer et al., 2009; Harrison, 1976b) that could explain differences in closely located tiltmeter records. Geologically, the Äspö HRL is situated in Äspö diorite cut by granitic and pegmatitic dykes (SKB, 2013). However, the variety in E and ν between samples of the same rock type is larger than the variety between rock types. The different rock types have mean Poisson ratios of 0.23–0.24 and mean E modulus between 73 and 78 GPa (Stille & Olsson, 1996). Consequently, we do not expect a significant influence of the lithology onto the tilt signal, but very local effects cannot be ruled out. Besides the rock type itself, fracture zones and faults can influence the deformation/tilt pattern in magnitude and direction

Journal of Geophysical Research: Solid Earth 10.1029/2021JB023057

(Jentzsch & Koβ, 1997). There are several faults and hydraulically conductive zones between the two seismometers and also partly between the seismometers and the injection intervals (dashed lines in Figure 5b) that could deflect the tilt direction. Quantifying the biases is beyond the scope of this study, if it is feasible at all, due to a lack of information about rock parameters and detailed knowledge about the fault zone geometry. Estimating a first-order influence of the complex tunnel system onto the tilt signals would require a 3D-modeling of stress changes based on discrete elements (DEM) or finite elements (FEM).

The dip angle, and especially the fracture volume, which relates to the fracture opening, has a major influence on the modeled tilt magnitude, while the orientation of the tilt signal is mostly influenced by the strike of the modeled fracture (Lecampion et al., 2005). The steep decay of the tilt signal in the bleed-off phase is directly caused by the outflow of the injected fluid which reduces the fracture volume (see negative flow in Figure 3).

Additionally, we observe a moderate decay of the tilt signal in the shut-in phase (∼10%). This can be explained by the diffusion of fluids under high pressure into the rock, which is also causing a volume loss. However, the diffusivity of granitic rock is rather low and, therefore, we assume that other processes contribute to this decay. We assessed the sensitivity of the fracture parameters which are not resolved due to the limitation arising from the relatively small fracture extents compared to the sensor distances (e.g., area or length/width ratio) by calculating the theoretical tilt for a set of seismometers located at a distance of less than one half-length away from each mapped fracture (here 2 m for all experiments). To test the influence of each parameter, we forward model the induced tilt for a range of values around the parameters given in Table 1. In the azimuthal direction of the seismometer BB1, we find that the decay of the tilt signal after the end of the injection can be explained by aftergrowth, the growth of the fracture (increase of the fracture area) after stopping the injection (see also Dahm et al., 2010). A dominance of either diffusion or aftergrowth cannot be resolved by using the limited tilt data from the seismometers, but the hypothesis of aftergrowth is supported when considering the AE activity. AEs are predominately induced not only during the injection phases but also during the shut-in phases (Niemz et al., 2020). For HF1 and HF2, the tilt rate drops quickly and becomes negative (backward tilting) at the beginning of the shut-in phase, while the AE rate is decaying more slowly (Figure 6c). In this phase, AEs occur predominately at the outermost part of the macrofracture (Niemz et al., 2020), implying a dominance of aftergrowth instead of diffusion processes that would be expected to occur all along the macrofracture. In general, diffusion cannot be ruled out, but the low porosity of the stimulated granitic rocks of 0.2%–0.4% (Johansson et al., 1998) is supposed to inhibit a dominance of this process.

For the progressive injection experiment HF3, the tilt rate and the AE rate decay simultaneously (Figure 6d), which indicates a lack or a reduction of aftergrowth. This is favorable because the reduction of post shut-in growth can lead to a safer stimulation aiming for the mitigation of seismic hazard (Zang et al., 2021), since many important injection-induced events, such as in Basel or Pohang (Grigoli et al., 2018; Häring et al., 2008), occurred after the borehole was shut-in.

The insights obtained from the tilt signals presented in this study stress the advantage of considering low-frequency signals in addition to high-frequency AEs in HF monitoring. The in-depth analysis relying on a unique combination of tilt signals from broadband seismometers and AE activity provides independent constraints on fracture parameters, that can help to understand differences between injection schemes and the energy partition during HF in crystalline rock (Zang et al., 2021). For future in situ experiments, we think this broad monitoring setup should be extended by precise measurements of the backflow and by the installation of tiltmeters. While the resolution of the tilt measurements is expected to be similar (in the range of nrad), this would avoid dealing with the manifold of tilt-like disturbances in broadband recordings (Zahradník & Plešinger, 2010). The combination of tiltmeters and broadband seismometers in a controlled environment may also serve as a calibration experiment which could help the interpretation of tilt observations on broadband sensors during volcanic intrusions. The analysis presented here using broadband seismometer-derived tilt signals can be applied to tiltmeter records directly. When aiming for an inversion for additional fracture parameters (e.g., fracture extent), the installation of borehole tiltmeters or fiber optic strainmeters very close to the fracture or within the well behind the packers could overcome the resolution limitations arising from using only two seismometers and contribute to a better understanding of the fracture growth in future in situ experiments.

Journal of Geophysical Research: Solid Earth 10.1029/2021JB023057

4. Conclusion

During a mine-scale injection experiment in crystalline rock at Äspö HRL at a depth of 410 m, we were able to record tilt-induced transients on broadband seismometers installed close to the injection intervals. Correlations of the tilt magnitude and the tilt duration with the injected volume and the injection duration, respectively, indicate that these tilt signals are directly caused by the (re)opening, the growth, and the closing of meter-scale hydraulic fractures. The complementary monitoring setup of AE sensors and broadband seismometers close to the hydraulic fractures provided the unique opportunity to jointly analyze AEs, which are the high-frequency, indirect response of the rock around the opening fracture, and tilt signals, the low-frequency, direct response to the deformation of the entire rock volume due to the fracture formation. Hence, the two observations depict different aspects of the fracturing process. We link these observations by modeling the theoretical deformation, thus the tilt at the position of the seismometers, caused by an opening fracture based on the fracture extent obtained in a previous study of the AE activity. The theoretical dislocation models with pure tensile opening provide similar tilt magnitudes as the observed ones, but the complex tunnel geometry and other influences deflect the observed tilt direction. The models do not only provide evidence for the interpretation of the tilt signal to be induced by the opening and closing of hydraulic fractures, but also show that the AE activity successfully mapped the fracture extent in most experiments. The models and the observations further depict a clear difference between the opening of single macrofractures in the experiments HF1 and HF2 and a complex fracture network in experiment HF3. The tilt signal shows that in one experiment no efficient macrofracture was created, as indicated, but not proven, by a lack of AE activity. The joint analysis presented in this study has implications going beyond the particular experiments. We show that the combination of AE and tilt signals can potentially differentiate between newly opened and reinflated macrofractures. The latter are influenced by the Kaiser effect, which is revealed by a delay in AE activity compared to the tilt signal which is increasing directly when the injection starts. For the macrofractures, we found evidence for aftergrowth reflected in AE activity while the tilt signal is slowly decaying. The identification and the study of aftergrowth processes is particularly important for the mitigation of induced seismicity, since many case of induced seismic events occurred after the stop of the injection. For future in situ experiments, we propose the installation of additional borehole tiltmeters to take full advantage of the joint interpretation of AE/microseismic activity and independent tilt measurements, eventually aiming for an inversion for fracture properties.

Data Availability Statement

The data set (Niemz et al., 2021) studied here is available at https://doi.org/10.5880/GFZ.2.1.2021.007. Data were processed using the python based seismology environment Pyrocko (Heimann et al., 2017), freely available at pyrocko.org.

Acknowledgments
We would like to thank Jiří Zahradník and an anonymous reviewer for constructive comments and suggestions that further improved the manuscript. P.N. was funded by the BMBF (German Federal Ministry of Education and Research) project SECURE (no. 03G0872A). G.P. received funding from DFG project "From Top to Bottom–Seismicity, Motion Patterns and Stress Distribution in the Alpine Crust" (no. 362440331), a subproject of "SPP 2017: Mountain Building Processes in 4D" (No. 313806092). S.C. has received funding from the European Commission Research Fund for Coal and Steel (RFCS) project PostMinQuake (no. 899192). The Äspö mine experiments were financially supported by the GFZ German Research Center for Geosciences (75%), the KIT Karlsruhe Institute of Technology (15%), and the Nova Center for University Studies, Research and Development (10%) with an additional in-kind contribution of SKB for using Äspö Hard Rock Laboratory as test site for geothermal research. We thank Gerd Klee (MeSy Solexperts) and Hana Semikova (ISATech Ltd) for performing the hydraulic testing. Open access funding enabled and organized by Projekt DEAL.

References

Amann, F., Gischig, V., Evans, K., Doetsch, J., Jalali, R., Valley, B., et al. (2018). The seismo-hydromechanical behavior during deep geothermal reservoir stimulations: Open questions tackled in a decameter-scale in situ stimulation experiment. *Solid Earth*, *9*(1), 115–137. https://doi.org/10.5194/se-9-115-2018

Aoyama, H., & Oshima, H. (2008). Tilt change recorded by broadband seismometer prior to small phreatic explosion of Meakan-dake volcano, Hokkaido, Japan. *Geophysical Research Letters*, *35*, L06307. https://doi.org/10.1029/2007GL032988

Battaglia, J., Aki, K., & Montagner, J.-P. (2000). Tilt signals derived from a GEOSCOPE VBB Station on the Piton de la Fournaise Volcano. *Geophysical Research Letters*, *27*(5), 605–608. https://doi.org/10.1029/1999GL010916

Cornet, F. H., Helm, J., Poitrenaud, H., & Etchecopar, A. (1997). Seismic and aseismic slips induced by large-scale fluid injections. In S. Talebi (Ed.), *Seismicity associated with mines, reservoirs and fluid injections* (pp. 563–583). Birkhäuser. https://doi.org/10.1007/978-3-0348-8814-1_12

Dahm, T. (2001). Rupture dimensions and rupture processes of fluid-induced microcracks in salt rock. *Journal of Volcanology and Geothermal Research*, *109*(1–3), 149–162. https://doi.org/10.1016/S0377-0273(00)00309-7

Dahm, T., Hainzl, S., & Fischer, T. (2010). Bidirectional and unidirectional fracture growth during hydrofracturing: Role of driving stress gradients. *Journal of Geophysical Research*, *115*, B12322. https://doi.org/10.1029/2009JB006817

Dahm, T., Manthei, G., & Eisenblätter, J. (1999). Automated moment tensor inversion to estimate source mechanisms of hydraulically induced micro-seismicity in salt rock. *Tectonophysics*, *306*(1), 1–17. https://doi.org/10.1016/S0040-1951(99)00041-4

Eaton, D., van der Baan, M., Tary, J.-B., Birkelo, B., Spriggs, N., Cutten, S., & Pike, K. (2013). Broadband microseismic observations from a Montney hydraulic fracture treatment, northeastern B.C., Canada. *CSEG Recorder*, *38*, 44–53. https://csegrecorder.com/articles/view/broadband-microseismic-observations-from-a-montney-hydraulic-fracture

Forbriger, T. (2012). Recommendations for seismometer deployment and shielding. In *New manual of seismological observatory practice 2*. (NMSOP-2, pp. 1–10). https://doi.org/10.2312/GFZ.NMSOP-2_IS_5.4

Gambino, S., Campisi, O., Falzone, G., Ferro, A., Guglielmino, F., Laudani, G., & Saraceno, B. (2007). Tilt measurements at Vulcano Island. *Annals of Geophysics*, *50*(2), 233–247. https://doi.org/10.4401/ag-4419

Journal of Geophysical Research: Solid Earth 10.1029/2021JB023057

Gebauer, A., Kroner, C., & Jahr, T. (2009). The influence of topographic and lithologic features on horizontal deformations. *Geophysical Journal International*, *177*(2), 586–602. https://doi.org/10.1111/j.1365-246X.2009.04072.x

Genco, R., & Ripepe, M. (2010). Inflation–deflation cycles revealed by tilt and seismic records at Stromboli volcano. *Geophysical Research Letters*, *37*, L12302. https://doi.org/10.1029/2010GL042925

Grigoli, F., Cesca, S., Rinaldi, A. P., Manconi, A., López-Comino, J. A., Clinton, J. F., et al. (2018). The November 2017 Mw 5.5 Pohang earthquake: A possible case of induced seismicity in South Korea. *Science*, *360*(6392), 1003–1006. https://doi.org/10.1126/science.aat2010

Guglielmi, Y., Cappa, F., Avouac, J.-P., Henry, P., & Elsworth, D. (2015). Seismicity triggered by fluid injection–induced aseismic slip. *Science*, *348*(6240), 1224–1226. https://doi.org/10.1126/science.aab0476

Häring, M. O., Schanz, U., Ladner, F., & Dyer, B. C. (2008). Characterisation of the Basel 1 enhanced geothermal system. *Geothermics*, *37*(5), 469–495. https://doi.org/10.1016/j.geothermics.2008.06.002

Harrison, J. C. (1976a). Cavity and topographic effects in tilt and strain measurement. *Journal of Geophysical Research*, *81*(2), 319–328. https://doi.org/10.1029/JB081i002p00319

Harrison, J. C. (1976b). Tilt observations in the Poorman mine near Boulder, Colorado. *Journal of Geophysical Research*, *81*(2), 329–336. https://doi.org/10.1029/JB081i002p00329

Heimann, S., Kriegerowski, M., Isken, M., Cesca, S., Daout, S., Grigoli, F., & Dahm, T. (2017). *Pyrocko—An open-source seismology toolbox and library*. GFZ Data Services. https://doi.org/10.5880/GFZ.2.1.2017.001

Holzhausen, G. R., Haase, C., Stow, S., & Gazonas, G. (1985). Hydraulic-fracture growth in dipping anisotropic strata as viewed through the surface deformation field. *Paper presented at Proceedings of the 26th U.S. Symposium on Rock Mechanics, Rapid City, SD* (Vol. ARMA-85-0341-1). https://onepetro.org/ARMAUSRMS/proceedings-abstract/ARMA85/All-ARMA85/ARMA-85-0341-1/129567

Jahr, T., Jentzsch, G., Gebauer, A., & Lau, T. (2008). Deformation, seismicity, and fluids: Results of the 2004/2005 water injection experiment at the KTB/Germany. *Journal of Geophysical Research*, *113*, B11410. https://doi.org/10.1029/2008JB005610

Jentzsch, G., & Koß, S. (1997). Interpretation of long-period tilt records at BlåSjø, southern Norway, with respect to variations in the lake level. *Physics and Chemistry of the Earth*, *22*(1–2), 25–31. https://doi.org/10.1016/S0079-1946(97)00073-6

Johansson, H., Siitari-Kauppi, M., Skålberg, M., & Tullborg, E. L. (1998). Diffusion pathways in crystalline rock—Examples from Äspö–diorite and fine-grained granite. *Journal of Contaminant Hydrology*, *35*(1–3), 41–53. https://doi.org/10.1016/S0169-7722(98)00114-4

Kaiser, J. (1950). *An investigation into the occurrence of noises in tensile tests, or a study of acoustic phenomena in tensile tests* (dissertation). Munich, Germany: Technical University of Munich.

Kinoshita, S. (2008). Tilt measurement using broadband velocity seismograms. *Bulletin of the Seismological Society of America*, *98*(4), 1887–1897. https://doi.org/10.1785/0120070230

Kwiatek, G., Martínez-Garzón, P., Plenkers, K., Leonhardt, M., Zang, A., von Specht, S., et al. (2018). Insights into complex Subdecimeter fracturing processes occurring during a water injection experiment at depth in Äspö Hard Rock Laboratory, Sweden. *Journal of Geophysical Research: Solid Earth*, *123*, 6616–6635. https://doi.org/10.1029/2017JB014715

Lecampion, B., Jeffrey, R., & Detournay, E. (2005). Resolving the geometry of hydraulic fractures from tilt measurements. *Pure and Applied Geophysics*, *162*(12), 2433–2452. https://doi.org/10.1007/s00024-005-2786-4

McClure, M. W., & Horne, R. N. (2014). An investigation of stimulation mechanisms in Enhanced Geothermal Systems. *International Journal of Rock Mechanics and Mining Sciences*, *72*, 242–260. https://doi.org/10.1016/j.ijrmms.2014.07.011

Niemz, P., Cesca, S., Heimann, S., Grigoli, F., von Specht, S., Hammer, C., et al. (2020). Full-waveform-based characterization of acoustic emission activity in a mine-scale experiment: A comparison of conventional and advanced hydraulic fracturing schemes. *Geophysical Journal International*, *222*(1), 189–206. https://doi.org/10.1093/gji/ggaa127

Niemz, P., Milkereit, C., & Zang, A. (2021). Long-period transients (tilt signals) on continuous broadband seismograms recorded during meter-scale hydraulic fracturing experiments at Äspö Hard Rock Laboratory. *GFZ Data Services*. https://doi.org/10.5880/GFZ.2.1.2021.007

Okada, Y. (1992). Internal deformation due to shear and tensile faults in a half-space. *Bulletin of the Seismological Society of America*, *82*(2), 1018–1040. https://doi.org/10.1785/bssa0820021018

Petersen, G. M., Cesca, S., Kriegerowski, M., & The AlpArray Working Group. (2019). Automated quality control for large seismic networks: Implementation and application to the AlpArray seismic network. *Seismological Research Letters*, *90*(3), 1177–1190. https://doi.org/10.1785/0220180342

Rodgers, P. W. (1968). The response of the horizontal pendulum seismometer to Rayleigh and Love waves, tilt, and free oscillations of the earth. *Bulletin of the Seismological Society of America*, *58*(5), 1385–1406. https://doi.org/10.1785/bssa0580051385

Rohde, M. D., Ringler, A. T., Hutt, C. R., Wilson, D. C., Holland, A. A., Sandoval, L. D., & Storm, T. (2017). Characterizing local variability in long-period horizontal tilt noise. *Seismological Research Letters*, *88*(3), 822–830. https://doi.org/10.1785/0220160193

Rutledge, J., Downie, R., Maxwell, S., & Drew, J. (2013). Geomechanics of hydraulic fracturing inferred from composite radiation patterns of microseismicity. In *SPE Annual Technical Conference and Exhibition* (Vol. SPE 166370). New Orleans, LA: Society of Petroleum Engineers. https://doi.org/10.2118/166370-MS

SKB. (2013). *Äspö Hard Rock Laboratory—Annual report 2012* (Tech. Rep. No. TR-13-10). Svensk Kärnbränslehantering AB.

Stille, H., & Olsson, P. (1996). *SKB progress report: Summary of rock mechanical results from the construction of Äspö Hard Rock Laboratory* (Tech. Rep. No. HRL-96-07). Svensk Kärnbränslehantering AB.

Weise, A., Jentzsch, G., Kiviniemi, A., & Kääriäinen, J. (1998). Comparison of long-period tilt measurements: Results from the two clinometric stations Metsähovi and Lohja, Finland. *Journal of Geodynamics*, *27*(2), 237–257. https://doi.org/10.1016/S0264-3707(97)00067-7

Wielandt, E. (2002). 18—Seismometry. In W. H. K. Lee, H. Kanamori, P. C. Jennings, & C. Kisslinger (Eds.), *International geophysics* (Vol. 81, pp. 283–304). Academic Press. https://doi.org/10.1016/s0074-6142(02)80221-2

Wielandt, E. (2012). Seismic sensors and their calibration. In *New manual of seismological observatory practice 2* (NMSOP-2, pp. 1–46). Deutsches GeoForschungsZentrum GFZ. https://doi.org/10.2312/GFZ.NMSOP-2_ch5

Wielandt, E., & Forbriger, T. (1999). Near-field seismic displacement and tilt associated with the explosive activity of Stromboli. *Annals of Geophysics*, *42*(3). https://doi.org/10.4401/ag-3723

Wiens, D. A., Pozgay, S. H., Shore, P. J., Sauter, A. W., & White, R. A. (2005). Tilt recorded by a portable broadband seismograph: The 2003 eruption of Anatahan Volcano, Mariana Islands. *Geophysical Research Letters*, *32*, L18305. https://doi.org/10.1029/2005GL023369

Wilson, D., Ringler, A. T., & Hutt, C. R. (2017). Detection and characterization of pulses in broadband seismometers. *Bulletin of the Seismological Society of America*, *107*(4), 1773–1780. https://doi.org/10.1785/0120170089

Zahradník, J., & Plešinger, A. (2005). Long-period pulses in broadband records of near earthquakes. *Bulletin of the Seismological Society of America*, *95*(5), 1928–1939. https://doi.org/10.1785/0120040210

Zahradník, J., & Plešinger, A. (2010). Toward understanding subtle instrumentation effects associated with weak seismic events in the near field. *Bulletin of the Seismological Society of America*, *100*(1), 59–73. https://doi.org/10.1785/0120090087

Journal of Geophysical Research: Solid Earth 10.1029/2021JB023057

Zang, A., Oye, V., Jousset, P., Deichmann, N., Gritto, R., McGarr, A., et al. (2014). Analysis of induced seismicity in geothermal reservoirs – an overview. *Geothermics*, *52*, 6–21. https://doi.org/10.1016/j.geothermics.2014.06.005

Zang, A., Stephansson, O., Stenberg, L., Plenkers, K., Specht, S., Milkereit, C., et al. (2017). Hydraulic fracture monitoring in hard rock at 410 m depth with an advanced fluid-injection protocol and extensive sensor array. *Geophysical Journal International*, *208*(2), 790–813. https://doi.org/10.1093/gji/ggw430

Zang, A., Zimmermann, G., Hofmann, H., Niemz, P., Kim, K. Y., Diaz, M., et al. (2021). Relaxation damage control via fatigue-hydraulic fracturing in granitic rock as inferred from laboratory-, mine-, and field-scale experiments. *Scientific Reports*, *11*(1), 6780. https://doi.org/10.1038/s41598-021-86094-5

Zimmermann, G., Zang, A., Stephansson, O., Klee, G., & Semiková, H. (2019). Permeability enhancement and fracture development of hydraulic in situ experiments in the Äspö Hard Rock Laboratory, Sweden. *Rock Mechanics and Rock Engineering*, *52*, 495–515. https://doi.org/10.1007/s00603-018-1499-9

6 | Third publication

Relaxation damage control via fatigue-hydraulic fracturing in granitic rock as inferred from laboratory-, mine-, and field-scale experiments

A. Zang, G. Zimmermann, H. Hofmann, **P. Niemz**, K. W. Kim, M. Diaz, L. Zhuang, J. S. Yoon (2021)

Published in Scientific Reports, 11(6780):81–96.

https://doi.org/10.1038/s41598-021-86094-5

Due to the format of the manuscript with methodological details contained in the supplement, I also include the supplemental material here.

www.nature.com/scientificreports

scientific reports

Check for updates

OPEN

Relaxation damage control via fatigue-hydraulic fracturing in granitic rock as inferred from laboratory-, mine-, and field-scale experiments

Arno Zang[1,2]✉, Günter Zimmermann[1], Hannes Hofmann[1], Peter Niemz[1,2], Kwang Yeom Kim[3], Melvin Diaz[3], Li Zhuang[4] & Jeoung Seok Yoon[5]

The ability to control induced seismicity in energy technologies such as geothermal heat and shale gas is an important factor in improving the safety and reducing the seismic hazard of reservoirs. As fracture propagation can be unavoidable during energy extraction, we propose a new approach that optimises the radiated seismicity and hydraulic energy during fluid injection by using cyclic- and pulse-pumping schemes. We use data from laboratory-, mine-, and field-scale injection experiments performed in granitic rock and observe that both the seismic energy and the permeability-enhancement process strongly depend on the injection style and rock type. Replacing constant-flow-rate schemes with cyclic pulse injections with variable flow rates (1) lowers the breakdown pressure, (2) modifies the magnitude-frequency distribution of seismic events, and (3) has a fundamental impact on the resulting fracture pattern. The concept of fatigue hydraulic fracturing serves as a possible explanation for such rock behaviour by making use of depressurisation phases to relax crack-tip stresses. During hydraulic fatigue, a significant portion of the hydraulic energy is converted into rock damage and fracturing. This finding may have significant implications for managing the economic and physical risks posed to communities affected by fluid-injection-induced seismicity.

Successfully utilising unconventional energy resources relies critically on understanding and controlling the mechanical deformations of fractured rock mass in the Earth's upper crust. Examples of such utilisation include creating and sustaining fracture networks in enhanced geothermal systems (EGS) as well as in unconventional oil- and gas reservoirs. Each of these subsurface technologies is governed by the intrinsic properties of fractured rock and its response to primary, natural stresses (lithostatic, tectonic) as well as to secondary, applied stresses (hydraulic stimulation) at a variety of scales. Understanding the mechanisms that control the fracture nucleus and growth is particularly relevant in such complex stress conditions[1]. The principles of fracture growth in the presence of large-scale anisotropic discontinuous rock mass must be studied by observing deformation and fluid flow in mine-scale underground tests[2–6], which requires instrumenting, monitoring, and interpreting rock-mass behaviour in situ. The fracture architecture, instrument choice, and sensor resolution all affect the overall result of the seismic and aseismic signals that are captured[7,8]. Zang et al.[9] proposed an iterative process of optimising the necessary observations by combining both underground- and laboratory tests. This process allows a variety of fluid-injection schemes to be applied in the laboratory before testing the most promising schemes in several in-situ experiments in the same rock type.

Human activity perturbs subsurface stresses, thereby causing fractures to become unstable, to propagate, and to coalesce, as documented in induced seismicity[10,11]. This induced seismicity results from various individual causes[12,13], such as wastewater disposal[14,15], hydraulic fracturing[16,17], carbon capture and storage[18,19], and geothermal operations[20,21]. Although the radiated seismic energy represents only a small fraction of the pumped-in

[1]Helmholtz Centre Potsdam GFZ German Research Centre for Geosciences, Telegrafenberg, 14473 Potsdam, Germany. [2]Institute of Geosciences, University of Potsdam, 14469 Potsdam, Germany. [3]Korea Maritime and Ocean University, Busan, Republic of Korea. [4]Korea Institute of Civil Engineering and Building Technology, Goyang, Republic of Korea. [5]DynaFrax UG (Limited), Helmholtzstr. 6, 14467 Potsdam, Germany. ✉email: zang@gfz-potsdam.de

hydraulic energy, perceptions of induced seismic events caused by human operations in the Earth's subsurface have led to the termination of energy projects[22–25]. The primary goal of energy projects is therefore to manage subsurface operations without the occurrence of seismic events of economic concern[26]. While many scientific articles have reported on induced seismicity[11,12,14,23,27], few have dealt with suggestions of how to mitigate and reduce fluid-induced seismicity[9]. One option is to use seismic traffic-light systems, which are widely accepted as a risk-mitigation procedure in hydraulic treatment[28,29]. Many concepts have been proposed[30], but few such systems have actually been applied in the field[31–34]. In these traffic-light systems, fluid injection is stopped, either the treatment pressure is reduced, or the well is shut in or flowed back if certain thresholds of seismic magnitudes are exceeded during injection[35]. Magnitude thresholds are also used when refined advanced and adaptive traffic-light systems are applied[36]. Another option for controlling injection-induced seismicity is to modify the seismic-event distribution via the injection style[17,37]. Using hydro-mechanical-coupled numerical simulations of a naturally fractured geothermal reservoir with Soultz-sous-Forets properties, Yoon et al.[38] demonstrated that compared with a monotonic injection, a cyclic injection of fluid has the capacity to lower the number of larger-magnitude seismic events while increasing the overall number of smaller events.

This work aims to assess the process of hydraulic-fracture growth during injection experiments in light of both associated induced seismicity and hydro-mechanical parameters, such as formation-breakdown pressure (FBP) and fracture-permeability evolution. For this purpose, we present rich experimental datasets consisting of (1) results from a decametre-scale in-situ test at Äspö Hard Rock Laboratory (HRL) in Sweden performed in June 2015 at a depth of 410 m and (2) results from laboratory hydraulic-fracture tests under triaxial and true-triaxial stress conditions performed at the Korea Institute of Civil Engineering and Building Technology (KICT) from 2016 to 2020. Both datasets are compared with a field-stimulation treatment at an EGS site performed in 2017[39]. While the injection rate[40], the cumulative injection volume[41,42], and the injection pressure[43] have been demonstrated to impact the likelihood of associated induced seismic events, a systematic cross-scale study that investigates the interrelation of fracture growth, seismicity, and permeability enhancement has not yet been performed. In this study, we investigate innovative injection schemes that use cyclic- and pulse-pumping protocols—so-called hydraulic-fatigue tests—to optimise the fracture-growth process. Optimisation includes the analysis of fracturing and re-fracturing stages, acoustic-emission hypocentres and their magnitude-frequency distributions, and fracture-pattern- and related permeability improvement. We find that breakdown pressure decreases with an increasing number of injection cycles, particularly in laboratory testing with hundreds of cycles as well as in the mine. In all scales, seismic *b*-values determined from magnitude-frequency distributions indicate a trend towards larger values in hydraulic fatigue compared with results from conventional tests using monotonic-fluid-pressure injection. This finding reveals that a safer treatment that can mitigate larger seismic events indeed exists. Resulting fracture patterns are quantified with X-ray CT and microscopic inspection in the laboratory and are investigated via impression-packer analysis and seismic-event-hypocentre tracking in the mine. Compared with monotonic-injection tests, laboratory-fatigue tests reveal a more-complex fracture pattern resulting from branching, which is mainly caused by stress release at the fracture tips (cyclic injection) and by rock chips being removed from fracture walls (pulse injection). Decreasing breakdown pressure and seismicity by creating a broader damage zone is in line with our concept of hydraulic fatigue, which is expanded upon in the supplementary material. This concept is also supported by the energy budget analysed in conventional and fatigue tests across scales. In addition to engineering elements that control fluid-injection-fracture growth in rock (breakdown pressure, induced seismicity, permeability), we also investigate the energy budget of the fracture-growth process. In this work, we compute individual energy terms, such as seismically radiated-, hydraulic-, and fracture energy, and estimate the deformation energy from stimulated volumes of rock. Although the absolute energy values differ by orders of magnitude from scale to scale, a scale-independent tendency for a lower ratio of radiated seismic energy to exist with respect to hydraulic energy is documented in the fatigue test as compared with in monotonic injection.

Hydraulic-fatigue experiments

A naturally fractured granitic rock cube with a side length of 30 m was monitored at the mine scale during hydraulic-fracturing tests at a depth of 410 m in a Swedish hard-rock[2]. Six hydraulic fractures were propagated from a 28-m-long horizontal borehole that served as an injection borehole in the cube centre. Three injection styles including conventional and fatigue hydraulic fracturing (e.g. cyclic and pulse progressive fracturing) were tested in situ (Fig. 1). Stress conditions at depth indicated maximum horizontal stress as maximum principal stress. The minimum and intermediate principal stresses were oriented sub-horizontally and sub-vertically. The magnitude of maximum principal stress (22 MPa) was about double the value of the minimum and intermediate principal stresses (11–12 MPa)[44]. An injection borehole with a diameter of 102 mm was drilled from the TASN tunnel in the direction of minimum horizontal stress (Fig. 1a). Figure 1b displays the hydraulic-fatigue packer system with a short mandrel for pulsing being inserted into the injection borehole[45]. All injection tests were monitored by an extensive acoustic-emission- (AE), seismic- (geophone, broadband sensor), and electromagnetic-sensor (EME, MT) network. In Fig. 1c, the geometry of the high-frequency monitoring array is shown with eleven AE sensors (70 kHz) located in the monitoring boreholes and the nearby tunnel roofs (Fig. 1c, *cones*). In the testing borehole, pressures were monitored in injection intervals that were free of pre-existing fractures (Fig. 1c, HF1–HF6). Fracture inspection was carried out by combining core logs, the impression packer, and the borehole results. A televiewer tool was used to map the injection borehole before and after hydraulic testing. Upon completing the fracturing and re-fracturing stages, the borehole wall was mapped with an impression packer. The shape of the fractures and their extensions were reconstructed via the impression-packer results and the AE-hypocentre-tracking results[46]. The fracture aperture was computed via the extension of the AE cloud and the measured hydraulic back-flow values. The evolution of permeability was calculated from decline-pressure

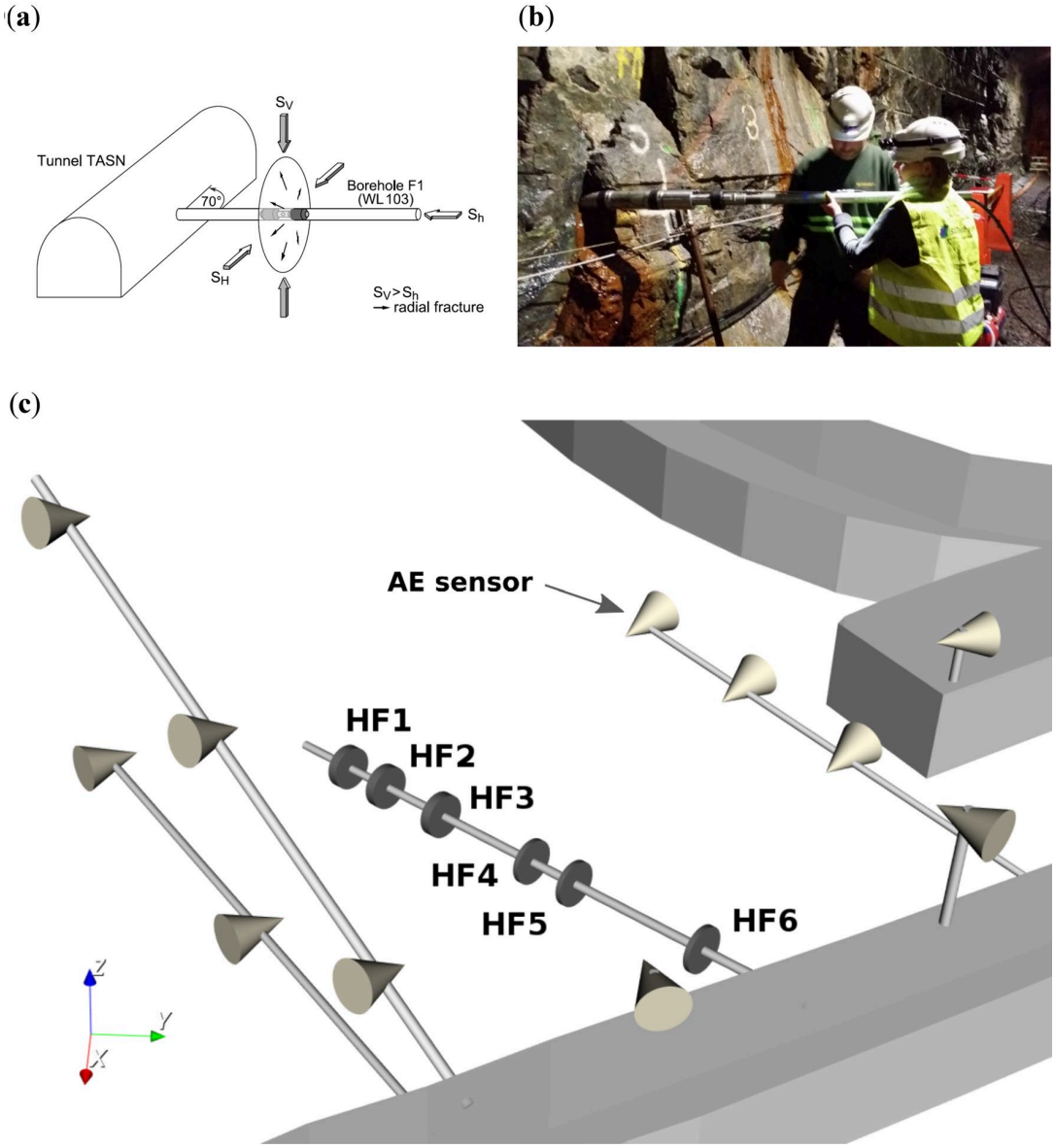

Figure 1. Hydraulic-fracture design at depth of 410 m at Äspö HRL, Sweden. (**a**) A hydraulic-testing borehole (diameter: 102 mm; length: 28 m) is diamond-drilled subparallel to the minimum horizontal stress. The hydraulic fracture (*disk*) opens perpendicular to the minimum principal stress and rapidly grows in the plane of intermediate (vertical) and maximum principal stress (horizontal). (**b**) Photograph of pulse-fatigue hydraulic-fracturing-packer system as it is inserted into the horizontal-injection borehole. (**c**) Geometry of injection borehole with six injection intervals (HF1–HF6) and inclined monitoring boreholes (diameter: 76 mm; length: up to 30 m), which are equipped with 70-kHz AE sensors (*cones*).

curves after each injection stage—that is, during shut-in—while taking into account the superposition principle and assuming an infinitely acting radial flow[47,48]:

$$k = \frac{q\mu}{4\pi h \Delta p} ln\left(\frac{t_0 + \Delta t}{\Delta t}\right), \tag{1}$$

with h = interval length, q = flow rate, μ = dynamic viscosity of the fluid, t_0 = injection time, Δt = shut-in time, Δp = pressure difference, and ln = natural logarithm.

Hydraulic-fracturing intervals from tests HF1, HF2, and HF3 are located in Ävrö granodiorite (AG) in the deeper part of the hydraulic-testing borehole, HF4 and HF5 intervals are located in fine-grained diorite-gabbro (fgDG), and the HF6 interval is situated in fine-grained granite (fgG) at a distance of 5 m from the tunnel wall (Fig. 1c).

At the laboratory scale, water-injection experiments were performed on Pocheon granite under triaxial[49] and true-triaxial stress conditions[50] at KICT. We used true triaxial loading equipment, which is capable of performing hydraulic-fracturing tests while controlling either the injection rate or the pressurisation rate. Samples were cut into cubes with a side length of 100 mm. Hydraulic fractures were propagated from an injection borehole with a diameter of 5 mm using six different injection schemes. The applied stresses were prescribed at 4 MPa, 6 MPa, and 3 MPa for the vertical-, maximum horizontal-, and minimum horizontal stress, respectively. A well-described sample of Jurassic granite from the Pocheon quarry, South Korea, with three distinct planes of weakness (so-called rift, grain, and hardway) was used throughout the tests[49]. The first set of injection-rate-control tests comprised constant-rate-continuous, stepwise-rate continuous, and cyclic-progressive injection schemes analogous to the mine tests. The second set of pressurisation-rate control tests included stepwise-, stepwise pulse-, and cyclic pulse pressurisation. A total of 20 tests were carried out using tap water as injection fluid. Unlike the field test, AE activity was monitored with an array of eight *nano* sensors, two of which directly attached to each lateral face of the sample, thereby leaving the top and bottom of the cube blank. A high-vacuum grease-coupling agent enhanced the contact between the sensors and rock surface. The lateral loading plates had small notches on the lower-left- and upper-right corners to allow space for the sensors. The sensors were fixed with bolts to prevent them from dislodging during the tests. The AE sensors (125–750 kHz) and the data-acquisition system were manufactured and developed by the Physical Acoustic Corporation (MISTRAS Group Inc., Princeton, USA). The AE signals were pre-amplified with a gain of 40 dB. During the tests, injection pressure and AE were monitored. Subsequently, the injectivity of the fractured granite samples was measured via water-injection tests at six different injection rates that had been carefully selected to avoid any further fracturing and ranged from 5–30 mm^3/s. As a result, an approximately linear relationship was obtained between the injection rate and the plateau of the injection pressure that corresponded with each injection rate. The injectivity was estimated from the slope of this linear relationship.

The cyclic-stimulation concept was first applied at the field scale in August 2017 at the Pohang EGS site in South Korea[39]. In Pohang, a ~ 160 °C granitic geothermal reservoir with low permeability was accessed with two > 4-km-deep wells, PX-1 and PX-2, with a spacing of ~ 600 m at reservoir depth. "Cyclic soft-stimulation treatment"[33,39] in August 2017 in PX-1 was performed after a conventional stimulation with continuous fluid injection from December 2016 to January 2017[51]. The treatment design was based on the previously described laboratory- and mine-scale experiments and adapted for the site-specific conditions[33]. Three additional stimulations, which are not discussed in this manuscript, were performed in the second well (PX-2) before and after the two PX-1 stimulations reported here.

Results

Breakdown pressure and injection-induced seismicity. Figure 2 displays results from three hydraulic-fracturing tests in the deeper part of the injection borehole at Äspö HRL inside Ävrö granodiorite (see Fig. 1c, HF1–HF3). The plotted hydraulic parameters are the interval pressure and the flow rate in the injection interval (Fig. 2, left axis). The plotted induced-seismicity parameters are the cumulative number and magnitude of the AE events (Fig. 2, black curve and red dots) obtained from the continuous-recording system[46]. The upper-two panels in Fig. 2 display conventional tests with a monotonic-pressure increase (HF1, HF2), and the lower panel shows the fatigue test with cyclic-progressive fluid injection (HF3). The first pressure increase in each experiment resulted from an integrity test, which was stopped before the formation-breakdown pressure (FBP) had been reached. (FBP is the pressure at which a fracture begins to propagate from the wellbore into the formation).

The peak pressure during the first injection cycle after the integrity test corresponded to this FBP. As seen in Fig. 2, the breakdown pressure of fatigue test HF3 was 9.2 MPa, which was lower than the value obtained in the conventional tests in the same rock type (Fig. 3, HF1 and HF2, with FBP = 13.1 MPa and 10.9 MPa, respectively). The same tendency was observed in the neighbouring rock type, which was a fine-grained diorite gabbro[2] (HF4 in Fig. S5a and HF5 in Fig. S5b, with FBP = 10.6 MPa and 9.0 MPa, respectively). No fatigue test could be performed in fine-grained granite due to the lack of fracture-free test intervals. The conventional test (Fig. S5c, HF6), however, was completed in this rock type. The full dataset of pressure-flow charts and seismic activity for these tests (HF4, HF5, and HF6) is provided in the supplement (Figure S5).

AE activity began to occur when the sealed section of the borehole was pressurised, except for with fatigue-hydraulic treatment (Fig. 2c, HF3 for times < 1300 s). AE activity decreased when the pressure in the interval was released and the borehole was shut in (Fig. 2, end of flow rectangle). Fracturing- and re-fracturing stages were accompanied by induced seismic events (Fig. 2, red dots). AE was absent in both post-shut-in- and cyclic-fatigue-fracturing stages only for AE events with magnitude estimation. Weaker events could also be found in the seismic catalogue in the post-shut-in and during cyclic injection[46].

The total number of AEs in fatigue test HF3 was only half of the value of the conventional tests, although the detection threshold used and the amount of water injected were the same. In test HF3, the cumulative number of AEs was ~ 3000 as compared with ~ 6000 AEs for the conventional tests (Fig. 2, black curve). Moreover, the AE activity in the fatigue test began at a later stage in the treatment, and the maximum AE magnitudes observed tended to be lower compared with the conventional tests. The different total timings of the tests described in Fig. 2 resulted from the fact that impression-packer tests had been carried out at several stages of the hydraulic-fracturing operation. Fatiguing the rock has another striking side-effect: Post-shut-in seismic events seem to be suppressed when comparing conventional stimulation (Fig. 2a, b) with the hydraulic-fatigue test (Fig. 2c). One explanation for this finding may be the larger volume of rock that is affected by stress-release (relaxation) in fatigue injection compared with in conventional injection. If two or more fractures are generated at the wall of the stimulation interval, the pressure inside the fractures can communicate via the fluid volume. Instead of frequently observed post-shut-in seismic events in monotonic-injection tests (Fig. 2a, b), the fatigue operation

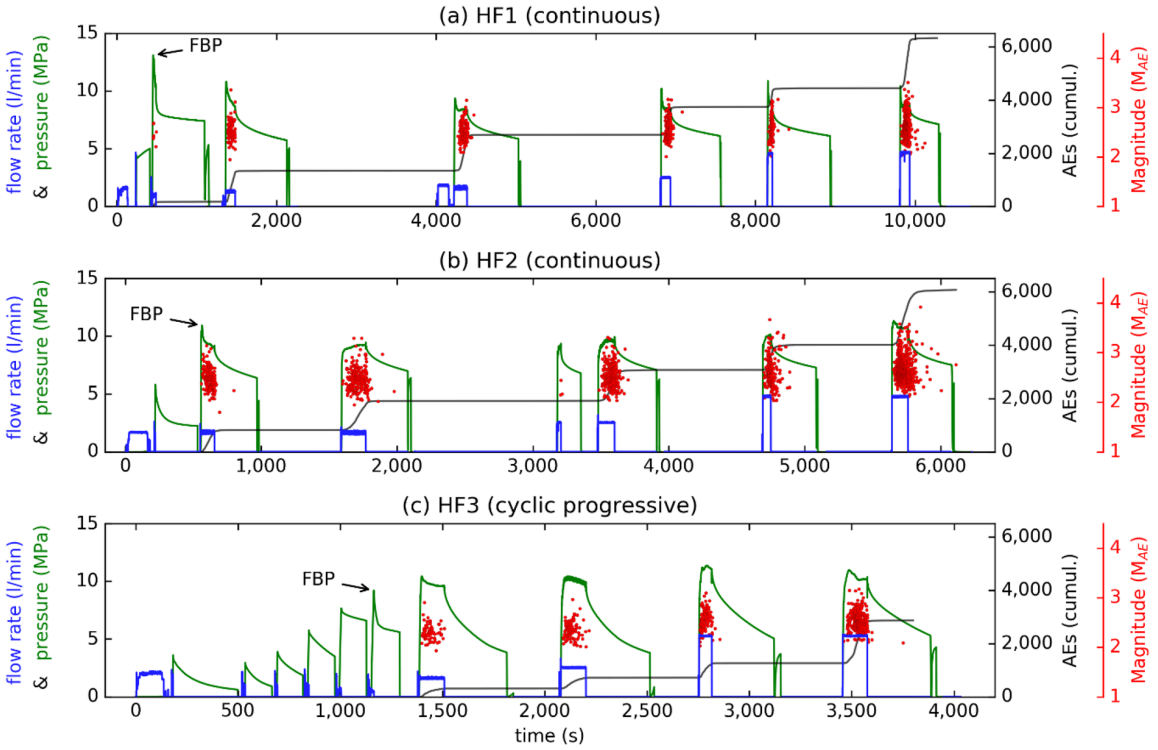

Figure 2. Results of three hydraulic-fracturing tests in Ävrö granodiorite at mine scale. HF1 (**a**) and HF2 (**b**) are conventional fracturing- and re-fracturing tests, respectively, with continuous water injection. HF3 (**c**) is a fatigue test with cyclic, progressive fluid injection before the occurrence of breakdown pressure. Left ordinate indicates flow rate (*blue*) and fluid pressure (*green*). Right ordinate shows cumulative number of AEs (*black curve*) and their magnitudes (*red dots*) over time (s) in the stimulation.

may channelise the energy into rock fragmentation that lies below the seismic threshold because the energy released—as in "venting a valve" via monotonic-pressure increases—causes post-shut-in events with similar magnitudes compared with the pre-shut-in events, whereas the fatigue test allows for the release of smaller-magnitude events since the rock is gradually fragmented in fatigue cycles beforehand.

Figure 3 displays three hydraulic-fracturing tests on Pocheon granite cubes in the laboratory in which flow-rate-control injection was applied. Hydraulic parameters (Fig. 3, pressure, injection rate) are shown against time together with induced AE characteristics, such as amplitude and cumulative event number. In the conventional continuous test, the injection of 24 ml/min was stopped after breakdown had occurred, which was identified by a simultaneous decrease in pressure and an increase in AE activity (Fig. 3a, FBP = 18.5 MPa). The injection was stopped (shut in) ~ 11.5 s after breakdown had occurred. The pressure decreased, and the total number of AEs sharply increased at FBP (Fig. 3a, black curve), and then both continued to increase until shut-in had been reached. After shut-in, the total number of events did not increase considerably. The AE activity was highest at FBP, at which point most of the shear cracks formed (Fig. 3a, light blue dots). Tensile cracks occurred more continually (Fig. 3a, red dots).

In the stepwise progressive injection test (Fig. 3b), breakdown was identified by a clear drop in pressure during the seventh injection cycle (FBP = 18.6 MPa). Unlike in constant continuous injection, the accumulated number of AEs increased only slightly after shut-in. Unlike in the previous test, injection was not stopped after shut-in but continued as planned until it had reached a maximum-flow rate of 6 ml/min. As with continuous injection, the majority of AEs occurred at breakdown. In addition, it was at this point that most of the shear cracks developed (Fig. 3b), which indicated fracture propping.

In the cyclic-progressive injection test (Fig. 3c, fatigue test), the injection rate was increased gradually from 1.2 to 6 ml/min, but each stage also included phases of low injection (0.6 ml/min) that reduced the pressure within each cycle. For this case, no apparent breakdown pressure was observed, and the maximum recorded pressure was 19.2 MPa. Few AEs occurred before shut-in, which coincided with the high-pressure parts of each cycle. Although the AE activity increased after shut-in, the overall cumulative value was lower than for the other cases (Fig. 3, black curve). Almost no shear cracks occurred, which is in line with the apparent lack of breakdown pressure. The remaining diagrams of the pressure-controlled laboratory tests are presented in the supplementary material (Fig. S4).

Fracture geometry- and permeability-enhancement process. In the following section, we discuss the fracture pattern in the granitic rock as revealed via impression-packer results in the mine (Fig. 4) and via

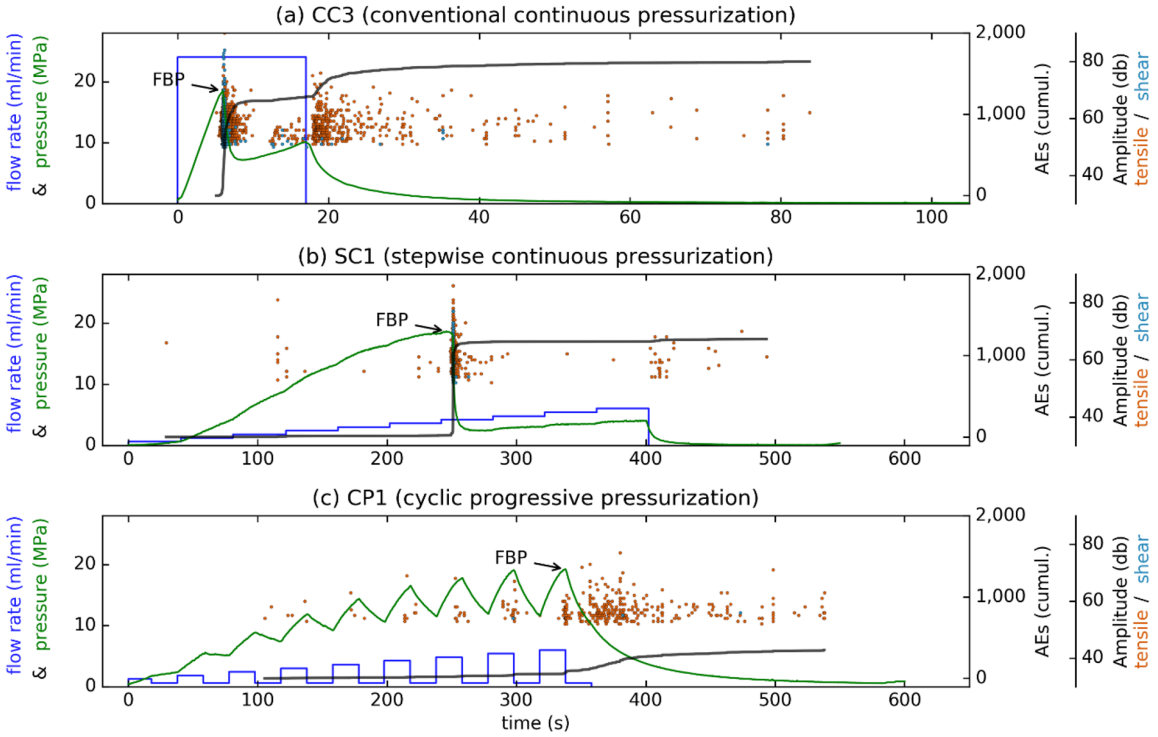

Figure 3. Laboratory hydraulic-fracturing results on true triaxially stressed Pocheon granite cubes with three fluid-injection schemes. Flow-rate-control tests with (**a**) conventional- continuous, (**b**) stepwise-continuous, and (**c**) cyclic-progressive pressurisation. *Red dots* indicate induced AE tensile failure; *light-blue dots* indicate induced AE shear failure. Other parameters were chosen to be analogous to those in Fig. 2.

X-ray CT-image analysis after laboratory hydraulic-fracturing experiments (Fig. 5). In Fig. 4, the resulting fracture patterns from two mine-injection tests that were conducted next to each other (Fig. 2, HF2 and HF3) are displayed as having been cause by the impression packer. While only one fracture trace could be found in the conventional test at a mid-injection interval depth of 22.5 m in the horizontal testing borehole (Fig. 4a, HF2), in the fatigue test, two fracture traces were visible at a mid-injection interval depth of 19 m (Fig. 4b, HF3 fracture trace A and B). Niemz et al.[46] mapped the hydraulic fractures farther away from the wellbore using the expectation–maximisation algorithm. A single plane or multiples planes were fitted to the cloud of the AE hypocentres by maximising the expectation value of the underlying Gaussian distributions. During this process, outliers are assigned to a noise class, while the remaining hypocentres are attributed to a plane that is spanned by strike and rake. The estimated fracture planes support the observation of multiple fault planes with varying strike- and dip values for HF3. Our argument that the double-fracture phenomenon was caused by the fatigue-pumping scheme is as follows: Since the two branches of hydraulic fracture in HF3 developed directly from the borehole wall (as confirmed by impression-packer results and full-waveform AE-hypocentre tracking) and the wall of the test interval was found to be fracture-free before testing (BIPS borehole televiewer and core logs), we have strong support indicating that the double fracture resulted from the fatigue-testing scheme. We admit, however, that the in-situ stress deviator can play a significant role in fracture reorientation as soon as the fracture moves away from the injection interval. Moreover, pre-existing natural fractures in a rock mass can affect a growth path.

Figure 4c displays the results of hypocentre-expectation maximisation. The maximum extension of the fracture plane was assumed to correspond to the outer rim of the cloud of computed AE hypocentres. The average aperture of the hydraulic fractures was estimated using measured backflow values and fracture extension from maximisation expectation[52]. The conventional test generated a fracture of ~ 20 m^2 with an aperture of ~ 130 µm. The fatigue test generated two fractures with a total fracture surface of ~ 37 m^2 and an average aperture of ~ 49 µm each. This finding indicates that a different fracture- and permeability-evolution process occurred in hydraulic fatigue as compared with in conventional fracturing. The observation that the fracture geometry of HF3 is farther away from the injection interval, however, cannot have been caused by the pumping scheme alone. Other factors, such as pre-existing fractures or the stress-shadow effect of neighbouring fractures, could have played an equally important role.

However, in the laboratory-test results in which optical microscopy and X-ray CT images were used, the difference in fracture patterns caused by continuous and cyclic fluid injection into granitic rock was characterised quantitatively. Monotonic fluid injection caused single through-going bi-wing fractures to develop (Fig. 5a). Cyclic injection, on the other hand, led to multiple asymmetric fracture growths with greater tortuosity (Fig. 5b, c). Increasing the number of fluid-injection cycles led to more fractures in the process- and damage

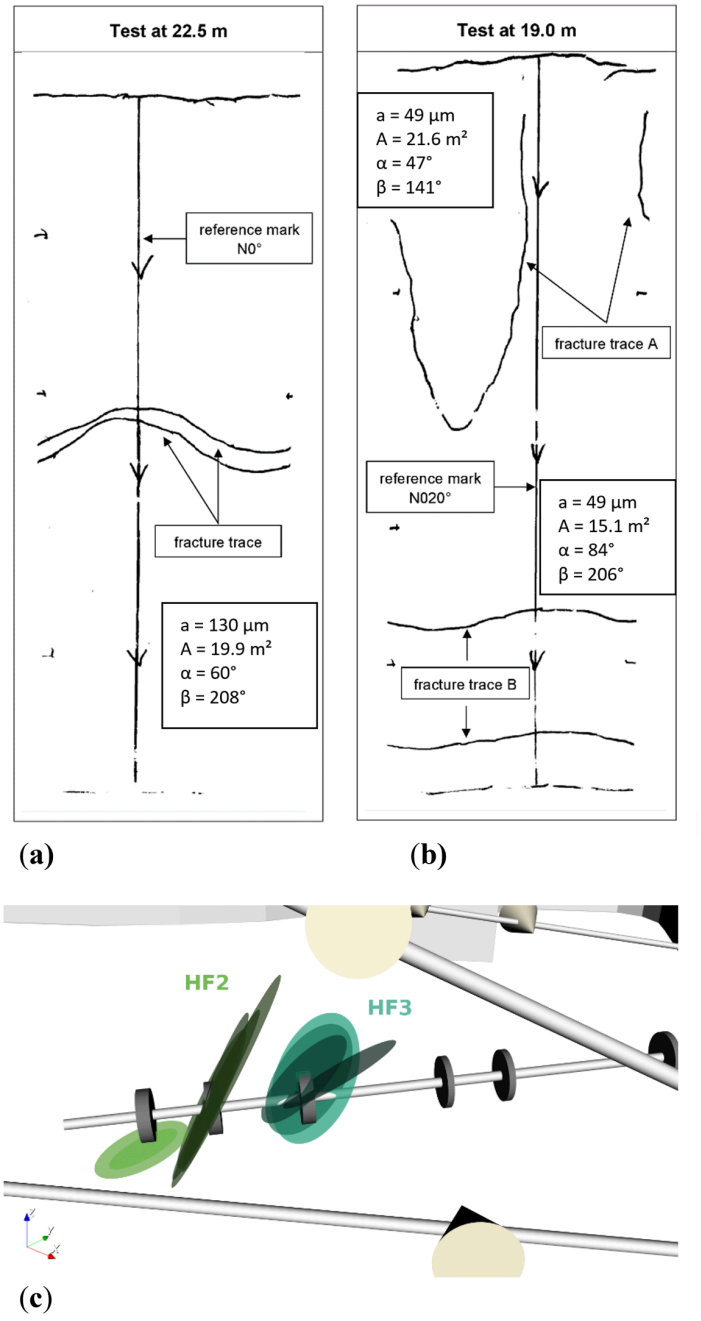

Figure 4. Integrated fracture data from impression packer with interval length of 0.75 m, back flow, and AE hypocentre analysis. Impression packer results shown are (**a**) from conventional test HF2 at a mid-interval depth of 22.5 m and (**b**) from fatigue test HF3 at a mid-interval depth of 19.0 m. Dip (α) and dip direction (β) of the fractures come from impression-packer analysis[48]. Fracture aperture (*a*) and area of fracture plane (*A*) come from AE -hypocentre extension and back-flow data[52]. In (**c**), fracture-plane orientations computed via full-waveform AE analysis are shown[46].

zone. Asymmetric fracture growth and the process-zone-enlargement mechanism are characteristic features of fatigue tests (Fig. 5b, c). Using optical microscopy, quartz fragments were found in the process zone of the fatigue fractures[50]. This finding strengthens our fatigue-hydraulic-fracturing concept, which postulated that rock chips would be generated by the secondary pump from open fracture walls (see supplementary material). For granitic rock, these natural proppants can be identified as the strongest minerals of the aggregate (here: quartz grains) (see Figure S7 in the supplement).

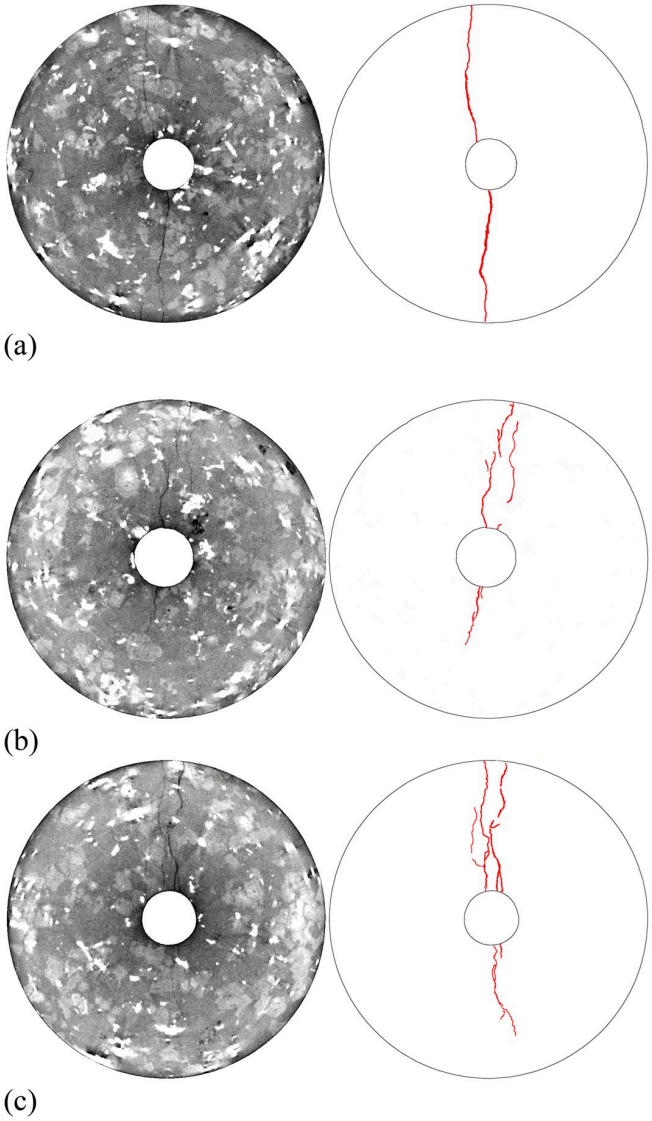

Figure 5. X-ray CT images (left) and fracture traces (right) after triaxial-injection tests on Pocheon granite cores (diameter: 50 mm; injection-borehole diameter: 8 mm). Continuous injection (**a**) led to single through-going bi-wing fractures, whereas cyclic injection with 43 cycles (**b**) and 150 cycles (**c**) led to multiple asymmetric fractures with a broader damage zone[49].

The third part of the engineering puzzle involves the evolution of permeability. Below, we demonstrate that fatigue tests are able to enhance permeability, as documented in conventional hydraulic fracturing. Figure 6 summarises the permeability evolution across scales. At the laboratory scale (Fig. 6a), permeability enhancement is quantified as the fold of increase (FOI), which describes the ratio of injectivity after injection in comparison with the initial state before the treatment. This FOI is compared with the maximum magnitude of acoustic events via the different injection protocols. The greatest increase in the FOI is observed for the stepwise (SPP3) and cyclic (CPP1) pulsed experiments (see supplement, Figure S4). The conventional, constant-rate-injection test (CC3) reveals the greatest maximum magnitude of acoustic events.

In Fig. 6b, permeability enhancement versus the cumulative number of AEs is shown for the six field tests carried out at the Äspö Hard Rock Laboratory. The greatest permeability increase is observed for the pulsed hydraulic-fracture test, with progressively increasing flow rates and pulses on top (Fig. S5b, HF5) and without any seismicity observed. It should be noted that this test and HF4 were performed in fine-grained diorite gabbro. The cyclic hydrofrac test with a progressively increasing flow rate in Ävrö granodiorite (Fig. 2c, HF3) displayed the lowest observed seismicity when compared with the other conventional tests with constant-flow rates. The permeability evolution is among the highest, with intermediate absolute permeability occurring at the end of the test.

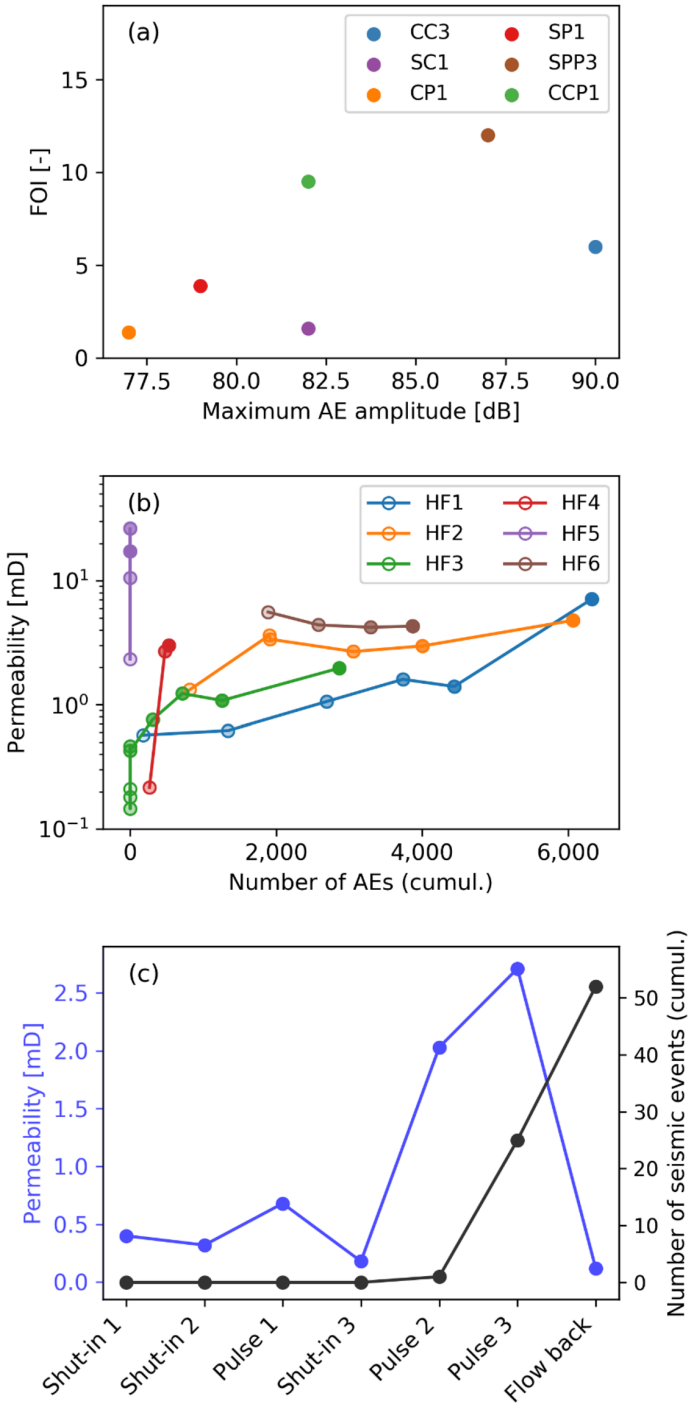

Figure 6. Permeability evolution across scale. (**a**) Fold of increase (FOI) of laboratory hydraulic fracturing test with different injection protocols: Flow-rate-controlled tests (CC3, SC1, CP1) and pressure-controlled tests (SP1, SPP3, CPP1). (**b**) Permeability enhancement for six field tests carried out in Äspö Hard Rock Laboratory: Conventional (HF1, HF2, HF4, HF6) and fatigue hydraulic tests (HF3, HF5). (**c**) Permeability development and seismicity observed during the field hydraulic test in the well PX1 in Pohang, South Korea.

The permeability development and the seismicity observed during the field hydraulic test in the PX1 well in Pohang, Korea, is displayed in Fig. 6c. Permeability differs substantially for shut-in periods during cyclic

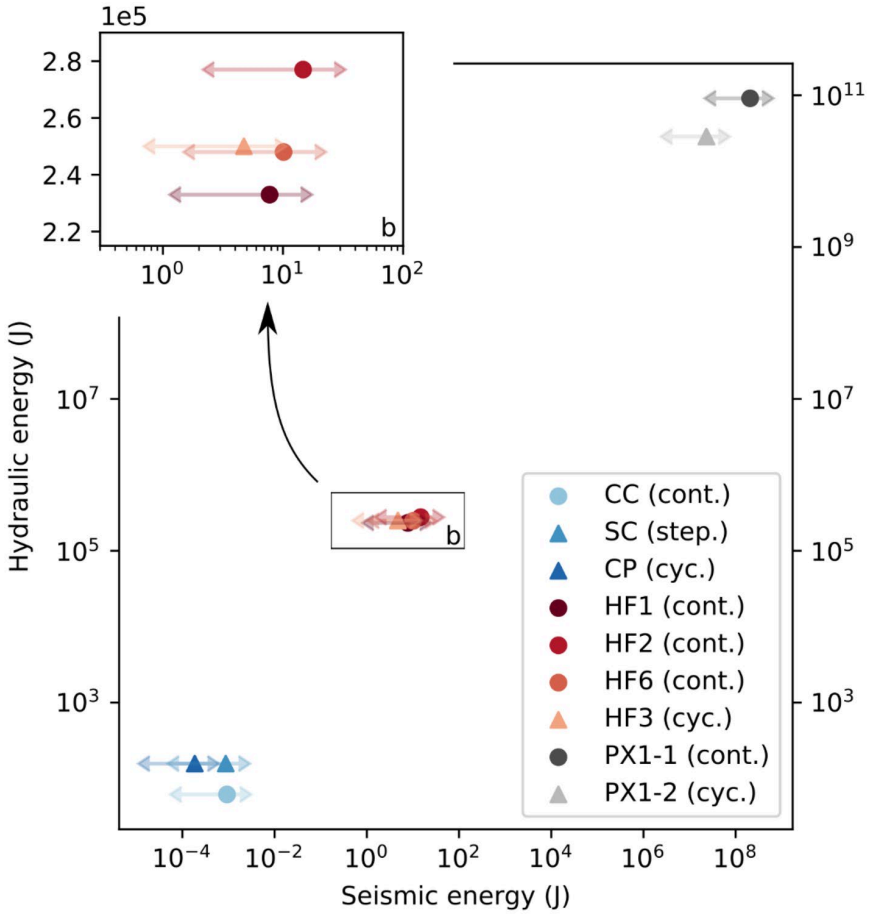

Figure 7. Hydraulic versus radiated seismic energy across scales.

injection with pulses and subsequent flow-back because the fracture system begins to open dynamically during the injection phases and begins to close subsequently in the shut-in phases and during the flow-back. Seismicity began at the very end of the treatment during pulsed injection due to the Kaiser effect[39], which describes the delay of seismicity due to the previous stimulation in the well. Therefore, no comparison between conventional and fatigue-injection protocols is possible in terms of the occurrence of seismic events.

Energy partition. In Figs. 7 and 8, energy values from laboratory-, mine-, and field-scale fluid-injection experiments are compared. In Fig. 7, the hydraulic energy is plotted against the radiated seismic energy throughout the three scales discussed in this study. Individual tests revealed the difference between conventional (continuous injection) and fatigue hydraulic fracturing (cyclic injection). The orders of difference between the hydraulic and seismic energy stem from the fact that the rock volume and fluid-injection volume were very different. The histograms in Fig. 8 reveal the complete set of energy values computed with the full dataset presented in the supplementary material (Table S8).

We observe a scale dependence in the ratio of radiated seismic and hydraulic energy, with values in the range of 1.9×10^{-7} to 6.7×10^{-5} for the laboratory tests (Fig. 8a), 3.4×10^{-6} to 9.7×10^{-5} for the mine tests (Fig. 8b), and 1.5×10^{-4} to 4×10^{-3} for the field tests (Fig. 8c). Regarding the injection styles, a trend of lower seismic-energy release can be seen for the cyclic-injection protocols. This finding highlights the efficiency of hydraulic-fatigue tests in flow-rate-control mode.

Energy ratios are displayed on the right of Fig. 8. In the laboratory tests, the values of E_{seis} with respect to E_{Hydro} (as well as E_{Hydro} and E_{Def}) were not the same. The difference, however, was very small because E_{Def} in the small laboratory rock cube was small (0.5 J) when compared with E_{Hydro} (with values ranging from between 55 and 839 J). Therefore, the sum of both energy terms is dominated by the hydraulic part of the energy budget (see also Table S8). Both ratios E_{seis}/E_{hydr} and $E_{seis}/(E_{hydr} + E_{def})$ were computed with the effective stress law and yielded similar values. This finding is independent of scale and within a range of two orders of magnitude. It appears that a larger rock volume that stored greater deformation energy also released more seismic energy.

The deformation energy computed from principal stresses and the rock volume was greater than the hydraulic energy in the mine- and field-scale injection tests. This result is mainly due to the rock volume involved in the

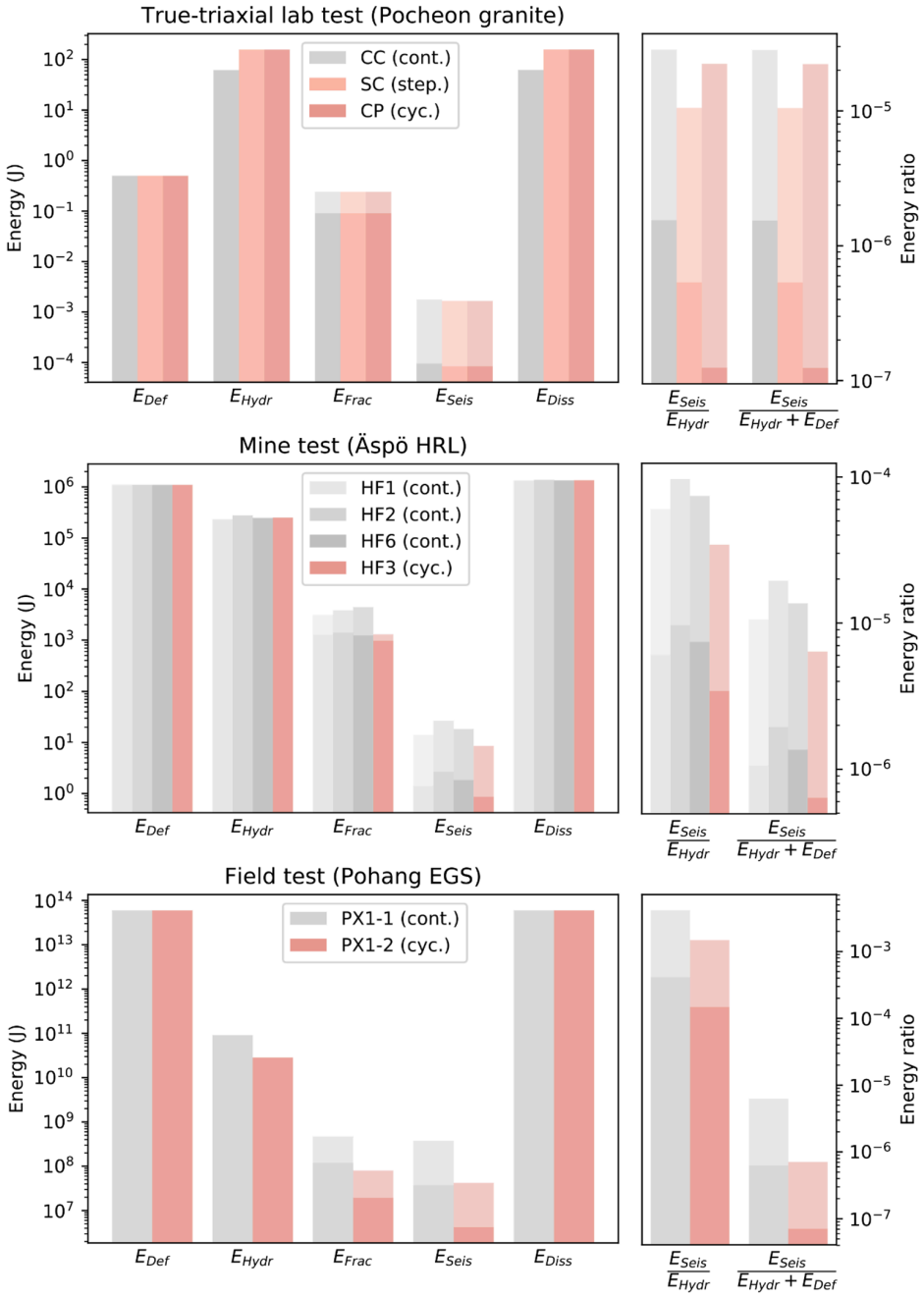

Figure 8. Energy partition in hydraulic-stimulation process. (**a**) True triaxial laboratory tests in Pocheon granite (CC = constant rate continuous, SC = stepwise rate continuous, CP = cyclic progressive); (**b**) underground test in naturally fractured granodiorite at Äspö HRL, Sweden (HF = hydraulic fracturing experiment); and (**c**) field stimulation at Pohang EGS site (PX1 = borehole PX1). All tests performed at all scales are flow-rate controlled.

injection tests. As uncertainty existed concerning the rock volume (especially for the field scale), the volume could have easily been overestimated by one order of magnitude. At the laboratory scale, the hydraulic energy was greater than the deformation energy. This partition of energy terms was directly related to the finite size of the rock samples. Finite rock volume is a general limitation of laboratory tests compared with mine- and field tests and is clearly documented in Fig. 8.

The fracture energy for tensile opening was greater than the radiated seismic energy in the laboratory-scale- and the mine-scale tests. In contrast, the field-scale values showed greater radiated seismic energy as an upper

bound. This finding is likely related to the shearing of pre-existing fractures with relatively greater seismic energy release as compared with tensile fractures. Moreover, fracture energy in the field was estimated using the stimulated volume obtained via micro-seismicity observations only. In the Äspö HRL underground test, we had two independent sources of fracture-area estimates: one from the impression packer and one from the induced-seismic-cloud-extension- and back-flow measurements. In this regard, our underground tests were more reliable.

Discussion of field application and evidence

The major findings in this study come from the joint interpretation of fluid-injection experiments at three scales with an underlying innovative mechanical concept of hydraulic-fatigue fractures. One category of findings (the engineering element) is related to the optimisation of the stimulation- and hydraulic-fracture-growth process, which is documented in breakdown pressure, fracture permeability, and induced-seismicity-evolution results. The second category of findings (the science element) is related to the energy budget of hydraulic fatigue versus the hydraulic-fracture process. In the following section, we discuss our new findings in relation to previous works.

Since the fatigue-hydraulic-fracturing concept was first introduced[37] and cyclic and progressive pulse-injection schemes for hard rock at mine scale were first applied[2], many authors have found evidence of differences between monotonic and cyclic fluid injection. In general, the benefit reported is threefold: First, hydraulic-fatigue testing allows the breakdown pressure to be lowered. Laboratory tests of cyclic hydraulic fracturing on Tennessee sandstone[53], Pocheon granite[49], Fontainebleau sandstone[54], and cement-core plugs with variable strength properties[55] have been reported. The percentage of the reported reduction of breakdown pressure varies for different rock types and with the porosity and strength of individual rock types. For Tennessee sandstone, the decrease in the breakdown pressure caused by cyclic fracturing can largely be attributed to the reduction in tensile strength due to water saturation[53]. In ultra-tight concrete, the reduction percentage is higher (25%) compared with in low- and medium-strength cement blocks (15%)[55]. This finding on concrete is in line with experiments on Xujiahe sandstone[56]. These authors reported smaller breakdown-pressure reduction (7%) in high-porosity samples (13%) as compared with a larger reduction (19%) in low-porosity sandstone (1%). In our study, we compared the reduction in breakdown pressure at the laboratory- and mine scales. In the supplement, we provide data on the cyclic-fatigue-breakdown pressure that have been normalised to the monotonic breakdown pressure of individual tests, and we plot this ratio against the log number of injection cycles (Figure S6). Data indicate a clear trend of breakdown-pressure reduction as a function of injection cycles. At the mine scale, we show data from two different rock types (Fig. S6, triangles). The 5-cycle HF3 experiment was performed in Ävrö granodiorite (Fig. S6, open triangle), while the 700-cycle HF5 experiment was performed in fine-grained diorite gabbro (Fig. S6, solid triangle). In fatigue test HF3, progressive cyclic injection was applied (Fig. 2), while in fatigue test HF5, a hydraulic hammer was used (i.e. cyclic pulse injection) (Fig. S5b). Therefore, the rock type and the fatigue-injection scheme in the mine can have an impact on breakdown-pressure reduction in Figure S6. However, more tests at the mine scale are required in order to separate individual impact factors on breakdown.

Second, fatigue-fluid-injection schemes have the power to modify the frequency-magnitude distributions of seismic events. Generally, the distribution can be described by the Gutenberg–Richter law[57], in which the *b*-value represents the slope of the cumulative histogram of the observed magnitudes. An increase in the seismic *b*-value can be observed in all scales (see supplementary material). Although absolute *b*-values at different scales are difficult to compare due to magnitude-scaling issues, a general trend of relatively higher *b*-values for cyclic injections compared with for continuous injections could be observed at all scales (Fig. S3). This finding is new, and to our knowledge, has not been addressed in any previous work by other authors. An increase in *b*-values indicates a redistribution of seismic events towards smaller magnitudes. In the maximum-likelihood approach, the *b*-value is inversely related to the mean magnitude of the dataset (supplement, Eq. (13)). An increase in the *b*-value corresponds with a decrease in mean magnitude and thereby with more small-magnitude events or less large-magnitude events (or, in any case, with a larger number of smaller events compared with the number of large events) as long as the Gutenberg–Richter relation holds. Theoretically, the *b*-value itself is independent of the total number of events. However, small datasets with a limited number of events can have larger asymptotic errors in their *b*-value estimation. In the geothermal context, the mitigation of larger induced events is of utmost importance since many authorities rely on seismic traffic-light systems that include maximum-magnitude thresholds yet that sometimes neglect the total amount of released seismic energy. Many small events—even those with greater cumulative seismic energy than might be expected for *b*-values larger than 1.5—would not cause a red light and halt the injection activity. If designed properly, cyclic injection can systematically replace several larger-magnitude seismic events with a larger number of smaller-magnitude seismic events because hydraulic fatigue is an efficient rock-fragmentation process (see supplement, fracture-mechanics formulation of hydraulic fatigue). Future tests should search for injection parameters that minimise the seismic-energy release. We suggest evaluating the effect of fracturing-fluid viscosity in combination with—inter alia—the number of injection cycles, crack resting times, duration times, amplitudes, and the phase shift of pressurisation intervals. Although the total energy budget in situ is fixed, with some limits, the partition of seismic and fracture-surface energy during the rock-degradation process is optimisable.

Fracturing fluids are known to exert an impact on the hydraulic-fracture-growth process. A variety of fluids are commonly used in the laboratory, including freshwater, oil, CO_2 (liquid, super-critical), and gas (CO_2, N_2). The viscosities of these fluids can range from between several orders of magnitude (10^{-2} and 10^{-6} mPa s). Results indicate that the viscosity of the injection fluid exerts a significant impact on the hydraulic fracturing of granites[58,59] as well as of other rock types[60,61]. Ishida et al.[62] compared four different fluids of super-critical and liquid CO_2, water, and viscous oil with a low to high viscosity of 0.051 to 337 mPa s and confirmed that breakdown pressure increases with increasing viscosity.

The impact of fluid viscosity on hydraulic-fracture growth is seen as follows: For a given rock type, high-viscosity fluids have a smaller infiltration rate compared with low-viscosity fluids, even at the same injection rate. As a result, the rock can be fractured at different breakdown pressures. Jung et al.[63] compared the total volume of injection fluid infiltrated into granite samples when using water and various oil-based fluids (80, 122, and 152 mPa s) at the same constant-injection rate. The measured results reveal that the total amount of oil infiltration is about half that of water infiltration. Breakdown pressure by oil fracturing is about two times that by water fracturing, which is explained by a shift in fracturing behaviour from viscosity-dominated- to toughness-dominated regimes[64].

Changing the fracturing fluid in hydraulic fatigue can be beneficial in designing short and compact- versus long and persistent fractures. If short and compact fractures are desired, water-hammer fracturing can be applied, while if long and persistent fractures are desired, highly viscous gel and cyclic-progressive fatigue tests can be applied. The hydraulic-fatigue concept can also be of value for field EGS applications when massive conventionally stimulated cloud-like fractures need to be replaced by controlled multi-stage fractures for the sake of optimising geothermal heat exchangers.

Third, compared with monotonic injections, cyclic fluid injections into the geo-reservoir have been demonstrated to increase the hydraulic performance of the fracture network[54]. This finding has important implications for EGS stimulations, in which an increase in reservoir permeability and dilatancy would enhance reservoir productivity. Noel et al.[54] demonstrated that a dilatancy threshold exists (~ 1% for Fontainebleau sandstone) after which macroscopic failure occurs. For reservoir applications, approaching this critical dilatancy could provoke fast failure of the reservoir and associated induced seismic activity. We recommend applying hydraulic fatigue in order to better control fracture growth and induced seismicity at a level below the critical dilatancy threshold, where other stimulation methods may fail. Controlling fracture growth via hydraulic fatigue, on the other hand, goes hand in hand with sophisticated stimulation techniques and longer treatment times.

In mine testing, a combination of cyclic-progressive and pulse-hydraulic fracturing yields the best increase in permeability (Fig. 6b). To our knowledge, combining cyclic- and pulse-pumping schemes is a new concept and has not been written about by other authors. Cyclic injection promotes the development of more fractures in a broader zone as has been documented in laboratory tests on sandstone and granite. The extension of the fracture process zone in Tennessee sandstone after cyclic hydraulic fracturing has been reported to be about twice that of the process zone in the conventional treatment[53]. The corresponding increase in fracture permeability by cyclic injection into Tennessee sandstone has been reported to correspond to a factor 3–10 times higher than that of conventional hydraulic fracturing. Zhuang et al.[50] reported a denser network of grain-boundary shear cracks in Pocheon granite after hydraulic-fatigue testing as compared with conventional treatment with primarily intra- and inter-granular tensile cracks in a narrow band. In the same study, quartz grain fragments in the main fracture were reported as being natural proppants after hydraulic-fatigue testing.

Simple cyclic pumping has also been used in shale-gas fracturing and has been demonstrated at the field scale with the concept of "relax a frac", in which part of the stimulation treatment is pumped, followed by an extended shutdown to relax the formation[65]. In addition, perforation clusters have been demonstrated at the laboratory scale to be able to efficiently stimulate multiple fractures in horizontal wells[66]. By applying fatigue hydraulic fracturing with the reported gain in permeability enhancement (one order of magnitude in mine testing)[48], perforated facture stages can superimpose individual permeability performance, which renders the treatment more efficient for shale-gas production. Perforation clusters can also be used in geothermal (EGS) development.

First attempts have also been made to apply cyclic stimulations in the field of EGS. In the cyclic soft-stimulation-concept treatment performed in August 2017 at the Pohang EGS site, a total of 1756 m^3 of surface water was injected into the PX-1 well at flow rates of between 1 and 10 l/s, with a maximum wellhead pressure of 23 MPa[39]. During the treatment, a total of 52 induced micro-earthquakes were detected in near-real-time. The largest event had a magnitude of Mw = 1.9, which was below the critical-threshold level of Mw = 2.0 set in advance. A second project using varying flow-rate stimulation and a near-real-time seismic-event-control concept in the framework of EGS stimulation was performed one year later at the campus of Aalto University, located at Espoo near Helsinki, Finland. In June and July 2018, a total of 18,160 m^3 of fresh water was pumped into crystalline rocks at a depth of 6.1 km over 49 days[67]. The locations, magnitude, and evolution of seismic and hydraulic energy were used to control hydraulic-fracture growth and stabilisation during the stimulation treatment in line with the fatigue-hydraulic-fracturing concept.

The focus of this study was on optimising fluid injection, induced seismicity, and permeability evolution during the hydraulic-fracture-growth process in naturally fractured granitic rock masses. At this point, it is necessary to indicate that fluid injection close to or directly into a fault is a different problem, as is documented, for example, by the detection of "runaway fractures" via fluid-injection-induced seismicity at EGS sites[21,25,68].

Relaxation damage control via hydraulic-fatigue cycles not only seems to work in granite at the grain-boundary scale (laboratory) and at the scale of naturally fractured granitic rock mass (mine), but it is also a candidate for being applied at the field scale. The basic ingredients in cyclic fatigue testing—including variable flow rates, multiple crack-tip resting times, and more-tortuous and denser fracture-network evolutions—can be seen scale-independently, although the intrinsic properties of different rocks are involved at various scales.

We admit that more rock types need to be investigated in the future, and each individual rock type may need a tailor-made cyclic- and pulse-injection scheme in order to increase the overall confidence in the hydraulic-fatigue concept presented in this study.

Methods: computation of radiated seismic-, fracture-surface- and hydraulic energy

We compared hydraulic-fracture nucleation- and growth process by analysing seismic signals recorded with high-frequency acoustic-emission (AE) sensors, including their magnitude–frequency distribution, radiated seismic energy, and cumulative seismic-energy release. Second, we analysed hydraulic parameters in terms of formation-breakdown pressure and permeability evolution. Third, we estimated fracture geometrical parameters—such as aperture, area, and tortuosity—using AE hypocentre locations in the mine test as well as micro-X-ray CT image analysis of granite specimens after the laboratory test.

We estimated radiated seismic energy (E_{Seis}) via an AE analysis. We computed fracture-surface energy (E_{Frac}) via fracture-geometry data and experimentally determined fracture-toughness data. We computed hydraulic energy (E_{Hydr}) via pressure–time charts and the net volume of fluid injected. We did not know the value of energy dissipated during the hydraulic-fracturing process (E_{Diss}). Using a rough estimate of the stored elastic strain energy of the granite cubes stimulated under stress at different scales (E_{Def}), we computed a lower-bound value (E_{Diss}). The energy balance of a change in a given stress state (i.e. hydraulic stimulation) was given by Eq. (2):

$$E_{Def} + E_{Hydr} = E_{Seis} + E_{Frac} + E_{Diss}. \quad (2)$$

For more details about computing and estimating individual energy terms, please consult the supplementary material section.

Data availability

The datasets generated and/or analysed during the current study are summarised in Supplementary Table S8. Raw and unprocessed data are available upon request at niemz@gfz-potsdam.de.

Received: 4 November 2020; Accepted: 9 March 2021
Published online: 24 March 2021

References

1. Zang, A. & Stephansson, O. *Stress field of the Earth's crust* (Springer, Dordrecht, 2010).
2. Zang, A. *et al.* Hydraulic fracture monitoring in hard rock at 410 m depth with an advanced fluid-injection protocol and extensive sensor array. *Geophys. J. Int.* **208**, 790–813. https://doi.org/10.1093/gji/ggw430 (2017).
3. Amann, F. *et al.* The seismo-hydromechanical behavior during deep geothermal reservoir stimulations: open questions tackled in a decametre-scale in situ stimulation experiment. *Solid Earth* **9**, 115–137. https://doi.org/10.5194/se-9-115-2018 (2018).
4. Gischig, V. S. *et al.* On the link between stress field and small-scale hydraulic fracture growth in anisotropic rock derived from microseismicity. *Solid Earth* **9**, 39–61. https://doi.org/10.5194/se-9-39-2018 (2018).
5. Kneafsey, T. J. *et al.* An overview of the EGS collab project: Field validation of coupled process modeling of fracturing and fluid flow at the sanford underground research facility, lead, SD. In *PROCEEDINGS 43rd Workshop on Geothermal Reservoir Engineering*, vol. SGP-TR-213 (Stanford University, Stanford, California, 2018).
6. Gischig, V. S. *et al.* Hydraulic stimulation and fluid circulation experiments in underground laboratories: Stepping up the scale towards engineered geothermal systems. *Geomech. Energy Environ.* **24**, 100175. https://doi.org/10.1016/j.gete.2019.100175 (2020).
7. Guglielmi, Y., Cappa, F., Avouac, J.-P., Henry, P. & Elsworth, D. Seismicity triggered by fluid injection–induced aseismic slip. *Science* **348**, 1224–1226. https://doi.org/10.1126/science.aab0476 (2015).
8. De Barros, L., Cappa, F., Guglielmi, Y., Duboeuf, L. & Grasso, J.-R. Energy of injection-induced seismicity predicted from in-situ experiments. *Sci. Rep.* **9**, 4999. https://doi.org/10.1038/s41598-019-41306-x (2019).
9. Zang, A. *et al.* How to reduce fluid-Injection-induced seismicity. *Rock Mech. Rock Eng.* **52**, 475–493. https://doi.org/10.1007/s00603-018-1467-4 (2019).
10. Shapiro, S. A. *Fluid-Induced Seismicity* (Cambridge University Press, Cambridge, 2015).
11. Foulger, G. R., Wilson, M. P., Gluyas, J. G., Julian, B. R. & Davies, R. J. Global review of human-induced earthquakes. *Earth-Sci. Rev.* **178**, 438–514. https://doi.org/10.1016/j.earscirev.2017.07.008 (2018).
12. Ellsworth, W. L. Injection-induced earthquakes. *Science* https://doi.org/10.1126/science.1225942 (2013).
13. McGarr, A. *et al.* Coping with earthquakes induced by fluid injection. *Science* **347**, 830–831. https://doi.org/10.1126/science.aaa0494 (2015).
14. Weingarten, M., Ge, S., Godt, J. W., Bekins, B. A. & Rubinstein, J. L. High-rate injection is associated with the increase in U.S. mid-continent seismicity. *Science* **348**, 1336–1340. https://doi.org/10.1126/science.aab1345 (2015).
15. Alghannam, M. & Juanes, R. Understanding rate effects in injection-induced earthquakes. *Nat. Commun.* **11**, 3053. https://doi.org/10.1038/s41467-020-16860-y (2020).
16. Warpinski, N. R., Du, J. & Zimmer, U. Measurements of hydraulic-fracture-induced seismicity in gas shales. *SPE Prod. Oper.* **27**, 240–252 (2012).
17. Schultz, R. *et al.* Hydraulic fracturing-induced seismicity. *Rev. Geophys.* **58**, e2019RG000695. https://doi.org/10.1029/2019RG000695 (2020).
18. Evans, K. F., Zappone, A., Kraft, T., Deichmann, N. & Moia, F. A survey of the induced seismic responses to fluid injection in geothermal and CO_2 reservoirs in Europe. *Geothermics* **41**, 30–54. https://doi.org/10.1016/j.geothermics.2011.08.002 (2012).
19. Rutqvist *et al.* Fault activation and induced seismicity in geological carbon storage - Lessons learned from recent modeling studies. *J. Rock Mech. Geotech. Eng.* **8**(6), 789–804. https://doi.org/10.1016/j.jrmge.2016.09.001 (2016).
20. Majer, E., Nelson, J., Robertson-Tait, A., Savy, J. & Wong, I. Protocol for addressing induced seismicity associated with enhanced geothermal systems. Tech. Rep. DOE/EE-0662, 1219482, U.S. Department of Energy (2012). https://doi.org/10.2172/1219482.
21. Zang, A. *et al.* Analysis of induced seismicity in geothermal reservoirs—an overview. *Geothermics* **52**, 6–21. https://doi.org/10.1016/j.geothermics.2014.06.005 (2014).
22. Giardini, D. Geothermal quake risks must be faced. *Nature* **462**, 848–849. https://doi.org/10.1038/462848a (2009).
23. Grigoli, F. *et al.* The November 2017 Mw 5.5 Pohang earthquake: a possible case of induced seismicity in South Korea. *Science* **360**, 1003–1006. https://doi.org/10.1126/science.aat2010 (2018).
24. Ellsworth, W. L., Giardini, D., Townend, J., Ge, S. & Shimamoto, T. Triggering of the Pohang, Korea, earthquake (Mw 5.5) by enhanced geothermal system stimulation. *Seismol. Res. Lett.* **90**, 1844–1858. https://doi.org/10.1785/0220190102 (2019).
25. Woo, J.-U. *et al.* An in-depth seismological analysis revealing a causal link between the 2017 MW 5.5 Pohang earthquake and EGS project. *J. Geophys. Res. Solid Earth* **124**, 13060–13078. https://doi.org/10.1029/2019JB018368 (2019).
26. Grünthal, G. Induced seismicity related to geothermal projects versus natural tectonic earthquakes and other types of induced seismic events in Central Europe. *Geothermics* **52**, 22–35. https://doi.org/10.1016/j.geothermics.2013.09.009 (2014).

27. Rathnaweera, T. D., Wu, W., Ji, Y. & Gamage, R. P. Understanding injection-induced seismicity in enhanced geothermal systems: from the coupled thermo-hydro-mechanical-chemical process to anthropogenic earthquake prediction. *Earth Sci. Rev.* **205**, 103182. https://doi.org/10.1016/j.earscirev.2020.103182 (2020).
28. Bommer, J. J., Crowley, H. & Pinho, R. A risk-mitigation approach to the management of induced seismicity. *J. Seismol.* **19**, 623–646. https://doi.org/10.1007/s10950-015-9478-z (2015).
29. Maxwell, S. C., Zhang, F. & Damjanac, B. Geomechanical modeling of induced seismicity resulting from hydraulic fracturing. *Lead. Edge* **34**, 678–683. https://doi.org/10.1190/tle34060678.1 (2015).
30. Mena, B., Wiemer, S. & Bachmann, C. Building robust models to forecast the induced seismicity related to geothermal reservoir enhancement. *Bull. Seismol. Soc. Am.* **103**, 383–393. https://doi.org/10.1785/0120120102 (2013).
31. Bommer, J. J. *et al.* Control of hazard due to seismicity induced by a hot fractured rock geothermal project. *Eng. Geol.* **83**, 287–306. https://doi.org/10.1016/j.enggeo.2005.11.002 (2006).
32. Häring, M. O., Schanz, U., Ladner, F. & Dyer, B. C. Characterisation of the Basel 1 enhanced geothermal system. *Geothermics* **37**, 469–495. https://doi.org/10.1016/j.geothermics.2008.06.002 (2008).
33. Hofmann, H., Zimmermann, G., Zang, A. & Min, K.-B. Cyclic soft stimulation (CSS): A new fluid injection protocol and traffic light system to mitigate seismic risks of hydraulic stimulation treatments. *Geotherm. Energy* **6**, 27. https://doi.org/10.1186/s40517-018-0114-3 (2018).
34. Broccardo, M. *et al.* Induced seismicity risk analysis of the hydraulic stimulation of a geothermal well on Geldinganes, Iceland. *Nat. Hazards Earth Syst. Sci.* **20**, 1573–1593. https://doi.org/10.5194/nhess-20-1573-2020 (2020).
35. Baisch, S., Koch, C. & Muntendam-Bos, A. Traffic Light Systems: To what extent can induced seismicity be controlled?. *Seismol. Res. Lett.* **90**, 1145–1154. https://doi.org/10.1785/0220180337 (2019).
36. Wiemer, S., Kraft, T., Trutnevyte, E. & Roth, P. "Good Practice" Guide for Managing induced seismicity in deep geothermal energy projects in Switzerland. Report, ETH Zurich (2017). https://doi.org/10.3929/ethz-b-000254161.
37. Zang, A., Yoon, J. S., Stephansson, O. & Heidbach, O. Fatigue hydraulic fracturing by cyclic reservoir treatment enhances permeability and reduces induced seismicity. *Geophys. J. Int.* **195**, 1282–1287. https://doi.org/10.1093/gji/ggt301 (2013).
38. Yoon, J. S., Zang, A. & Stephansson, O. Numerical investigation on optimized stimulation of intact and naturally fractured deep geothermal reservoirs using hydro-mechanical coupled discrete particles joints model. *Geothermics* **52**, 165–184. https://doi.org/10.1016/j.geothermics.2014.01.009 (2014).
39. Hofmann, H. *et al.* First field application of cyclic soft stimulation at the Pohang Enhanced Geothermal System site in Korea. *Geophys. J. Int.* **217**, 926–949. https://doi.org/10.1093/gji/ggz058 (2019).
40. Frohlich, C. Two-year survey comparing earthquake activity and injection-well locations in the Barnett Shale, Texas. *Proc. Natl. Acad. Sci.* **109**, 13934–13938. https://doi.org/10.1073/pnas.1207728109 (2012).
41. McGarr, A. Seismic moments and volume changes. *J. Geophys. Res.* **1896–1977**(81), 1487–1494. https://doi.org/10.1029/JB081i008p01487 (1976).
42. McGarr, A. Maximum magnitude earthquakes induced by fluid injection: Limits on fluid injection earthquakes. *J. Geophys. Res. Solid Earth* **119**, 1008–1019. https://doi.org/10.1002/2013JB010597 (2014).
43. Block, L. V., Wood, C. K., Yeck, W. L. & King, V. M. The 24 January 2013 ML 4.4 earthquake near Paradox, Colorado, and its relation to deep well injection. *Seismol. Res. Lett.* **85**, 609–624. https://doi.org/10.1785/0220130188 (2014).
44. Klee, G. & Rummel, F. Rock stress measurements at the Äspö HRL. Hydraulic fracturing in boreholes KA2599G01 and KF0093A01. Tech. Rep. IPR-02-02, Swedish Nuclear Fuel and Waste Management Co., Stockholm (2002).
45. Jiráková, H., Frydrych, V., Vintera, J., Krásny, O. & Vanecek, M. Results of the rock hydraulic fracturing research project. *Tunel-Undergr. Constr. Mag. Czech Tunneling Assoc. Slovak Tunneling Assoc.* **24**, 57–64 (2015).
46. Niemz, P. *et al.* Full-waveform-based characterization of acoustic emission activity in a mine-scale experiment: a comparison of conventional and advanced hydraulic fracturing schemes. *Geophys. J. Int.* **222**, 189–206. https://doi.org/10.1093/gji/ggaa127 (2020).
47. Horne, R. N. *Modern well test analysis: a computer-aided Approach* 2nd edn. (Petroway Inc, Palo Alto, 1995).
48. Zimmermann, G., Zang, A., Stephansson, O., Klee, G. & Semiková, H. Permeability enhancement and fracture development of hydraulic in situ experiments in the Äspö Hard Rock Laboratory, Sweden. *Rock Mech. Rock Eng.* **52**, 495–515. https://doi.org/10.1007/s00603-018-1499-9 (2019).
49. Zhuang, L. *et al.* Cyclic hydraulic fracturing of pocheon granite cores and its impact on breakdown pressure, acoustic emission amplitudes and injectivity. *Int. J. Rock Mech. Min. Sci.* **122**, 104065. https://doi.org/10.1016/j.ijrmms.2019.104065 (2019).
50. Zhuang, L. *et al.* Laboratory true triaxial hydraulic fracturing of granite under six fluid injection schemes and grain-scale fracture observations. *Rock Mech. Rock Eng.* **53**, 4329–4344. https://doi.org/10.1007/s00603-020-02170-8 (2020).
51. Park, S. *et al.* Observations and analyses of the first two hydraulic stimulations in the Pohang geothermal development site, South Korea. *Geothermics* **88**, 101905. https://doi.org/10.1016/j.geothermics.2020.101905 (2020).
52. Zang, A., von Specht, S., Niemz, P., Stephansson, O. & Zimmermann, G. Fatigue hydraulic fracturing: Concept and application in hard rock. In *Rock Mechanics for Natural Resources and Infrastructure Development-Full Papers: Proceedings of the 14th International Congress on Rock Mechanics and Rock Engineering (ISRM 2019), September 13–18, 2019, Foz Do Iguassu, Brazil*, 3019–3026 (CRC Press, 2019).
53. Patel, S. M., Sondergeld, C. H. & Rai, C. S. Laboratory studies of hydraulic fracturing by cyclic injection. *Int. J. Rock Mech. Min. Sci.* **95**, 8–15. https://doi.org/10.1016/j.ijrmms.2017.03.008 (2017).
54. Noël, C., Passelègue, F. X., Giorgetti, C. & Violay, M. Fault reactivation during fluid pressure oscillations: Transition from stable to unstable slip. *J. Geophys. Res. Solid Earth* **124**, 10940–10953. https://doi.org/10.1029/2019JB018517 (2019).
55. Tariq, Z., Mahmoud, M., Abdulraheem, A., Al-Shehri, D. & Murtaza, M. An environment friendly approach to reduce the breakdown pressure of high strength unconventional rocks by cyclic hydraulic fracturing. *J. Energy Resour. Technol.* **142**, 2020. https://doi.org/10.1115/1.4045317 (2020).
56. Kang, H. *et al.* Cyclic injection to enhance hydraulic fracturing efficiency: insights from laboratory experiments. *Geofluids* **2020**, 8844293. https://doi.org/10.1155/2020/8844293 (2020).
57. Gutenberg, B. & Richter, C. F. Frequency of earthquakes in California. *Bull. seism. Soc. Am.* **34**, 185–188 (1944).
58. Ishida, T. *et al.* Acoustic emission monitoring of hydraulic fracturing laboratory experiment with supercritical and liquid CO_2. *Geophys. Res. Lett.* **39**(16), 1–6 (2012).
59. Chen, Y., Nagaya, Y. & Ishida, T. Observations of fractures induced by hydraulic fracturing in anisotropic granite. *Rock Mech. Rock Eng.* **48**, 1455–1461 (2015).
60. Chitrala, Y., Sondergeld, C., Rai, C. Acoustic emission studies of hydraulic fracture evolution using different fluid viscosities. The 46th US rock mechanics/geomechanics symposium. Chicago, 24–27 June, ARMA 12-597 (2012).
61. Fallahzadeh, S. H., Hossain, M., Cornwell, A. & Rasouli, V. Near wellbore hydraulic fracture propagation from perforations in tight rocks: the roles of fracturing fluid viscosity and injection rate. *Energies* **10**, 359. https://doi.org/10.3390/en10030359 (2017).
62. Ishida, T. *et al.* Features of CO_2 fracturing deduced from acoustic emission and microscopy in laboratory experiments. *J. Geophys. Res. Solid Earth* **121**, 8080–8098 (2016).
63. Jung, S.G., Diaz, M., Zhuang, L., Kim, K.Y., Shin, H.S., Jung, J.H. Influence of injection rate and viscosity on hydraulic fracturing behaviour of granite. The 9th Asian Rock Mechanics Symposium, October 18–20, Bali (2016).
64. Detournay, E. Propagation regimes of fluid-driven fractures in impermeable rocks. *Int. J. Geomech.* **4**(1), 1–11 (2004).

65. Inamdar, A. *et al.* Evaluation of stimulation techniques using microseismic mapping in the Eagle Ford shale. In *Tight Gas Completions Conference*. https://doi.org/10.2118/136873-MS (Society of Petroleum Engineers, 2010).
66. Zhou, Z.-L. *et al.* A laboratory study of multiple fracture initiation from perforation clusters by cyclic pumping. *Rock Mech. Rock Eng.* **52**, 827–840. https://doi.org/10.1007/s00603-018-1636-5 (2019).
67. Kwiatek, G. *et al.* Controlling fluid-induced seismicity during a 6.1-km-deep geothermal stimulation in Finland. *Sci. Adv.* **5**, eaav7224. https://doi.org/10.1126/sciadv.aav7224 (2019).
68. Galis, M., Ampuero, J. P., Mai, P. M. & Cappa, F. Induced seismicity provides insight into why earthquake ruptures stop. *Sci. Adv.* **3**, eaap7528. https://doi.org/10.1126/sciadv.aap7528 (2017).

Acknowledgements
This work was supported by funding received from the European Union's Horizon 2020 research and innovation programme, grant agreement No. 691728 (DESTRESS). HH kindly acknowledges the financial support of the Helmholtz Association's Initiative and Networking Fund for the Helmholtz Young Investigator Group ARES (contract number VH-NG-1516). Additionally, three anonymous reviewers provided valuable comments that improved the overall quality of this manuscript.

Author contributions
A.Z. wrote the first draft of this manuscript and was principal investigator of the 2015 mine-scale Äspö HRL underground experiments. G.Z. and H.H. served as principal investigators of the 2017 cyclic-injection field-scale tests. H.H. drafted the field-test description for the revision, and P.N. computed energy- and *b*-values in the supplementary material. K.Y.K., M.D., and L.Z. conducted the fluid-injection (true-)triaxial laboratory tests and the subsequent X-ray CT analysis. All authors reviewed the manuscript.

Funding
Open Access funding enabled and organized by Projekt DEAL.

Competing interests
The authors declare no competing interests.

Additional information
Supplementary Information The online version contains supplementary material available at https://doi.org/10.1038/s41598-021-86094-5.

Correspondence and requests for materials should be addressed to A.Z.

Reprints and permissions information is available at www.nature.com/reprints.

Publisher's note Springer Nature remains neutral with regard to jurisdictional claims in published maps and institutional affiliations.

Supplementary material for the article:
Relaxation damage control via fatigue-hydraulic fracturing in granitic rock as inferred from laboratory-, mine- and field-scale experiments

Arno Zang[1,2*], Günter Zimmermann[1], Hannes Hofmann[1], Peter Niemz[1,2], Kwang Yeom Kim[3], Melvin Diaz[3], Li Zhuang[4], Jeoung Seok Yoon[5]

[1]German Research Centre for Geosciences GFZ, Telegrafenberg, 14473 Potsdam, Germany
[2]Institute of Geosciences, University of Potsdam, 14469 Potsdam, Germany
[3]Korea Maritime and Ocean University, Busan, Republic of Korea
[4]Korea Institute of Civil Engineering and Building Technology, Goyang, Republic of Korea
[5]DynaFrax UG (limited), Helmholtzstr. 6, 14467 Potsdam, Germany

[*]Corresponding author: Arno Zang (zang@gfz-potsdam.de; +49 331 2881325); GFZ Section 2.6 Seismic Hazard and Risk Dynamics

This file contains:

- Supplementary methods: fracture-mechanics formulation of hydraulic fatigue
- Energy partition of hydraulic fracturing in granitic rock across scales
- Analysis of seismic *b*-value, additional fluid-injection experiments, normalised breakdown pressure and microscopic inspection of rock chips
- Supplementary Figures S1 to S7
- Supplementary Table S8

Supplementary methods

Fracture-mechanics formulation of hydraulic fatigue

The characteristic difference between conventional hydraulic fracturing with continuous pumping and a single flow rate on the one hand and fatigue hydraulic fracturing engineered by cyclic and pulse pressurisation with multiple flow rates on the other hand lies in the formation of the fracture-process zone. A synoptic picture of the process zone in hydraulic fatigue as compared with monotonic injection in conventional hydraulic fracturing is provided by Zang et al.[1] (see Figure S1). The key component of the process-zone development in hydraulic fatigue is the relaxation of crack-tip stresses. Relaxation damage is controlled (a) by frequent phases of pressurisation and depressurisation, for example, by cyclic fluid injection, and (b) by pulse-pressure oscillations that are superimposed using a second pump[2]. In contrast to the Kiel process[3], secondary-pump oscillations efficiently generate rock chips from the fracture walls (natural proppants). In line with the Kiel process, the proppants are transported to the crack tip and change the stress field locally. The fatigue-fracture process zone is enlarged by multiple branching fractures (Fig. S1, FHF). Its size and individual micro-fracturing sources are different from classical fracture mechanics (Fig. S1, HF).

Rinne et al.[4] created a fracture-mechanics representation of mechanical fatigue (their Figs. 2.8 and 2.9). In Figure S2, we schematically modified these figures for the case of hydraulic fatigue. First, the sinusoidal excitation in mechanical fatigue (Fig. S2a, *black curve*) shows relatively higher values of the stress-intensity factor K compared with the sinusoidal excitation in hydraulic fatigue (Fig. S2a, *blue curve*) because K depends on the degree of saturation. Moreover, the difference between the maximum and minimum stress-intensity factor ΔK is different in both scenarios. Second, in Figure S2b, the increment in fracture length per loading cycle (da/dN) is displayed in a double-logarithmic plot, where ΔK_{th} is the stress-intensity-factor difference below which no crack growth occurs. Critical crack growth in fatigue begins at a threshold value referred to as the critical stress-intensity-factor difference, or ΔK_{IC}. In Figure S2b, three phases of crack propagation are distinguished: I = decelaration, II = stationary, and III = acceleration. Crack growth can be described by the *Donahne law* in Phase I, by the *Paris-Erdogan law* in Phase II, and by the *Forman law* in Phase III[4]. Unified Eq. (1) – the so-called *Erdogan-Ratwani law* – covers all three phases of crack

propagation in mechanical-fatigue tests with three material constants: *c*, *m*, and *n*.

$$\frac{da}{dN} = \frac{C(1+\beta)^m \cdot (\Delta K - \Delta K_{th})^n}{K_C - (1+\beta)\cdot \Delta K}; \ \beta = \frac{K_{max} + K_{min}}{K_{max} - K_{min}} \quad (1)$$

This concept of mechanical fatigue can be translated into the new concept of hydraulic fatigue. In so doing, stress-intensity factors from dry rock are replaced by stress-intensity factors of saturated rock. Second, mechanical loading cycles (*N*) are replaced by pressure cycles (*Np*) in the *Erdogan-Ratwani law*. Eq. (2) respresents the hydraulic-fatigue equivalent to eq. (1) and is introduced as *Erdogan-Ratwani-Zang* law.

$$\frac{da}{dNp} = \frac{C(1+\beta)^m \cdot (\Delta K_{wet} - \Delta K_{th,wet})^n}{K_{C,wet} - (1+\beta)\cdot \Delta K_{wet}} \quad (2)$$

Energy partition of hydraulic fracturing in granitic rock across scales

Hypothesis. In the conventional hydraulic-fracturing test, the injection pressure is increased monotonically until fracture breakdown occurs (single flow-rate test). As a consequence, the hydraulic energy pumped into the rock mass is an end-member maximum value that is much larger than the dissipated fracture- and friction energy, the plastic energy, and the radiated seismic energy. In hydraulic fatigue (variable flow rates), the crack-tip stresses are relaxed multiple times, and a different energy balance follows that is characterised by a total hydraulic energy input that is comparable to the dissipated energy from fracturing-, friction-, plastic-, and radiated seismic energy. As a result, variable flow-rate tests allow multiple branching fractures to be formed ahead of the fatigue-fracture tip and leave behind a broader damage-zone fracture network that also makes a difference in permeability enhancement as compared with conventional fracturing. Hydraulic fatigue is an optimised energy-conversion process. A significant portion of the hydraulic energy is converted into damage and fracturing of the rock mass using pressure cycles and pulses. Since energy dissipation and damage evolution are both stress-path-dependent, so too is fatigue hydraulic fracturing.

Energy computation. To quantify the energy-partition process, we isolated deformation energy and hydraulic energy on the input side of the energy equation and isolated the fracture energy, radiated seismic energy, and dissipated energy on the consumption side. Table S8 lists all parameters introduced in the following sections as well as energy estimates in all three scales. The following assumptions and equations were used to compute individual energy terms.

Deformation (strain) energy

The deformation (strain) energy (E_{Def}) within a finite rock volume (V) that was subjected to three effective principal stresses ($\sigma_1' > \sigma_2' > \sigma_3'$; principal stress minus formation pressure, here assumed to be hydrostatic) was calculated by

$$E_{def} = \sum_{i=\sigma_1'}^{\sigma_3'} \frac{V}{2E} i^2, \quad (3)$$

with E being the rock Young's modulus. At the laboratory scale, the volume corresponded to the sample size. At the mine- and field scales, the rock volume was chosen based on the scatter of AE and seismic sources, thereby providing a rough estimate of the activated/stimulated volume.

Fracture (surface) energy

The energy required to open a pure tensile fracture (*Mode I*) in intact rock (E_{Frac}) was calculated using the total rupture (fracture) area (A_r) and the energy-release rate (G_{IC}):

$$E_{Frac} = G_{IC} A_r, \quad (4)$$

with

$$G_{IC} = \frac{(1-\upsilon^2)K_{IC}^2}{E}, \quad (5)$$

where K_{IC} is the stress-intensity factor for *Mode-I* fractures and υ is the rock Poisson's ratio. Eq. (5) is valid for plane-strain conditions. To account for variabilities in K_{IC}, we used upper- and lower-bound values of 1.05 and 1.58 MPa $m^{1/2}$, respectively, from minimum and maximum mean values determined via three-point bending tests on Pocheon granite[5]. Values of K_{IC} were used for energy computations throughout all scales. Ambient K_{IC} values were corrected for confining stress conditions[6]:

$$K_{IC\_corr} = K_{IC(0.1MPa)}(1 + 0.037\sigma_3'). \quad (6)$$

The corrected value of the stress-intensity factor was used in Eq. (5) to calculate the energy-release rate (G_{IC}). We estimated the fracture area (A_{r_lab}) using the laboratory tests of Zhuang et al.[4]. In so doing, we used the hydraulic-fracture half-length (L_f) and the length (h) of the open-hole section of the injection borehole (70 mm) as the fracture-height upper bound:

$$A_{r\_lab} = 2L_f h. \quad (7)$$

In the mine-scale experiment, the fracture-surface area was inferred from the extension of the acoustic-emission cloud[7]. In the field scale, we used the cumulative fracture area of all seismic events from Hofmann et al.[8], which was based on the empirical scaling relation between moment magnitude (*Mw*) and the rupture area from Wells and Coppersmith[9]:

$$A_{r\_field} = 10^{\frac{Mw-3.49\pm0.16}{0.91\pm0.03}}. \quad (8)$$

As for K_{IC}, we set upper- and lower-bound values for the fracture areas (Table S8).

Hydraulic energy

The hydraulic energy (E_{Hydr}) resulting from an injection during time t with downhole pressure P and volume-flow rate $\dot{V}$ was calculated according to Goodfellow et al.[10]:

$$E_{Hydr} = \int_0^t P\dot{V}dt. \quad (9)$$

Radiated seismic energy

Following Hanks and Kanamori[11], the radiated seismic energy E_{Seis} was calculated by

$$E_{Seis} = \frac{\Delta\sigma m_0}{2\mu}, \quad (10)$$

with stress drop $\Delta\sigma$, shear modulus μ, and scalar seismic moment m_0, assuming earthquake self-similarity. Kwiatek et al.[12] demonstrated that this assumption is reasonable for the Äspö experiment. Stress drop is commonly assumed to be between 1 and 10 MPa[13], but 0.1 MPa has also been reported[14]. In this study, we estimated E_{Seis} with a lower-bound stress drop of 0.1 MPa and an upper-bound stress drop of 1 MPa. The rock's shear modulus (μ) was calculated using Young's modulus and the Poisson ratio (Table S8). Using the definition of moment magnitude (M_w) for m_0 in Nm[13], we calculated the scalar seismic moment:

$$m_0 = 10^{1.5M_w+9.1}. \quad (11)$$

For Äspö mine-scale experiments, we applied a magnitude scaling that assumed a linear relationship between the relative magnitude (M_{AE}) used in the extended-event catalogue[7] and M_w as calculated for a subset of larger events[12]. A best-fitting linear regression for M_w- and M_{AE} estimates of 195 events contained in both catalogues was calculated using the RANSAC algorithm[15].

At the laboratory-test scale, we calibrated the AE sensors via ball-drop experiments. Small steel spheres (diameter: 1 mm and 2 mm) were dropped onto a granite block from a pre-defined height of 100–200 mm with same AE-sensor setup and sensitivity as was used in the true triaxial experiments. In this manner, we were able to directly relate the AE amplitude provided by the AE recording- and analysis system (MITRAS) to the potential energy resulting from the impact of the sphere. Subsequently, we applied the log-amplitude–log-energy relation from the ball-drop calibration experiment to the event amplitudes from the true triaxial-deformation experiments.

Dissipated energy

The dissipated energy (E_{Diss}) was calculated via Eq. (2) in the main text:

$$E_{Diss} = E_{Hydr} + E_{Def} - E_{Frac} - E_{Seis}. \quad (12)$$

Analysis of seismic *b*-value, additional fluid-injection experiments, normalised breakdown pressure and microscopic inspection of rock chips

Hypothesis. The mechanism leading to a reduction in event magnitude by cyclic injection was hypothesised to be the development of a larger number of smaller events compared with fewer large events caused by continuous injection. One reason for this development was the division of the injected hydraulic energy into smaller parts, which was expected to lead to a division of the radiated seismic energy.

Computation of b-values. For all scales, we consistently estimated the Gutenberg–Richter *b*-values[16] using a maximum-likelihood approach corrected for measurement errors and magnitude binning[17,18]:

$$b = \frac{1}{\ln(10)\Delta M}\ln(p), \quad (13)$$

with

$$p = 1 + \frac{\Delta M}{\hat{\mu} - M_c}, \quad (14)$$

magnitude of completeness M_c, bin size ΔM and mean magnitude $\hat{\mu}$. M_c was determined independently by applying a bootstrap-based change-point detection method[19].

References

1. Zang, A. *et al.* How to reduce fluid-Injection-induced seismicity. *Rock Mech. Rock Eng.* **52**, 475–493, DOI: 10.1007/ s00603-018-1467-4 (2019).
2. Zang, A. *et al.* Hydraulic fracture monitoring in hard rock at 410 m depth with an advanced fluid-injection protocol and extensive sensor array. *Geophys. J. Int.* **208**, 790–813, DOI: 10.1093/gji/ggw430 (2017).
3. Kiel, O. M. The Kiel process - reservoir stimulation by dendritic fracturing. Tech. Rep., Society of Petroleum Engineers (1977).
4. Rinne, M., Stephansson, O., Shen, B. & Konietzky, H. Introduction to the theories of rock fracturing. In *Modelling Rock Fracturing Processes*, 7–24 (Springer, 2020).
5. Zhuang, L. *et al.* Laboratory true triaxial hydraulic fracturing of granite under six fluid injection schemes and grain-scale fracture observations. *Rock Mech. Rock Eng.* DOI: 10.1007/s00603-020-02170-8 (2020).
6. Müller, W. Brittle crack growth in rocks. *Pure and Applied Geophysics* **124**, 693–709, DOI: 10.1007/BF00879605 (1986).
7. Niemz, P. *et al.* Full-waveform-based characterization of acoustic emission activity in a mine-scale experiment: A comparison of conventional and advanced hydraulic fracturing schemes. *Geophys. J. Int.* **222**, 189–206, DOI: 10.1093/gji/ ggaa127 (2020).
8. Hofmann, H. *et al.* First field application of cyclic soft stimulation at the Pohang Enhanced Geothermal System site in Korea. *Geophys. J. Int.* **217**, 926–949, DOI: 10.1093/gji/ggz058 (2019).
9. Wells, D. L. & Coppersmith, K. J. New empirical relationships among magnitude, rupture length, rupture width, rupture area, and surface displacement. *Bull. Seismol. Soc. Am.* **84**, 974–1002 (1994).
10. Goodfellow, S. D., Nasseri, M. H. B., Maxwell, S. C. & Young, R. P. Hydraulic fracture energy budget: Insights from the laboratory. *Geophys. Res. Lett.* **42**, 3179–3187, DOI: 10.1002/2015GL063093@10.1002/(ISSN)1944-8007.FRACKING (2016).
11. Hanks, T. C. & Kanamori, H. A moment magnitude scale. *J. Geophys. Res. Solid Earth* **84**, 2348–2350, DOI: 10.1029/ JB084iB05p02348 (1979).
12. Kwiatek, G. *et al.* Insights into complex subdecimeter fracturing processes occurring during a water injection experiment at depth in Äspö Hard Rock Laboratory, Sweden. *J. Geophys. Res. Solid Earth* **123**, 6616–6635, DOI: 10.1029/2017JB014715 (2018).
13. Kanamori, H. & Brodsky, E. E. The physics of earthquakes. *Reports on Prog. Phys.* **67**, 1429–1496, DOI: 10.1088/ 0034-4885/67/8/R03 (2004).
14. Collins, D. S. & Young, R. P. Lithological controls on seismicity in granitic rocks. *Bull. Seismol. Soc. Am.* **90**, 709–723, DOI: 10.1785/0119990142 (2000).
15. Fischler, M. A. & Bolles, R. C. Random sample consensus: A paradigm for model fitting with applications to image analysis and automated cartography. *Commun. ACM* **24**, 381–395, DOI: 10.1145/358669.358692 (1981).

16. Gutenberg, B. & Richter, C. F. Frequency of earthquakes in California. *Bull. Seismol. Soc. Am.* **34**, 185–188 (1944).

17. Tinti, S. & Mulargia, F. Confidence intervals of b values for grouped magnitudes. *Bull. Seismol. Soc. Am.* **77**, 2125–2134 (1987).

18. Marzocchi, W. & Sandri, L. A review and new insights on the estimation of the b-value and its uncertainty. *Annals Geophys.* **46**, 1271–1282, DOI: 10.4401/ag-3472 (2009).

19. Amorèse, D. Applying a change-point detection method on frequency-magnitude distributions. *Bull. Seismol. Soc. Am.* **97**, 1742–1749, DOI: 10.1785/0120060181 (2007).

20. Stille, H. & Olsson, P. Summary of rock mechanical results from the construction of Äspö Hard Rock Laboratory. *Stock. SKB Prog. Rep. HRL-96-07* (1996).

21. Kwon, S. *et al.* Characterization of 4.2-km-deep fractured granodiorite cores from Pohang geothermal reservoir, Korea. *Rock Mech. Rock Eng.* **52**, 771–782, DOI: 10.1007/s00603-018-1639-2 (2019).

Supplementary Figures

Figure S1. The process zone in hydraulic fatigue.

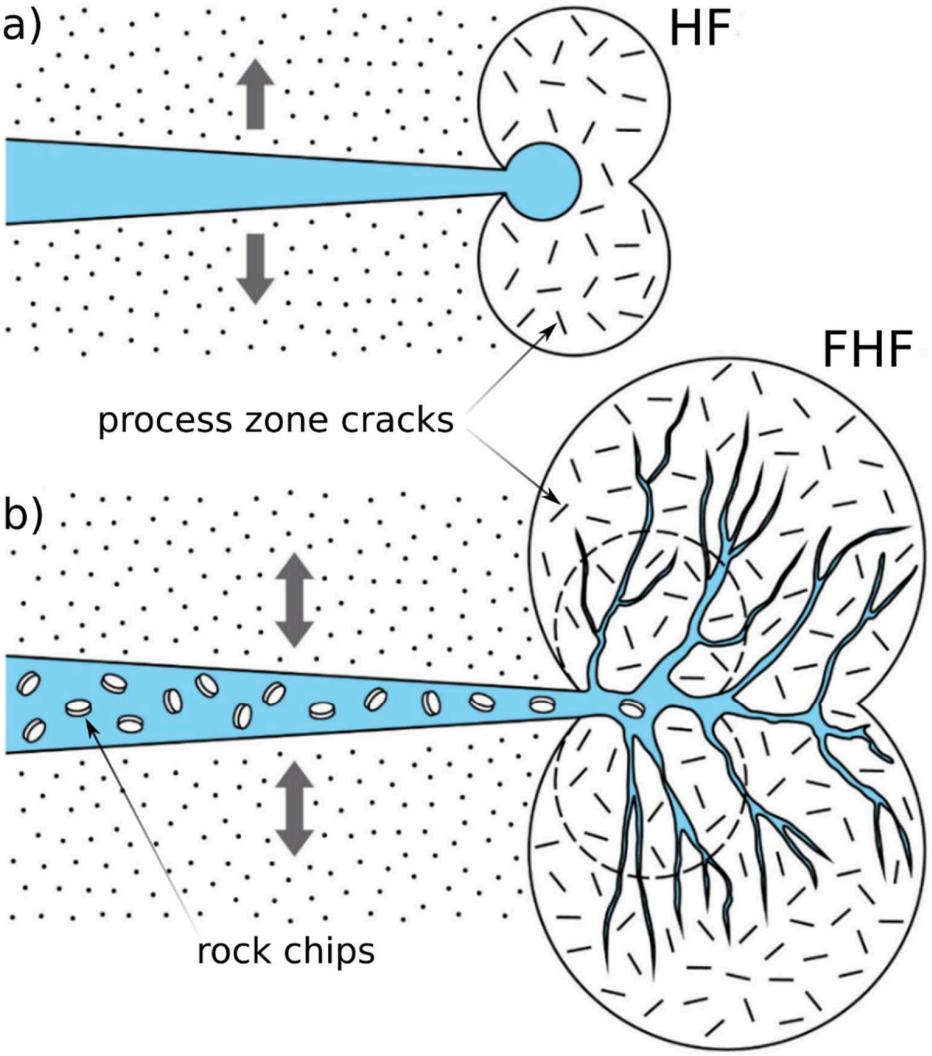

Figure S1. Fracture-mechanics approach to hydraulic fatigue. Synoptic picture of a fracture process zone developing in (**a**) conventional hydraulic fracturing with continuous fluid injection and a kidney-shaped Mode-I secondary-cracking area at the crack tip and (**b**) fatigue hydraulic fracturing with progressive and dynamic pulse pressurisation resulting in a larger process zone due to frequent lowering of crack-tip stresses (modified from Zang et al.[1]). In (**b**), the transport of fracture-wall material (*rock disks* = natural proppants) towards the crack tip allows the local stress field to change and multiple branching fractures to develop, thereby forming an enlarged damage zone.

Figure S2. Crack growth rate in hydraulic fatigue.

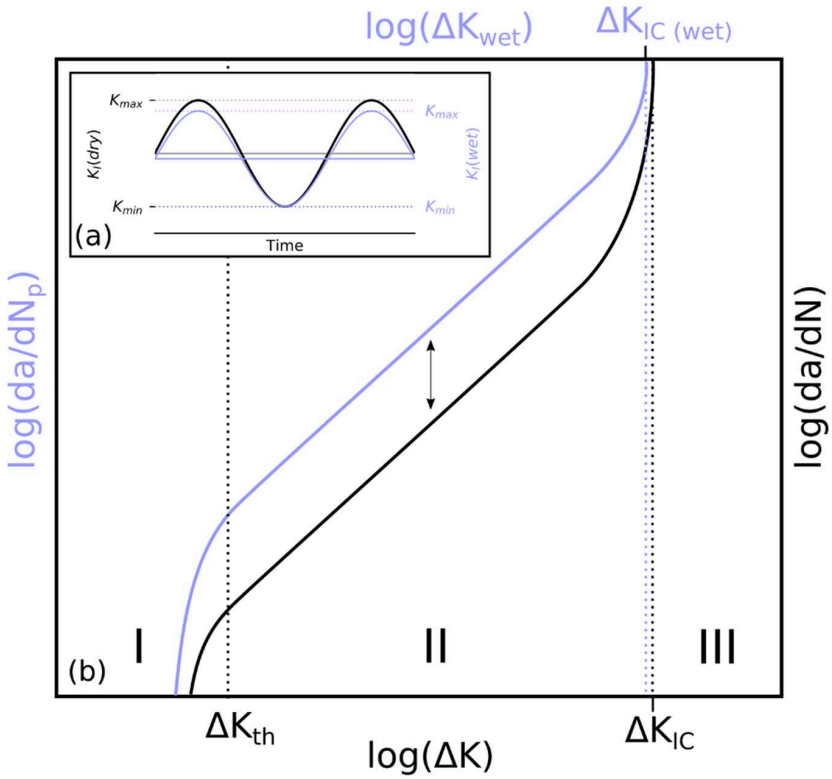

Figure S2. Fracture-mechanics formulation of mechanical fatigue (*black* curves) and hydraulic fatigue (*blue* curves). In (**a**), sinusoidal excitation of the stress-intensity factor (K) against time is shown for mechanical cycles (*black*) and hydraulic cycles (*blue*) with presumably lower stress-intensity factors. In (**b**), growth of fracture length per cycle (da/dN) is displayed against stress-intensity factor (ΔK) in a double-logarithmic plot. In the hydraulic-fatigue process, a fracture-growth rate is indicated that is higher compared with that in mechanical fatigue (**b**, *arrow*).

Figure S3. Seismic b-value determination in geothermal-injection tests across scales.

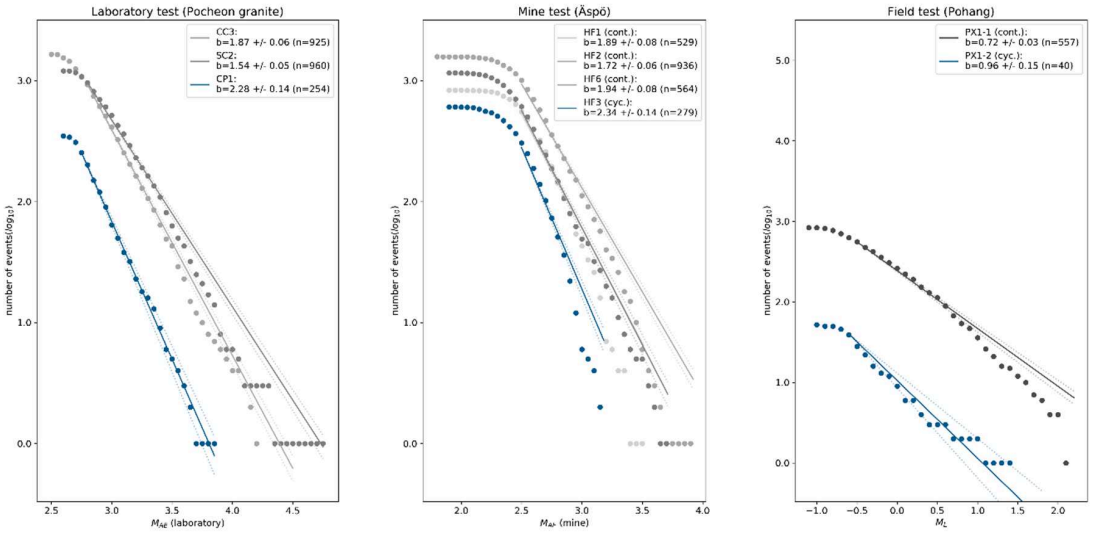

Figure S3. Seismic *b*-values determined via an analysis of acoustic-emission events in granitic rock at (**a**) laboratory scale and (**b**) mine scale in in-situ hydraulic-fracturing experiments. At field scale (**c**), micro-seismic events were used to compute magnitude-frequency distributions. The range of y-axis in (**c**) is adjusted to keep the ratio 1:1 (x:y) in all scales. Cyclic injection in *blue*; conventional, continuous injection experiments in *grey/black*.

Figure S4. Additional laboratory pressure-controlled fracturing tests on Pocheon granite.

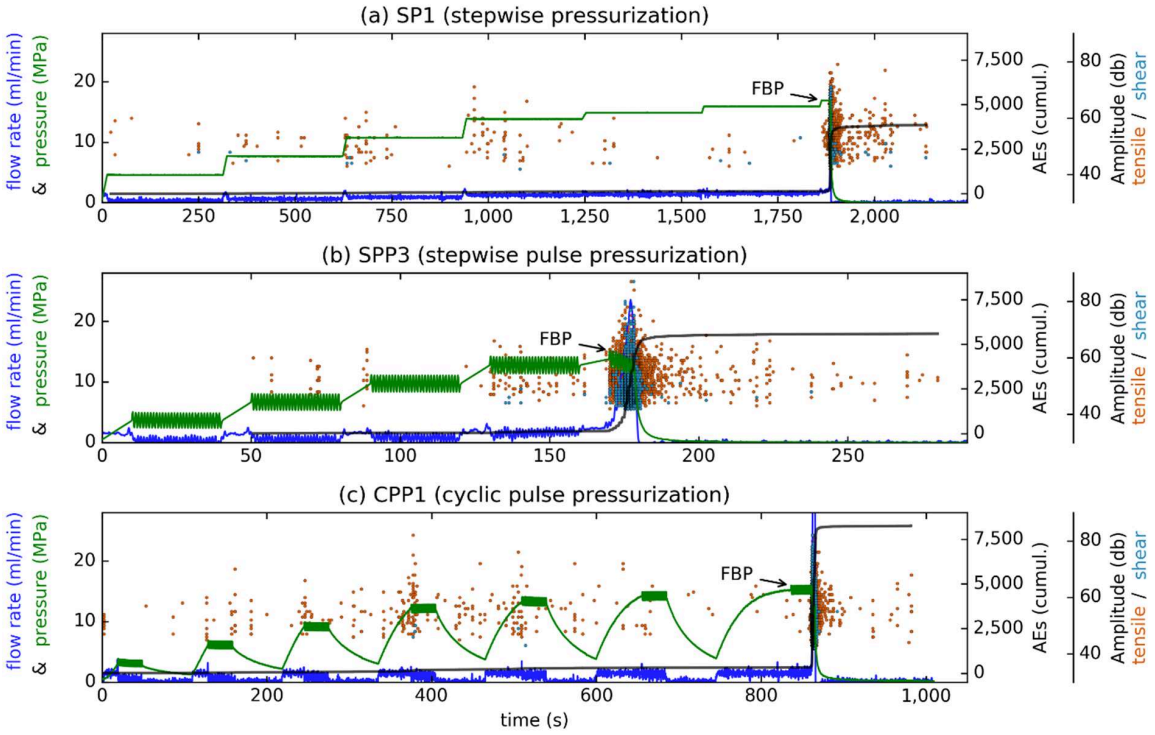

Figure S4 Laboratory hydraulic-fracturing results on true triaxially stressed Pocheon granite cubes under pressure control. (**a**) Stepwise (SP1), (**b**) stepwise-progressive (SPP3), and (**c**) cyclic-progressive pulse pressurisation (CPP1). *Red dots* indicate induced AE tensile failure; *light-blue dots* indicate induced AE shear failure.

Figure S5. Additional mine hydraulic fracturing tests in two different rock types.

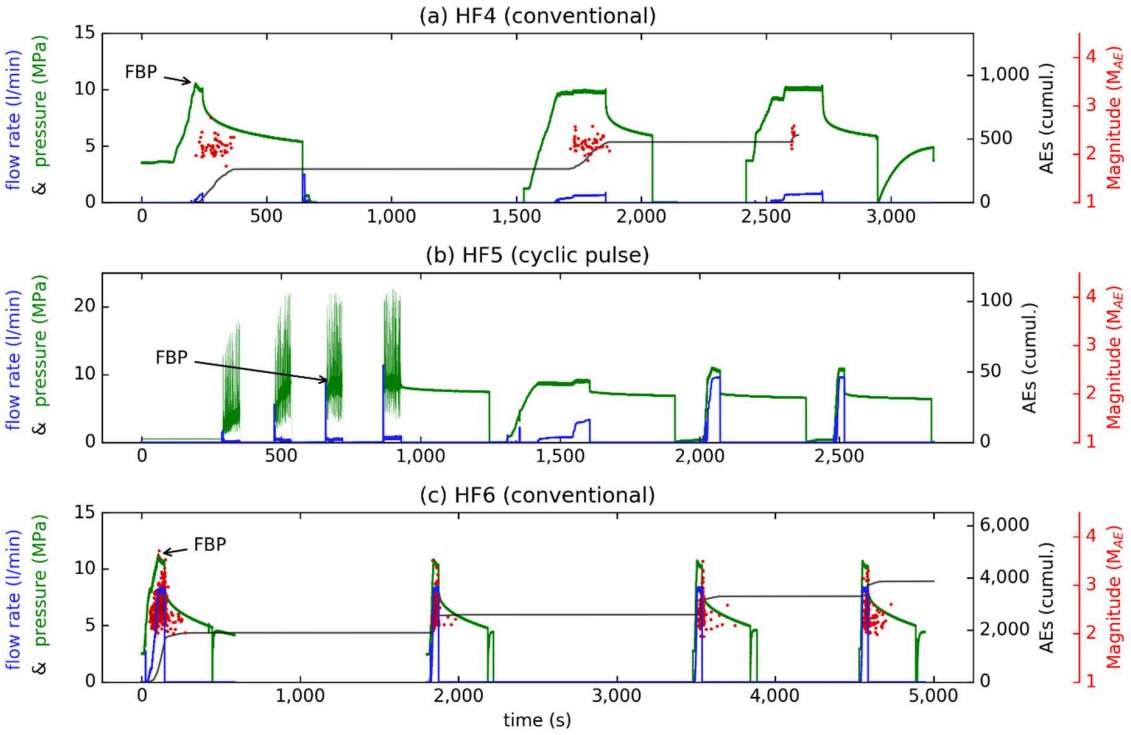

Figure S5 Mine hydraulic-fracturing results in two additional rock types. (**a**) Conventional fracturing in test HF4 and (**b**) cyclic-pulse fracturing in test HF5 with hydraulic hammer, both performed in fine-grained diorite-gabbro. (**c**) Conventional hydraulic fracturing (HF6) in fine-grained granite at six meter distance from tunnel wall.

Figure S6. Breakdown pressure versus injection cycles in laboratory and mine tests

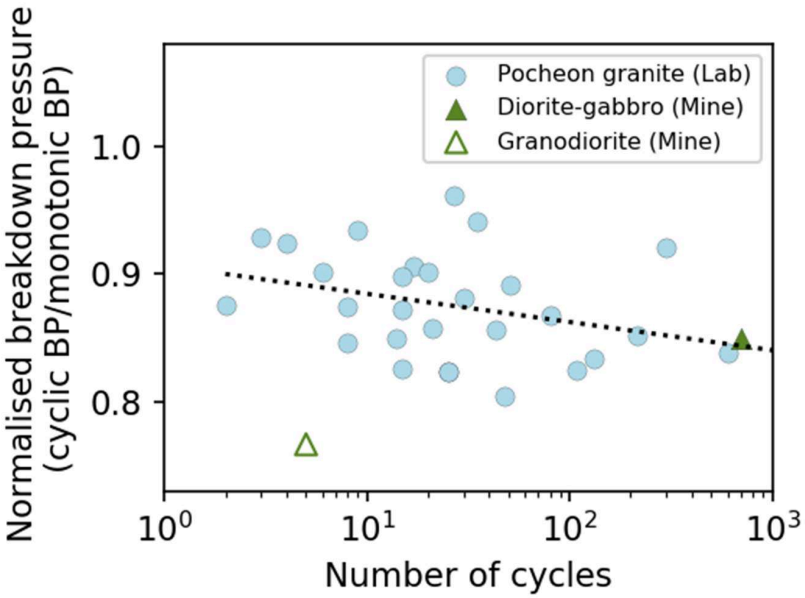

Figure S6 Cyclic breakdown pressure normalized to average conventional breakdown pressure as a function of log number injection cycles. *Dots* indicate laboratory tests on Pocheon granite. *Triangles* indicate mine tests. The 5-cycle fatigue test is performed in granodiorite (HF3), and the 700 cycles fatigue test with hydraulic hammer is performed in diorite gabbro (HF5).

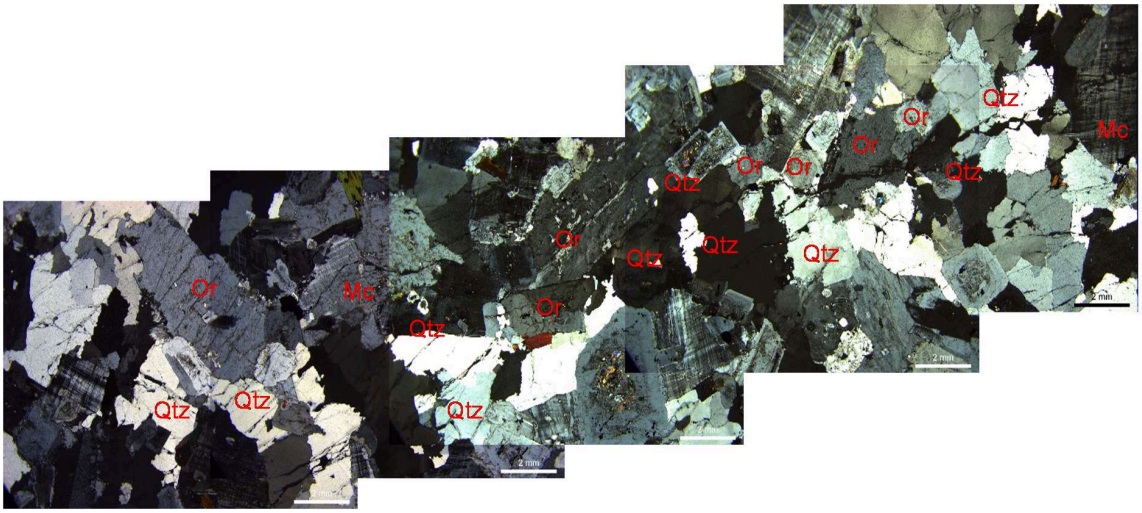

(a)

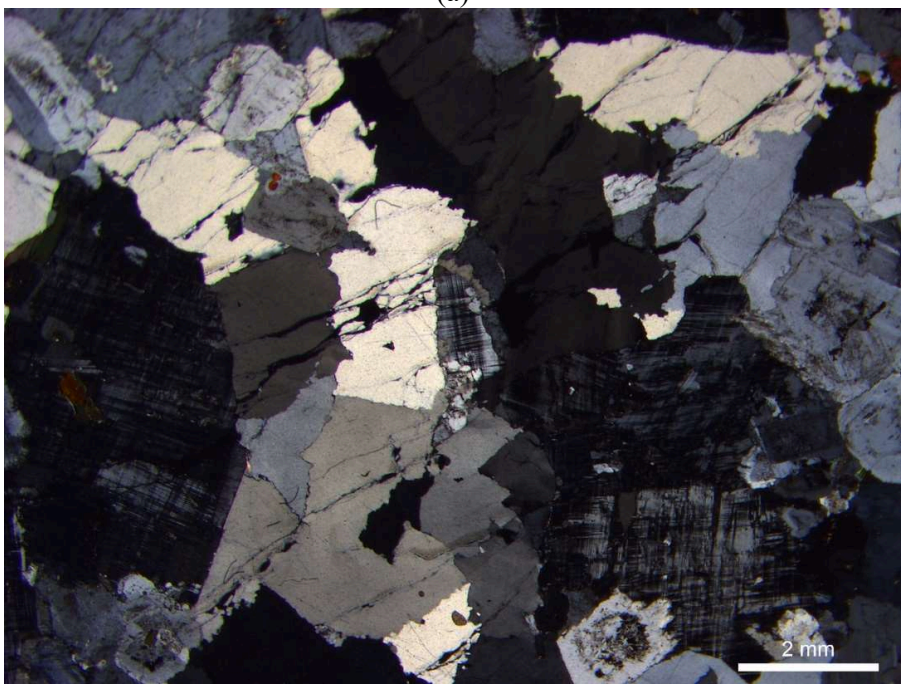

(b)

Figure S7. Fracture inspection after laboratory stepwise pulse pressurization test on Pocheon granite. (**a**) Microscopic photo collage with mineral identification along the hydraulic fracture path (borehole wall to the right). Mc-Microcline, Or-Orthoclase, Qtz-Quartz. (**b**) Selected enlarged section showing quartz fragments in hydraulic fractures. Scale bar is 2 mm in individual photographs.

Table S8. Full set of data used for computing energy terms of conventional and fatigue hydraulic fracturing across three scales: laboratory-, mine-, and field tests in granitic rock mass. Upper and lower bound values are given in brackets.

	True triaxial laboratory test (Pocheon granite)	Mine test (Äspö HRL,)	Field test (Pohang EGS)
Dimension [m]	0.1 x 0.1 x 0.1[5]	10 x10 x 3 (single experiment)	1000 x 500 x 500
Depth [m]	100*	410[2]	4200[8]
Principal stresses (σ_1, σ_2, σ_3) [MPa]	6, 4, 3 [5]	22, 12, 11 [2]	139, 110, 82 [8]
Young's modulus E [GPa]	58 [5]	60[20]	33 [8]
E_{Def} [J]	0.5	1.1e+06	59.56e+12
Poisson ratio υ	[0.25, 0.31][5]	0.25[20]	0.21 [21]
G_{IC} (corrected) [MPa m$^{0.5}$]	[21, 53]	[34, 77]	[512, 1159]
Fracture area [m^2]	CC: 0.00448 SC: 0.00448 CP: 0.00225	HF1: [37.0, 40.4][7] HF2: [41.0, 49.6][7] HF3: [28.4, 30.0][7] HF6: [36.3, 57.3][7]	Cont.: [37877,68882] Cyc.: [231728, 407174]
E_{Frac} [J]	CC: [0.09,0.24] SC: [0.09,0.24] CP: [0.05, 0.12]	HF1: [1.26e+03, 3.12e+03] HF2: [1.40e+03, 3.83e+03] HF3: [9.69e+02, 1.33e+03] HF6: [1.24e+03, 4.44e+03]	Cont: [1.94e+07, 7.98e+07] Cyc.: [1.19e+08, 4.72e+08]
E_{Hyd} [J]	CC: 61.8 SC: 157.4 CP: 157.3	HF1: 233.5e+03 HF2: 277.4e+03 HF3: 249.7e+03 HF6: 248.0e+03	Cont: 91.0e+09 Cyc.: 28.5e+09
Stress drop [MPa]	-	[0.1,1]	[0.1,1]
Shear modulus [GPa]	-	24	14
E_{Seis} [J]	CC: [9.563e-05, 1.759e-03] SC: [8.423e-05, 1.656e-03] CP: [1.959e-05, 0.351e-03]	HF1: [1.22, 12.23] HF2: [2.33, 23.25] HF3: [0.75, 7.47] HF6: [1.6, 16.0] total: [5.99, 59.9]	Cont.: [3.74e+07, 3.74e+08] Cyc.: [4.22e+06, 4.22e+07]
E_{Diss} [J]	CC:[62.06,62.21] SC:[157.66, 157.81] CP:[157.68,157.75]	HF1: [1.33e+06, 1.33e+06] HF2: [1.37e+06, 1.38e+06] HF3: [1.35e+06, 1.35e+06] HF6: [1.34e+06, 1.35e+06]	Cont.: [5.97e+13, 5.97e+13] Cyc.: [5.96e+13, 5.96e+13]
$\frac{E_{Seis}}{E_{Hydr}}$	CC:[1.547e-06, 2.846e-05] SC:[5.351e-07, 1.052e-05] CP:[1.245e-07, 2.231e-05]	HF1: [6.052e-06, 6.034e-05] HF2: [9.639e-06, 9.653e-05] HF3: [3.440e-06, 3.436e-05] HF6: [7.419e-06, 7.415e-05]	Cont.: [4.110e-04,4.110e-03] Cyc.: [1.481e-04, 1.481e-03]
$\frac{E_{Seis}}{E_{Hydr} + E_{Def}}$	CC:[1.535e-06, 2.823e-05] SC:[5.334e-07, 1.049e-05] CP:[1.241e-07, 2.224e-05]	HF1: [1.058e-06, 1.055e-05] HF2: [1.939e-06, 1.942e-05] HF3: [6.370e-07, 6.363e-06] HF6: [1.365e-06, 1.364e-05]	Cont.: [6.270e-07,6.270e-06] Cyc.: [7.082e-08, 7.082e-07]

*estimated from true triaxial stresses

7 | Discussion

In this chapter, I answer the overarching research questions from Chapter 2 while discussing the aggregated major findings of the publications contained in this cumulative thesis. The general discussion on hydraulic fracture growth as observed during the injection experiments at Äspö HRL (Section 7.1) is followed by a more detailed discussion on processes acting during hydraulic fracturing and how these processes can be studied (Section 7.2). The differences between continuous and cyclic injections regarding fracture geometry and seismic impact are discussed in Section 7.3. In the last part of the discussion (Section 7.4), I introduce preliminary results of relative waveform analyses that help to address outstanding questions regarding fracture interactions and rupture processes during different phases of the injections. The discussion on applied and developed methods is mainly limited to Chapter 3 and the corresponding paragraphs in Chapter 4, Chapter 5, and in the supplement section of Chapter 6.

7.1 Hydraulic fracture growth

The mine-scale experiments at Äspö bridge the gap between two very different scales regarding the fracture extent: a few centimeters in laboratory experiments and several hundreds of meters or a few kilometers in field experiments or commercial injections. While laboratory experiments can depict the fracture evolution in great detail, the realistic reproduction of processes depends on the chosen experimental setup, which mimicks the natural conditions (Qian et al., 2020). In the field-scale, the injections are conducted in natural conditions, but the large depth and increased costs hinder the monitoring. Mine-scale, in-situ experiments combine the advantage of a close monitoring with more appropriate in-situ conditions compared to laboratory tests. The meter-scale experiments at Äspö HRL allowed a detailed study of fracture growth (Publication 1 and 2, Chapter 4 and 5) including processes like post-injection seismic activity, a possible reactivation of a preexisting fault, and the continued growth of the fracture after the stop of the injection (aftergrowth).

Hydraulic fractures are expected to grow into the direction of the maximum principal stress while opening in the direction of the least principal stress, as soon as the fluid pressure inside the injection interval exceeds the fracture breakdown pressure (Zang & Stephansson, 2010). During the mine-scale injection experiments at Äspö HRL, sub-vertical hydraulic fractures were opened, in accordance with the local stress regime, in which the maximum principal stress is sub-vertical. The mapped hydraulic fractures predominately grew upwards away from the injec-

tion interval. While the increasing volume of injected fluids drives the fracture growth after the initial breakdown, stress gradients (Dahm et al., 2010; Fischer et al., 2009), and localized stress heterogeneities, e.g., due to nearby fault and fractures (Wright et al., 1999), might influence the direction and the asymmetry of growth. The predominant upward propagation of the fractures can be explained by vertical stress gradients since the overburden mass and consequently the vertical stress magnitude decreases at lower depths. This holds as long as the minimum horizontal stress is the minimum principal stress (Cornet, 2016). An additional contribution can be attributed to buoyancy effects (e.g., Dahm, 2000), because the injected fluid is less dense than the rock.

Fischer et al. (2009) have shown that local lateral stress gradients can cause an asymmetric growth of hydraulic fractures relative to the injection interval. Their model predicts a dominant fracture growth into the direction of decreasing stress, while the growth in the opposite direction is limited. The influence of lateral stress gradients could explain the location of the fracture planes, which predominately develop at only one side of the injection borehole in the Äspö experiments. Another explanation could be stress shadowing effects in multi-stage fracturing (Wasantha et al., 2019), as conducted within the Äspö experiments.

Asymmetric or unilateral growth was also reported within other recent mine-scale experiments (Schoenball et al., 2020; Villiger et al., 2020) and was attributed to local stress heterogeneities and stress gradients, e.g., due to thermal effects from the adjacent tunnel (Fu et al., 2021; Schoenball et al., 2020). Such influences can be strongly localized. In the Äspö experiments, the stress field was altered by the free surface of the tunnel wall, manifested by switching growth directions for experiment HF6. Even more critical is the alteration of the stress field due to the tunnel wall when considering the dip angle of the approximated fracture planes from the AE analysis (Publication 1, Chapter 4). The dip of the fracture planes decreases with the distance from the vertical tunnel wall. Such free surface effects were also described in hydraulic fracturing experiments in rock salt (Manthei, Eisenblätter, & Dahm, 2001). Contrary to the dip angle, the strike direction of the mapped hydraulic fractures is not significantly influenced by the tunnel since the injection borehole was drilled sub-parallel to the direction of the least principal stress, while the tunnel is oriented approximately perpendicular to the direction of the least principal stress.

In the early stages of the experiments HF1-HF3, the mapped strike directions of the hydraulic fractures deviate from the expected orientation. However, in later stages the strike directions approaches 120 degrees in accordance with the previously determined local stress direction (Klee & Rummel, 2002; Niemz et al., 2020). Increased uncertainties cannot explain the deviation in the clustering results, which represent the fracture orientation (see uncertainties of strike directions in Table 1 in Chapter 4). Consequently, the deviation from the expected fracture orientation resolves local stress heterogeneities close to the injection borehole, probably caused by the borehole itself. This shows that we are able to map small-scale secondary stress changes that influence the fracture growth in the mine-scale experiments. A similar deflection of the fracture from the orientation expected from the regional stress regime close to the borehole was reported from the EGS Collab experiments (Guglielmi et al., 2021). In this case, the deflection was attributed to the foliation of the rock, providing a weakness where a hydraulic fracture could

initiate.

The fractures predominantly grew during the injections. Thanks to the complementary monitoring setup, I could provide evidence for aftergrowth, the continuing growth of the fracture after the fluid injection stopped. This phase of fracture growth is very important for understanding potential seismic risks since many commercial EGS use traffic light systems, that stop the injection as soon as a given magnitude or peak ground acceleration is reached (,e.g., Baisch et al., 2019). However, pronounced aftergrowth might threaten the reliability of this risk mitigation approach because the fracture might grow further even after the injection stops, but the interval is still under pressure. The fracture could potentially reach and activate preexisting faults, which is the most critical seismic hazard in EGS. In fact, in many EGS, the largest induced event occurred after the end of the injection, e.g., in Pohang (Grigoli et al., 2018) or Basel (Häring et al., 2008). Alternative injection schemes, discussed in Section 7.3, may help to reduce the aftergrowth.

A secondary fracture observed in experiment HF2 might point towards a reactivation of a preexisting fault after the end of the injection. AEs attributed to this secondary fracture were predominately active during the shut-in phases of the late refracturing stages. A similar post-injection reactivation was hypothesized for a large-scale injection at Soultz-sous-Forêt (Cornet, 2016), and at Goeven EGS, close to Strasbourg, France (Schmittbuhl et al., 2021). By considering only the subset of AEs occurring below the borehole during experiment HF2 close to this secondary fracture, I found a reduced b-value, closer to 1, as well as an increase in magnitudes, which supports the activation of a natural fault (Downie et al., 2010; Maxwell et al., 2009). A more detailed analysis of the secondary fracture zone using waveform clustering analyses is described in Chapter 7.4.

7.2 A glimpse on processes observed during hydraulic fracturing

Apart from the extent and the orientation of macro-fracture, the data recorded during the experiments revealed more details on processes accompanying the hydraulic fracture growth. These processes and their manifestation in the data are discussed in this section.

Thanks to the complementary seismic monitoring setup with AE sensors and broadband seismometers, I was able to shed light on different aspects of the hydraulic fracture evolution with information gained independently from both sensor types (Niemz et al., 2020; Niemz et al., 2021). The tilt signals recorded by the seismometers directly depict the opening and closing of hydraulic fractures during and after the fluid injection, which produces a deformation in the surrounding rock volume (light green arrows in Fig. 7.1). In contrast, the AE activity reflects effective stress changes primarily caused by the opening of new hydraulic fractures. AEs (orange stars in Fig. 7.1) are considered an indirect response because AEs are attributed to microcracks in the fracture process zone —at the fracture tip and to a smaller extent around the fracture— activated by the stress change (Zang et al., 2000). The microcracks activated by the AEs are either oriented favorably to slip in the local stress regime or might have very heterogeneous orientations (Kao et al., 2011). Increased stress changes in the process zone around the fracture could explain the heterogeneous orientations of the focal mechanisms estimated for the largest induced events in the Äspö experiments by Kwiatek et al. (2018). Moreover, the similar magnitudes of the

intermediate and least principal stresses (Ask, 2003, 2006; Klee & Rummel, 2002), resulting in a variable stress regime, could cause such heterogeneous orientations (Kwiatek et al., 2018).

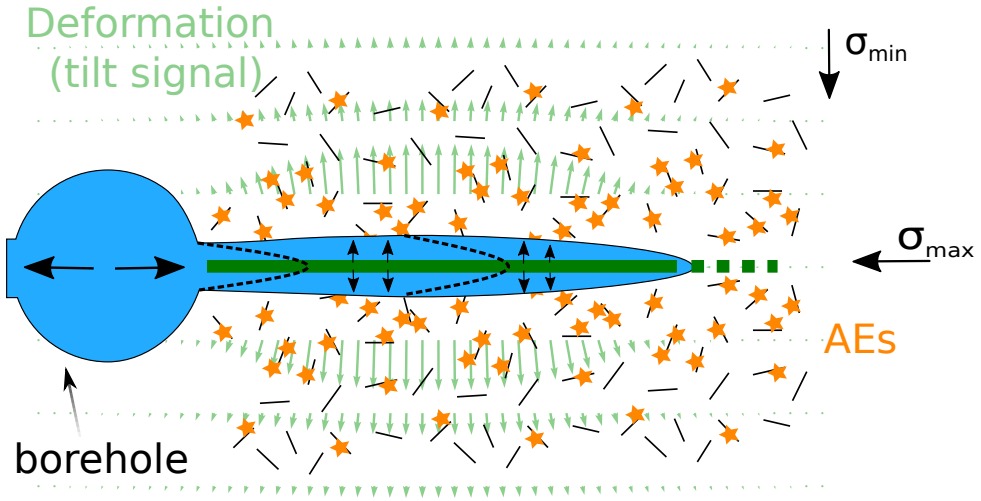

Figure 7.1: Simplified 2-D schematic of the fracture growth model for a single fracture. For simplicity, the fracture growth is only shown in one direction. AEs (orange stars) are predominately induced at the fracture tip, here indicated for three steps in time (dashed black lines within the opening fracture). The dark green line represents the fracture plane approximation as obtained from the AE clustering. Light green arrows show the theoretical deformation of the opening fracture. The tiny differential vertical deformation below the seismometer feet (farther away from the fracture and not shown here) causes the measured tilt.

The knowledge of particular AE focal mechanisms is not critical for the tracking of permeability changes, since the mapping of fracture growth is commonly done based on the hypocentral locations of induced microseismic events (e.g., Albright & Pearson, 1982; Warpinski et al., 1998). A reliable mapping via microseismic or AE activity requires a low detection threshold because the seismic impact of the opening and the propagation of new fractures is generally small and often not detected, which may somehow bias the overall picture of the involved deformations (McClure & Horne, 2014). If the detection threshold is too high, the microseismic analysis would be unable to resolve the geometry of the hydraulic fractures. In such cases, aseismic processes have been hypothesized (e.g. Cornet et al., 1997; Guglielmi et al., 2015; Schmittbuhl et al., 2014). In fact, as long as there is a hydraulic fracture opening, there are local stress changes expected in its vicinity that cause a seismic response (Warpinski et al., 2004). Whether this response is registered depends on the detection threshold. In the mine-scale experiments at Äspö HRL, the largest events induced around the opening fracture have moment magnitudes (M_w) of -3.5, while most magnitudes are below M_w-4. This is several magnitudes below the typical detection thresholds of geophone arrays in boreholes and at the surface (e.g., Pankow et al., 2020). With a different or more distant AE monitoring setup, the tilt signal would have been the only record of the hydraulic fracture growth, and the processes acting during the Äspö experiments would be considered aseismic. However, considering the energy budget of hydraulic fracturing, it becomes evident that most energy is not seismically radiated (see Section 7.3, Publication 3, Chapter 4, Zang et al., 2021). In the Äspö experiments, the fracture evolution can be tracked in great detail (e.g., Fig. 12 in Chapter 4) thanks to the increased detection capabilities arising from the continuously recording AE monitoring network. The continuous recording revealed a

massive activity of approximately 20,000 AEs in the fracture process zones (Niemz et al., 2020), a 100-fold increase compared to the triggered catalog of Kwiatek et al. (2018).

As a first-order approximation, the applied cluster analysis reveals planar fracture zones for the conventional experiments (Niemz et al., 2020). The approximation as planar fractures is independently supported by the second data set from the broadband seismometers, which serve as tiltmeters in this experimental setup. By modeling the theoretical tilt signal due to the tensile opening of a hydraulic fracture with rectangular dislocation sources, defined by the AE fracture plane approximations (see schematic in Fig. 7.1), I showed that the fracture extent is well mapped (Niemz et al., 2021). However, the fracture planes may also represent a possibly more complex set of conjugated or parallel fractures (Goebel et al., 2017; McClure & Horne, 2014) instead of a single fracture plane. The deviating fracturing geometries of the alternative injection schemes are discussed in Section 7.3.

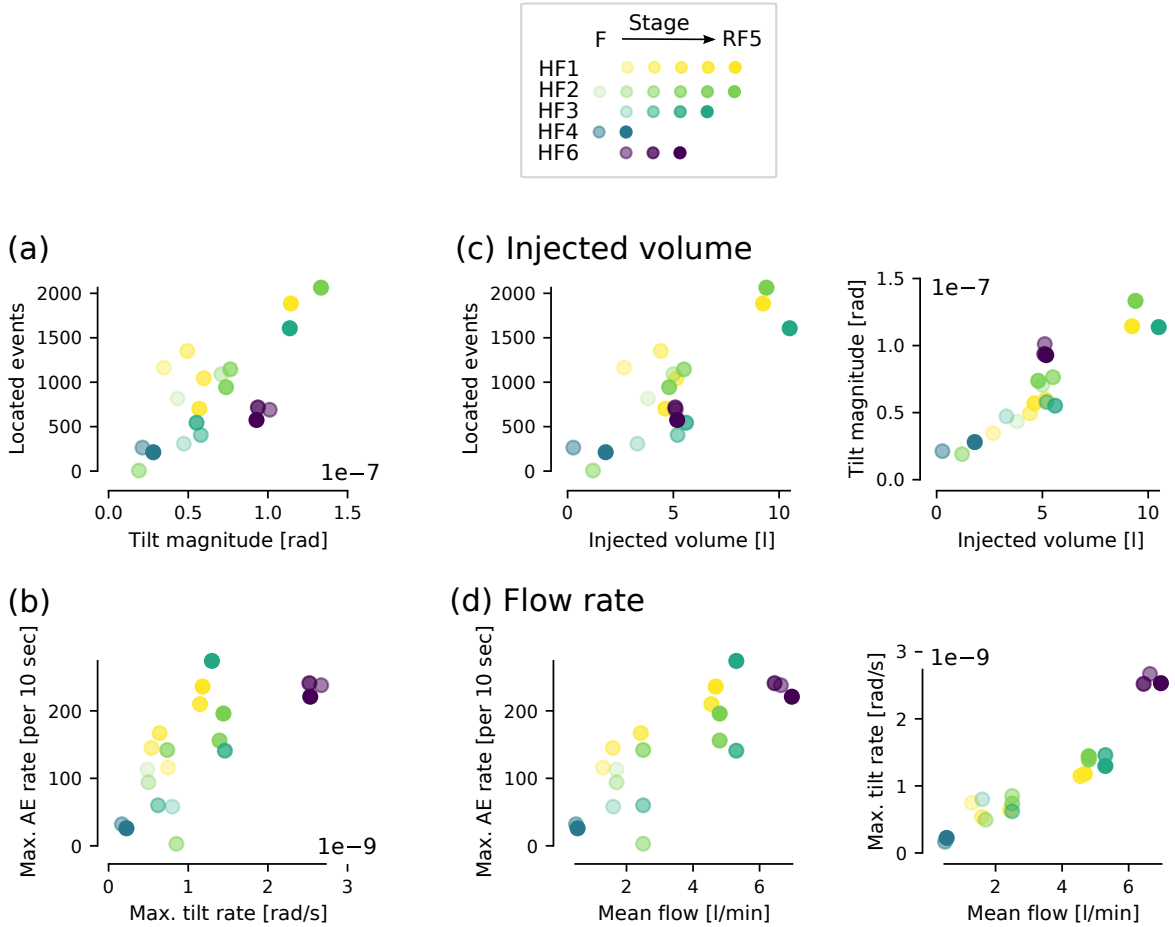

Figure 7.2: The number of located AEs and the tilt magnitude are well correlated (a). The same applies to the corresponding maximum rates (b). These correlations are fundamentally caused by the opening and the growth of the hydraulic fractures and governed by the injected volume (c) and the mean flow rate (d).

While the observed AEs and the tilt signals recorded by the seismometers provide independent information, both are caused by the same processes: the opening, the growth, and the closing of hydraulic fractures (see Fig. 7.1). The correlation between the tilt magnitude and the number

of induced AEs, on the one hand, and the correlation between the tilt rate and the AE rate, on the other hand, (Fig. 7.2a and 7.2b) illustrate this causal connection. The injected volume governs the first correlation (Fig. 7.2c). For the given fracture-seismometer configuration, the tilt magnitude directly and almost exclusively depends on the fluid volume inside the fracture (Niemz et al., 2021). The growth of the fracture away from the borehole and the increased fracture opening accommodate the increasing fracture volume during the injection. The fracture growth disturbs the stress field in the vicinity of the fracture and induces new events in zones not activated before (Fig. 7.2c). By considering the temporal evolution of the fracture, the same applies to the rates of the aforementioned process: the tilt rate and AE rate increase with the flow rate (Fig. 7.2d). The increased scatter of the AE number and rate can be explained by the influence of local stress heterogeneities and differences in the distribution of preexisting micro-fractures, which are supposed to be activated in the fracture process zone surrounding the opening fracture.

Although the detection threshold of the AE monitoring system installed in the Äspö experiments is very low, inherent stress memory effects within the rock, the Kaiser effect (Kaiser, 1950), hinder the tracking of very early fracturing processes in the refracturing stages. Kaiser (1950) first described the phenomenon that AEs in laboratory experiments are only induced after the previously applied stress is exceeded. In the case of hydraulic fracturing, this corresponds to a start of AE activity only after the previously opened fracture is reinflated. By analyzing the tilt signal, I resolved the early stage of fracture reopening and provided evidence for the Kaiser effect in the in-situ injection experiments (Niemz et al., 2021).

To conclude, the opening of the fracture can be tracked by the tilt measurement, while the further growth of the fracture or the fracture extent, respectively, is best mapped by the AE activity during the Äspö experiments. Evidence for aftergrowth is found from the joint analysis of both data sets, AE and tilt. This shows that this combination is highly beneficial as it provides complementary information on processes that a monitoring with only one of the sensors could not fully depict. The joint analysis confirms that the AE mapping using AE sensors as close as 10 to 20 meters to the fractures provides good first-order approximations of the fracture extent. The independent insights into the fracture geometry allow for a detailed characterization of the conventional and the alternative injection schemes in the following section.

7.3 Influence of alternative injection schemes on the seismic impact and fracture geometry

Two out of six injection experiments conducted at the Äspö HRL and studied in this thesis tested innovative injection schemes. These schemes deviate from the conventional, continuous injection style (Fig. 1.2): HF3 with a cyclic progressive injection scheme and HF5 with a cyclic pulse pressurization approach.

In this section, I will focus on the influence of the injection scheme on the seismic footprint and the fracture geometry. This discussion combines findings from all three main publications, starting from the observations during the Äspö experiments (Chapter 4 and Chapter 5) and

incorporating results from laboratory and field-scale summarized in Chapter 6.

7.3.1 Cyclic progressive injection (HF3)

The cyclic progressive injection scheme applied in HF3 was studied using both, AEs (Publication 1, Chapter 4 Niemz et al., 2020) and tilt measurements (Publication 2, Chapter 5 Niemz et al., 2021). Contrary to the single planar fracture zones mapped for the conventional experiments (e.g., HF1 and HF2), HF3 produced a cloud-like AE distribution with multiple fractures. The multiple-fracture geometry was independently mapped by Niemz et al. (2020) based on the AE fracture plane approximations and by Zimmermann et al. (2019) through fracture traces on impression packers. These rubber sleeves are pressed against the borehole wall to imprint newly created fractures in the previously fracture-free borehole after the stimulation. The cloud-like AE distribution and the multi-fracture setup hint at an alteration of the local stress regime during experiment HF3. The stress alteration is assumed to be caused by the cyclic stimulation during the initial fracturing stages (see Fig. 1.2). The stimulation weakens the rock around the injection interval by fatigue, allowing fractures to grow with varying orientations (Publication 3,Chapter 6 Zang et al., 2021). From the tilt analysis, I found that the first-order approximation of multiple fracture planes based on the AE distribution is probably too simple, and the fracture network is even more complex (see also Section 7.4). The increased b-value found for HF3 is another argument for different processes acting during the cyclic injection. An increased b-value implies an increased number of small events compared to the number of larger ones, which means that the seismic energy emitted during the injection was divided into more small events. Additionally, the number of seismic events and the seismic energy emitted during the experiment HF3 was considerably lower compared to the conventional experiments (Niemz et al., 2020; Zang et al., 2021), while the injected volume and, therefore, the hydraulic energy supplied to the system was similar.

The maximum magnitude induced during the experiment HF3 is $M_{AE}3.18$, but $M_{AE}3.92$ for experiment HF2. The activation of a natural fault segment during HF2, as suggested above, may bias this comparison, but also when excluding the events attributed to the assumed reactivated fault (see Chapter 7.4), the maximum magnitude induced during HF2 is larger ($M_{AE}3.67$). This shows that the seismic impact was reduced in the studied cyclic experiment. A first-order correlation between injected volume and the maximum expected magnitude ($\hat{M}_{max}$) (Galis et al., 2017; McGarr, 2014; van der Elst et al., 2016) cannot explain the difference in the maximum induced magnitudes of HF2 and HF3. When considering the net injected volume (injected volume corrected for backflow), the volume is even larger for HF3 compared to HF2 (21.4 l vs. 26.4 l) since there was no significant backflow during the bleed-off phase of the cyclic experiment HF3. The rather simple model of McGarr (2014) is known to overestimate $\hat{M}_{max}$ in laboratory and mine-scale experiments (e.g., Duboeuf et al., 2017; Galis et al., 2017). The physics-based $\hat{M}_{max}$-model of Galis et al. (2017) does not only include the injected volume and rock parameters but also covers the background stress state within the reservoir and the reservoir height. The model provides the largest magnitude estimated for an arrested fracture within the reservoir but does not cover runaway ruptures through the activation of faults on which failure propagates

far beyond the reservoir. In the case of the Äspö experiments, the reservoir corresponds to the stimulated rock volume. For the same (pore) pressure increase, a larger stimulated rock volume, as mapped by the AEs for experiment HF2, can induce larger events (Galis et al., 2017). Following this argument, the more compact cloud-like volume stimulated by the cyclic injection during HF3 contributes to the reduction of the seismic impact. The cloud-like hypocentral distribution coincides with an increased b-value estimated for HF3: Smaller b-values like those estimated for the conventional experiments are expected for rather planar event distributions, while larger b-values are expected for cloud-like distributions (Wessels et al., 2011). The b-value is also attributed to the stress regime: A reduced b-value points to an increased differential stress (Scholz, 1968) implying a stress redistribution in the case of HF3, which could be attributed to the injection scheme.

With experiment HF3, the Äspö experiments could only provide one example of an innovative injection scheme that can be studied using acoustic emission and tilt analyses. This single experiment provides initial evidence for a reduction of the seismic impact and an alteration of the fracture geometry due to the cyclic injection. Unlike the conventional experiments, the cyclic experiment did not show aftergrowth (Niemz et al., 2021), implying a reduction of post-injection seismicity. There is additional evidence from the laboratory scale that the cyclic progressive injection scheme produces a more complex fracture network. Zhuang et al. (2019) showed that cyclic injections produce conjugated, broader fracture zones, which agrees with the observation of more cloud-like AE distributions in HF3 compared to the experiments HF1, HF2, and HF6.

7.3.2 Cyclic pulse pressurization (HF5)

The cyclic pulse pressurization test HF5 induced neither locatable AE activity (Niemz et al., 2020) nor a consistent tilt signal (Niemz et al., 2021). The two independent observations proved to be crucial to assure that missing AE activity is not caused by a reduced detection capability but by the lack of a hydraulic macro-fracture, which could alter the stress field and induce AEs. Consequently, a detailed study of processes acting during the pulse pressurization injection based on the seismic activity was not possible. The uniform detection capability of the AE sensor network is documented by the AE activity of the neighboring conventional experiments HF4 and HF6. The number of induced AEs in both experiments follows the general correlation between injected volume and the number of located events (see Fig. 7.2c). A varying attenuation of seismic waves in the stimulated volume of the experiments HF4 and HF5, which would cause a deviation in the detection capability, is unlikely because both experiments were conducted in the same rock type. However, very local heterogeneities in the vicinity of the injection interval may still significantly influence the emission of seismic energy. Additional mine-scale experiments testing the cyclic pulse injection scheme should be conducted to verify the first mine-scale observations and evaluate whether the reduction of AE activity and the increased hydraulic performance as found in laboratory test by Zhuang et al. (2020) can be reproduced in mine tests.

7.3.3 Energy partitioning in hydraulic fracturing

This thesis provides an essential contribution to the further optimization of innovative injection schemes by linking laboratory and field experiments via the study of the mine-scale experiments in Äspö. After all, the alternative injection schemes that I studied were developed to reduce injection-induced seismicity in large-scale EGS while retaining permeability enhancements.

Apart from tests at Äspö and in the laboratory (Zhuang et al., 2020; Zhuang et al., 2019), the cyclic progressive injection scheme was also applied in field-scale by Hofmann et al. (2019). While optimizing the injection scheme in the laboratory can provide important insight into small-scale processes, the application at field-scale is expected to produce more complex interactions, e.g., with preexisting fracture networks (Hofmann et al., 2018). Zang et al. (2021) (Publication 3, Chapter 6) approach this problem from a novel energy budget point of view spanning from laboratory tests over mine-scale experiments to the field application. The comparative energy budgets provide a first-order insights into differences and similarities between the three aforementioned scales.

The conversion between seismic moment and radiated seismic energy includes considerable uncertainties. First and foremost, we have to assume that self-similarity holds for very small events in the laboratory scale (Scholz, 1968) and the mine-scale (Kwiatek et al., 2011), implying that the apparent stress drop is constant and scale-independent. However, laboratory tests and seismological studies show that the apparent stress drop can vary considerably (Choy & Boatwright, 2012). This variability is accounted for by the uncertainties given for the seismic energy.

In the small-scale experiments (laboratory and mine), the energy estimated for the process of fracture opening is much larger than the radiated seismic energy. While this might be partially explained by inadequacies in the seismic energy calculation and by differences in detection capabilities, it may also imply a difference in the subsurface processes acting in the field-scale.

Laboratory and mine-scale show a similar ratio between the radiated seismic energy E_{seis} and the supplied hydraulic energy E_{hyd} (injection efficiency), but the ratio is much lower in the field case (see parallel dashed lines in Fig. 7.3). On the one hand, the seismic catalog of the field application is less complete compared to those of the well-monitored laboratory and mine experiments, so the injection efficiency might be even smaller in the field case. On the other hand, the largest events should dominate the cumulative radiated seismic energy. The increased fractions of emitted seismic energy and fracture energy in the field case could be attributed to slip along preexisting, sub-critical faults, favorably oriented for failure biasing the energy budget calculation. A reduced b-value (<1) further supports the assumption of a reactivation of shear faults in the field application. Apart from the relative differences observed between the small-scale experiments and the field test, the energy budgets show that the fraction of seismically radiated energy is generally very small in all studied experiments, even in the field-scale ($<0.5\%$ of E_{hyd}).

At the same time, we observe a consistent reduction in E_{seis}/E_{hyd} when using advanced injection schemes (cyclic/stepwise) in the studied laboratory experiments, the Äspö mine-scale

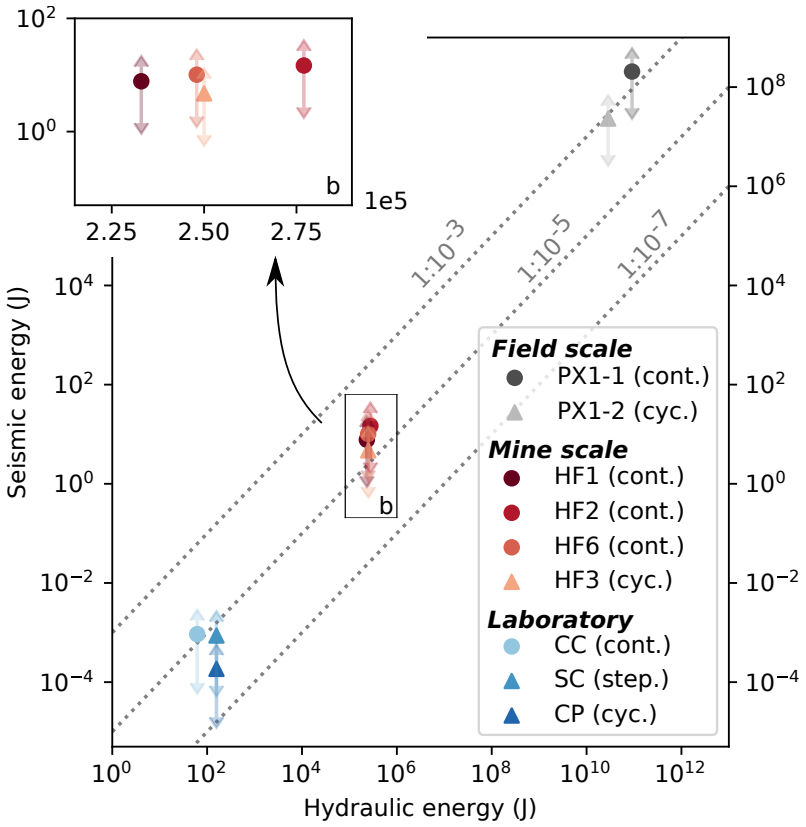

Figure 7.3: Hydraulic versus seismically radiated energy of high-pressure fluid injections at three different scales: laboratory (cm), mine (m), field (up to km). Circles: conventional injections. Triangles: innovative injection schemes (cyclic progressive and stepwise). Blue shades: Laboratory scale experiments. Red shades: mine-scale experiments. Black shades: Field application. Dashed lines indicate the ratio of seismic to hydraulic energy. Figure modified from Zang et al. (2021).

experiments, and the field application (Fig. 7.3, Zang et al., 2021). In all these experiments and applications, the b-value is consistently larger for cyclic injections compared to the conventional injections (Zang et al., 2021). These observations provide evidence that the alternative injection schemes have the potential to reduce the seismic impact of high-pressure fluid injections. The schemes also alter the fracture geometry, leading to more distributed, complex fracture networks, as seen in laboratory scale (Zhuang et al., 2020; Zhuang et al., 2019) and mine-scale (Niemz et al., 2020; Niemz et al., 2021).

7.4 Exploiting relative information from small AEs via full-waveform clustering

The continuous recordings of the AE network were used to obtain hypocentral locations, origin times, and magnitudes. So far, this discussion was mainly based on the resulting AE catalog. Nevertheless, the waveforms contain much more information on the fracturing process. Directly extracting information on focal mechanisms is limited to a few larger events in the case of the Äspö experiments (Kwiatek et al., 2018). Low SNRs and the high-frequency content of the signals hinder the analysis aiming for small AEs. Furthermore, the coupling of the AE sensors to

the rock and the response of the sensors are not well known. Relative approaches can overcome the limitations mentioned above. The waveform-based clustering toolbox *Clusty* (Publication 4,

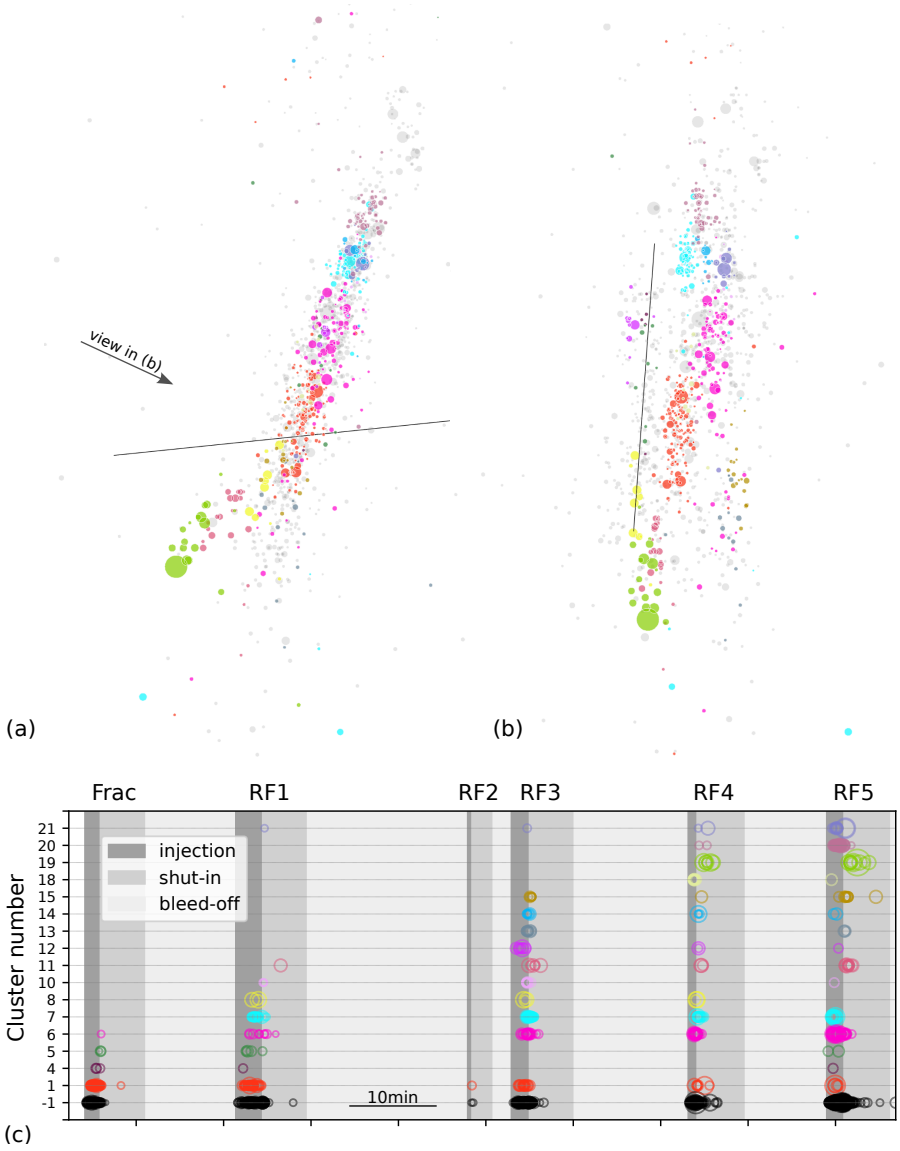

Figure 7.4: (a) Side view and frontal view onto the fracture plane as depicted by the AE cloud of experiment HF2. Only AEs with magnitude estimates are shown and scaled accordingly. Color-coded based on waveform-clustering results from *Clusty*. Non-clustered events in grey. Only the most prominent cluster are shown. (c) Timing of cluster activity across different (re-)fracturing stages (F to RF5).

see also the Section 3.2.1) was specifically developed for such a relative analysis. It proved to be helpful in studying natural (Publication 4, Petersen and Niemz et al., 2021) and induced earthquake sequences (Publication 5, Cesca et al., 2021). The approach implemented in the Clusty toolbox was used to map a complex faulting system offshore Zakynthos, Greece, using waveform information from an aftershock sequence with many small seismic events that do not qualify for MT inversions (Petersen and Niemz et al., 2021). The network-based waveform similarity analysis of the aftershock sequence of the M_w6.8 Zakynthos earthquake provided a more detailed insight into a complex fracture system and revealed previously unmapped faults. I applied the same approach to an induced seismic sequence at the Castor gas storage side, offshore

Spain (Cesca et al., 2021) to provide additional evidence for the activation of another previously unmapped fault activated within the induced sequence. The waveform similarity clustering showed that the events have similar waveforms across the sensor network. The waveforms only change slightly along the dominant direction of the seismic event migration, which maps the proposed fault plane.

By applying the network similarity approach to the AE catalog from the Äspö experiments (Publication 1, Chapter 4), I am able to study differences in underlying rupture processes implicitly. Details on the setup of the clustering toolbox are described in Appendix A. In the following, I will discuss insights on the fracturing process acting during the experiments HF2 and HF3 as obtained from the waveform-similarity analysis. Only AEs with magnitude estimates were considered here.

The growing macro-fracture in HF2, as inferred from AE and tilt observations, is depicted by a clear spatial clustering of events (Fig. 7.4a and b), which also implies a distinct time-dependence. Clusters active in the first stages die out or become less active in the following stages. The red cluster 1 is very active during the fracturing stage and the first refracturing stages, but only a few events are induced in later stages (Fig. 7.4c). This observation can be attributed to the Kaiser effect, as described in previous sections. Most of the micro-cracks in the vicinity of the opening and closing fracture already failed, and the failure of other microcracks (e.g., farther away from the opening fracture or with less favorable orientations) would require larger changes of the effective stresses. Figure 7.4 shows the most prominent clusters induced during HF2. Apart from the clusters 4 and 5 (Fig. 7.4c), there are more small clusters that show the same behavior as cluster 1. New clusters are induced in every refracturing stage. The new clusters are mainly attributed to the further growth of the fracture with an increased AE activity at the fracture tip (e.g., clusters 6 (pink), 7 (cyan), and 20 (reddish-brown)). These clusters are first active in the shut-in phase but grow predominately during the injection phases of the following stages. This observation might be attributed to the further growth of the fracture into the rock volume after the end of the injection (aftergrowth) in the very first stage of the cluster appearance, while in the following stages, an increased opening of the fracture alters the stress field around it and induces more AEs.

The clusters 11 (light red) and 19 (green) below the borehole map a secondary fracture zone. The events almost exclusively occur in the shut-in phase. Both clusters have an increased ratio of large events above $M_{AE}3$. Another cluster with an increased ratio of large events is cluster 8 (yellow), also located below the borehole. By analyzing the waveforms of these three clusters together with the small clusters 0 and 2 (not shown in Fig. 7.4) collocated with cluster 8, I find clear differences between those two groups of clusters. The waveforms of the clusters 8, 11, and 19 change only slightly due to their change in location, but their waveforms are very different compared with the two small clusters 0 and 2 (Fig. 7.5). The latter clusters represent the early hydraulic fracture opening near the borehole.

The waveform differences, increased magnitudes of the events below the borehole during HF2, and the reduced b-value strongly hint at an activation of a preexisting fault in the secondary fracture zone (Downie et al., 2010, see also Section 7.3). Cluster 8 might serve as a connection between the AE activity around the opening new fracture, as mapped by most clusters above

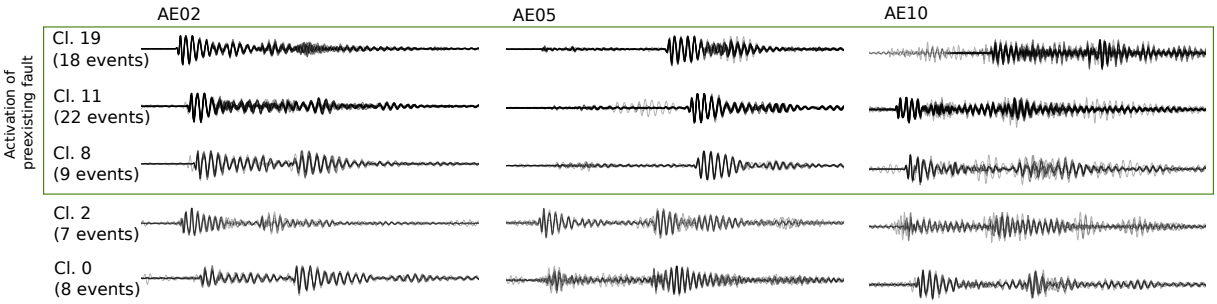

Figure 7.5: HF2. Stacked waveforms of clustered events in the clusters dominant below the borehole (8,11,19) and from two clusters (0,2) collocated with cluster 8. The difference is most evident on the sensors AE02 and AE05.

the borehole, and the activity on the preexisting fault, enabling the slip along this fault in the shut-in phases of HF2-RF4 and HF2-RF5.

The secondary fracture zone mapped by clusters 11 and 19 was considered a possible hydraulic connection between HF2 and the neighboring experiment HF1 (Kwiatek et al., 2018) based on the spatial analysis of AEs (see Fig. 7.4 and Fig. 7b in Chapter 4). If there was a hydraulic connection, the injection should induce similar events across the hydraulically communicating experiments (Eisner et al., 2006) when the fluid enters into a previously created fracture and causes further growth. A joint cluster analysis for the AEs induced during HF1 and HF2 shows that the AEs have very different waveforms while being relatively close to each other below the borehole. Consequently, I can exclude a direct hydraulic communication. Under the assumption that the secondary fracture in HF2 below the borehole is rather a preexisting, activated fault, a direct communication would have induced similar events if the hydraulic fracture of HF1 also reached this preexisting fault. However, an influence of the fracture opened during HF1 onto the local stress regime that might have contributed to the activation of the alleged natural fault cannot be ruled out.

The clustering result obtained for experiment HF3 is very different from the one obtained for HF2 (Fig. 7.6). The reactivation of clusters in more than one stage is limited to the first two refracturing stages (Fig. 7.6c). These clusters are very small and show a large scatter of events. Cluster 5 (green) might be interpreted as a cluster of AEs induced at the tip of the growing fracture farther away from the borehole ahead of the previously induced cluster 3 (orange). This points to a rearrangement in the fracture geometry, which implies changes in the local stress regime farther away from the borehole, where the cyclic injection possibly did not weaken the rock volume (Zang et al., 2017; Zang et al., 2021). However, there are no other dominant clusters that map the growth of a macro-fracture at the tip. For HF3, the relative number of clustered events is low compared to HF2 (18% vs. 39%). This difference could be attributed to the sparser seismic activity during HF3 and the smaller magnitudes of the induced events, which remain undetected and could not link larger AEs in the network-based similarity analysis. I ruled out this bias possibly arising from a sparse AE activity during experiment HF3 by repeatedly resampling the catalog of HF2, so it contains the same number of events as the catalog of HF3 (see Appendix A.2). The waveform clustering analyses for the resampled catalogs show no significant change in the general cluster pattern. Consequently, the lower ratio of clustered events implies a larger variability in the recorded waveforms in experiment HF3. This interpretation is

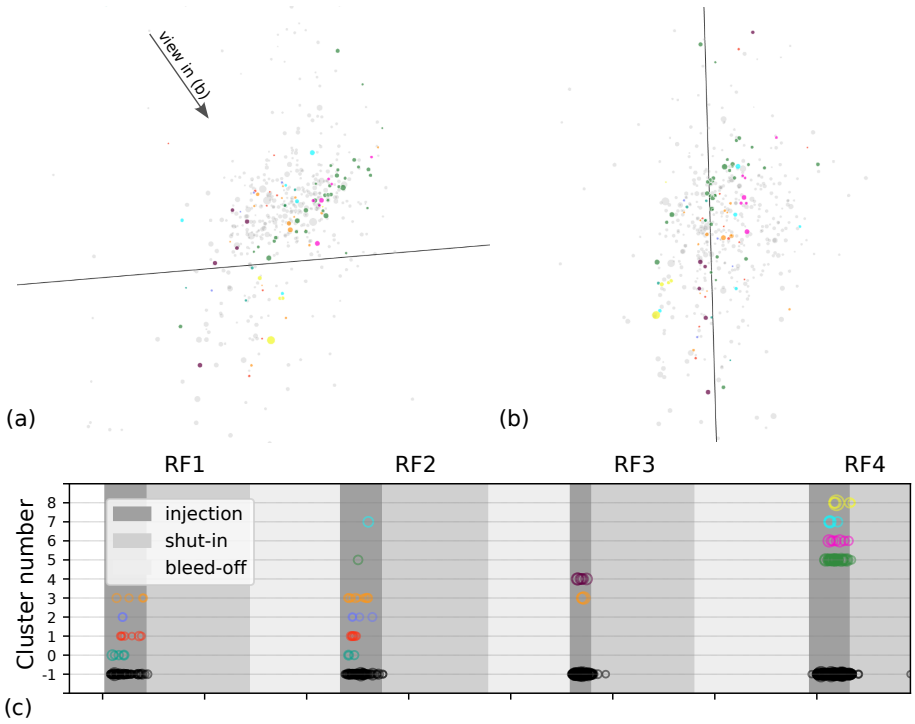

Figure 7.6: (a) Side view and frontal view onto the fracture plane as depicted by the AE cloud of experiment HF3. Only AEs with magnitude estimates are shown and scaled accordingly. Color-coded based on waveform-clustering results from *Clusty*. Non-clustered events in grey. All clusters are shown. (c) Timing of cluster activity across different fracturing stages (RF1 to RF4). There was no significant AE activity in the fracturing stages that could be clustered.

supported by the observation that for HF3, the first events are only clustered when allowing for larger differences in the network similarity compared to HF2 (see Fig. A.1). A larger variability of waveforms hints at a larger spatial separation of events or an increased variability in focal mechanisms. Regardless of which is dominant, both reasons provide additional independent evidence for an increased fracture complexity in the cyclic injection experiment HF3.

To my knowledge, the full-waveform-based AE clustering, presented here, is a novel approach for studying hydraulic fracturing processes at the mine-scale. While a more detailed analysis is beyond the scope of this chapter, the approach bears the opportunity to gain insight into faulting mechanisms while overcoming the limits of focal mechanism studies, which are generally only successful for the largest events.

8 | Conclusions and outlook

Conclusions

In this thesis, I jointly analyzed data sets from multiple HF experiments with varying injection schemes conducted at Äspö Hard Rock Laboratory. The experiments aimed for the optimization of HF in crystalline rocks regarding the seismic impact and the fracture geometry. Studying both aspects is critical to assess and mitigate the seismic hazard that accompanies the sustainable energy production in enhanced geothermal systems.

Induced seismicity

The application of full-waveform techniques to highly sampled, continuous AE recordings in the implemented semi-automated workflow of detection, classification, and location proved that such methods are applicable at very small scales, characterizing events with rupture sizes of cm to dm. Relying on full-waveform analyses, I was able to compile an enhanced catalog of approximately 20,000 AEs, induced during the injection experiments, increasing the number of events by a factor of 100 compared to the triggered catalog.

The analysis of the enhanced AE catalog revealed striking differences in the seismic response of the rock to conventional continuous injections and alternative injection schemes, namely cyclic (HF3) and cyclic pulse injections (HF5). The cyclic injection induced fewer AEs with a lower maximum magnitude compared to the conventional injections, while the injected volume was similar. The reduced seismic impact of the cyclic injections is also documented by an increased b-value, implying a decreased number of large events compared to the number of small ones. The mitigation of large induced events is a key point for a successful implementation of enhanced geothermal systems. A safe injection approach helps to foster a broader public acceptance of this important source of renewable energy.

The reactivation of existing faults poses an additional seismic hazard. My thesis shows how such a reactivation can be studied based on our newly developed waveform-based network similarity clustering. During the late refracturing stages of the conventional injection HF2, a secondary zone of AE activity developed below the borehole. In addition to the increase of induced magnitudes and a reduction of the b-value for those events, the network-based waveform similarity analysis provided strong evidence for the reactivation of a preexisting fault in experiment HF2. The waveform similarity analysis also showed that this structure did not enable a direct hydraulic

communication with the neighboring experiment HF1, as hypothesized in earlier studies.

Fracture geometry

Besides the seismic impact, the difference between conventional and cycling injections is manifested in the fracture geometry. The unique combination of a hypocenter-based clustering, a waveform-based clustering, and the analysis of tilt signals revealed that the conventional injections form planar, sub-vertical macro-fractures growing continuously during subsequent refracturing stages, while there is evidence for an increased fracture complexity for the cyclic injection experiment HF3. The latter experiment developed multiple fractures or a complex fracture network, only partly activated during different refracturing stages. This difference in the fracture geometry can be attributed to an alteration of the local stress regime imposed by the cyclic injection, which is supposed to weaken the rock in the vicinity of the injection interval. The alteration of the local stress conditions is also reflected in the direction of fracture growth. The conventional experiments show a pronounced unilateral growth, which might be attributed to local stress gradients and stress heterogeneities in the vicinity of the growing hydraulic fracture. In contrast, the AE cloud induced during HF3 is symmetric relative to the borehole. It remains unclear whether the stress gradients are canceled out by the cyclic stimulation. Farther away from the borehole, the fracture geometry of experiment HF3 appears to rearrange into a more planar structure, implying that the stress alteration imposed by the injection would reduce with the distance from the injection interval. The cyclic pulse injection did not induce any AE. Independent information from tilt signals points to the lack of a growing macro-fracture, which explains the lack of induced seismicity. This example outlines the importance of a complementary monitoring setup and a joint analysis of independent data sets.

Hydraulic fracture growth

The unique observation of tilt signals on broadband seismometers and the joint analysis with the AE activity helped to shed light on details of the fracturing process. I found evidence for the Kaiser effect at the beginning of the injection, which describes a lack of seismic response until the previous stress state is exceeded or, in the case of hydraulic fractures, as soon as the opening and the extent of the fracture exceeds previous values. At the end of the injection phase of the conventional experiment HF2, I also found evidence for aftergrowth, the continued growth of the fracture after the stimulation stopped. In contrast, no aftergrowth was observed for the cyclic experiment HF3, which is another striking argument for a safer stimulation.

General applicability of the mine-scale findings

By analyzing energy budgets from high-pressure fluid injection from three scales, I outlined that the cyclic injection scheme does not only reduce the seismic impact in the mine-scale experiment, but this is also consistently observed at laboratory-scale and in a field application. The reduced seismic impact is represented by an increased b-value, a reduction of the seismic efficiency, and a decrease in the maximum induced magnitude across all scales when comparing conventional and

cyclic injections. If consistently observed in additional mine-scale and field-scale experiments using cyclic injections, the reduction of the maximum induced magnitude would be a key point regarding the seismic hazard management in EGS.

The findings of this thesis are an important contribution to the ongoing in-situ research on hydraulic fracturing processes in crystalline rocks, providing valuable insights for ongoing and future in-situ experiments that will eventually lead towards a successful and safe application of large scale EGS, a cornerstone of future sustainable energy production.

Outlook

Full-waveform approaches, as applied in this study, are recently implemented for quasi-real time processing (e.g., Li et al., 2020; Palgunadi et al., 2019). With increasing computational capacities, these techniques will also replace the usage of triggered recordings for highly sampled data (up to 1 MHz). These approaches could provide automated detections and locations for a first-order, near-real-time insight into the fracture evolution as mapped by thousands of AEs. The incorporation of a Hidden Markov Model (HHM) classification tool within the workflow already points into the direction of machine learning approaches, which became more and more important recently with massively increasing amounts of seismological data (Bergen et al., 2019). HHM-based classifications are used in speech recognition and were adopted to seismic signals by Hammer et al. (2012). Also, the detection and the location of seismic events have recently been achieved via machine learning techniques, such as deep neural networks (Kriegerowski et al., 2019; Zhu & Beroza, 2019). Machine learning algorithms already outperform event detection in macroseismic data sets (Zhu & Beroza, 2019), but the usage in different settings, such as AE monitoring, requires a training data set. In this sense, the catalog compiled in this thesis could serve as a reference for the training of deep neural networks for AE monitoring systems, which could considerably lower the computational resources needed for real-time processing.

Extending the full-waveform analyses of detection, classification, and location by the study of source processes of small AEs using full-waveforms would necessarily be the next step. Instrumental limitations hinder the usage of existing full-waveform inversion approaches, but relative source inversion methods (Dahm, 1996; Dahm et al., 2000) could be promising. The network-based waveform similarity approach (*Clusty*) applied to the injection-induced AEs already points in this direction. During the waveform similarity analysis, I identified anti-correlated events within the AE catalog. AEs with a very high anti-correlation imply an opposite mechanism acting at the same micro crack in the vicinity of the opening hydraulic fracture. An opposite mechanism, however, requires a reversed stress regime. Such a setting might be plausible if the effective stress change induced by the opening hydraulic fracture first causes a slip at a microcrack, which slips back when the hydraulic fracture is closing, and the regional stress field becomes dominant again. However, a detailed analysis of this observation is still pending.

The single experiments for the cyclic injection (HF3) and the cyclic pulse injection (HF5) at Äspö HRL provide first evidence for a successful mitigation of large induced events via the application of novel injection techniques. The further optimization of the injection scheme, e.g., regarding a sustainable permeability enhancement, as needed for EGS energy production, would

profit from further mine-scale tests. Additionally, the installation of borehole tiltmeters could provide a better resolution of deformation signals induced by the tilting of the rock volume during the injection.

Bibliography

Albright, J. N., & Pearson, C. F. (1982). Acoustic Emissions as a Tool for Hydraulic Fracture Location: Experience at the Fenton Hill Hot Dry Rock Site. *Society of Petroleum Engineers Journal*, *22*(04), 523–530. https://doi.org/10.2118/9509-PA

Amann, F., Gischig, V., Evans, K., Doetsch, J., Jalali, R., Valley, B., Krietsch, H., Dutler, N., Villiger, L., Brixel, B., Klepikova, M., Kittilä, A., Madonna, C., Wiemer, S., Saar, M. O., Loew, S., Driesner, T., Maurer, H., & Giardini, D. (2018). The seismo-hydromechanical behavior during deep geothermal reservoir stimulations: Open questions tackled in a decameter-scale in situ stimulation experiment. *Solid Earth*, *9*(1), 115–137. https://doi.org/10.5194/se-9-115-2018

Amorèse, D. (2007). Applying a change-point detection method on frequency-magnitude distributions. *Bulletin of the Seismological Society of America*, *97*(5), 1742–1749. https://doi.org/10.1785/0120060181

Ask, D. (2003). Evaluation of measurement-related uncertainties in the analysis of overcoring rock stress data from Äspö HRL, Sweden: A case study. *International Journal of Rock Mechanics and Mining Sciences*, *40*(7), 1173–1187. https://doi.org/10.1016/S1365-1609(03)00114-X

Ask, D. (2006). Measurement-related uncertainties in overcoring data at the Äspö HRL, Sweden. Part 2: Biaxial tests of CSIRO HI overcore samples. *International Journal of Rock Mechanics and Mining Sciences*, *43*(1), 127–138. https://doi.org/10.1016/j.ijrmms.2005.05.012

Aster, R. C., & Scott, J. (1993). Comprehensive characterization of waveform similarity in microearthquake data sets. *Bulletin of the Seismological Society of America*, *83*(4), 1307–1314.

Baisch, S., Weidler, R., Voros, R., Wyborn, D., & de Graaf, L. (2006). Induced Seismicity during the Stimulation of a Geothermal HFR Reservoir in the Cooper Basin, Australia. *96*(6), 2242–2256. https://doi.org/10.1785/0120050255

Baisch, S., Koch, C., & Muntendam-Bos, A. (2019). Traffic Light Systems: To what extent can induced seismicity be controlled? *Seismological Research Letters*, *90*(3), 1145–1154. https://doi.org/10.1785/0220180337

Battaglia, J., Aki, K., & Montagner, J.-P. (2000). Tilt signals derived from a GEOSCOPE VBB Station on the Piton de la Fournaise Volcano. *Geophysical Research Letters*, *27*(5), 605–608. https://doi.org/10.1029/1999GL010916

Bergen, K. J., Chen, T., & Li, Z. (2019). Preface to the focus section on machine learning in seismology. *Seismological Research Letters*, *90*(2A).

Bohnhoff, M., Dresen, G., Ellsworth, W. L., & Ito, H. (2009). Passive Seismic Monitoring of Natural and Induced Earthquakes: Case Studies, Future Directions and Socio-Economic Relevance. In S. Cloetingh & J. Negendank (Eds.), *New Frontiers in Integrated Solid Earth Sciences* (pp. 261–285). Springer Netherlands. https://doi.org/10.1007/978-90-481-2737-5_7

Bommer, J. J., Oates, S., Cepeda, J. M., Lindholm, C., Bird, J., Torres, R., Marroquín, G., & Rivas, J. (2006). Control of hazard due to seismicity induced by a hot fractured rock geothermal project. *Engineering Geology*, *83*(4), 287–306. https://doi.org/10.1016/j.enggeo.2005.11.002

Cesca, S., Grigoli, F., Heimann, S., González, Á., Buforn, E., Maghsoudi, S., Blanch, E., & Dahm, T. (2014). The 2013 September–October seismic sequence offshore Spain: a case of seismicity triggered by gas injection? *Geophysical Journal International*, *198*(2), 941–953. https://doi.org/10.1093/gji/ggu172

Cesca, S., Stich, D., Grigoli, F., Vuan, A., López-Comino, J. Á., Niemz, P., Blanch, E., Dahm, T., & Ellsworth, W. L. (2021). Seismicity at the Castor gas reservoir driven by pore pressure diffusion and asperities loading. *Nature Communications*, *12*(1), 4783. https://doi.org/10.1038/s41467-021-24949-1

Choy, G. L., & Boatwright, J. L. (2012). Radiated seismic energy and energy magnitude. *New manual of seismological observatory practice 2 (nmsop-2)* (pp. 1–9). Deutsches GeoForschungsZentrum GFZ.

Clarke, H., Eisner, L., Styles, P., & Turner, P. (2014). Felt seismicity associated with shale gas hydraulic fracturing: The first documented example in Europe. *Geophysical Research Letters*, *41*(23), 8308–8314. https://doi.org/10.1002/2014GL062047

Cornet, F. H., Helm, J., Poitrenaud, H., & Etchecopar, A. (1997). Seismic and Aseismic Slips Induced by Large-scale Fluid Injections. In S. Talebi (Ed.), *Seismicity Associated with Mines, Reservoirs and Fluid Injections* (pp. 563–583). Birkhäuser Basel.

Cornet, F. H. (2016). Seismic and aseismic motions generated by fluid injections. *Geomechanics for Energy and the Environment*, *5*, 42–54. https://doi.org/10.1016/j.gete.2015.12.003

Cox, S., & Meredith, P. (1993). Microcrack formation and material softening in rock measured by monitoring acoustic emissions. *International Journal of Rock Mechanics and Mining Sciences & Geomechanics Abstracts*, *30*(1), 11–24. https://doi.org/10.1016/0148-9062(93)90172-A

Dahm, T. (1996). Relative moment tensor inversion based on ray theory: Theory and synthetic tests. *Geophysical Journal International*, *124*(1), 245–257. https://doi.org/10.1111/j.1365-246X.1996.tb06368.x

Dahm, T. (2000). Numerical simulations of the propagation path and the arrest of fluid-filled fractures in the Earth. *Geophys J Int*, *141*(3), 623–638. https://doi.org/10.1046/j.1365-246x.2000.00102.x

Dahm, T. (2001). Rupture dimensions and rupture processes of fluid-induced microcracks in salt rock. *Journal of Volcanology and Geothermal Research*, *109*(1), 149–162. https://doi.org/10.1016/S0377-0273(00)00309-7

Dahm, T., Hainzl, S., & Fischer, T. (2010). Bidirectional and unidirectional fracture growth during hydrofracturing: Role of driving stress gradients. *Journal of Geophysical Research*, *115*(B12322), 1–18. https://doi.org/10.1029/2009JB006817

Dahm, T., Horálek, J., & Šílený, J. (2000). Comparison of Absolute and Relative Moment Tensor Solutions For The January 1997 West Bohemia Earthquake Swarm. *Studia Geophysica et Geodaetica*, *44*(2), 233–250. https://doi.org/10.1023/A:1022166926987

Deichmann, N., & Giardini, D. (2009). Earthquakes Induced by the Stimulation of an Enhanced Geothermal System below Basel (Switzerland). *Seismological Research Letters*, *80*(5), 784–798. https://doi.org/10.1785/gssrl.80.5.784

Dempster, A. P., Laird, N. M., & Rubin, D. B. (1977). Maximum Likelihood from Incomplete Data Via the EM Algorithm. *Journal of the Royal Statistical Society: Series B (Methodological)*, *39*(1), 1–22. https://doi.org/10.1111/j.2517-6161.1977.tb01600.x

Diehl, T., Kraft, T., Kissling, E., & Wiemer, S. (2017). The induced earthquake sequence related to the St. Gallen deep geothermal project (Switzerland): Fault reactivation and fluid interactions imaged by microseismicity: Induced Seismicity St. Gallen. *Journal of Geophysical Research: Solid Earth*, *122*(9), 7272–7290. https://doi.org/10.1002/2017JB014473

Downie, R., Kronenberger, E., & Maxwell, S. C. (2010). Using microseismic source parameters to evaluate the influence of faults on fracture treatments: A geophysical approach to interpretation. *SPE Annual Technical Conference and Exhibition*, *SPE 134772*. https://doi.org/10.2118/134772-MS

Duboeuf, L., Barros, L. D., Cappa, F., Guglielmi, Y., Deschamps, A., & Seguy, S. (2017). Aseismic Motions Drive a Sparse Seismicity During Fluid Injections Into a Fractured Zone in a Carbonate Reservoir. *Journal of Geophysical Research: Solid Earth*, *122*(10), 8285–8304. https://doi.org/10.1002/2017JB014535

Duboeuf, L., Oye, V., Berre, I., & Keilegavlen, E. (2019). Induced seismicity in the reykjanes geothermal reservoir, iceland: Seismic event monitoring, characterization and clustering. *Proceedings of the European Geothermal Congress*.

Eisner, L., Fischer, T., & Le Calvez, J. H. (2006). Detection of repeated hydraulic fracturing (out-of-zone growth) by microseismic monitoring. *The Leading Edge*, *25*(5), 548–554. https://doi.org/10.1190/1.2202655

Ellsworth, W. L. (2013). Injection-induced earthquakes. *Science*, *341*(6142). https://doi.org/10.1126/science.1225942

Ellsworth, W. L., Giardini, D., Townend, J., Ge, S., & Shimamoto, T. (2019). Triggering of the Pohang, Korea, earthquake (Mw 5.5) by enhanced geothermal system stimulation. *Seismological Research Letters*, *90*(5), 1844–1858. https://doi.org/10.1785/0220190102

Ester, M., Kriegel, H.-P., Sander, J., Xu, X., et al. (1996). A density-based algorithm for discovering clusters in large spatial databases with noise. *kdd*, *96(34)*, 226–231.

Fischer, T., Hainzl, S., & Dahm, T. (2009). The creation of an asymmetric hydraulic fracture as a result of driving stress gradients. *Geophysical Journal International*, *179*(1), 634–639. https://doi.org/10.1111/j.1365-246X.2009.04316.x

Foulger, G. R., Wilson, M. P., Gluyas, J. G., Julian, B. R., & Davies, R. J. (2018). Global review of human-induced earthquakes. *Earth-Science Reviews*, *178*, 438–514. https://doi.org/10.1016/j.earscirev.2017.07.008

Fu, P., Schoenball, M., Ajo-Franklin, J. B., Chai, C., Maceira, M., Morris, J. P., Wu, H., Knox, H., Schwering, P. C., White, M. D., Burghardt, J. A., Strickland, C. E., Johnson, T. C., Vermeul, V. R., Sprinkle, P., Roberts, B., Ulrich, C., Guglielmi, Y., Cook, P. J., ... Kneafsey, T. J. (2021). Close Observation of Hydraulic Fracturing at EGS Collab Experiment 1: Fracture Trajectory, Microseismic Interpretations, and the Role of Natural Fractures. *Journal of Geophysical Research: Solid Earth*, *126*(7), e2020JB020840. https://doi.org/10.1029/2020JB020840

Galis, M., Ampuero, J. P., Mai, P. M., & Cappa, F. (2017). Induced seismicity provides insight into why earthquake ruptures stop. *Science Advances*, *3*(12), eaap7528. https://doi.org/10.1126/sciadv.aap7528

Gambino, S., Campisi, O., Falzone, G., Ferro, A., Guglielmino, F., Laudani, G., & Saraceno, B. (2007). Tilt measurements at Vulcano Island. *Annals of Geophysics*, *50*(2), 233–247. https://doi.org/10.4401/ag-4419

Geller, R. J., & Mueller, C. S. (1980). Four similar earthquakes in central california. *Geophysical Research Letters*, *7*(10), 821–824. https://doi.org/10.1029/GL007i010p00821

Giardini, D. (2009). Geothermal quake risks must be faced. *Nature*, *462*(7275), 848–849. https://doi.org/10.1038/462848a

Gischig, V. S., Giardini, D., Amann, F., Hertrich, M., Krietsch, H., Loew, S., Maurer, H., Villiger, L., Wiemer, S., Bethmann, F., Brixel, B., Doetsch, J., Doonechaly, N. G., Driesner, T., Dutler, N., Evans, K. F., Jalali, M., Jordan, D., Kittilä, A., ... Valley, B. (2020). Hydraulic stimulation and fluid circulation experiments in underground laboratories: Stepping up the scale towards engineered geothermal

systems. *Geomechanics for Energy and the Environment*, *24*, 100175. https://doi.org/10.1016/j.gete.2019.100175

Gischig, V. S., & Preisig, G. (2015). Hydro-fracturing versus hydro-shearing: A critical assessment of two distinct reservoir stimulation mechanisms. *13th ISRM International Congress of Rock Mechanics*.

Goebel, T. H., Kwiatek, G., Becker, T. W., Brodsky, E. E., & Dresen, G. (2017). What allows seismic events to grow big?: Insights from b-value and fault roughness analysis in laboratory stick-slip experiments. *Geology*, *45*(9), 815–818. https://doi.org/10.1130/G39147.1

Got, J.-L., & Fréchet, J. (1993). Origins of Amplitude Variations In Seismic Doublets: Source Or Attenuation Process? *Geophys J Int*, *114*(2), 325–340. https://doi.org/10.1111/j.1365-246X.1993.tb03921.x

Grigoli, F., Cesca, S., Rinaldi, A. P., Manconi, A., López-Comino, J. A., Clinton, J. F., Westaway, R., Cauzzi, C., Dahm, T., & Wiemer, S. (2018). The November 2017 Mw 5.5 Pohang earthquake: A possible case of induced seismicity in South Korea. *Science*, *360*(6392), 1003–1006. https://doi.org/10.1126/science.aat2010

Grigoli, F., Cesca, S., Vassallo, M., & Dahm, T. (2013). Automated Seismic Event Location by Travel-Time Stacking: An Application to Mining Induced Seismicity. *Seismological Research Letters*, *84*(4), 666–677. https://doi.org/10.1785/0220120191

Grigoli, F., Cesca, S., Amoroso, O., Emolo, A., Zollo, A., & Dahm, T. (2014). Automated seismic event location by waveform coherence analysis. *Geophysical Journal International*, *196*(3), 1742–1753. https://doi.org/10.1093/gji/ggt477

Grigoli, F., Cesca, S., Priolo, E., Rinaldi, A. P., Clinton, J. F., Stabile, T. A., Dost, B., Fernandez, M. G., Wiemer, S., & Dahm, T. (2017). Current challenges in monitoring, discrimination, and management of induced seismicity related to underground industrial activities: A European perspective. *Reviews of Geophysics*, *55*(2), 310–340. https://doi.org/10.1002/2016RG000542

Guglielmi, Y., Cook, P., Soom, F., Schoenball, M., Dobson, P., & Kneafsey, T. (2021). In situ continuous monitoring of borehole displacements induced by stimulated hydrofracture growth. *Geophysical Research Letters*, *48*(4), e2020GL090782.

Guglielmi, Y., Cappa, F., Avouac, J.-P., Henry, P., & Elsworth, D. (2015). Seismicity triggered by fluid injection–induced aseismic slip. *Science*, *348*(6240), 1224–1226. https://doi.org/10.1126/science.aab0476

Gutenberg, B., & Richter, C. F. (1944). Frequency of earthquakes in California. *Bulletin of the Seismological Society of America*, *34*, 185–188.

Haimson, B. C. (1981). Large scale laboratory testing of hydraulic fracturing. *Geophysical Research Letters*, *8*(7), 715–718. https://doi.org/10.1029/GL008i007p00715

Hammer, C., Beyreuther, M., & Ohrnberger, M. (2012). A Seismic-Event Spotting System for Volcano Fast-Response Systems. *Bulletin of the Seismological Society of America*, *102*(3), 948–960. https://doi.org/10.1785/0120110167

Hammer, C., Ohrnberger, M., & Fäh, D. (2013). Classifying seismic waveforms from scratch: A case study in the alpine environment. *Geophysical Journal International*, *192*(1), 425–439. https://doi.org/10.1093/gji/ggs036

Häring, M. O., Schanz, U., Ladner, F., & Dyer, B. C. (2008). Characterisation of the Basel 1 enhanced geothermal system. *Geothermics*, *37*(5), 469–495. https://doi.org/10.1016/j.geothermics.2008.06.002

Heimann, S., Kriegerowski, M., Isken, M., Cesca, S., Daout, S., Grigoli, F., Juretzek, C., Megies, T., Nooshiri, N., Steinberg, A., Sudhaus, H., Vasyura-Bathke, H., Willey, T., & Dahm, T. (2017). Pyrocko - An open-source seismology toolbox and library. https://doi.org/10.5880/GFZ.2.1.2017.001

Hofmann, H., Zimmermann, G., Zang, A., Yoon, J. S., Stephansson, O., Kim, K. Y., Zhuang, L., Diaz, M., & Min, K.-B. (2018). Comparison of cyclic and constant fluid injection in granitic rock at different scales. *Paper presented at the 52nd U.S. Rock Mechanics/Geomechanics Symposium, Seattle, Washington, USA*, ARMA-2018–691. https://onepetro.org/ARMAUSRMS/proceedings/ARMA18/All-ARMA18/ARMA-2018-691/122546

Hofmann, H., Zimmermann, G., Farkas, M., Huenges, E., Zang, A., Leonhardt, M., Kwiatek, G., Martinez-Garzon, P., Bohnhoff, M., Min, K.-B., Fokker, P., Westaway, R., Bethmann, F., Meier, P., Yoon, K. S., Choi, J. W., Lee, T. J., & Kim, K. Y. (2019). First field application of cyclic soft stimulation at the Pohang Enhanced Geothermal System site in Korea. *Geophysical Journal International*, *217*(2), 926–949. https://doi.org/10.1093/gji/ggz058

Hofmann, H., Zimmermann, G., Huenges, E., Regenspurg, S., Aldaz, S., Milkereit, C., Heimann, S., Dahm, T., Zang, A., Grigoli, F., Karvounis, D., Broccardo, M., Wiemer, S., Hjörleifsdóttir, V., Kristjánsson, B. R., Hersir, G. P., Ásgeirsdóttir, R. S., Magnússon, R., & Árnadóttir, S. (2021). Soft stimulation treatment of geothermal well RV-43 to meet the growing heat demand of Reykjavik. *Geothermics*, *96*, 102146. https://doi.org/10.1016/j.geothermics.2021.102146

Kaiser, J. (1950). *An investigation into the occurrence of noises in tensile tests, or a study of acoustic phenomena in tensile tests* (dissertation). Technical University of Munich, Germany.

Kao, C.-S., Carvalho, F., & Labuz, J. (2011). Micromechanisms of fracture from acoustic emission. *International Journal of Rock Mechanics and Mining Sciences*, *48*(4), 666–673. https://doi.org/10.1016/j.ijrmms.2011.04.001

Keranen, K. M., Weingarten, M., Abers, G. A., Bekins, B. A., & Ge, S. (2014). Sharp increase in central Oklahoma seismicity since 2008 induced by massive wastewater injection. *Science*, *345*(6195), 448–451. https://doi.org/10.1126/science.1255802

Kim, K.-H., Ree, J.-H., Kim, Y., Kim, S., Kang, S. Y., & Seo, W. (2018). Assessing whether the 2017 Mw 5.4 Pohang earthquake in South Korea was an induced event. *Science*, *360*(6392), 1007–1009. https://doi.org/10.1126/science.aat6081

Klee, G., & Rummel, F. (2002). *Rock stress measurements at the Äspö HRL. hydraulic fracturing in boreholes ka2599g01 and kf0093a01* (tech. rep. IPR-02-02). Swedish Nuclear Fuel and Waste Management Co. Stockholm.

Köhler, N., Spies, T., & Dahm, T. (2009). Seismicity patterns and variation of the frequency-magnitude distribution of microcracks in salt. *Geophysical Journal International*, *179*(1), 489–499. https://doi.org/10.1111/j.1365-246X.2009.04303.x

Kriegerowski, M., Petersen, G. M., Vasyura-Bathke, H., & Ohrnberger, M. (2019). A deep convolutional neural network for localization of clustered earthquakes based on multistation full waveforms. *Seismological Research Letters*, *90*(2A), 510–516.

Kwiatek, G., Martínez-Garzón, P., Plenkers, K., Leonhardt, M., Zang, A., von Specht, S., Dresen, G., & Bohnhoff, M. (2018). Insights into Complex Subdecimeter Fracturing Processes Occurring during a Water Injection Experiment at Depth in Äspö Hard Rock Laboratory, Sweden. *Journal of Geophysical Research: Solid Earth*, *123*(8), 6616–6635. https://doi.org/10.1029/2017JB014715

Kwiatek, G., Plenkers, K., Dresen, G., & JAGUARS Research Group. (2011). Source Parameters of Picoseismicity Recorded at Mponeng Deep Gold Mine, South Africa: Implications for Scaling Relations. *Bulletin of the Seismological Society of America*, *101*(6), 2592–2608. https://doi.org/10.1785/0120110094

Kwiatek, G., Saarno, T., Ader, T., Bluemle, F., Bohnhoff, M., Chendorain, M., Dresen, G., Heikkinen, P., Kukkonen, I., Leary, P., Leonhardt, M., Malin, P., Martínez-Garzón, P., Passmore, K., Passmore, P., Valenzuela, S., & Wollin, C. (2019). Controlling fluid-induced seismicity during a 6.1-km-deep geothermal stimulation in Finland. *Science Advances*, *5*(5), eaav7224. https://doi.org/10.1126/sciadv.aav7224

Li, L., Tan, J., Schwarz, B., Staněk, F., Poiata, N., Shi, P., Diekmann, L., Eisner, L., & Gajewski, D. (2020). Recent Advances and Challenges of Waveform-Based Seismic Location Methods at Multiple Scales. *Reviews of Geophysics*, *58*, e2019RG000667. https://doi.org/10.1029/2019RG000667

López-Comino, J. A., Cesca, S., Heimann, S., Grigoli, F., Milkereit, C., Dahm, T., & Zang, A. (2017). Characterization of Hydraulic Fractures Growth During the Äspö Hard Rock Laboratory Experiment (Sweden). *Rock Mechanics and Rock Engineering*, *50*(11), 2985–3001. https://doi.org/10.1007/s00603-017-1285-0

Maghsoudi, S., Cesca, S., Hainzl, S., Kaiser, D., Becker, D., & Dahm, T. (2013). Improving the estimation of detection probability and magnitude of completeness in strongly heterogeneous media, an application to acoustic emission (AE). *Geophysical Journal International*, *193*(3), 1556–1569. https://doi.org/10.1093/gji/ggt049

Manthei, G., & Eisenblätter, J. (2008). Acoustic Emission in Study of Rock Stability. In C. Grosse & M. Ohtsu (Eds.), *Acoustic Emission Testing* (pp. 239–310). Springer. https://doi.org/10.1007/978-3-540-69972-9_11

Manthei, G., Eisenblätter, J., & Dahm, T. (2001). Moment tensor evaluation of acoustic emission sources in salt rock. *Construction and Building Materials*, *15*(5-6), 297–309. https://doi.org/10.1016/S0950-0618(00)00078-7

Manthei, G., Eisenblätter, J., & Dahm, T. (2001). Moment tensor evaluation of acoustic emission sources in salt rock. *Construction and Building Materials*, *15*(5-6), 297–309.

Marzocchi, W., & Sandri, L. (2009). A review and new insights on the estimation of the b-value and its uncertainty. *Annals of Geophysics*, *46*(6), 1271–1282. https://doi.org/10.4401/ag-3472

Maurer, H., & Deichmann, N. (1995). Microearthquake cluster detection based on waveform similarities, with an application to the western Swiss Alps. *Geophysical Journal International*, *123*(2), 588–600. https://doi.org/10.1111/j.1365-246X.1995.tb06873.x

Maxwell, S. C., Jones, M., Parker, R., Miong, S., Leaney, S., Dorval, D., D'Amico, D., Logel, J., Anderson, E., & Hammermaster, K. (2009). Fault activation during hydraulic fracturing. *SEG Technical Program Expanded Abstracts*, 1552–1556.

McClure, M. W., & Horne, R. N. (2014). An investigation of stimulation mechanisms in Enhanced Geothermal Systems. *International Journal of Rock Mechanics and Mining Sciences*, *72*, 242–260. https://doi.org/10.1016/j.ijrmms.2014.07.011

McGarr, A. (2014). Maximum magnitude earthquakes induced by fluid injection: Limits on fluid injection earthquakes. *Journal of Geophysical Research: Solid Earth*, *119*(2), 1008–1019. https://doi.org/10.1002/2013JB010597

Mignan, A., & Woessner, J. (2012). Estimating the magnitude of completeness for earthquake catalogs. *Community Online Resource for Statistical Seismicity Analysis*. https://doi.org/10.5078/corssa-00180805

Niemz, P., Cesca, S., Heimann, S., Grigoli, F., von Specht, S., Hammer, C., Zang, A., & Dahm, T. (2020). Full-waveform-based characterization of acoustic emission activity in a mine-scale experiment: A comparison of conventional and advanced hydraulic fracturing schemes. *Geophysical Journal International*, *222*(1), 189–206.

Niemz, P., Dahm, T., Milkereit, C., Cesca, S., Petersen, G., & Zang, A. (2021). Insights into hydraulic fracture growth gained from a joint analysis of seismometer-derived tilt signals and acoustic emissions. *submitted to JGR Solid Earth*, *'X'*('X'), XXX–XXX.

Okada, Y. (1992). Internal deformation due to shear and tensile faults in a half-space. *Bulletin of the Seismological Society of America*, *82*(2), 1018–1040.

Oye, V., Bungum, H., & Roth, M. (2005). Source Parameters and Scaling Relations for Mining-Related Seismicity within the Pyhäsalmi Ore Mine, Finland. *Bulletin of the Seismological Society of America*, *95*(3), 1011–1026. https://doi.org/10.1785/0120040170

Palgunadi, K. H., Poiata, N., Kinscher, J., Bernard, P., De Santis, F., & Contrucci, I. (2019). Methodology for Full Waveform Near Real-Time Automatic Detection and Localization of Microseismic Events Using High (8 kHz) Sampling Rate Records in Mines: Application to the Garpenberg Mine (Sweden). *Seismological Research Letters*, *91*(1), 399–414. https://doi.org/10.1785/0220190074

Pankow, K., Mesimeri, M., Mclennan, J., Wannamaker, P., & Moore, J. (2020). Seismic Monitoring at the Utah Frontier Observatory for Research in Geothermal Energy. *Workshop on Geothermal Reservoir Engineering*, 9.

Petersen and Niemz, P., Cesca, S., Mouslopoulou, V., & Bocchini, G. (2021). Clusty, the waveform-based network similarity clustering toolbox: Concept and application to image complex faulting offshore zakynthos (greece). *Geophysical Journal International*, *224*(3), 2044–2059.

Qian, Y., Guo, P., Wang, Y., Zhao, Y., Lin, H., & Liu, Y. (2020). Advances in Laboratory-Scale Hydraulic Fracturing Experiments. *Advances in Civil Engineering*, *2020*, e1386581. https://doi.org/10.1155/2020/1386581

Rodgers, P. W. (1968). The response of the horizontal pendulum seismometer to Rayleigh and Love waves, tilt, and free oscillations of the earth. *Bulletin of the Seismological Society of America*, *58*(5), 1385–1406.

Schmittbuhl, J., Lambotte, S., Lengliné, O., Grunberg, M., Jund, H., Vergne, J., Cornet, F., Doubre, C., & Masson, F. (2021). Induced and triggered seismicity below the city of Strasbourg, France from November 2019 to January 2021. *Comptes Rendus. Géoscience*, *353*(S1), 1–24. https://doi.org/10.5802/crgeos.71

Schmittbuhl, J., Lengliné, O., Cornet, F., Cuenot, N., & Genter, A. (2014). Induced seismicity in EGS reservoir: The creep route. *Geothermal Energy*, *2*(1), 14. https://doi.org/10.1186/s40517-014-0014-0

Schoenball, M., Ajo-Franklin, J. B., Blankenship, D., Chai, C., Chakravarty, A., Dobson, P., Hopp, C., Kneafsey, T., Knox, H. A., Maceira, M., Robertson, M. C., Sprinkle, P., Strickland, C., Templeton, D., Schwering, P. C., Ulrich, C., Wood, T., & The EGS Collab Team. (2020). Creation of a Mixed-Mode Fracture Network at Mesoscale Through Hydraulic Fracturing and Shear Stimulation. *Journal of Geophysical Research: Solid Earth*, *125*(12). https://doi.org/10.1029/2020JB019807

Scholz, C. H. (1968). The frequency-magnitude relation of microfracturing in rock and its relation to earthquakes. *Bulletin of the Seismological Society of America*, *58*(1), 399–415.

Schultz, R., Beroza, G., Ellsworth, W., & Baker, J. (2020). Risk-Informed Recommendations for Managing Hydraulic Fracturing Induced Seismicity via Traffic Light Protocols. *Bulletin of the Seismological Society of America*, *110*(5), 2411–2422. https://doi.org/10.1785/0120200016

Schultz, R., Skoumal, R. J., Brudzinski, M. R., Eaton, D., Baptie, B., & Ellsworth, W. (2020). Hydraulic fracturing-induced seismicity. *Reviews of Geophysics*, *58*(3), e2019RG000695. https://doi.org/10.1029/2019RG000695

Shelly, D. R., Hardebeck, J. L., Ellsworth, W. L., & Hill, D. P. (2016). A new strategy for earthquake focal mechanisms using waveform-correlation-derived relative polarities and cluster analysis: Application to the 2014 Long Valley Caldera earthquake swarm: A New Strategy for Focal Mechanisms. *Journal of Geophysical Research: Solid Earth*, *121*(12), 8622–8641. https://doi.org/10.1002/2016JB013437

Specht, S., Heidbach, O., Cotton, F., & Zang, A. (2017). *Data-driven earthquake focal mechanism cluster analysis* (tech. rep. No. 17/01). GFZ German Research Centre for Geosciences. Potsdam.

Stauffacher, M., Muggli, N., Scolobig, A., & Moser, C. (2015). Framing deep geothermal energy in mass media: The case of Switzerland. *Technological Forecasting and Social Change*, *98*, 60–70. https://doi.org/10.1016/j.techfore.2015.05.018

Tinti, S., & Mulargia, F. (1987). Confidence intervals of b values for grouped magnitudes. *Bulletin of the Seismological Society of America*, *77*(6), 2125–2134.

van der Elst, N. J., Page, M. T., Weiser, D. A., Goebel, T. H., & Hosseini, S. M. (2016). Induced earthquake magnitudes are as large as (statistically) expected. *Journal of Geophysical Research: Solid Earth*, *121*(6), 4575–4590. https://doi.org/10.1002/2016JB012818

van Thienen-Visser, K., & Breunese, J. N. (2015). Induced seismicity of the Groningen gas field: History and recent developments. *The Leading Edge*, *34*(6), 664–671. https://doi.org/10.1190/tle34060664.1

Villiger, L., Gischig, V. S., Doetsch, J., Krietsch, H., Dutler, N. O., Jalali, M., Valley, B., Selvadurai, P. A., Mignan, A., Plenkers, K., Giardini, D., Amann, F., & Wiemer, S. (2020). Influence of reservoir geology on seismic response during decameter-scale hydraulic stimulations in crystalline rock. *Solid Earth*, *11*(2), 627–655. https://doi.org/10.5194/se-11-627-2020

Warpinski, N., Branagan, P., Peterson, R., Wolhart, S., & Uhl, J. (1998). Mapping Hydraulic Fracture Growth and Geometry Using Microseismic Events Detected by a Wireline Retrievable Accelerometer Array. https://doi.org/10.2523/40014-MS

Warpinski, N., Wolhart, S., & Wright, C. (2004). Analysis and Prediction of Microseismicity Induced by Hydraulic Fracturing. *SPE Journal*, *9*(01), 24–33. https://doi.org/10.2118/87673-PA

Wasantha, P. L. P., Konietzky, H., & Xu, C. (2019). Effect of in-situ stress contrast on fracture containment during single- and multi-stage hydraulic fracturing. *Engineering Fracture Mechanics*, *205*, 175–189. https://doi.org/10.1016/j.engfracmech.2018.11.016

Wells, D. L., & Coppersmith, K. J. (1994). New empirical relationships among magnitude, rupture length, rupture width, rupture area, and surface displacement. *Bulletin of the Seismological Society of America*, *84*(4), 974–1002.

Wessels, S., Kratz, M., & De La Pena, A. (2011). Identifying fault activation during hydraulic stimulation in the Barnett shale: Source mechanisms, b values, and energy release analyses of microseismicity. *SEG Technical Program Expanded Abstracts*, 1463–1467.

Wielandt, E., & Forbriger, T. (1999). Near-field seismic displacement and tilt associated with the explosive activity of Stromboli. *Annals of Geophysics*, *42*(3). https://doi.org/10.4401/ag-3723

Wright, C. A., Weijers, L., Davis, E. J., & Mayerhofer, M. (1999). Understanding Hydraulic Fracture Growth: Tricky but Not Hopeless. https://doi.org/10.2118/56724-MS

Zang, A., von Specht, S., Niemz, P., Stephansson, O., & Zimmermann, G. (2019). Fatigue hydraulic fracturing: Concept and application in hard rock. *Rock Mechanics for Natural Resources and Infrastructure Development-Full Papers: Proceedings of the 14th International Congress on Rock Mechanics and Rock Engineering (ISRM 2019), September 13-18, 2019, Foz Do Iguassu, Brazil*, 3019–3026.

Zang, A., Oye, V., Jousset, P., Deichmann, N., Gritto, R., McGarr, A., Majer, E., & Bruhn, D. (2014). Analysis of induced seismicity in geothermal reservoirs – An overview. *Geothermics*, *52*, 6–21. https://doi.org/10.1016/j.geothermics.2014.06.005

Zang, A., & Stephansson, O. (2010). *Stress field of the Earth's crust*. Springer Netherlands. https://doi.org/10.1007/978-1-4020-8444-7

Zang, A., Stephansson, O., Stenberg, L., Plenkers, K., Specht, S., Milkereit, C., Schill, E., Kwiatek, G., Dresen, G., Zimmermann, G., Dahm, T., & Weber, M. (2017). Hydraulic fracture monitoring in hard rock at 410 m depth with an advanced fluid-injection protocol and extensive sensor array. *Geophysical Journal International*, *208*(2), 790–813. https://doi.org/10.1093/gji/ggw430

Zang, A., Wagner, F. C., Stanchits, S., Janssen, C., & Dresen, G. (2000). Fracture process zone in granite. *Journal of Geophysical Research: Solid Earth*, *105*(B10), 23651–23661. https://doi.org/10.1029/2000JB900239

Zang, A., Yoon, J. S., Stephansson, O., & Heidbach, O. (2013). Fatigue hydraulic fracturing by cyclic reservoir treatment enhances permeability and reduces induced seismicity. *Geophysical Journal International*, *195*(2), 1282–1287. https://doi.org/10.1093/gji/ggt301

Zang, A., Zimmermann, G., Hofmann, H., Niemz, P., Kim, K. Y., Diaz, M., Zhuang, L., & Yoon, J. S. (2021). Relaxation damage control via fatigue-hydraulic fracturing in granitic rock as inferred from laboratory-, mine-, and field-scale experiments. *Scientific reports*, *11*(1), 1–16.

Zhu, W., & Beroza, G. C. (2019). Phasenet: A deep-neural-network-based seismic arrival-time picking method. *Geophysical Journal International*, *216*(1), 261–273.

Zhuang, L., Jung, S. G., Diaz, M., Kim, K. Y., Hofmann, H., Min, K.-B., Zang, A., Stephansson, O., Zimmermann, G., & Yoon, J.-S. (2020). Laboratory true triaxial hydraulic fracturing of granite under six fluid injection schemes and grain-scale fracture observations. *Rock Mechanics and Rock Engineering*. https://doi.org/10.1007/s00603-020-02170-8

Zhuang, L., Kim, K. Y., Jung, S. G., Diaz, M., Min, K.-B., Zang, A., Stephansson, O., Zimmermann, G., Yoon, J.-S., & Hofmann, H. (2019). Cyclic hydraulic fracturing of pocheon granite cores and its impact on breakdown pressure, acoustic emission amplitudes and injectivity. *International Journal of Rock Mechanics and Mining Sciences*, *122*, 104065. https://doi.org/10.1016/j.ijrmms.2019.104065

Zimmermann, G., Zang, A., Stephansson, O., Klee, G., & Semiková, H. (2019). Permeability enhancement and fracture development of hydraulic in situ experiments in the Äspö Hard Rock Laboratory, Sweden. *Rock Mechanics and Rock Engineering*, *52*, 495–515. https://doi.org/10.1007/s00603-018-1499-9

A | Setting up the waveform similarity clustering

A.1 Setup of the network similarity calculation

AEs without magnitude estimates were excluded from the catalog before starting the waveform similarity analysis. The excluded AEs are characterized by low SNRs, which reduce waveform similarities due to random noise overlaying the signals. Additionally, I used only six sensors (AE01, AE02, AE04, AE05, AE09, AE10) in the analysis. The remaining sensors were either farther away from the injection intervals or had a low coupling to the rock. The reduction of the data set and the limitation of the studied sensors assure that waveforms with low SNRs would not be cross-correlated to save computation time.

The waveform clustering results discussed in Chapter 7.4 were obtained by cross-correlating bandpass-filtered (7-15 kHz) waveforms cut 2 ms before and 8 ms after the theoretical arrival of the P phase. The P phase arrivals were calculated from the event origin time and the travel time of the P phase between the source and the sensor. The P wave velocity was set to 5800 m/s, as used in the full waveform location. I tested multiple frequency bands between 3 kHz and 15 kHz with a minimum bandwidth of 3 kHz. The general cluster pattern remains stable across the tested frequency ranges. Lower frequency bands result is simple waveforms that show a higher similarity (higher cross correlation value), but cannot resolve small differences in location and mechanism. Therefore, I chose a higher frequency range that helps to resolve small differences between event waveforms. The chosen frequency range covers most of the radiated seismic energy (Fig. 4. in Chapter 4). Due to the single-component sensors, the simple homogeneous velocity model and predominantly emergent S wave arrivals, waveform similarities were calculated for the entire waveform snippet, without a separation of P, S or other phases.

The trimmed mean method for the calculation of the network similarity from the stations-wise waveform similarities (cross-correlation values) proved to be reliable in previous applications of *Clusty* (Cesca et al., 2021; Petersen and Niemz et al., 2021). It was also chosen for the analysis of the AE activity from the Äspö experiments. The cut-off was set to 30%. The value corresponds to the rejection of the two smallest cross correlation values before the mean is calculated from the remaining four sensors. Event pairs are only considered for further analyses if at least 3 sensors provide a cross-correlation value above 0.6. The setup described here was used for both experiments HF2 and HF3 to obtain comparable clustering results.

A.2 Tuning of clustering parameters

DBSCAN clusters events based on the density or more specifically their density-reachability (see details in Ester et al., 1996; Petersen and Niemz et al., 2021). By using the network-based waveform-similarity, the density is not based on a spatial metric, but rather on an abstract metric in a location-mechanism space. Similar events, with similar waveforms across the sensor network are close to each other in this space. The DBSCAN clustering result is governed by two clustering parameters: *minPts* and *eps*. DBSCAN searches for neighbouring events in a radius *eps* around the event. If there are at least *minPts* neighbours within the radius *eps* DBSCAN assigns this event to a cluster and repeats this analysis step for all neighboring points. If less then *minPts* neighbours can be reached from one of the analysed events the algorithm does not follow this path any further. The described procedure results in a chain-like clustering. The influence of *minPts* onto the clustering result is secondary (Petersen and Niemz et al., 2021), so a commonly used value of 5 was chosen. There is no general best value for *eps* but it depends on the aim of the clustering analysis. Searching for repeaters requires a small *eps* value, while the mapping of faults and fractures is favored by an increased *eps* value. Since *eps* indirectly reflects the cross-correlations between waveforms it is influenced by the SNR of studied waveforms, the length of the time window and the frequency content. The tuning of the *eps* value is done in multiple steps. Figure A.1 shows the clustering result for different *eps* values broken down to three metrics: (1) the number of clustered events, (2) the number of clusters, and (3) the silhouette score. The silhouette score is a measure of the homogeneity of the clusters (Petersen and Niemz et al., 2021). A high silhouette score at low *eps* reflect the clustering of very similar events in distinct clusters (repeaters). A decreasing silhouette score is expected for larger *eps* (Petersen and Niemz et al., 2021). For the mapping of fracture zones, as intended here, the silhouette score is expected to be low for the appropriate choice of *eps* since integrating events with similar mechanisms along an elongated feature results in internally heterogeneous clusters. For a first coarse estimation of an appropriate *eps* value I first identify the *eps* range in which the number of clusters is maximized. For HF2 this is the range of 0.21 to 0.26 (Fig. A.1a). For HF3, this range includes *eps* values between 0.31 and 0.36 (Fig. A.1a). Beyond these ranges the clusters quickly collapse into larger, very heterogeneous, clusters, as reflected by a decrease in the number of clusters and in the silhouette score (Fig. A.1).

Secondly, I consider the gradient of the silhouette score. Lower gradients proved to be another marker for a well-adjusted *eps* value (Fig. A.1). This is verified by a more detailed analysis based on Clusty's silhouette coefficient plot (Fig. A.2). A high silhouette coefficient for an event implies that this event is similar to each event in this cluster, while all the events in other clusters are very different. A value below zero indicates that this particular event is more similar to an event in another cluster compared to the average similarity to its own cluster members, which might happen when the chain-like clustering includes AEs across an increasing volume. The silhouette plots (Fig. A.2) for the *eps*-values 0.245 (HF2) and 0.345 (HF3) depict a good separation between the clusters. The lower *eps* value for experiment HF2 is attributed to the higher density of the AE cloud induced during HF2. To test whether the sparsity of the AE catalog from experiment HF3 influences the clustering result, I repeatedly drew a sample of events from the catalog of

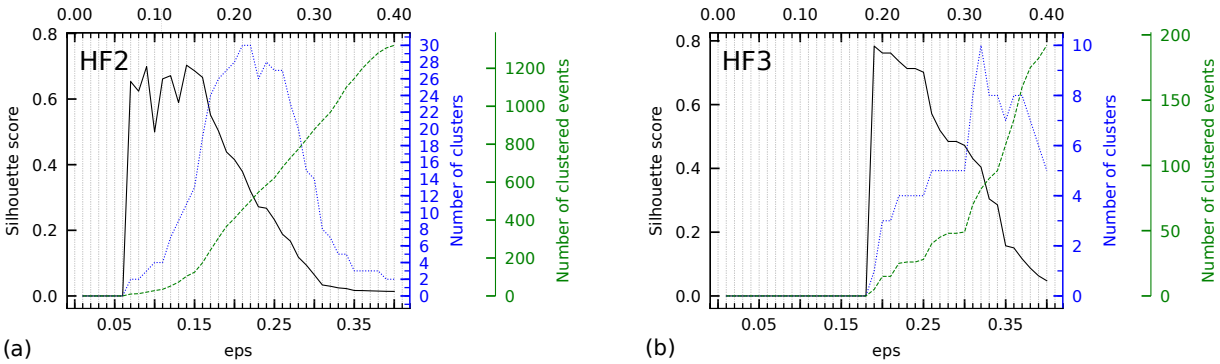

Figure A.1: The clustering results of HF2 (a) and HF3 (b) are broken down into three metrics to obtain a first idea of an appropriate choice of the *eps* value. The largest number of clusters together with a consideration of gradients help to constrain the eps value for the purpose of fault/fracture mapping.

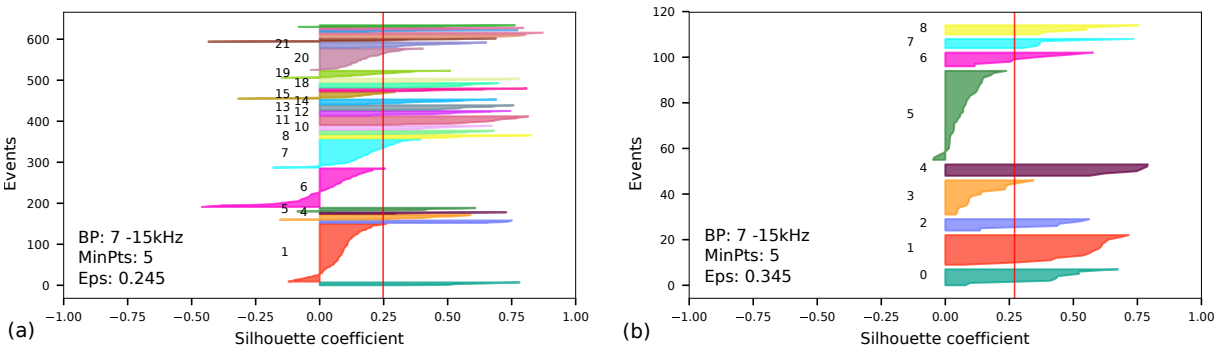

Figure A.2: The silhouette coefficient plots for HF2 (a) and HF3 (b) depict the homogeneity within each cluster and among different clusters, respectively. Each colored block represents one cluster, with events sorted by their silhouette coefficient. The red vertical line marks the silhouette score, the mean of the silhouette coefficients of all clustered events.

HF2 matching the number of events in the catalog of experiment HF3. In this way, I simulated a sparse catalog comparable to the AE catalog of HF3. Subsequently, the sparse catalogs were clustered in the same way as the original catalog. I found that the general cluster pattern remains stable, but the clustering parameter *eps* has to be adjusted to allow for larger differences in the network similarity due to increased location differences between neighboring events in the sparse catalog. The fact that for HF2 first clusters are found for *eps* 0.06, but in case of HF3 only for an *eps* value of 0.18 can be explained by this location effect but might also reflect larger differences in the mechanisms.

Acknowledgments

First of all, I would like to thank my PhD supervisors Arno Zang, Torsten Dahm and, last but not least, Simone Cesca for their support and mentoring during my doctoral studies. I learned a lot in the last four years. I'd also like to thanks all the other members of Section 2.1 and 2.6 for scientific/administrative/technical discussions in the hallway, in the garden or during seminars.

Gesa Petersen, obviously we made it... best Co-PhD. I hope that our scientfic cooperation will prosper in the future... it is fun working with you and you are a great scientist. Tim Davis, thanks for working on fractures too, so I was not the only fracking PhD in the institute... This was quite comforting. Djamil Al-Halbouni, Nima Nooshiri and Marius Kriegerowski, you stable geniuses. You helped me to adjust to the new environment and passed valuable knowledge in coding, science and coping with being a PhD student in general. Honorably mentioned here: Malte Metz and Carla Valenzuela, for being great fellow PhDs. By the way, I just dropped your full names, so that, at some point, when somebody else is searching for your names (in case you get famous), the person will end up with my thesis... Well, I could have cited you...

Svenja, danke für deine unerschütterliche Geduld und deine Unterstüzung vor allem in den letzten 1,5 Jahren im Home Office. Du warst immer da, wenn es mal nicht lief mit der Arbeit und ich an einem Problem hängengeblieben bin. Du hast immer verständnisvoll genickt, wenn ich dir im Überschwang eines kleinen Durchbruchs total unverständlich erklärt habe, warum ich mich so freue.

Ohne die Unterstützung und die Geduld meiner Eltern wäre ich jetzt nicht da wo ich bin. Danke, an euch. Und Grüße auch an meine Oma...

Clemens, Anne, Willi, Fine, Kevin, Christian, Anni, und Matze, obwohl ihr wissenschaftlich nicht viel beitragen konntet, wart ihr super wichtig dafür, dass ich das Leben nicht aus den Augen verliere vor lauter Wissenschaft.